The synergy between Gravitational wave and Electromagnetic data of compact binaries

Proefschrift

ter verkrijging van de graad van doctor
aan de Radboud Universiteit Nijmegen
op gezag van de rector magnificus prof. dr. Th.L.M. Engelen,
volgens besluit van het college van decanen
in het openbaar te verdedigen op
maandag 24 november 2014
om 12:30 uur precies

door

Sweta Shah

geboren op 4 oktober 1984
te Kathmandu, Nepal

Promotor:	Prof. dr. Gijs Nelemans	KU Leuven, België
Copromotor:	Dr. Marc van der Sluys	
Manuscriptcommissie:	Prof. dr. Tom Heskes	
	Prof. dr. Bernard Schutz	Albert Einstein Institute, Duitsland
	Prof. dr. Paul Groot	
	Dr. Chris van den Broeck	Nikhef
	Dr. Samaya Nissanke	University of Colorado, Verenigde Staten

The synergy between Gravitational wave and Electromagnetic data of compact binaries
PhD thesis, Radboud University Nijmegen, The Netherlands
Cover design by Shivendra Shah. Image: Gravitational waves generated by the white dwarf pair. Image credit: NASA, ESA, SSC, CXC, and STScI

This work is part of the research program of the Foundation of Fundamental Research on Matter (FOM), which is part of the Netherlands Organization of Scientific Research (NWO).

ISBN: 978-94-6259-409-8

CONTENTS

ABSTRACT

Most of what is known about the formation and evolution of compact Galactic binaries made of white-dwarfs, neutrons stars and stellar black holes are inferred from about ~ 100 observations of these sources in the electro-magnetic wavelengths. This is in contrast with the theory that predicts that there are $\sim 10^8$ of them in our Galaxy. Soon we will observe thousands of these systems by directly detecting their loss of orbital energy to the gravitational wave radiation. This thesis aims to quantitatively estimate how can knowing and combining information from both electromagnetic (EM) radiation and gravitational wave (GW) radiation improve our knowledge of the astrophysical parameters (e.g. masses, orbital periods) of these systems. This in turn will help us in understanding the most important physical processes that lead to their formation and evolution. Gravitational wave observations alone will measure the GW frequency of all sources with accuracies better than 10^{-6}Hz thus providing a quantity with a large sample for a direct comparison with that in our theories. While the inclinations of optimally oriented (face-on) sources will have huge uncertainties in their inclination measurements, the same for the eclipsing sources will be constrained much better giving us opportunity to discover eclipsers electro-magnetically. Measuring their sky positions from the EM observations in return can improve the parameter uncertainties significantly. Additionally, EM data on radial velocity will break the degeneracy between the masses and improve our knowledge of the intrinsic parameters of the binary. The opportunity of doing tidal physics in these sources before they transfer mass will only be possible for extreme systems if we discover them. Finally, we find that combining EM data on orbital decay rate from the observations of the eclipse timings with GW data on amplitude and inclination will be very valuable in constraining eLISA binary parameters. We have also studied the high frequency compact binaries made of neutron stars and black holes, which will merge in timescales of minutes-seconds and will be soon observed by the ground-based GW detectors. Here we find that having one or two spinning objects influences the mass parameters significantly, This may help us to distinguish binary black hole from neutron star black hole system that have same chirp mass.

CHAPTER 1

INTRODUCTION

Gravitational waves (GW) are at the verge of being directly detected (~ 2016). Undoubtedly this will open a whole new way of observing, interpreting and understanding our universe and will in many ways be a complementary tool to electromagnetic (EM) radiation. Gravitational wave radiation, predicted by Einstein's General theory of Relativity is essentially the propagation of perturbations of the space-time. Unlike its EM counterpart GWs propagate unimpeded, making it the only (so far known) tool to directly detect the electromagnetically unattainable like the infant Universe. A thorough review on this subject can be found in e.g. Thorne [1987].

General Relativity predicts that the whole Universe should be bathing in gravitational waves. GWs are caused by any kind of accelerated motion of an asymmetric mass distribution. The theory, despite being devised almost 100 years ago in 1915, is yet to be directly tested. This unusual long delay in astrophysics between theory and detection is caused by its observational challenge: the perturbation amplitude of space-time is incredibly tiny due to the 'rigidity' of space-time. This means the following: GWs are disturbances of space-time and so any GW experiment requires a detection of a fractional squeezing of this space-time whose amplitude (h) is given by $h \sim \Delta L/L$, where L is the length scale between the test particles that are being squeezed perpendicular to the GWs that are propagating. The quantity h is of the order of 10^{-21}, which clearly is a very tiny number for any measurement even by modern science standards.

It is only in the past 20 years that we have been able to devise viable experimental setups to detect these small amplitudes of the disturbances. A number of these experiments have now culminated into international projects, which have made remarkable progress over the past decade, finally arriving at a point of being able to measure the minute perturbations directly. One such (future) class of experiments is the space-based gravitational wave detector, eLISA, which stands for the *evolved Laser Interferometer Space Antenna* [Amaro-Seoane et al., 2013]. One of the most ubiquitous sources, Galactic binaries will be targeted by eLISA, which is also the main focus of this thesis. Typically, the GW detectors are a version of an interferometer made of two or more arms exchanging lasers in between the test masses placed at the end of each arm. The basic response of such a laser interferometer to an incoming GW signal will be to squeeze and stretch the arms according to the polarisation of the GW wave. This minute fractional change in the armlength is measured by the change in the laser phase. This technique is often referred to as GW interferometry based on which the space-based GW detector, eLISA and the ground-based detectors, Laser Interferometer Gravitational-wave Observatory (LIGO[1] in the USA), Virgo[2] (in Europe) function. Strictly speaking, eLISA is only a working design for an approved GW space mission with a launch date of 2034. The ground-based detectors on the other hand, which are presently undergoing upgrades, will be online soon (∼2015-2016) and start collecting GW data. Unlike EM detectors, GW detectors are broadband instruments which collect information from the entire sky simultaneously and are very often given an analogy of hearing 'ears'. The all-sky coverage implies we can 'listen' to the Universe but it will be impossible to ascertain where in the sky the source is with the precision that many EM detectors are capable of. The gravitational wave landscape is very rich. Similar to the EM spectrum the GW spectrum also spans orders of magnitude in the frequency with guaranteed, promising and potential new sources in every frequency band. Figure 1.1 is a schematic representation of the variety of sources and the corresponding detectors that are either already functioning or will become online in the future. As can be read from the figure, most of the (known) astrophysical sources are some sort of binaries consisting of supermassive black holes or stellar compact objects, the latter of which is the major focus of this thesis.

GWs are coherent superpositions arising from bulk motion of the source, whereas EMs are incoherent superpositions of radiation caused by the motion of charged particles in in the source/environment. Therefore, the two types of information coming from the same source are very different from each other and can be complementary in learning about the source. Since we anticipate on obtaining a new type of information on some of the astrophysical sources, we need to investigate what will the new information reveal about these sources and what can be the added benefit of combining the new information with EM data. This is the primary topic of investigation in this thesis.

The following subsections explain the gravitational waves (namely the GW waveforms) radiated from one of the most prominent and promised sources for both the ground-based and space-based GW detectors, namely the Galactic binaries; the astrophysical knowledge of these sources from EM observations and theory; the GW observable from the eLISA detector; our method of analysing the GW signals and extracting source information from them; and finally our main findings from each of the following thesis chapters.

---

[1] www.ligo.caltech.edu/

[2] www.ego-gw.it/

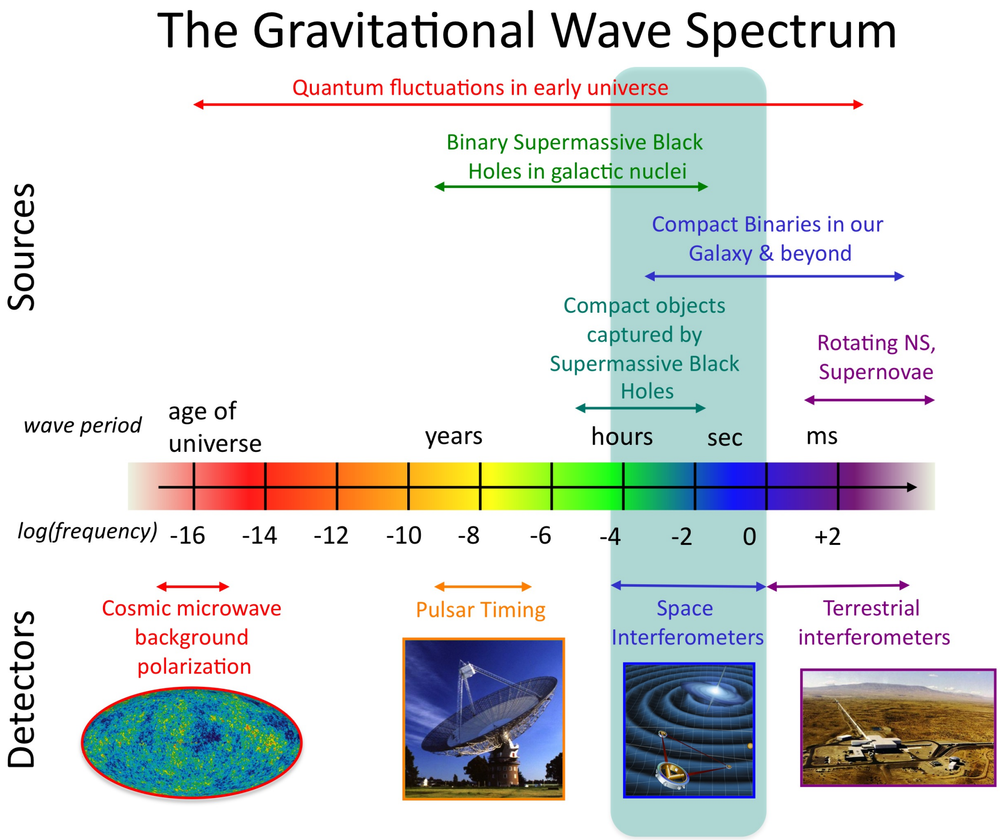

Figure 1.1: The entire gravitational wave spectrum with examples of sources in each frequency regime. In the bottom of the figure various GW detectors are shown targeting different frequency regimes. These detectors are either already functioning/being upgraded or in future plans.

1.1 GW radiation from Galactic binaries

The aim of this section is to motivate gravitational waves (GW) as oscillations of the space-time, which are generated by an accelerating non-spherical gravitational source (two point mass in our case) and their propagation through vacuum space sufficiently far way from the source. Since GWs arise from bulk motion of the source, they reflect the overall dynamics of the emitting source. The quantity $g_{\mu\nu}$, a 4 dimensional metric tensor is a fundamental quantity in General Relativity (GR) that characterises the properties of space-time. In GR there is a direct link between this space-time metric and the energy density (mass distribution for two point objects considered in this thesis) and therefore this allows for a solution of the structure and dynamics of space-time as a function of the structure and dynamics of the masses. As explained below this is very hard to do and physically motivated approximations are posed to make progress in deriving the gravitational waves from a two point binary system.

The starting point is the foundation of the theory of General relativity that is posed in the following Einstein Field equations (EFE) that link the space-time curvature to an underlying metric due to matter and energy:

$$R_{\mu\nu} - \frac{1}{2} g^{\mu\nu} R \equiv G_{\mu\nu} = 8\pi T^{\mu\nu} \tag{1.1}$$

In the equation above, $R_{\mu\nu}$ is the Ricci curvature tensor and R is the Ricci scalar. $R_{\mu\nu}$ is a function of the metric $g_{\mu\nu}$ and its first and second derivatives and R is the trace or contraction of $R_{\mu\nu}$. These two quantities can be written in the form of the Einstein tensor $G_{\mu\nu}$, which describes the geometry of the space-time. The stress-energy tensor on the right hand side of Eq. 1.1, $T^{\mu\nu}$, describes the density and flux of energy and momentum. This equation is basically a shorthand of a set of ten non-linear partial differential equations for which there exists no general solution to date. Nonetheless, the equation characterises the interplay between matter, space-time and energy and if the distribution in the matter has a temporal evolution then the curvature can also have such a time-variation. This variation in curvature (or metric) will propagate away from the varying matter and energy distribution (i.e. the source) creating ripples in space-time in the form of the gravitational waves.

The GW source discussed primarily in this thesis is characterised as a system that has two stars in a (circular) orbit: a binary. Thus, in order to derive the GW radiation for a two-point mass, we realise that far away from the source (in the distant wave zone) the effect of GWs is a small/weak perturbation in the underlying flat space-time (Minkowski) metric $\eta_{\mu\nu}$, expressed as:

$$g_{\mu\nu} = \eta_{\mu\nu} + h_{\mu\nu}, \tag{1.2}$$

where $|h| \ll 1$. This allows us to understand linearised waves as small-scale variations propagating across the surface of a background space-time, a formalism known as the "shortwave approximation" (Brill & Hartle). However, in order to study the production of the wave in the vicinity of the source (strong wave regime) the formalism should take into account the metric, $g_{\mu\nu}$, close to the source. In order to make progress Eq. 1.1 is *linearised* where the Ricci tensor and scalar are taken to the linear order in the metric perturbation (Eq. 1.2). The result takes the form:

$$\Box \bar{h}^{\mu\nu} = -16\pi T_{\mu\nu}, \tag{1.3}$$

where the $\Box = -\frac{\partial_t^2}{c^2} + \partial_x^2 + \partial_y^2 + \partial_z^2$ is the flat space d'Almbertian operator and c is the speed of light. This formalism resulting in the above equation is called to the linearlised theory in GR. It can be directly applied to the production of the gravitational waves where the GW corresponds to the metric perturbation, $h_{\mu\nu}$. Eq. 1.3 in vacuum ($T_{\mu\nu} = 0$) is interpreted as the source free wave equation. The solutions satisfy the differential equation $\Box \bar{h}^{\mu\nu} = 0$, and take the following familiar form:

$$\bar{h}^{\mu\nu} = \mathcal{R}\left[A_{\mu\nu} e^{ik_\alpha x^\alpha}\right], \tag{1.4}$$

where $A_{\mu\nu}$ are the complex components of a complex constant amplitude tensor, k_α are wave vector components, x^α are the cartesian coordinate components, and $\mathcal{R}\left[\cdot\right]$ is the real-part operator. Applying the real part operator in Eq. 1.4 gives physical solutions to the wave equation, which is of the form:

$$\bar{h}^{\mu\nu} = |A_{\mu\nu}| \cos(\omega t \ + \ \vec{k} \cdot \vec{x} + \ \delta), \tag{1.5}$$

where ω is angular frequency and δ is a constant related to the real and imaginary parts of $A_{\mu\nu}$. The above equation implies that gravitational waves propagate in the $\hat{k}$ direction with frequency $2\pi\omega$. Eq. 1.3 with the source term is usually solved by invoking Green's function. The solution is derived by considering the solutions far away from the isolated source and not-relativistic source motion, which implies $\lambda \sim \frac{c}{v} r$, where v is source velocity and r is distance to the source. This condition simplifies the $T_{\mu\nu}$ to T_{ij}, which has only spatial components. In this limit, the leading order multipole expansion of T_{ij} is the quadrupole moment of the mass distribution is given by $I_{ij}(t) = \int \rho(\mathbf{x}) x^i x^j d^3x$ where ρ is the source's mass density. The wave equation becomes

$$\bar{h}^{ij}(\mathbf{x}) = \frac{2}{r} \frac{d^2 I_{ij}(t_r)}{dt^2}, \tag{1.6}$$

where $t_r = t - r/c$ is the retarded time. The above equation is called the *quadrupole formula* for the amplitude of the gravitational wave. The leading order component of the gravitational wave radiation is given by the '00' component of the energy tensor:

$$\int T^{00}(t, \vec{x}) x^{ij} \, d^3x = M^{ij}(t), \tag{1.7}$$

where T^{00} is the energy density of the source and $\vec{x}$ is the spatial coordinate of the GW source distribution. This dominant term gives the following solution to Eq. 1.3:

$$h_{ij}^{TT}(t) \ = \ \frac{2}{r} \ddot{M}^{ij}(t - r), \tag{1.8}$$

where the TT means the symmetric, transverse and traceless part of the tensor. The GW detectors measure the relative difference between two distances, the so-called strain, often written as h or as a function of time $h(t)$. Like its EM counterpart, $h(t)$ has two polarisations: + and × that are given by:

$$h_+ \;=\; \frac{1}{r}\left(\ddot{M}^{11} - \ddot{M}^{22}\right), \quad h_\times \;=\; \frac{2}{r}\ddot{M}^{12}. \tag{1.9}$$

The differentiation of the quadrupole moment components with respect to the time gives the following result:

$$\ddot{M}^{11} \;=\; \ddot{M}^{22} \;=\; 2\mu r^2\omega^2\cos\left(2\int_0^t \omega(t')dt'\right), \quad \ddot{M}^{12} \;=\; -2\mu r^2\omega^2\sin\left(2\int_0^t \omega(t')dt'\right). \tag{1.10}$$

The above derivation assumes the time-varying quadrupole moment is evaluated in the transverse-traceless frame and the gravitational waves propagate along the z direction and this is referred to as the "radiation frame". Thus the summary of the above formalism describes the binary system and the propagating gravitational waves in different coordinate systems. In the Newtonian limit[3], the GW signal emitted by a binary system whose location is in the direction of $\vec{k}$ is given by the two polarisations:

$$h^+ = h_0\frac{(1+\cos^2\iota)}{2}\cos(2\omega t+\phi_0), \qquad h^\times = h_0\cos\iota\sin(2\omega t+\phi_0) \tag{1.11}$$

where ϕ_0 is initial phase of the signal and h_0 is given by,

$$h_0 = \frac{(4G\mathcal{M}_c)^{5/3}}{c^4 d}\left(\frac{\omega}{2}\right)^{2/3} \tag{1.12}$$

where

$$\mathcal{M}_c = \frac{(m_1 m_2)^{3/5}}{(m_1+m_2)^{1/5}}, \tag{1.13}$$

is the chirp mass, d is the distance to the source and ω is the GW angular frequency of the GW signal at some reference time $t = 0$. m_1 and m_2 are the individual masses of the binary system.

1.2 Formation and evolution of the compact Galactic binaries

A brief summary of important (well known/or not known) processes of compact binary formation, the methods of studying their evolution and a survey of what is known from the electromagnetic data are presented in this section. For a thorough history on the emergence of the interest of studying close binaries as sources of Gravitational Waves (GW) (long

---

[3] implying that the typical speed of source $v \ll c$

after they were predicted from the General theory of Relativity) can be found in Postnov & Yungelson [2014]. The latest stages of the close compact binaries are driven by emission of GWs and how this radiation depends on the time varying mass quadrupole defining the binary. GW observations of such sources will provide a testbed for the General theory of Relativity and more importantly allow us to understand the properties and the processes leading to the formation of these binaries that are often made of White dwarf (WD), a neutron star (NS) or black hole (BH). The initial masses of stars range from $0.1 - 100$ the mass of the Sun (a solar mass, indicated as $M_{\odot} = 1.98 \times 10^{30}$ kg). Depending on the initial mass of a star it will evolve into a WD, NS and BH, which are also known as *compact* stellar objects. A compact star is an object that has a very strong internal gravitational field, which is determined by the so called "compactness parameter" given by $GM/(Rc^2)$. M, R are the mass and radius of the star respectively. The compactness parameter for our Sun is $\sim 10^{-6}$, a typical WD is $\sim 10^{-4}$, a typical NS is ~ 0.3 and a typical stellar BH is ~ 0.5. Stars like our Sun will end up as a WD, whereas stars with initial masses of $8 - 25 M_{\odot}$ will evolve into NS and those more massive will likely collapse into BHs at the end of their stellar evolution. For the space based GW detector eLISA, the most relevant Galactic binaries are the double WDs, interacting WDs that are called AM CVns and the ultra compact X-ray binaries (where the accretor is a NS or a BH). The later two types of sources are also known as mass-transferring binaries (described later in the section). These sources will radiate in the frequency range $10^{-4} - 1$Hz. For circular orbits, this frequency range translates to orbital periods of ~ 5hrs $- \sim 20$s. The ground-based detectors target the last stages of the evolution of NS and BH binaries where their orbital timescales for the inspiral and merging phase are in the order of minutes-milliseconds. In this section we are concerned with the properties and evolution of such compact binaries in our Galaxy.

The importance of understanding stellar binaries is reflected in their ubiquitous presence in our Universe. Observations imply that about $(40 - 60)\%$ of solar mass stars are in binaries and almost all of the massive A/B, O spectral type stars are binaries [Duchêne & Kraus, 2013]. A significant fraction of these binaries form at "close" separations where the close binary interactions greatly influence the evolution of their stellar components. From a (limited) number of electro-magnetic observations of such compact binaries (made of WD, NS, BH) and modelling of the most important physical processes from the main sequence stars in the binary up to their compact configuration, we have a rough idea of how such compact sources may be formed. However there are many aspects in this formation and evolution that are far from well understood and thus the prospects of observing these binaries via their GW radiation is very exciting and may help to illuminate our understanding of these sources.

The most important parameters of a binary system are its masses m_i/mass ratio (q) and its orbital separation a. The orbital separation is related to the orbital period P_{orb} through Kepler's third law, $a^3 \propto P_{\mathrm{orb}}^2$. It is fair to say that studying evolutionary processes in most systems in astrophysics is challenging because of the long timescales over which the physical processes occur and a large range of length scales in which numerous physical processes occur. This is no different in the case of studying compact binary systems. The starting point for a compact binary is a pair of main-sequence stars with initial sizes larger by factors of 1000. A significant fraction of the binary life-time (of billion-million years) is spent on nuclear burning in the individual stars after which the evolutionary expansion of the main-sequence stars will result in the more massive of the stars filling its Roche-lobe, leading to a mass-transfer to its companion. The roche-lobe describes the structure of the region around each of the stars in binary where its corresponding gravity is dominant and this is determined mainly by q. The nature of the mass-transfer (stable or not) is also primarily driven by q. It is widely believed that forming a compact binary requires ($\geq$ one) event of the so-called common-envelope phase during the initial evolution of binary system after nuclear burning. During this phase the mass transfer onto the accretor is so extreme that the entire system is engulfed in the (common) envelope of the expanding donor. The companion experiences friction while orbiting inside the envelope material and is thus loosing angular momentum and energy. It is believed that this process lasts from months-years only (which is like an eye-blink in the life-time of binaries) but is responsible for drastically changing the binary configuration by reducing its orbital size by factors of ten to hundred [Paczynski, 1976; Bulik, 2007]. Later the companion will also expand the binary may undergo a second common-envelope phase. At closer separations, gravitational radiation takes over and continues the inspiral of theses binaries, which are now made up of evolved stellar components (i.e. WD, NS, BH). Eventually the separation of the binary reduces to a few times the size of the compact object and at this point mass transfer may start. This will further affect the binary evolution whose details depend on the value of the q and which of the masses is accreting and what are the nature and properties of the accretor/donor.

The theoretical prediction of the evolution of different types of binaries made of the compact stars in frequency space is roughly charted in Figure 1.2 for the eLISA detector in the left part of the diagram. The neutron star/black hole binaries (shown in the grey shaded area) have stronger signals at the higher-frequency band as they inspiral and merge at much closer separations (higher f) and are observable by the ground-based GW detectors. GW observations of these binaries in statistically large numbers will allow us to test these predicted paths of their evolution. Due to the paucity of observations of these binaries and computational constraints there are a number of unsolved problems in the formation and evolution of binaries made of WD, NS and BH. These sources are hard to observe optically, because they are very small and very faint. To date there are less than 100 known low-f binaries with measured orbital periods where one of the stars is a WD. The number of observed double NS systems is smaller $\sim$ 10 and about half of them will merge within the Hubble time (i.e. the age of our Universe).There are no confirmed known GW sources with stellar mass black holes. Thus, the theoretical uncertainties also reflect the lack of observations where the properties of progenitors (such as their mass limits) of binaries with

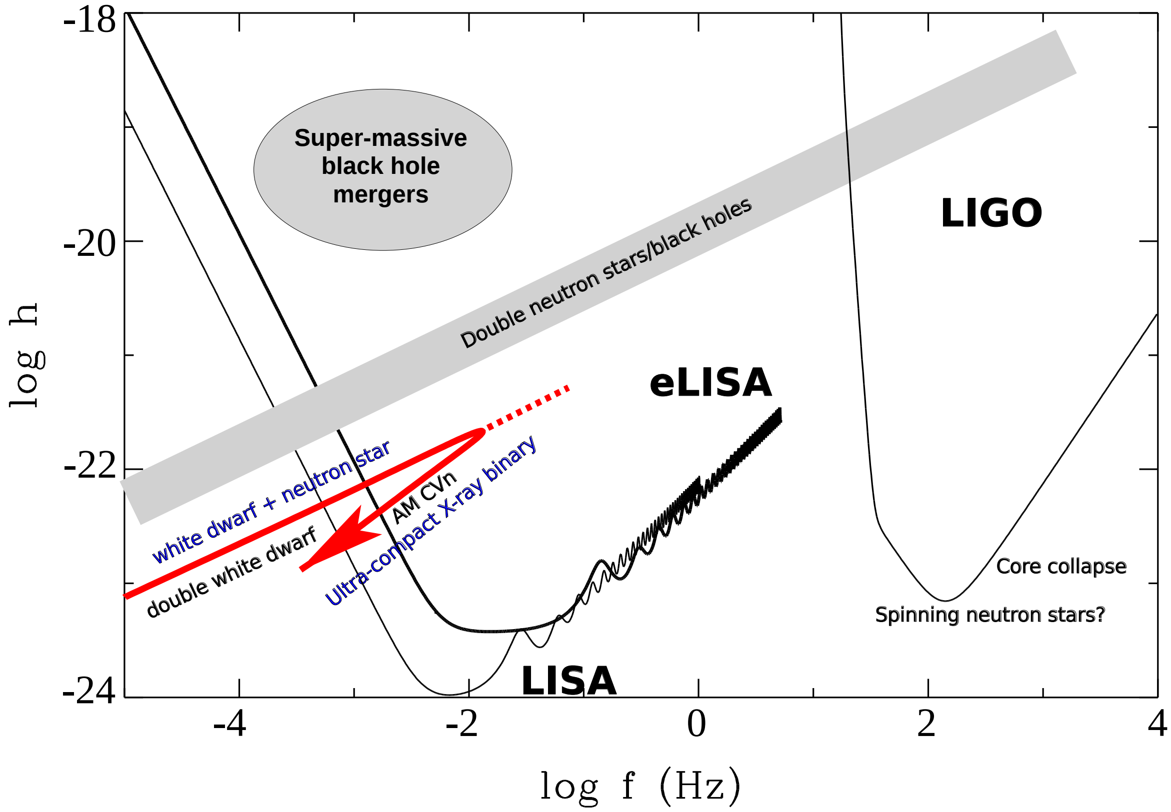

FIGURE 1.2: Strain versus GW frequency diagram showing the sensitivity curve of the proposed eLISA mission (in the thick black line) and ground-based detector, LIGO in the right side of the figure. The location and evolution of compact binaries in the low-f and high-f are shown. Because of the large size of WDs, binaries made of these stars are expected to radiate only at lower-f whereas the NS and BH binaries can inspiral to much smaller sizes radiating and merging at higher-f. Figure taken from Postnov & Yungelson [2014], which is based on Nelemans [2003].

NS and BH can be constrained.

The binary evolution is macroscopically and statistically studied by analytically modelling their physical processes from their main-sequence phase to their compact phases. One example of such study is the binary population synthesis (BPS) where an initial distribution of systems are picked and are evolved in time using analytical prescriptions for binary processes such as common-envelope phase, mass transfer, mass loss to stellar winds, tidal gravity to name a few [e.g. Webbink, 1984; Nelemans et al., 2001b; Toonen et al., 2014]. The stellar structure in such a method is not resolved and there are complementary studies that do the stellar structure studies in detail [Eggleton, 1971]. However, with the current computational capabilities detailed and simultaneous evolutionary studies of a statistically large number of binaries is not possible. The results of the BPS models are fundamental properties of binaries and the event rates of various types of binaries. These results have been used in this thesis in the context of computing typical uncertainties of the expected binaries from their GW observations. The inferred binary parameters from the EM observations of a number of these compact binaries are also used in this thesis in doing EM-GW synergy studies.

1.2.1 Measuring parameters: *Verification* binaries for eLISA

Unlike other GW detectors eLISA enjoys the privilege of the fact that there are guaranteed sources it should detect when it will start operating. These sources are a subset of compact binaries already known from electromagnetic observations that should also be detectable by eLISA and are therefore termed 'verification' binaries. In Figure 1.3 strain versus log GW f is shown, where the sensitivity curve is plotted as the solid black line. Everything above the line everything will be visible to eLISA. The green squares show the expected strain amplitude of HM CnC, V407Vul, ES Cet, AM CVn, HP Lib, V803 Cen, CR Boo and SDSS J0651+2844 (J0651, hereafter). A useful way of quantifying the strain (or the GW strength) for these binaries using Eq 1.12 is:

$$h \sim 10^{-21} \left(\frac{\mathcal{M}_c}{M_\odot}\right)^{5/3} \left(\frac{P_{\rm orb}}{1{\rm hr}}\right)^{-2/3} \left(\frac{1{\rm kpc}}{d}\right). \tag{1.14}$$

Except the last source listed above (J0651), the rest are interacting (or mass transferring) white-dwarf binaries. The interacting binaries are brighter and therefore more easy to recognise. However the detached should be more common (as most binaries have not evolved to the mass-transfer stage). However, with some dedicated efforts (targeting extremely low mass $\leq 0.25 M_\odot$ WDs) there have been numerous discoveries of short period detached WD binaries of which two are close and massive enough to be verification binaries for eLISA [Brown et al., 2011; Kilic et al., 2014]. The blue squares below the sensitivity curve in the figure are X-ray binaries where the accretor is a NS and WD systems with lower masses or larger distances. To date we do not have a confirmed source containing

BH although population synthesis predicts that in the order of $\sim 10^6$ of the them should exist [Nelemans et al., 2001a].

The parameters of the white-dwarf binaries are measured mainly from their optical spectra and light curve. For example, the mass-transferring AM CVn is a well-known system whose orbital period was measured by detecting the periodic movement of the "bright spot" (radiation from matter falling on the edge of the accretion disk) as the stars move in circular orbit around the centre-of-mass. By measuring the bolometric luminosity with the help of parallax-based distance to the source, mass transfer rates can be inferred, which in turn give an estimate of the donor mass [Roelofs et al., 2006]. The measurements of the spectra of one or both of the stars in the binary provide the measurements of their radial velocity.

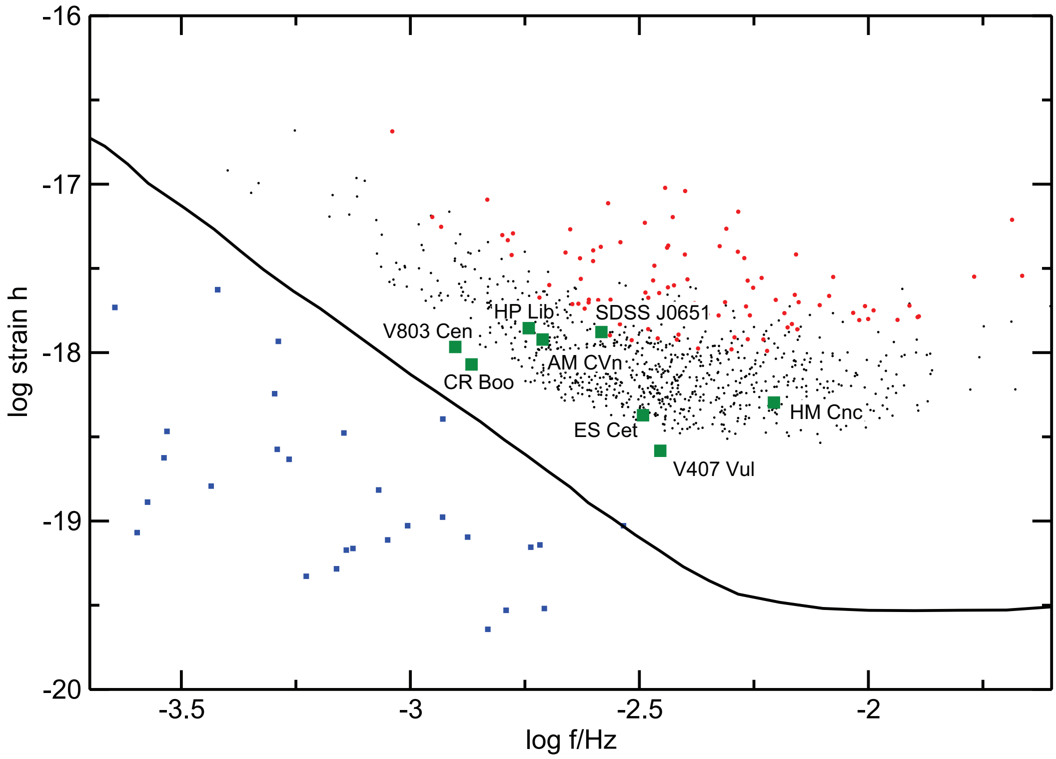

FIGURE 1.3: GW strain versus frequencies for the guaranteed (*Verification*) sources for the eLISA detector shown in filled green squares. The blue squares below the sensitivity line are also known EM sources (AM CVns, X-ray binaries, etc.) but are clearly too weak to be detected. The black and red dots are predicted sources from theory, which should be characterisable by the detector.

The radial velocity is related to both the masses, inclination and the orbital period and can be useful EM information that can be used to constrain inclination (see Chapter 4). If only one of the WDs is resolvable then we can have an estimate of the mass of the primary (or the brighter) object and its corresponding radial velocity as the object orbits the centre-of-mass. In case both the WDs are resolvable both their radial velocities K_i can be measured. This also gives an estimate of the mass-ratio via the relation $K_1/K_2 = m_2/m_1$. For detached systems the individual mass can be estimated by fitting WD models to the observed spectra. For eclipsing binaries the mass and radii parameters can be measure very accurately by observing the eclipses in the light curve. For example, for J0651, observation of ellipsoidal variations in its light curve provides its individual masses, accurate inclination and also the shape of the larger WD that is distorted by tides. The orbital parameters, f and its evolution $\dot{f}$ can also be inferred from its light curve by timing the eclipses over a long period of time and fitting a parabola to the curve. The implications of knowing these parameters of such binaries is very important in calibrating the BPS models and thus improving our knowledge of binary evolution. The EM information in combination with GW measurements of strain, GW frequencies, binary orientation (inclinations), etc. can enhance our knowledge of the binaries even further (see Chapter 5).

1.3 GW observables and detector response

Having motivated the importance of compact binaries with a brief summary on how we use EM observations to infer their parameters, we now turn to describing how their gravitational wave signals can be measured at a GW detector and what parameters these observations provide measurements of. Measuring GW signals from the binaries is hard, because the amplitude of these waves is very small. This can be realised by noting the G/c^4 factor in the GW strain Eq 1.12 and substituting some typical WD masses, their distance and orbital periods resulting in a strain amplitude in the order of 10^{-22} (see Eq 1.14), which is a small value. Observing GWs requires us to measure the small changes in the separations of the order of 10^{-22} between test masses, which is the effect of the propagating gravitational waves. With some dedicated effort in laser interferometry, measuring such small changes has become possible and in this section we briefly describe the method that is implemented in both the existing ground-based and the proposed space-based GW detectors. The existing method of detecting such signals relies on interferometry: by measuring the *relative phase difference between the incoming laser with that of the local laser when it is exchanged between pairs of test masses.* The separation between the test masses is determined by the size of the source (in our case this will be the size of the binary system). Since the GW wavelength emitted by the source is set by its size via Kepler's law, the size of the detector (or equivalently the separation between test masses) is set by the corresponding GW wavelength. For binaries made of neutron stars and black holes whose inspiraling phase is followed by merger phase taking place at higher frequencies (∼kHz), their sizes are in the order of ∼kilometres that are therefore targeted by the ground-based GW detectors such as LIGO and Virgo. The basic design of this detector consists of four (or two per arm) test masses that are suspended forming an 'L' shape with equal arm-lengths as shown in Figure 1.4. When a GW passes perpendicular to the plane of the detector, the armlenghts of the detector respond by stretching and squeezing in a way that keeps the total area of a static detector to a responding detector. Since a GW signal can have two polarisations (plus and cross), both will cause the armlenghts to stretch and squeeze reflecting a linear combination of the polarisations. The difference in the armlenghts caused by gravitational waves can be expressed as:

$$(L_1 - L_2)(t) = \Delta L(t) = Lh(t) \tag{1.15}$$

where L is the length of each detector arm. The response of the detector for both polarisation is given by:

$$h(t) = h_{+}(t)F^{+} \; + \; h_{\times}(t)F^{\times}, \tag{1.16}$$

where the $F^{\times,+}$ are the antenna sensitivities (i.e. geometric factors) for each of the polarisations for a source at a given location in the sky and are independent of time. This is the case for ground-based detectors where the masses are oriented in an 'L' shape. For the low-frequency Galactic binaries whose frequencies are in the mHz regime implying source sizes of 10^5km, a million km size arm-length detector is required which can only exist in space. The leading design for such a detector is the space-based gravitational wave detector often referred to as *eLISA (evolved Laser Interferometer Space Antenna).* As the name implies, eLISA also uses interferometric principles but its design is somewhat different from those of the LIGO-Virgo detectors (see Figure 1.5). The proposed design consists of four identical test masses where two of the test masses (housed in mother spacecraft) will be exchanging the laser with the remaining two test masses (housed in the daughter spacecrafts). The four test masses however will be in their individual orbit around the Sun trailing behind the Earth making a triangular form as they complete their heliocentric orbits once a year. Besides the translational motion around the Sun, the triangle made by the test masses will also make a 'cartwheeling' motion and this pattern of the orbit is depicted in Figure 1.5. The response of the eLISA detector to an incoming GW signal (and noises) is slightly different than that of the ground-base detectors. The periodically varying separations of the test masses due to the basic orbital dynamics induce a non-cancelling laser noise in the detector. This is not an issue for the ground-based detectors as they are fixed on Earth, which means that the laser noise from test mass A to test mass B will be cancelled exactly by the laser noise from test mass B to test mass A as the test masses themselves are stationary. Since the distances between test masses in space oscillate, the laser noises do not cancel exactly and moreover these oscillations are larger than that caused by the GW sources by many orders of magnitude (but at a different frequency). This has led to a novel formulation and development of so-called time-delay interferometry (TDI) to be

FIGURE 1.4: One of the several ground-based GW detector, namely the LIGO detector in Livingston, USA, with an armlength of 4 km. The other existing terrestrial detectors are: a second LIGO detector in Hanford, USA; Virgo in Italy; GEO in Germany; and KAGRA, which is being built in Japan.

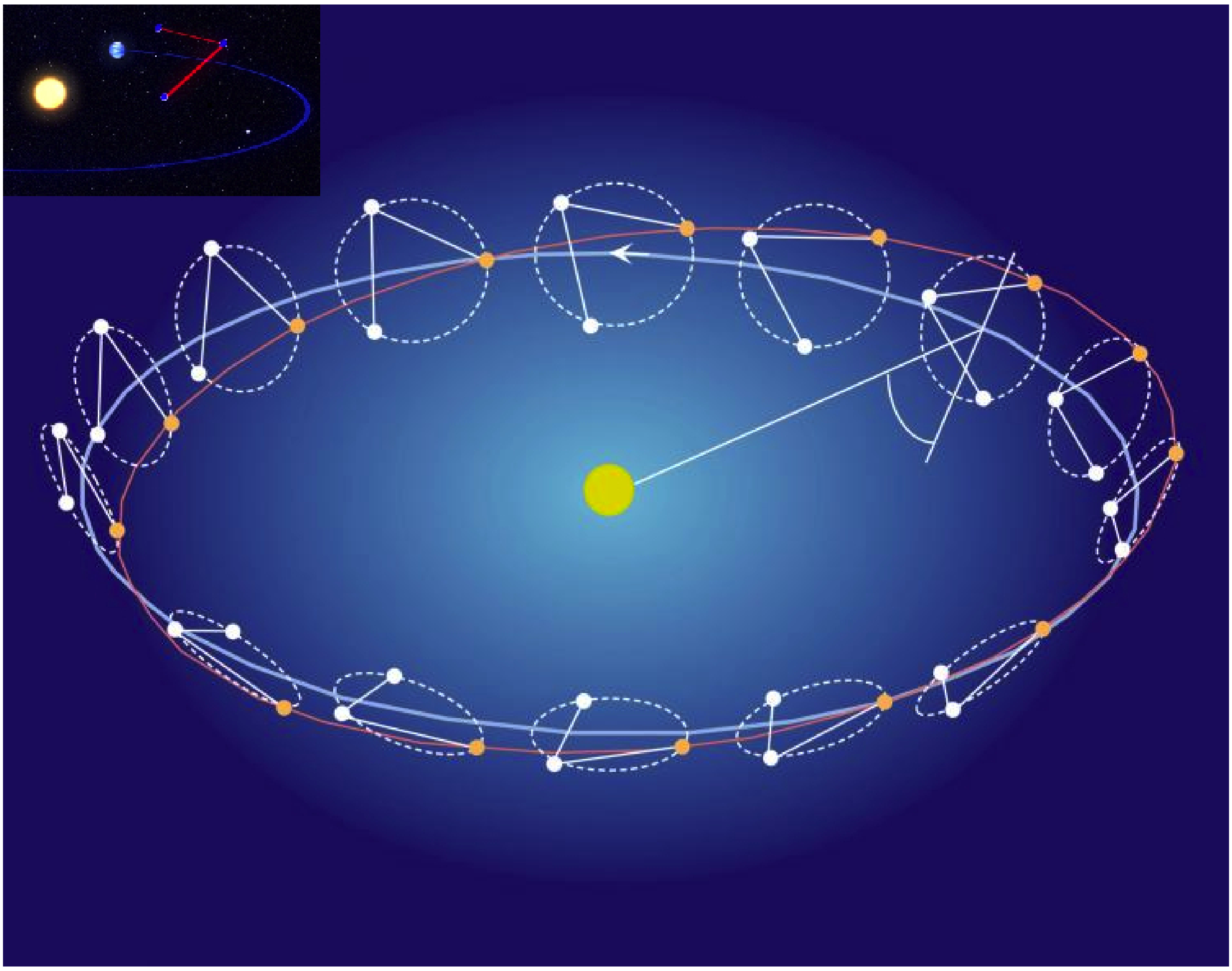

FIGURE 1.5: Depiction of eLISA orbiting around the Sun for a period of 1 year. The three freely falling space crafts separated at 1 million km are labelled in filled circles. They make a triangle and have a translational motion around the Sun. Additionally, the triangle makes a “cartwheel” as it orbits the Sun.

implemented in eLISA, which is designed to suppress the laser noise. The sensitivity curve of the detector is shown in Figure 1.2, where the GW strain amplitude is plotted against the log of GW f. Everything above the black solid line will be visible to eLISA and thus objects with strains larger than the black line can be characterised by the detector. The green squares in the figure are the verification binaries introduced in Section 1.2.1. The black dots are the 1000 of the strongest sources predicted from BPS models, which should be resolvable by eLISA and the red dots are the 100 strongest sources. The blue squares are other known sources that are below the sensitivity curve of eLISA.

The fundamental observable of an eLISA detector is the difference in phase between the local laser and the incoming laser, which will contain the fluctuations caused by the propagating GW signal. These phase-differences are converted into fractional-frequency differences (which is related to the phase-shifts by a time integration) that form the basic *Doppler observables* labelled by y_{sr}. It is defined as the fractional-frequency difference between received beam at the **r**eceiving spacecraft and the **s**ending spacecraft. This is the quantity that is coupled to the GW response for a plane GW and the instrumental noises in the spacecrafts made up of phase, shot and acceleration noises. As mentioned above, in order to suppress the laser noise, a specific combination of the phase differences/Doppler observables combined with specific time-delay in such a way that the laser noise cancels and this produces the data stream from the observations made by the detector. There are a set of such phase combinations, which satisfy the laser noise cancelling criteria and they are known as *TDI (Time Delay Interferometric)* variables. In the results presented throughout this thesis, the particular TDI variable called 'X' [Tinto & Armstrong, 1999] is used, which is given by the following time-delayed combination of phase-shifts between the three spacecrafts labelled as 1,2,3:

$$X(t) = y_{12}(t_{21}) + y_{21} + y_{13}(t_{31}) + y_{31} - y_{12}(t'_{21}) - y_{21}(t_{13}) + y_{13}(t'_{31}) + y_{31}(t_{12}), \quad (1.17)$$

where $t_{ij} = t - l_{ij}(t')$ and l_{ij} is the time-dependent length of the arm as measured between spacecrafts i and j. This formalism, which is independent of coordinates, can be applied to any configuration of space-detectors. Detailed derivation of the noise responses, the coupling of the noises and the gravitational wave signals can be found elsewhere [e.g. Tinto & Dhurandhar, 2004; Vallisneri, 2005a].

As mentioned above, the motion of eLISA is translational and the three spacecrafts orbit in such a way that they make a cartwheeling motion once a year in their heliocentric orbits. This will spread the power of a (monochromatic) gravitational wave signal (in frequency space) into frequency bins centred at the frequency at which the source radiates most of its GW radiation. In the time-domain signal the effect of the eLISA motion will manifest itself in modulating the (monochromatic) signal of a low-frequency compact binary in its amplitude, phase and frequency due to the sweeping of the detector sensitivity and the relative motion of the detector with respect to the long-lived source. The intrinsic information about the physical source (e.g. its GW strength, the frequency at which it

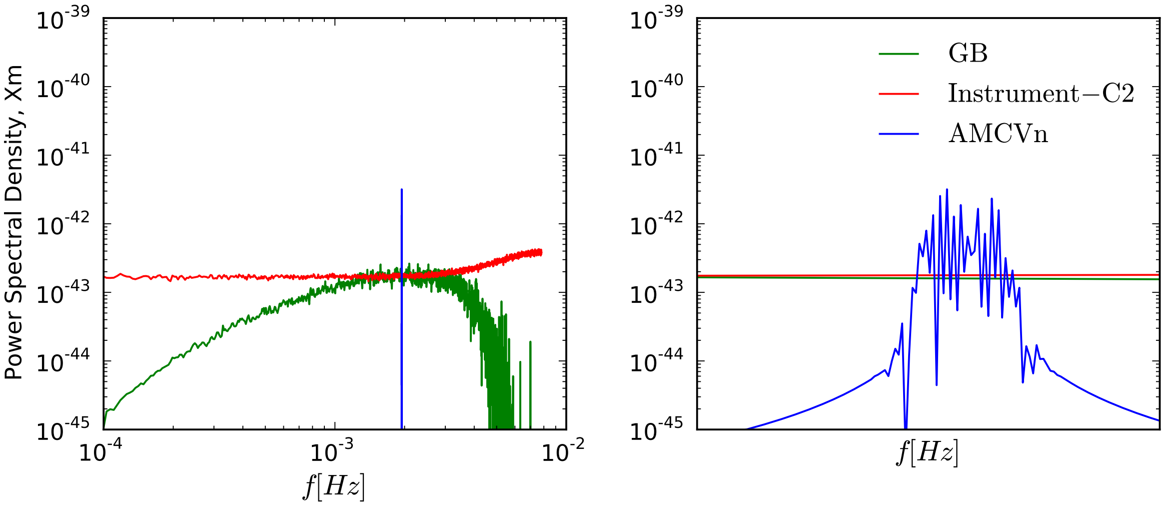

FIGURE 1.6: Gravitational wave spectra of AM CVn (verification) binary, instrumental noise and the Galactic foreground radiation as labelled in the right panel. The vertical axis is the *TDI* observable, Xm, which includes the eLISA response of 2 years of observation time. The right panel is a zoom around the $f = 0.001944 \pm 0.02$Hz of AM CVn, where the left side to the right side of the plot range from 0.001942 to 0.001946 in order to show the various modulations in the GW signal. At this frequency both the foreground (green) and the instrumental noises (red) are comparable and roughly constant in frequency.

radiates) is encoded in the GW signal that is emitted, unlike the orbital orientation, and the extrinsic information (angular parameters), which depend on the relative position of the source with respect to the detector, are encoded in the various modulations to the monochromatic signal. Thus the added complications in the GW signal induced by the orbital motion are for the advantage of extracting information on the angular and orientation parameters of the (monochromatic) source, which would otherwise not be possible as the GW detectors are all sky-monitors. The GW spectrum of the verification binary AM CVn is shown in Figure 1.6 along with the instrumental and the Galactic foreground noise as labelled. In the right panel of the figure the area around the signal is zoomed in to show the spread of the power of the GW signal in different frequency bins caused by the modulations arising from the detector motion with respect to the sources. The Galactic foreground is a cumulation of millions of short period binaries (mostly with $f \leq 3mHz$), where most of the binaries are expected to overlap in frequency bins forming a Galactic foreground noise. Most of these sources will be unresolvable and will be at the level of detector noise as can be seen in Figure 1.6. This foreground is generated using BPS models.

1.4 GW Data Analysis

Since the GW signals of many of the Galactic binaries will be buried in the noise of the detector (see Figure 1.6) for both the space-based and ground-based GW detectors, the data analysis techniques for the continuous/periodic sources rely on methods that filter out the astrophysical signal from the noise. Reliable models of the waveforms (i.e. GW signals) of these *inspiraling* sources, especially the (slowly) inspiraling binaries in the low frequencies (for eLISA) and coalescing binaries in the high frequencies (for LIGO Virgo), are available means that we can employ *matched-filtering methods* [Finn, 1992; Finn & Chernoff, 1993; Cutler & Flanagan, 1994] in signal detection and parameter estimation. The basic idea of the matched-filtering method is to cross-correlate the signal with the data with an additive (Gaussian) noise and find a best fitting model to the data to filter out the signal. Specifically, the unknown set of source/signal parameters are determined by maximising the correlation of the data with an entire family of templates that correspond to different sets of values of the parameters. The set of parameters that maximises the matched filtering result is taken as the best estimate of the *real* parameters of the astrophysical signal. Given a single experiment with a (Gaussian) noise, the measurement of the signal parameters will be given by a probability distribution function specifying the interval in that the true parameters lie at a specified confidence level.

The primary goal of this thesis is to quantitatively address how much we gain or learn about the sources by complementing the electromagnetic observations of the binary sources with that gravitational wave data or vice versa. More specifically, we ask what are the improvements in the accuracy with the Galactic binary parameters in their EM-GW synergy? For eLISA binaries their extremely slow inspiral and non-relativistic motions imply that the signals are Newtonian and therefore such monochromatic sources are completely characterised by seven parameters in GW observations. In some cases where the inspiral will be significant compared to the eLISA lifetime, an eighth parameter characterising the inspiral will be also important. For the coalescing binaries observable by the ground based detectors the relativistic motions are non-negligible and must be taken into account, which increases the parameters that characterise such systems to $\geq 9 - 17$ depending on whether spins are taken into account. Predicting our knowledge of what GW observations requires us to extract the parameter accuracies of the source parameters from the GW data which is a time-series.

In principle, doing this properly, i.e. mapping out the probability distributions of the parameters, demands a comprehensive exploration of the global ($\geq$ 7) parameter space that make use of for instance the Bayesian based Monte-Carlo methods [e.g. Christensen & Meyer, 1998; Cornish & Crowder, 2005; Nissanke et al., 2010]. While this is the most robust method we have, this way of analysing a source is severely limited since they are extremely time-consuming. For instance, extracting parameter uncertainties for just one monochromatic source (with 7 parameters) on a single laptop can takes several hours whereas for a binary with one spinning source that has 12 parameters the analysis take up to 3 weeks [van der Sluys et al., 2008]. While MCMC methods should be used in the actual data for signal detection and inferring its parameters, for our global studies we have used analytic methods, which predict the parameter uncertainties and are very fast to compute and are well-suited for our studies where the analyses need to be done for thousands of systems under certain conditions. One such method is a very well known and well worn method based on Fisher matrix methods, which is described in the following section. We implement this method, which forms the core method in analysing results in the chapters of this thesis. While the method is speedy, one must take care in interpreting Fisher-based results because of the method's limitations that will also be discussed in the next section.

1.4.1 Fisher matrix method

In this section we give a brief summary of the Fisher matrix method [Fisher, 1935] and its particular implementation used in this thesis. This is a method that is widely used in the GW community to *predict* the accuracies in the GW parameters which can be extracted from the GW observations. The most advantageous aspect of this method is that the GW parameter accuracies can be computed analytically and and therefore the computational speed is increased, which is the major disadvantage of Bayesian-based MCMC data analysis methods. Below a brief derivation of the Fisher-related quantities are given.

In most (observational) experiments what we have is data d and what we want to determine is the noise-dependent joint *posterior distribution* of a given set of parameters that we want to estimate. The posterior is written as $p(\vec{\theta}; n)$ given d and the noise n. The *likelihood* L of a data set d, for a given set of model parameters denoted with $\vec{\theta}$, is given by: $p(d|\vec{\theta})$. The goal in parameter estimation is to go from the likelihood to the posterior distribution. If there is no *prior* information about the parameters, $p(\vec{\theta}) =$ constant, and Bayes' Theorem implies $p(d|\vec{\theta}) = L$. This basically reads that the inferred posterior is given by the likelihood weighted the by the prior, which means that we update our conclusion on a given experiment by basing it on the information that has been acquired before the experiment and after the data has been obtained. To make progress, generally, Bayes' expression above is rewritten in log-quantities and the resulting log-likelihood is Taylor-expanded about its maximum. We then obtain derivatives of $\mathrm{Log}(L)$, where the constant term is not useful in ascertaining parameter constraints. The first derivative is 0 at the maximum of the likelihood by construction and therefore the first useful term in the Taylor-expansion is the second derivative or the Hessian (curvature matrix) of the likelihood. This defines the Fisher Matrix:

$$F_{ij} = -\left\langle \frac{\partial^2 \ln L}{\partial\theta_i \partial\theta_j} \right\rangle \tag{1.18}$$

where i, j label the parameters. For the case of a Gaussian likelihood, this is analytically computable, and can depend only on the expectation values of the data, and the covariance. In other words, if the signal strength is high enough the $p(\vec{\theta}; n)$ collapses around the maximum-likelihood into a Gaussian distribution with the covariance given by the inverse of the Fisher matrix, which is not a function of n. This is also known as the linearised-signal approximation since in this limit the GW waveforms are considered to be a linear function of the parameters. Thus, in essence Eq 1.18 is a measure of how fast the likelihood falls away from the best-fit (or true) parameter value giving us a measure of the parameter uncertainties and this in turn depends on how the GW signal changes with respect to the signal parameters as will be derived later. The likelihood of a signal in Gaussian noise is:

$$\begin{aligned} p(d|\theta) &\propto \exp\left[-\frac{(d-h(t,\vec{\theta})),(d-h(t,\vec{\theta}))}{2}\right] && (1.19)\\ &\propto \exp\left(-\frac{1}{2}\int dt_1 dt_2 n(t_1)\Omega(t_1,t_2)n(t_2)\right) && (1.20)\\ &\propto \exp\left(-\frac{1}{2}\int dt_1 dt_2 [d(t_1)-h(t_1;\vec{\theta})]\Omega(t_1,t_2)[d(t_2)-h(t_2;\vec{\theta})]\right), && (1.21)\end{aligned}$$

where $d(t) = h(t,\vec{\theta}) + n(t)$ is the data stream made of signal h plus a (Gaussian) noise realisation n and θ is the source parameter. The variable $\Omega(t_1,t_2)$ is defined in terms of the auto-correlation function of as:

$$\Omega(t_1,t_2) = R^{-1}(t_1,t_2), \tag{1.22}$$

where $R(t') = \langle n(t+t')n(t)\rangle^4$ is known as the auto-correlation function. The (a,b) used in Eq 1.19 is an inner product defined as:

$$(a,b) = 4\mathcal{R}\int_0^\infty \frac{\tilde{a}(f)^*\tilde{b}(f)}{S_n(f)}\,df, \tag{1.23}$$

where $\mathcal{R}[\cdot]$ is the real-part operator and $\tilde{a}(f)$ is the Fourier transfer of the time-series $a(t)$. The quantity $S_n(f)$ is the *one-sided power spectral density* of the detector noise defined as

$$S_n(f) \equiv \frac{1}{2}\int_{-\infty}^{\infty} dt' R(t') e^{i2\pi f t'}. \tag{1.24}$$

Upon substituting the above two equations in Eq. 1.18 we get the following:

$$\begin{aligned} F_{ij} &= -\left\langle \frac{\partial^2 \ln L}{\partial\theta_i\partial\theta_j}\bigg|_{\theta_0}\right\rangle_d && (1.25)\\ &= \frac{\partial^2 \ln p(d|\vec{\theta})}{\partial\theta_i\partial\theta_j}\bigg|_{\theta_0} && (1.26)\\ &= \int \mathcal{D}\, dt_1\, dt_2\, p(d|\vec{\theta_0})\left[\frac{\partial^2 h}{\partial\theta_i\partial\theta_j}(t_1;\vec{\theta_0})\Omega(t_1,t_2)\left\{d(t_2)-h(t_2;\vec{\theta_0})\right\}\right. && (1.27)\\ &\qquad \left. -\frac{\partial h}{\partial\theta_i}(t_1;\vec{\theta_0})\Omega(t_1,t_2)\frac{\partial h}{\partial\theta_j}(t_2;\vec{\theta_0})\right] && (1.28)\end{aligned}$$

---

[4] assuming ergodicity, i.e. the ensemble average of the Gaussian noise is given by time average

$\mathcal{D}$ in the equation above is functional integral is over all data realisations. In the limit where the signal-to-noise ratio (SNR) is high enough the first term in Eq 1.28 is negligible compared to the second term, and thus we get:

$$F_{ij} = \int dt_1\, dt_2 \left(\frac{\partial h}{\partial \theta_i}(t_1; \vec{\theta}_0) \Omega(t_1, t_2) \frac{\partial h}{\partial \theta_j}(t_2; \vec{\theta}_0) \right) \int d\, p(d|\vec{\theta}_0) \tag{1.29}$$

$$= \int dt_1\, dt_2 \left(\frac{\partial h}{\partial \theta_i}(t_1; \vec{\theta}_0) \Omega(t_1, t_2) \frac{\partial h}{\partial \theta_j}(t_2; \vec{\theta}_0) \right) \tag{1.30}$$

$$= \int df_1\, df_2 \left(\frac{\partial \tilde{h}}{\partial \theta_i}(f_1; \vec{\theta}_0) \tilde{\Omega}(-f_1, -f_2) \frac{\partial \tilde{h}}{\partial \theta_j}(f_2; \vec{\theta}_0) \right) \tag{1.31}$$

The auto-correlation in Eq. 1.22 and the one-sided power spectra density that is defined as $\frac{1}{2} S_n(f) = \int_{-\infty}^{\infty} dt' R(t')\, e^{i 2\pi f t'}$ gives $\tilde{\Omega}(f_1, f_2) = \frac{\delta(f_1+f_2)}{(1/2) S_n(f_1)}$. Using the above and assuming that $h(t)$ is real, we get:

$$F_{ij} = \int df_1\, df_2 \left(\frac{\partial \tilde{h}}{\partial \theta_i}(f_1; \vec{\theta}_0) \frac{\delta(-f_1 - f_2)}{(1/2) S_n(-f_1)} \frac{\partial \tilde{h}}{\partial \theta_j}(f_2; \vec{\theta}_0) \right) \tag{1.32}$$

$$= \int df_2 \left(\frac{\partial \tilde{h}}{\partial \theta_i}(-f_2; \vec{\theta}_0) \frac{1}{(1/2) S_n(f_2)} \frac{\partial \tilde{h}}{\partial \theta_j}(f_2; \vec{\theta}_0) \right) \tag{1.33}$$

$$= \int df_2 \left(\frac{\partial \tilde{h}^*}{\partial \theta_i}(f_2; \vec{\theta}_0) \frac{1}{(1/2) S_n(f_2)} \frac{\partial \tilde{h}}{\partial \theta_j}(f_2; \vec{\theta}_0) \right) \tag{1.34}$$

From the definition of the inner product we get the following definition of the Fisher matrix:

$$F_{ij} = \left(\frac{\partial h}{\partial \theta_i}, \frac{\partial h}{\partial \theta_j} \right), \tag{1.35}$$

where the Fisher element is the noise-weighted inner product of the partial derivatives of the signal with respect to the signal parameters. The inverse of the matrix in Eq. 1.35 is the so-called variance-covariance matrix whose diagonal elements are the squared parameter uncertainties and whose off-diagonal elements are the parameter covariances (or correlations).

The Fisher-based uncertainties can be interpreted in various ways: a lower bound (i.e. *Cramer-Rao bound*) of an unbiased estimator of true source parameters, error covariance for the *maximum-likelihood* (ML) estimator with Gaussian noise, and covariance of the *posterior probability distribution* around the true source parameters. For derivations of these quantities we refer to Vallisneri [2008]. The last interpretation of the Fisher matrix is often useful in interpreting Fisher-based results because very often there is a prior information available in some of the (angular/positive valued) parameters, which can be be implemented in the Fisher-method. This information can be incorporated in the Bayesian view of the Fisher uncertainties. For Gaussian noise and strong signals (or equivalently when the source parameters depend linearly on the GW signals) the Fisher uncertainties and covariances reduce to the posterior distribution of the parameters.

Thus, in the Fisher matrix formalism, it is assumed that the posterior distribution of the parameters is of the Gaussian form. In the chapters below we compute the above quantity for the a number of verification sources (whose (GW) parameters have been inferred from (EM) data). Thus the Fisher elements are computed centred at these (GW) parameters and the expected uncertainties are computed by assuming the likelihood is a smooth and has only one local maximum. It is important to realise that in analysing real data the likelihood function of the parameters can have more than one maximum especially for low signal strengths. Furthermore, since the linearised-signal-approximation (on which Fisher uncertainties are based on) depends on the type of GW signal and its parameter values, the Fisher-based results should be taken carefully as the approximation may not be fulfilled for certain cases. For the most of the thesis where we evaluate Fisher based uncertainties on monochromatic GW signals and for strong signals, this will not pose a significant issue except in a few cases. We explicitly discuss this in Chapters 4 and 6.

1.5 This thesis

The main question addressed in this thesis is: what can we learn about Galactic binaries from their gravitational wave (GW) data and more importantly whether adding their electromagnetic (EM) data to the GW data improves our knowledge of the binaries that populate our Galaxy in huge numbers. The Galactic binaries here mostly refer to the long-lived sources whose orbital periods ranging from hours to minutes, most of which are described as monochromatic sources where the increasing orbital frequency as a result of GW radiation is not significant over the time the binaries are observed. The most important result is that the improvement in the binary parameters (such as individual masses, distance, inclination and orbital periods) are *significant* when the two types of information is combined. In order to get to our goal, it is important to establish thoroughly all the underlying correlations/degeneracies between (astrophysical) GW parameters that we expect to get in the GW data of these binaries. In our studies we have used the 2 arm configuration of the space-based GW detector, eLISA, which is also the working design for scientific studies on low-frequency sources.

Chapter 2 introduces one of the most important results in EM-GW synergy, which is that for low-inclination system (for e.g. AM CVn binary), using GW data *alone* will not be sufficient to measure its inclination. This system has an inferred inclination of 43° from EM measurement with a small uncertainty of $\sim 2°$ and this can be used in reducing its GW amplitude by factor of 6 (see Figure 2.2) owing to the strong correlation between the two parameters. We find that for J0651-like systems however, at the same signal strength as AM CVn but at an eclipsing orientation (inclination of 89.6°) allows us to determine this measurement using GW data alone with $\sim 2°$. Thus, we can use GW data on eclipsing systems combined with their relatively small sky uncertainties (of ~ 1 square degree) to target eclipsers in our future EM surveys.

In **Chapter 3** we extend the discussion of EM-GW synergy by studying how useful it is to have sky position of the binaries from EM (optical) data. We find that having sky position (ecliptic latitude and longitude) can improve GW measurements of inclination and strain amplitude of Galactic binaries of certain orientations to up to factors of 2 at the ecliptic poles (see Figures 3.8 3.9). The improvements are suppressed for binaries of various orientations if their sky location is closer to the ecliptic plane. These improvements soar up to factors of 60 for the GW amplitude if EM information of inclination is simultaneously combined with sky position for the binaries with inclination of 30° (see Figure 3.10). A thorough analysis in other orientation parameters of the binaries (polarisation, phase and ecliptic longitude) reveals that these parameters have insignificant effect on the GW signal of the binaries and thus after inclination the strongest influence on the binary signal is due to the ecliptic latitude.

In **Chapter 4** we take the results from previous papers and combine the study with (all possible) EM measurements that are unique to the EM data. We determine quantitatively and qualitatively the effects of adding EM observations of *single-line, double line* spectroscopic binaries that provide measurements of one or more of the following quantities: radial velocity, individual mass, distance. We find that adding only single-line data to that of the GW data will break the degeneracy between chirp mass and distance parameters in the amplitude equation and thus providing estimates on the individual masses and distance of the binaries. Combining GW data with single-line and distance will provide much more accurate (secondary) mass of the binary. All of these estimates depend on the inclination of the system. EM data on double-line systems can be used to verify the GW measurements of the inclination independently with that inferred from the EM data.

In **Chapter 5** we complete the story about these long-lived and low-f compact binaries by including an analysis for those systems that will be inspiralling (also known as chirping) during the observation length of eLISA detector or in previous years from eclipse timings from ground observatories. We also investigate the possibility of measuring tidal deviations in compact detached white-dwarf binaries where the inspiral rate in the orbital evolution is further enhanced by tidal losses by a few percent compared to the contribution from the gravitational wave radiation. We find that unless we find an extremely massive white-dwarf system with orbital period at $\sim$ minutes, measuring tidal deviations for typical detached WD binaries will be not possible using both GW and EM data. However measuring a orbital decay rate from EM observations of timing the eclipses of the binaries will allow us to infer other astrophysically useful parameters of the binaries with sometimes greatly improved accuracies if combined with GW data. In particular combining EM information on $\dot{f}$ of 1% accuracy together with GW measurements of amplitude and inclination will constrain the chirp mass and distance to the source very precisely. Adding single-line spectroscopic measurements will further constrain the secondary mass and these constraints are significantly better compared to the binaries where there is no EM information on the orbital decay (studied in Chapter 3).

In **Chapter 6** we study the parameter uncertainties of coalescing binaries made of neutron stars (NS) and black holes (BH) that are some of the most well-studied sources for the ground based GW interferometers such as LIGO and Virgo. We investigate the uncertainties in total mass and the symmetric mass ratio for NS-BH and binary BH systems in the lower mass range $1-10M\odot$. We consider only the inspiral part of the signal and take the (aligned) spin of the BH into account in the GW waveform and GW data observable by advanced LIGO detector. From Fisher-based errors we find that a spinning BH in a NSBH binary reduces the errors in the total mass and symmetric mass ratio compared to a system with non-spinning BH, while in a for BBH with both components spinning the uncertainties increase. For the maximally spinning systems the relative error in the spin parameter, which represents the spin-orbit coupling reduces and thus this can be used to distinguish a spinning BBH system from a non-spinning BBH, or high mass binary NS or an NSBH system. However for binaries with low spins EM information on transients or kilonovae involving the NS will be required to distinguish an NSBH system from a BBH system that has same total mass and mass ratio.

CHAPTER 2

USING ELECTROMAGNETIC OBSERVATIONS TO AID GRAVITATIONAL-WAVE PARAMETER ESTIMATION OF COMPACT BINARIES OBSERVED WITH LISA

S. Shah, M. v.d. Sluys & G. Nelemans

A&A, 544:A153, August 2012

Abstract

We present a first-stage study of the effect of using knowledge from electromagnetic (EM) observations in the gravitational wave (GW) data analysis of Galactic binaries that are predicted to be observed by the new *Laser Interferometer Space Antenna* in the low-frequency range, $10^{-4}\text{Hz} < f < 1\text{Hz}$. In particular, we examine the extent to which the accuracy of GW parameter estimation improves if we use available information from EM data. We do this by investigating whether correlations exist between the GW parameters that describe these binaries and whether some of these parameters are also available from EM observations. We used verification binaries, which are known as the guaranteed sources for eLISA and will test the functioning of the instrument. We find that of the seven parameters that characterise such a binary, only a few are correlated. The most useful result is the strong correlation between amplitude and inclination, which can be used to constrain the parameter uncertainty in amplitude by making use of the constraint of inclination from EM measurements. The improvement can be up to a factor of ~ 6.5, but depends on the signal-to-noise ratio of the source data. Moreover, we find that this strong correlation depends on the inclination. For mildly face-on binaries ($\iota \leq 45°$), EM data on inclination can improve the estimate of the GW amplitude by a significant factor. However, for edge-on binaries ($\iota \sim 90°$), the inclination can be determined accurately from GW data alone, thus GW data can be used to select systems that will likely be eclipsing binaries for EM follow-up.

2.1 Introduction

The space-based gravitational wave (GW) detector in consideration by ESA, eLISA, is expected to observe millions of compact Galactic binaries [Nelemans, 2009; Amaro-Seoane et al., 2013] with periods shorter than about a few hours, amongst other astrophysical sources, and resolve several thousand of these binaries [Nissanke et al., 2012]. About 50 compact binary sources have been observed at optical, UV, and X-ray wavelengths [e.g. Roelofs et al., 2010]. The types of binaries known to us are interacting systems (AM CVn stars, ultra-compact X-ray binaries, and cataclysmic variables) and detached systems (double white dwarfs (WDs) and double neutron stars [Nelemans, 2009, 2011]). The AM CVn stars are binary systems where a WD accretes matter from a low-mass, helium-rich (hydrogen-deficient) object [Solheim, 2010]. Their mass transfer is driven by GW radiation loss. The known ultra-compact X-ray binaries consist of neutron stars that are accretors whose donors are inferred to be either helium rich or carbon/oxygen rich [in't Zand, 2005]. Double WDs are predicted to be the most common systems, which sometimes tend to be the outcome of many binary evolutionary paths [Webbink, 1984]. Of all these known systems, a handful lie in the eLISA band and will be individually detected. These are known as *verification binaries* since they are guaranteed sources for the detector. Parameter uncertainties in the verification binaries and Galactic binaries in general have been studied in the literature extensively by using Fisher information matrix (FIM) analyses [e.g. Cutler, 1998; Takahashi & Seto, 2002; Stroeer & Vecchio, 2006]. These studies have been done for various configurations of classic LISA [LISA Study Team, 1998], which was designed to have a larger baseline of five million km with six laser links interchanging between three stations located at the vertices of a triangle that was to house two proof masses each [Vallisneri et al., 2008]. Instead eLISA will have a baseline of one million km with four laser links interchanging between the proof masses. The parameter uncertainties depend intricately on the observation conditions and the geometry of the detector [Takahashi & Seto, 2002] and the same is true for the (possible) correlations between the parameters of a Galactic binary. In this study, we wish to quantify whether any such correlations exist that could be useful in constraining the GW parameter estimates. Some of the GW parameters are the same as or related to electromagnetic (EM) parameters, (e.g. $\text{inclination}_{\text{GW}} = \text{inclination}_{\text{EM}}$, $f_{\text{GW}} = 2/P_{\text{orb}}$, etc.). Thus, we can use an independent (EM) constraint of a (EM/GW) parameter that correlates strongly with another (GW) parameter to improve the accuracy of the latter. This work provides a first step towards developing strategic plans in observing those potentially useful EM parameters that can improve the GW parameter accuracy. In this paper, we present a FIM analysis to study whether correlations within GW parameters exist. For the useful correlations that we find, we predict quantitatively the improvement in the GW parameter when there is *prior* EM data in the correlated parameter. The paper is structured in the following way. In Section 2, we briefly summarise the signal models, both the instrumental and foreground noises, and our data analysis. We present our results and interpretations in Section 3. Finally, we discuss how the results differ from the old LISA detector in Section 4 and present our conclusions in Section 5.

2.2 Signal modelling and data analysis

2.2.1 Gravitational wave signals from a Galactic binary

We consider three verification sources, AM CVn, SDSS J0651+2844 (hereafter J0651), and RX J0806.3+1527 (HM Cnc), whose physical parameters are summarised in Table 5.1.

AM CVn and HM Cnc are mass-transferring systems known to astronomers as AM CVn binary systems, which were described in the introduction. J0651 [Brown et al., 2011] is an eclipsing detached WD binary system that was spectroscopically identified in the Sloan Digital Sky Survey (SDSS) catalogue. AM CVn and J0651 can be modelled as monochromatic GW sources, which means that they are described by seven parameters: dimensionless amplitude ($\mathcal{A}$), frequency (f), polarisation angle (ψ), initial GW phase (ϕ_0), inclination ($\cos\iota$), ecliptic latitude ($\sin\beta$), and ecliptic longitude (λ). HM Cnc can be modelled as a mild chirper with an additional eighth parameter, the chirping frequency ($\dot{f}$). The two polarised gravitational waveforms used in the strain for slowly evolving binaries are given by [e.g. Królak et al., 2004]

$$h_+(t) = \mathcal{A}\,\frac{1+\cos^2\iota}{2}\,\cos\left(2\pi f t + \pi \dot{f} t^2 + \phi_0\right); \tag{2.1}$$

$$h_\times(t) = \mathcal{A}\,\cos\,\iota\,\;\sin\left(2\pi f t + \pi \dot{f} t^2 + \phi_0\right), \tag{2.2}$$

where

$$\mathcal{A} = \frac{4(\mathrm{G}\,\mathcal{M})^{5/3}}{c^4\,d}(\pi f)^{2/3} \tag{2.3}$$

and

$$\dot{f} = \frac{96}{5}\frac{f}{\mathcal{M}}(\pi f \mathcal{M})^{8/3}. \tag{2.4}$$

In these expressions, $\mathcal{M} \equiv (m_1 m_2)^{3/5}/(m_1+m_2)^{1/5}$ is the chirp mass and d is the distance to the source. The monochromatic waveforms are given by setting $\dot{f} = 0$ in the expressions above.

TABLE 2.1: Physical properties of verification binaries based on observations summarised in Nelemans [2011]. The signal-to-noise ratio (S/N) listed in the second column is from GW data analysis, as explained in Section 3.

	S/N	$m_1[M_\odot]$	$m_2[M_\odot]$	d[kpc]	$\mathcal{A}^*$ [$\times 10^{-22}$]	$P_{\rm orb}$[s]	ι[°]	$\dot{P}_{\rm orb}$[s/s]	β[rad]	λ[rad]
J0651	10.7	0.55^a	0.25^a	$\sim 1^a$	1.67	765.4 ± 7.9^a	$86.9^{+1.6a}_{-1}$	-	0.101	1.769
AM CVn	11.5	0.71^b	0.13^b	$0.606^{+0.135c}_{-0.93}$	1.49	1028.73^d	43 ± 2^c	-	0.653	2.974
HM Cnc	39.7	0.55^e	0.27^e	5^e	6.38	321.529^f	$\approx 38^e$	3.75×10^{-11f}	-0.082	2.102

(a) Brown et al. [2011] (b) Roelofs et al. [2006] (c) Roelofs et al. [2007] (d) Skillman et al. [1999] (e) Roelofs et al. [2010] (f) Strohmayer [2005] (*) Eq. 6.10

2.2.2 Detector response to the GW signals

If a GW signal is present, then the output of a detector will contain the strain, $h(t)$, and noise, $n(t)$. Thus, the detector registers

$$s(t) = h(t;\vec{\theta}) + n(t), \tag{2.5}$$

where $\vec{\theta}$ is a vector characterising the seven (or eight) parameters of the binary. Since eLISA will have a motion around the Sun and a cartwheeling motion around its centre of mass, a monochromatic signal from a WD binary will be modulated in its amplitude, frequency, and phase in complicated ways. The resulting signal will be spread over a range of frequency bins of the detector [Cornish & Larson, 2003]. Galactic binaries typically radiate monochromatic signals at low frequencies[1] and thus the response at the detector can be written as [Cornish & Larson, 2003]

$$h(t) = A(t)\cos\Psi(t), \tag{2.6}$$

where

$$A(t) = [(F^{+}(t)h_{+}(t))^2 + (F^{\times}(t)h_{\times}(t))^2]^{1/2}. \tag{2.7}$$

The functions $F^{+,\times}(t)$ are the antenna beam patterns of the detector, and they depend on the source's sky position (λ, β), its orientation (ψ), and the detector configuration. The phase of the signal is given by

$$\Psi(t) = 2\pi f t + \phi_0 + \Phi_D(t) + \Phi_P(t), \tag{2.8}$$

where $\Phi_D(t), \Phi_P(t)$ are frequency (Doppler) and phase modulations, respectively [Cornish & Larson, 2003]. Doppler modulation is given by

$$\Phi_D(t) = 2\pi f L/c \;\; \sin\beta \;\cos(2\pi f_m t - \lambda), \tag{2.9}$$

where $f_m = 1/\text{year}$ is the modulation frequency. The phase modulation is given by

$$\Phi_P(t) = -\arctan\left(\frac{F^{\times}\, h_{\times}}{F^{+}\, h_{+}}\right). \tag{2.10}$$

Different architectures of the triangular space-based interferometer generate a number of independent data streams that provide different responses to the incoming GW signal [Vallisneri et al., 2008]. For the most recent interferometer design in consideration, eLISA, the output is a single unequal-arm Michelson data stream, X. This is a linear combination of phase shifts measured at the different spacecraft (by comparing the incoming light with a local reference source) shifted in time in such a way as to represent interference between two light beams travelling through the arms of the detector in opposite ways, which is a

---

[1] low f is a function of the detector transfer frequency, f_*,$f \ll f_*$. The f_* is defined according to the detector armlength, L, i.e. $f_* \equiv c/(2\pi L)$. For eLISA, $L = 10^9$m, $f_* \approx 5 \times 10^{-2}$Hz

particular implementation of so-called *time delay interferometry* (TDI, Armstrong et al. [1999]. Vallisneri [2005a] provide a detailed description of how TDI works and an explanation of why it produces an interferometry signal in which the phase shift induced by a passing GW is preserved, while the much larger shifts induced by instrumental noise are strongly suppressed. We made use of the existing numerical software *Synthetic LISA* [Vallisneri, 2005b] to simulate accurate time-domain series of the instrumental noise and the GW signals in the form of these TDI observables. The data stream is a discrete series for a given observational time $T_{\rm obs}$, where the samples are separated by Δt. The detector response to GWs and instrumental noises have been discussed extensively in the literature [e.g. Cutler, 1998; Cornish & Rubbo, 2003; Królak et al., 2004; Vallisneri, 2005b], hence we only summarise the most essential expressions relevant to our data analysis. In *Synthetic LISA*, the strain at the detector, $s(t)$, is modelled as the TDI X observable. This is the quantity we work with in our data analysis.

2.2.3 Noise

There are two types of noise to consider: instrumental noise and Galactic foreground noise due to unresolved compact binaries. For the particular geometry of eLISA used here, the instrumental noises (mostly from shot noise), acceleration noise, and other types of noise (e.g optical bench noise), are characterised by their power spectral densities (PSDs[2]) of $2.31 \times 10^{-38} f^2$, $6 \times 10^{-48} f^{-2}$, and $2.76 \times 10^{-38} f^2$, respectively, in units of $\rm Hz^{-1}$. The instrumental noise is modelled as a random, Gaussian process. We note that the sampling time, Δt, should be carefully chosen while simulating the instrumental noise in order to correctly interpret the TDI observables. The choice of Δt should correspond to a frequency that is several times higher than the highest frequency where the TDI responses have to be analysed [Vallisneri, 2005b]. This means that since AM CVn and J0651 have relatively low frequencies they can be analysed with samples of $\Delta t = 64$s, whereas for HM Cnc, we need a lower sampling time of at least $\Delta t = 16$s (see Figure 2.8 in Appendix B).

The foreground noise from the Galactic binaries is simulated using the *Lisasolve* [Vallisneri, 2011] software where every binary (monochromatic and/or mild chirper[3]) is modelled in the frequency domain [Cornish & Littenberg, 2007]. This differs from simulating signals using *Synthetic LISA*, where the signal is modelled accurately in the time-domain. *Lisasolve* instead makes use of the very slowly evolving nature of the binaries to approximately model the signals both directly and speedily in the frequency domain. We only use double-detached WD binaries because they form the majority of the foreground noise [Nelemans et al., 2001a; Petiteau, 2012]. We include more than 2.7×10^7 detached Galactic double WDs from a simulation with the same assumptions about binary evolution and

---

[2] Note there is no PSD for laser noise, since we assume that it is completely cancelled in the TDI observable X.

[3] Mild implies that $\dot{f}/f \ll 1/\mathrm{T_{obs}}$, where $\mathrm{T_{obs}}$ is the observational time.

Galactic distribution as those in Nelemans et al. [2004], but with (about a factor of ten) higher intrinsic resolution. These assumptions have also been used for the simulations of the Galactic binaries on which the Mock LISA Data Challenge (MLDC) rounds are based [Littenberg, 2011].

The *unresolvable* Galactic foreground noise is obtained by iteratively subtracting the *resolvable* sources (i.e. binaries expected to be detected) from the simulated population as follows:

1. The S/N (see Eq. 2.14) is computed for each binary against the Gaussian instrumental noise and *initial* Galactic foreground noise for $\mathrm{T_{obs}}$ of two years. The initial foreground noise is calculated using the initial catalogue of 2.7×10^7 detached Galactic double WDs.

2. All the sources with S/N > 5 are removed from the initial catalogue/dataset. The *reduced* dataset is used to simulate the reduced Galactic foreground.

3. Using the reduced Galactic foreground and the same instrumental noise, the S/N for each of the binaries in the reduced catalogue is calculated. The process is iterated with step 2.

We applied a perfect subtraction of the bright sources where any spurious effects in the data set were not taken into account (since the sources were removed from the population before generating the signals). A Markov chain Monte Carlo based data analysis of the MLDC shows that all the recovered parameters of the subtracted sources have a strong peak of zero bias when compared to their injected values in the training data set [Littenberg, 2011]. Thus, this perfect subtraction scheme is not expected to introduce strong biases in our results. From our subtraction procedure outlined above, we estimate the number of resolved WD binaries to be $\sim 11,000$. Using the same subtraction procedure and S/N threshold, Nissanke et al. [2012] estimate the number of bright sources to be half of our estimate, although their estimate is only for a $\mathrm{T_{obs}}$ of one year. Furthermore, using a higher S/N threshold of seven, the number of resolvable sources is 3,000 for an observation time of two years [Amaro-Seoane et al., 2013]. If we use a threshold S/N of seven, we find 4,500 resolvable sources. The PSD of the unresolvable Galactic background is consistent with findings in the literature where the foreground noise for eLISA is almost at the level of instrumental noise for this detector [Nissanke et al., 2012], unlike in the case of the classic LISA where the foreground noise was predicted to dominate at $f \leq 3$mHz [Nelemans et al., 2001a; Timpano et al., 2006].

2.2.4 Data analysis

For GW sources with known waveforms, one can use matched filtering methods [Finn, 1992; Cutler & Flanagan, 1994] to extract the signal parameters and estimate their uncertainties.

Consequently, when the noise is Gaussian, the parameter uncertainties are given by their joint Gaussian probability distribution function [Cutler, 1998]

$$p(\sigma_{\vec{\theta}}) = \sqrt{\det(\Gamma/2\pi)}\ \exp\left(-\frac{1}{2}\,\Gamma_{ij}\,\sigma_{\theta_i}\,\sigma_{\theta_j}\right), \tag{2.11}$$

where Γ is known as the Fisher information matrix (FIM) given by

$$\Gamma_{ij} \equiv \left(\frac{\partial h}{\partial \theta_i}\,\middle|\,\frac{\partial h}{\partial \theta_j}\right). \tag{2.12}$$

The inner product (...|...) is a generalisation of the time-domain correlation product and is conventionally defined as

$$(a|b) = 4\int_0^\infty df\ \frac{\tilde{a}^*(f)\,\tilde{b}(f)}{S_n(f)} \simeq \frac{2}{S_n(f_0)}\int_0^{T_{\rm obs}} dt\ \ a(t)\ b(t). \tag{2.13}$$

Eq. 2.13[4] holds for quasi-monochromatic binaries that have an almost constant noise PSD, $S_n(f)$, in the frequency region where the binary radiates [Cutler, 1998]. The S/N of a source is defined as the inner product of a signal with itself

$$\mathrm{S/N}^2 = (h|h). \tag{2.14}$$

In the limit of signals with a high signal-to-noise ratio (S/N $\gg$ 1), the inverse of the FIM gives the variance-covariance matrix $\mathcal{C} = \Gamma^{-1}$. The diagonal elements $\mathcal{C}_{ii}$ give variances (or mean square errors) in each parameter, $\langle(\sigma_i)^2\rangle$, and the off-diagonal elements describe the covariances (or correlations) between them. For each of our verification binaries, we calculate this matrix to investigate the correlations between the binary parameters. The derivative in Eq. 6.23, $\partial h/\partial\theta_i$, is numerically calculated in the time-domain

$$h'(t;\theta_i) \equiv \frac{h(t;\theta_i + d\theta_i) - h(t;\theta_i - d\theta_i)}{2d\theta_i}, \tag{2.15}$$

where $d\theta_i$ should be chosen carefully. In general, the quantity $d\theta_i$ should be as small as the machine accuracy allows for, but not too large to suffer from the truncation error[5]. Thus, for well-behaved functions, $d\theta_i \sim \sqrt{\epsilon}\,\theta_c$, where $\epsilon \sim 10^{-16}$ is the machine accuracy and θ_c is some typical value of the corresponding parameter [Press et al., 2002]. To find a good choice of $d\theta_i$, we compute σ_i for a range of $d\theta_i$ with logarithmic intervals and select the value for each corresponding parameter around which the standard deviations become stable. By stable, we mean that increasing or decreasing $d\theta_i$ by an order of magnitude should lead to values of σ_i that vary by no greater (smaller) factor than 1.1 (0.9). An example of the stabilisation of the variance-covariance matrix is provided in Table 2.2 of Appendix A for the case of AM CVn. We perform this stability check for all our verification binaries. For instance, in the case of AM CVn, $d\theta_{\mathcal{A}} \sim 10^{-30}$, $d\theta_f \sim 10^{-11}$, $d\theta_{\iota,\psi} \sim 10^{-8}$ etc. All our analysis is done for $T_{\rm obs} = 2$ years.

---

[4] The latter equality follows from Parseval's theorem.

[5] This error comes from higher-order terms in the Taylor-series expansion, $h(x+dx) = h(x) + dx\ h'(x) + \frac{1}{2}\,dx^2\ h''(x) + ...$

2.3 Results

Here we list the variance-covariance matrix $\mathcal{C}$ for AM CVn, HM Cnc, and J0651 and discuss the strongest correlations that we found. The off-diagonal elements are specified by the normalised correlations, c_{ij}, and the diagonal elements are quoted as the square root of the variances (or standard deviations), c_{ii}, i.e.

$$\mathrm{c}_{ij} = \frac{\mathcal{C}_{ij}}{\sqrt{\mathcal{C}_{ii}\mathcal{C}_{jj}}}, \quad \mathrm{c}_{ii} = \sqrt{\mathcal{C}_{ii}} \equiv \sigma_i . \tag{2.16}$$

Thus, c_{ij} can have values in the range $[-1, +1]$ where, $\mathrm{c}_{ij} = +1$ means maximally correlated and $\mathrm{c}_{ij} = -1$ means maximally anti-correlated. We consider highly correlated parameters θ_i, θ_j to be those for which $|\mathrm{c}_{ij}| > 0.8$. In the later subsections, we show that these correlations are affected when the inclination is varied.

The correlation matrices for the three verification binaries with observed parameters as shown in Table 5.1 are listed below. The measured GW parameter values are shown above each matrix. Since there are no EM measurements for ϕ_0 and ψ, we set them to π and $\pi/2$, respectively, for all three binaries. The choice of the ϕ_0 value does not influence the results shown below, whereas the choice for the ψ has an effect that will be addressed later. In the matrices, we take the medians of values obtained using 50 different instrumental-noise realisations and the standard deviations about these medians (σ(S/N) and $\sigma(\sigma_i)$). They are listed above and below each of the corresponding matrices, respectively. The values of S/N we find here are comparable to the ones found by other groups [Petiteau, 2012]. The normalised correlations are accurate within the quoted precision and hence their standard deviations from the instrumental noise are not listed.

J0651, S/N $= 10.72 \pm 0.23$.
Strong correlations (as defined above) are printed in bold face.

$$\begin{array}{l|rrrrrrr}
 & \mathcal{A} & \phi_0 & \cos\iota & f & \psi & \sin\beta & \lambda \\
\theta_i & 1.670 \times 10^{-22} & \pi & 0.01 & 2.614 \times 10^{-3} & \pi/2 & 0.10 & 1.77 \\
\hline
\mathcal{A} & 1.564 \times 10^{-23} & 0.01 & -0.05 & -0.02 & 0.02 & 0.03 & -0.08 \\
\phi_0 & & 0.208 & -0.01 & -\mathbf{0.89} & -0.02 & 0.13 & -0.13 \\
\cos\iota & & & 0.043 & 0.01 & 0.02 & -0.06 & 0.34 \\
f & & & & 8.375 \times 10^{-10} & 0.01 & -0.17 & 0.16 \\
\psi & & & & & 0.040 & -0.03 & 0.09 \\
\sin\beta & & & & & & 0.069 & 0.09 \\
\lambda & & & & & & & 0.020 \\
\hline
\sigma(\sigma_i) & 3.31 \times 10^{-25} & 0.004 & 0.001 & 1.771 \times 10^{-11} & 0.001 & 0.001 & 0.000
\end{array}$$

AM CVn, S/N $= 11.54 \pm 0.19$.

$$\left(\begin{array}{c|ccccccc}
 & \mathcal{A} & \phi_0 & \cos\iota & f & \psi & \sin\beta & \lambda \\
\theta_i & 1.494\times10^{-22} & \pi & 0.73 & 1.944\times10^{-3} & \pi/2 & 0.61 & 2.97 \\
\hline
\mathcal{A} & 1.084\times10^{-22} & 0.29 & -\mathbf{0.99} & -0.06 & -0.30 & -0.03 & -0.60 \\
\phi_0 & & 2.333 & -0.27 & -0.03 & -\mathbf{0.99} & 0.26 & -0.44 \\
\cos\iota & & & 0.580 & 0.06 & 0.28 & 0.04 & 0.60 \\
f & & & & 6.807\times10^{-10} & -0.03 & -0.11 & -0.19 \\
\psi & & & & & 1.170 & -0.27 & 0.03 \\
\sin\beta & & & & & & 0.029 & 0.03 \\
\lambda & & & & & & & 0.040 \\
\hline
\sigma(\sigma_i) & 1.821\times10^{-24} & 0.039 & 0.010 & 1.145\times10^{-11} & 0.020 & 0.000 & 0.001
\end{array}\right)$$

HM Cnc, S/N $= 39.75 \pm 0.82$.

$$\left(\begin{array}{c|ccccccc}
 & \mathcal{A} & \phi_0 & \cos\iota & f & \psi & \sin\beta & \lambda \\
\theta_i & 6.378\times10^{-23} & \pi & 0.79 & 6.22\times10^{-3} & \pi/2 & -0.08 & 2.10 \\
\hline
\mathcal{A} & 1.236\times10^{-23} & 0.01 & -\mathbf{0.99} & 0.00 & -0.01 & -0.12 & 0.07 \\
\phi_0 & & 0.916 & -0.01 & -0.14 & -\mathbf{0.998} & -0.16 & -0.08 \\
\cos\iota & & & 0.169 & 0.00 & 0.01 & -0.12 & -0.07 \\
f & & & & 2.257\times10^{-10} & 0.09 & 0.29 & -0.06 \\
\psi & & & & & 0.455 & 0.14 & -0.06 \\
\sin\beta & & & & & & 0.018 & -0.06 \\
\lambda & & & & & & & 0.002 \\
\hline
\sigma(\sigma_i) & 2.5\times10^{-25} & 0.019 & 0.003 & 4.6\times10^{-12} & 0.009 & 0.000 & 0.000
\end{array}\right)$$

HM Cnc, with $\dot{f}$, S/N $= 39.89 \pm 0.85$.

$$\left(\begin{array}{c|cccccccc}
 & \mathcal{A} & \phi_0 & \cos\iota & f & \dot{f} & \psi & \sin\beta & \lambda \\
\theta_i & 6.378\times10^{-23} & \pi & 0.79 & 6.22\times10^{-3} & -7.25\times10^{-16} & \pi/2 & -0.08 & 2.10 \\
\hline
\mathcal{A} & 1.240\times10^{-23} & 0.0 & -\mathbf{0.99} & 0.02 & -0.02 & 0.00 & 0.15 & -0.08 \\
\phi_0 & & 0.907 & 0.00 & -0.14 & 0.11 & \mathbf{0.995} & -0.02 & -0.04 \\
\cos\iota & & & 0.172 & -0.02 & 0.02 & -0.01 & -0.15 & 0.08 \\
f & & & & 9.58\times10^{-10} & -\mathbf{0.97} & -0.05 & -0.05 & -0.28 \\
\dot{f} & & & & & 2.971\times10^{-17} & 0.04 & 0.14 & 0.28 \\
\psi & & & & & & 0.448 & -0.01 & -0.07 \\
\sin\beta & & & & & & & 0.018 & 0.09 \\
\lambda & & & & & & & & 0.002 \\
\hline
\sigma(\sigma_i) & 2.6\times10^{-25} & 0.019 & 0.004 & 2.1\times10^{-11} & 5.96\times10^{-19} & 0.009 & 0.000 & 0.000
\end{array}\right)$$

2.3.1 The correlation between $\mathcal{A}$ and $\cos\iota$

The amplitude and inclination of AM CVn and HM Cnc (when modelled without the chirp, $\dot{f}$) are highly anti-correlated, with a value of $c_{\mathcal{A}\,\cos\iota} \approx -0.99$. The reason for this is that binaries with inclinations in the range from 0° to $\sim 45°$ (face-on or close to face-on) have signals with the same structure (see Figure 2.1), so the signals in this range can be transformed into each other by simply changing either the amplitude or the inclination. Thus, if we change the amplitude of one of these signals within its GW uncertainty, we can obtain a very similar signal by changing its inclination within its GW uncertainty as well. However, for inclinations in the range $\sim 45° - 90°$ (either close to edge-on or edge-on), this scaling does not apply. This is because the signals in this range not only vary in terms of the overall scale but also in their structure, when their inclination is changed. This is especially evident for a binary with $\iota \sim 90°$ (lines of $\iota = 60°, 90°$ in Figure 2.1). Since the inclinations of both AM CVn and HM Cnc are within the range where similar signals can be obtained by varying either the inclination or the strain amplitude, the parameters $\cos\iota$ and $\mathcal{A}$ are highly correlated. Furthermore since J0561 is an edge-on system with $\iota \sim 90°$, both $\cos\iota$ and $\mathcal{A}$ are distinguishable, as can be seen in Figure 2.1. This is potentially the most useful correlation from the GW analysis where an EM measurement of the inclination of a binary can constrain the error in the strain amplitude $\mathcal{A}$. For example for AM CVn, an EM constraint in ι with a 1-σ accuracy of 4° [Roelofs et al., 2006] improves the uncertainty in $\mathcal{A}$ from 1.084×10^{-22} to 1.65×10^{-23} as shown in Figure 2.2. The corresponding 1-σ accuracy in $\mathcal{A}$ is estimated by selecting the two-dimensional probability distribution function (2D PDF) points that lie in the range $41° < \iota < 45°$. This improves amplitude accuracy by a factor of 6.5 compared to the use of GW data alone.

HM Cnc's inclination measurement derived from the EM observation is quite uncertain compared to that for AM CVn. This is mainly due to the large uncertainty in the mass ratio and the assumption about the GW radiation that goes into estimating the inclination [Roelofs et al., 2010]. Hence, if we take an EM constraint in ι with a 1-σ uncertainty of 7°, the amplitude improves by a factor of 1.34 as shown in Figure 2.3. However, if we were to obtain a better ι constraint of 4° for HM Cnc, $\mathcal{A}$ would improve by a factor of three, which is still a smaller improvement than that of the AM CVn's. This is due to the higher S/N of HM Cnc: if we place AM CVn at a closer distance such that it has a higher SNR of ~ 40, the 1-σ accuracy of 4° constrains the amplitude more tightly by a factor of 2.95, which is very similar to the case of HM Cnc. By constraining the strain amplitude, we constrain the chirp mass, the distance, or a combination of the two $\frac{\mathcal{M}^{5/3}}{d}$ (see Eq. 6.10). The GW frequency, the third contributor to the amplitude, is already determined very precisely. Additionally, if $\dot{f}$ is measurable for a chirping binary, then from Eqs. 6.10 and 5.4 one can constrain the error in the distance [Schutz, 1996].

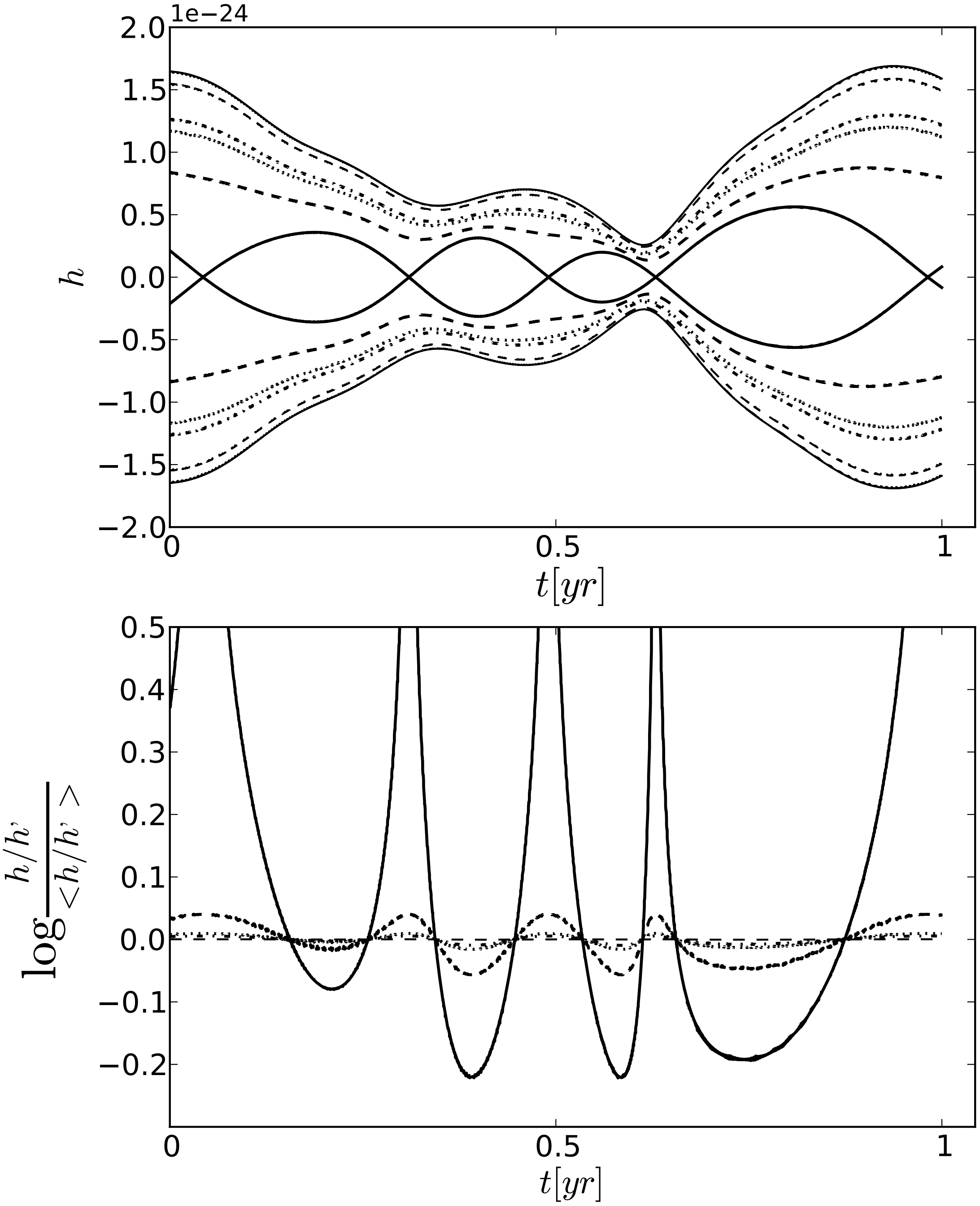

Figure 2.1: Left: Envelopes of the GW signal (TDI X observable) for binaries with parameters of AM CVn, but for various inclinations as a function of time (innermost to outermost envelopes correspond to $\iota = 90°, 60°, 45°, 40°, 20°, 0°$ respectively). The modulation of the signal is due to the complicated annual motion of eLISA around the Sun. For low inclinations ($\iota = 0° - 45°$), the signals only differ in amplitude, while the higher inclinations also differ in structure. To highlight this, we plot in the right panel the normalised ratio of the upper envelopes compared to the $\iota = 0°$ envelope using the same line styles (but now the $\iota = 90°$ is the outermost line). High inclination systems clearly have a unique structure, while low inclination envelopes only differ in amplitude, illustrating the degeneracy between ι and $\mathcal{A}$.

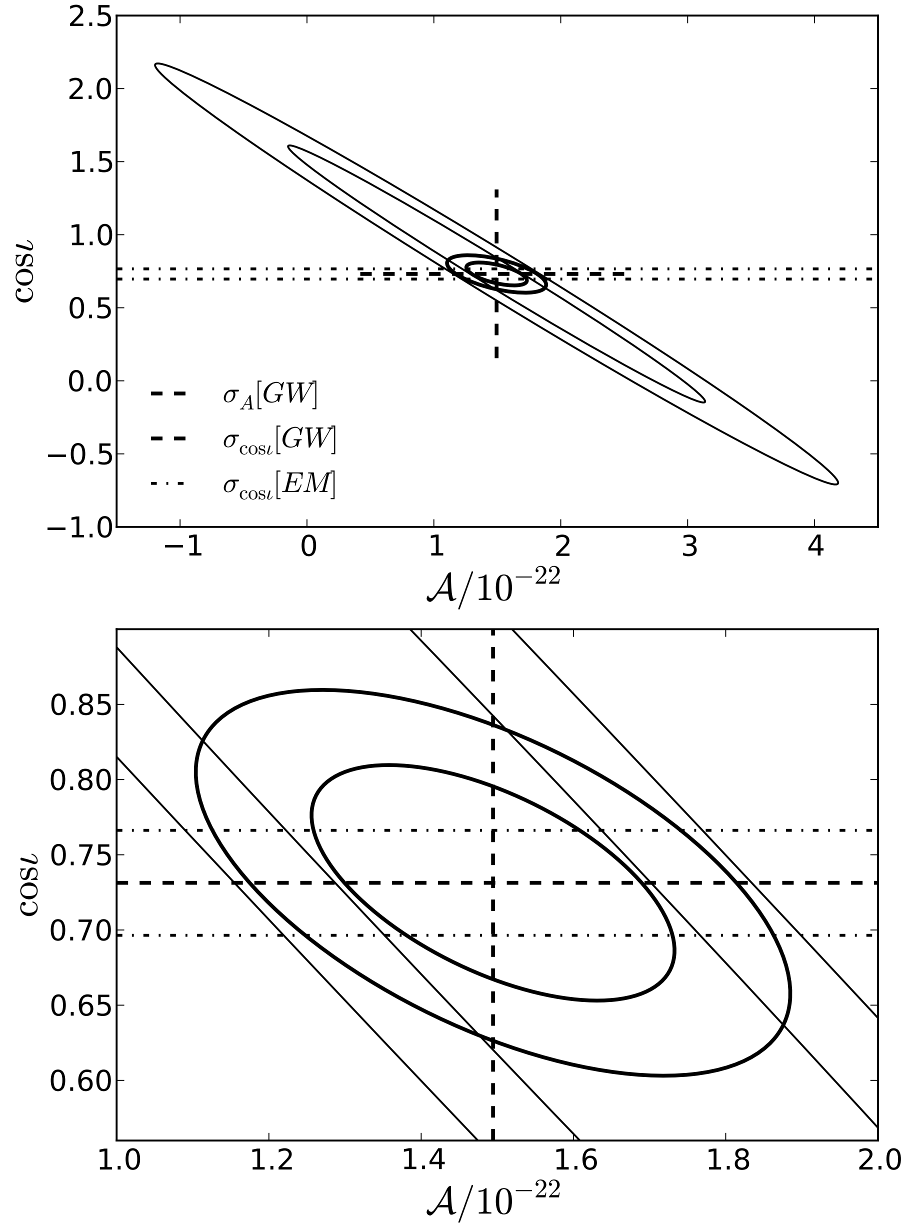

FIGURE 2.2: Left: Two-dimensional error ellipses of $\mathcal{A}$ and $\cos\iota$ extracted from the variance-covariance matrix, $\mathcal{C}$, for AM CVn. The two thin black lines represent 1-σ and 2-σ ellipses and the black dashed lines represent the 1-σ GW errors in $\mathcal{A}$ and $\cos\iota$ with the cross at the true value of the parameters. The unphysical values (i.e. negative numbers along the amplitude axis) are caused by the Gaussian tails of the parameter uncertainty about their true values. The right panel is a zoom of the area that is constrained by the 1-σ EM error of 4° shown in dash-dotted lines. The 1-σ GW standard deviation in $\mathcal{A}$ decreases from $\sim 1.08 \times 10^{-22}$ to $\sim 0.165 \times 10^{-22}$, roughly a factor of 6.5. The corresponding error ellipses for the reduced PDF are shown as thick black ellipses for 1-σ and 2-σ.

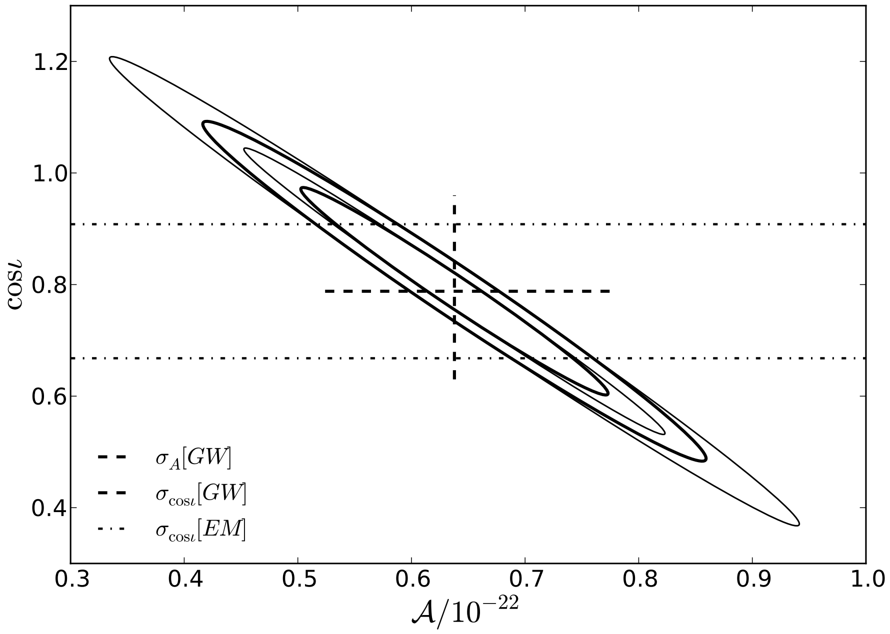

Figure 2.3: Two-dimensional error ellipses $\mathcal{A}$ and $\cos\iota$ extracted from the variance-covariance matrix, $\mathcal{C}$, for HM Cnc. See Figure 2.2 for details. The 1-σ EM constraint of 7° in inclination reduces the corresponding 1-σ uncertainty in $\mathcal{A}$ from $\sim 1.22 \times 10^{-23}$ to $\sim 0.89 \times 10^{-23}$, roughly a factor of 1.4.

2.3.2 Influence of the inclination, ι

We have seen above that $c_{\mathcal{A}\ \cos\ \iota}$ depends on the inclination of the binary. For the special case of exactly face-on binaries ($\iota = 0, \pi$), the Fisher matrix is ill-defined owing to the symmetry in the signal, namely, $h(t, \iota + d\iota) = h(t, \iota - d\iota)$. The derivatives are zero, so the terms including ι in the Fisher matrix are also zero, resulting in an ill-defined matrix that cannot be inverted. In general, it is hard to track the behaviour of the variance-covariance matrix from the FIM alone. Hence, to determine the influence of inclination, we fix all parameters except $\mathcal{A}$, ι, and λ, and calculate the matrices Γ and $\mathcal{C}$ for AM CVn as a function of ι. This can be justified, as most correlations with $\mathcal{A}$ and ι are not very strong; the largest correlation (of ~ 0.6) is for λ as shown in Figure 2.4. This means that for all inclinations

$$\mathcal{C} \sim \begin{pmatrix} \mathcal{C}_{\mathcal{A}\ \cos\iota\ \lambda} & 0 \\ 0 & \mathcal{C}_{\phi_0\ f\ \psi\ \sin\beta} \end{pmatrix}$$

thus we can focus on $\mathcal{A}$, cos ι, and λ independently and reduce the 7×7 matrix to a 3×3 matrix, which is easier to interpret[6].

---

[6] Another reason to consider a smaller matrix is that it is difficult to stabilise $\mathcal{C}$ for low inclinations $\iota \leq 10°$. We find that the optimal choice of $d\theta_i$ for which the parameter uncertainties σ_i are stable varies as a function of inclination. For low values of ι, the optimal $d\theta_i$ is orders of magnitude larger than for high

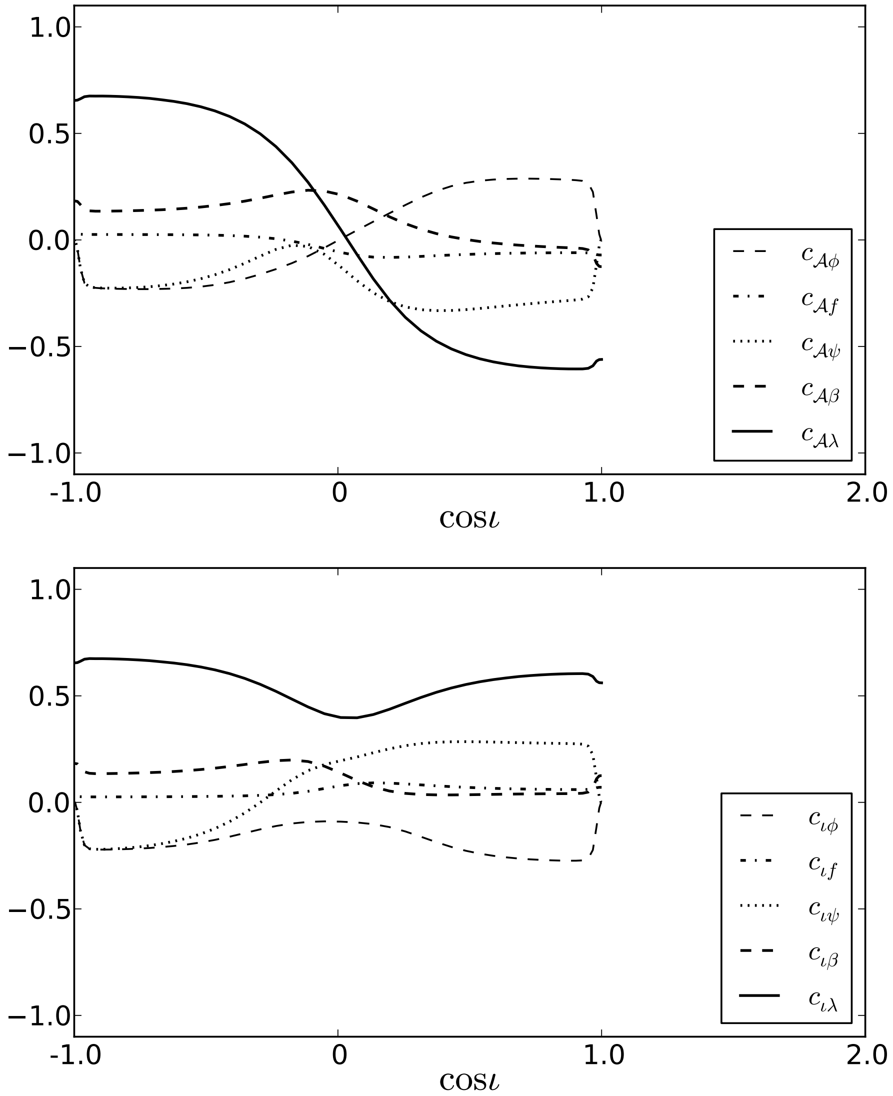

FIGURE 2.4: Correlations of the remaining parameters with $\mathcal{A}$ and ι for a binary with AM CVn's parameter values as a function of $\cos\iota$. Most correlations are weak for all inclinations except $c_{\mathcal{A}\lambda}$.

---

values of ι. Note that the FIM (as opposed to $\mathcal{C}$) is stable for the same choice of $d\theta_i$. In addition, the FIM choice of $d\theta_i$ that is made for the inclination affects only matrix elements that contain terms related to ι. However, this influence spreads to all matrix elements of $\mathcal{C}(=\Gamma^{-1})$, because of the matrix inversion.

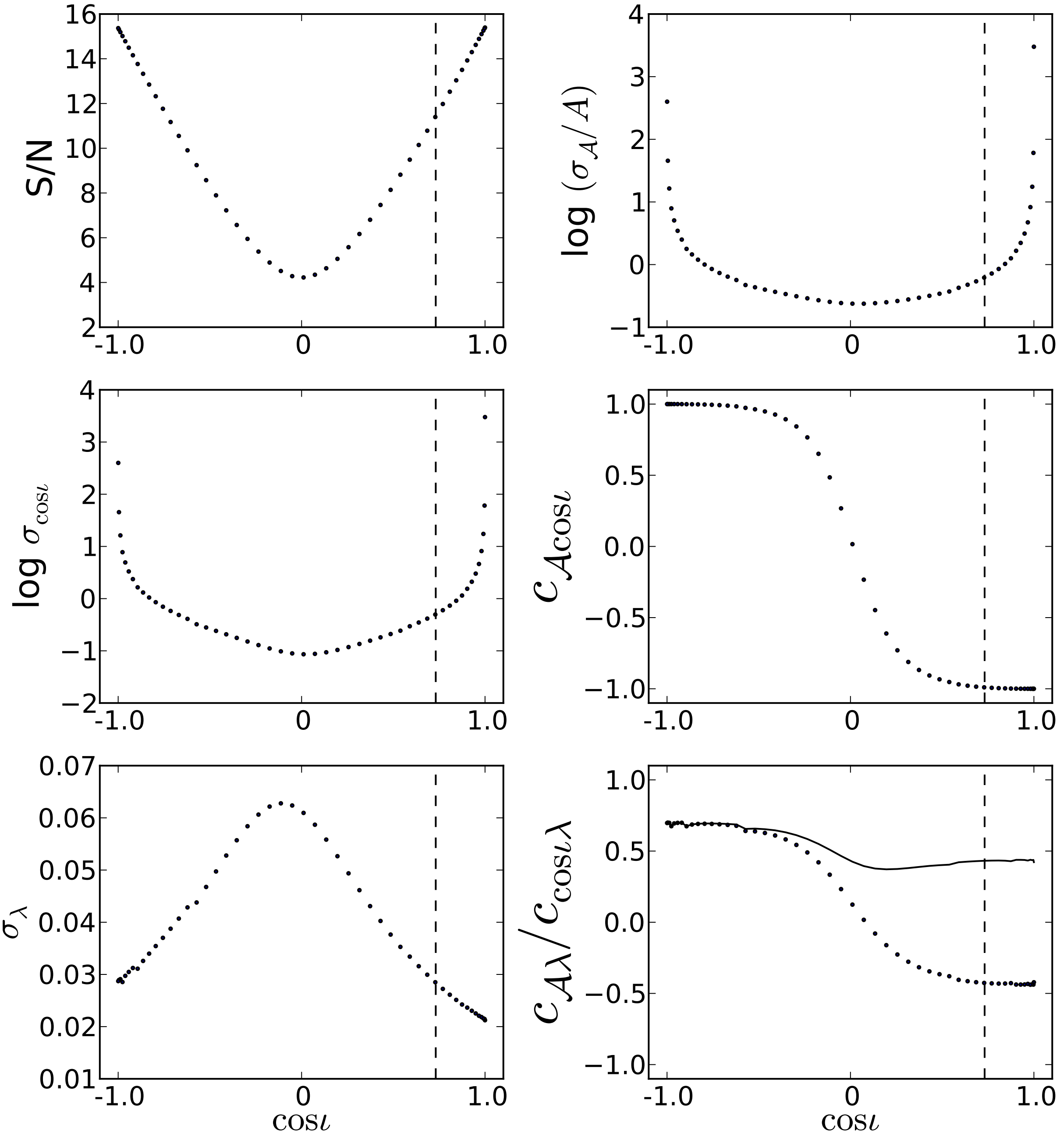

Figure 2.5: Signal-to-noise ratio, $\sigma_{\mathcal{A}}$, $\sigma_{\cos\iota}$, σ_λ, $c_{\mathcal{A}\cos\iota}$, $c_{\mathcal{A}\lambda}$, and $c_{\cos\iota\lambda}$ as a function of $\cos\iota$, keeping the other parameters fixed to the values of AM CVn. The vertical dashed line is the measured value of ι for this binary, 43°. The best known value for the amplitude is $\mathcal{A} = 1.49 \times 10^{-22}$. As expected, the S/N is higher for face-on than edge-on orientations. The relative uncertainties in the amplitude and inclination are very large for inclinations up to 10°. The bottom-right panel shows the normalised correlations $c_{\mathcal{A}\lambda}$ as the dotted line and $c_{\cos\iota\lambda}$ as the solid line.

In Figure 2.5, we show the S/N, (relative) parameter uncertainties and the normalised correlation for these three parameters as a function of inclination. It is obvious that for a source at a given distance, the S/N for an edge-on binary is lower than that for a face-on binary owing to the less favourable orientation of the latter. Thus, the S/N is a function of $\cos\iota$ and has a minimum at $\iota = 90^\circ$ ($\cos\iota = 0$). In general, we expect the parameter uncertainties to vary accordingly, i.e., a higher S/N should correspond to a higher precision and *vice-versa*. The longitude follows this behaviour in the bottom-left panel. However, for $\mathcal{A}$ and $\cos\iota$ this is not the case as the detector cannot accurately determine the inclination in the range of $0.7 \leq |\cos\iota| \leq 1$, as shown in the top-right and middle-left panels. For $\iota \leq 10^\circ$ and $\iota \geq 170^\circ$ in particular, the uncertainties in ι and $\mathcal{A}$ become very large. However, as shown in the middle-right panel, the correlations are maximal for these almost face-on binaries, thus by constraining one of the parameters from EM (or other) data, we constrain the range of values that the other parameter can take. This method cannot be applied to edge-on binaries as the correlation is very weak in these cases. If we take a value of $d\iota$ for which the computation of the 3×3 variance-covariance matrix is numerically stable for all ι and use it to produce the full 7×7 matrix, the parameter uncertainties behave as shown in Figures 2.6, 2.7. The uncertainties σ_{ϕ_0} and σ_ψ behave similarly to $\sigma_\mathcal{A}$ and σ_ι since ϕ_0, and ψ are also degenerate for nearly face-on systems. In contrast, the uncertainties σ_f, σ_λ, and $\sigma_{\sin\beta}$ behave as may be expected from the S/N since they are not strongly tied to any of the four parameters with strong correlations.

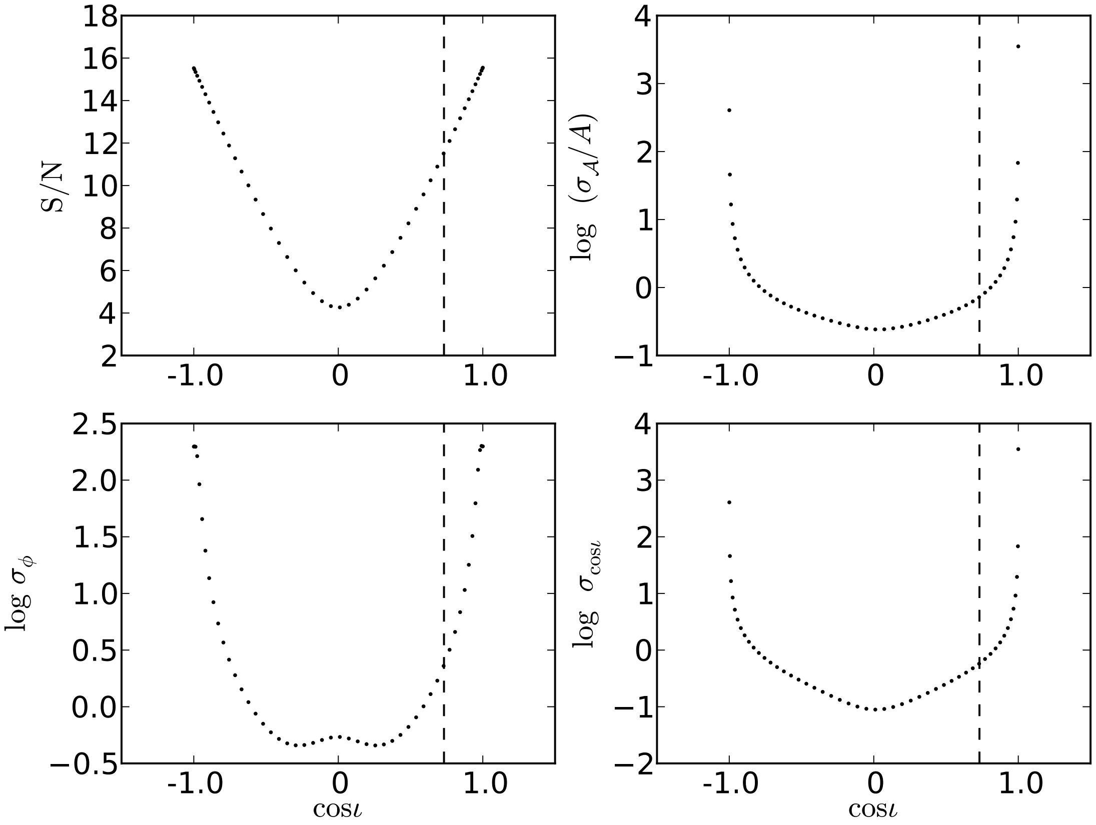

Figure 2.6: Signal-to-noise ratio and (relative) parameter uncertainties for AM CVn as a function of $\cos\iota$. The general behaviour for $\sigma_{\mathcal{A}}$, $\sigma_{\cos\iota}$ and σ_ϕ and σ_ψ is consistent with Figure 2.5 above.

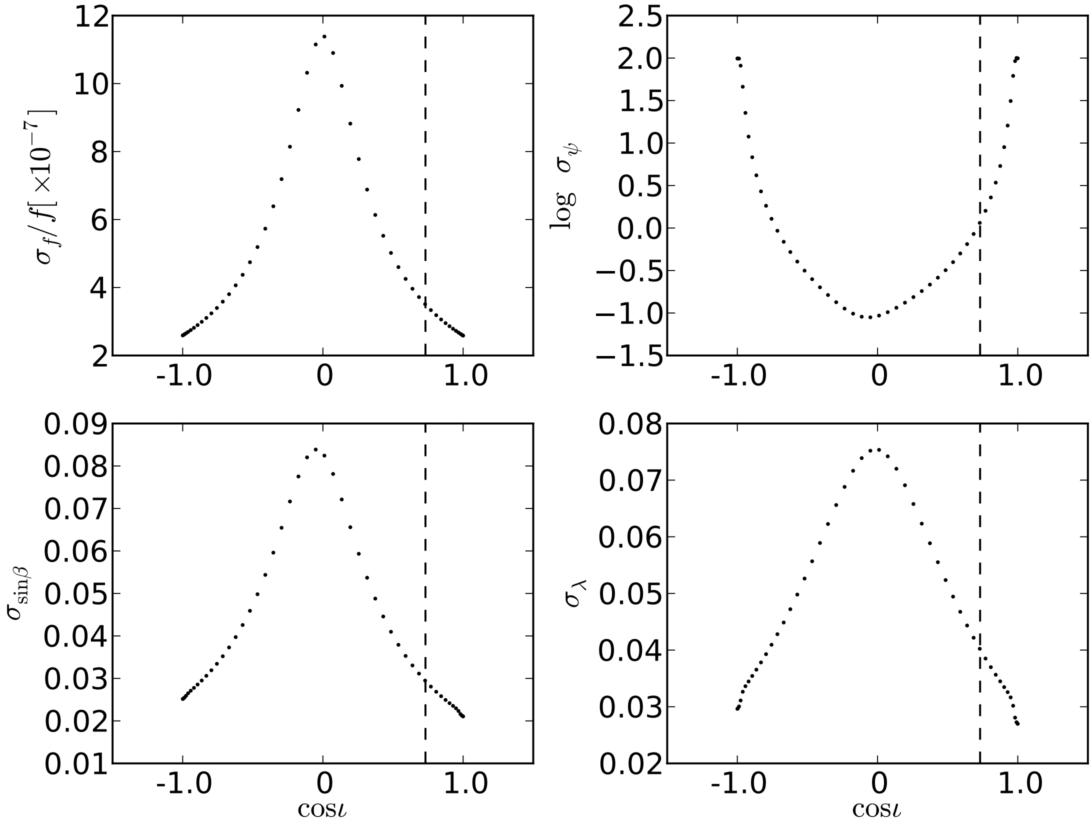

Figure 2.7: Signal-to-noise ratio and (relative) parameter uncertainties for AM CVn as a function of $\cos\iota$. The uncertainties in $\sigma_{\sin\beta}, \sigma_\lambda$, and σ_f behave as may be expected from the S/N, where parameters are more accurately determined for higher S/N.

2.3.3 The correlation between ϕ_0 and ψ

The orientation parameters ϕ_0 and ψ are also highly anti-correlated with $c_{\phi_0\psi} \approx -0.99$ for AM CVn and HM Cnc. This can also be explained by examining the geometry of the physical binary. The orbital phase ϕ is measured in the plane of the binary (perpendicular to the binary's angular momentum vector, $\hat{L}$), while ψ is measured in the plane perpendicular to the line of sight, $\hat{n}$. Both AM CVn and HM Cnc have an inclination in the range where the system appears to be face-on to the detector (see Section 3.1). Thus, ϕ_0 and ψ are practically degenerate for these binaries. In contrast, for J0651 $\hat{L}$ and $\hat{n}$ are almost perpendicular, and the effects of ϕ_0 and ψ can be more easily distinguished by eLISA. This correlation is not very noteworthy, because the parameters involved are of little astrophysical interest.

2.3.4 The correlation between f and ϕ_0

For J0651, there is a strong anti-correlation between f and ϕ_0, with a value of -0.89. This is because if the frequency of a signal is changed by a small fraction, δf, the signal accumulates a phase shift towards the end of the wave. This signal can be de-shifted in phase to obtain another signal with a similar match to the original, in turn making the two slightly dissimilar signals indistinguishable. Hence, the two parameters f and ϕ_0 are degenerate. This degeneracy is not present for AM CVn and HM Cnc owing to the strong anti-correlation between ϕ_0 and ψ and large errors in these two parameters.

2.3.5 The correlation between f and $\dot{f}$

If we model HM Cnc with an additional eighth parameter, $\dot{f}$, we find a strong anti-correlation between f and $\dot{f}$. This can be explained in a very similar way to the case of $c_{f\phi_0}$ above. Consider a signal which is obtained by changing the chirp by $\delta\dot{f}$, within its uncertainty. This will slightly change the frequency towards the end of the signal. By additionally changing f within its uncertainty, we can obtain a very similar signal to the one for which we changed only its chirp by $\delta\dot{f}$. Thus, the two parameters are degenerate for a mildly chirping binary. This could be a very useful correlation for constraining the $\dot{f}$ of the binary by using an EM constraint on f. However, the GW data analysis already provides a relative accuracy of $\sim 10^{-6}$ for the frequency, which is hard to improve with EM observations.

After providing a potential measurement of $\dot{f}$ for the J0651 source (M. Kilic, private communication), the correlation between f and $\dot{f}$ could be used to test one of the predictions of General Relativity in Eq. 5.4, which holds for a binary that evolves only because of GW radiation loss. Given that the individual masses and their f are measured, Eq. 5.4 can be used to test the prediction of $\dot{f}$.

2.4 Discussion

The S/N's of the data for the verification binaries listed in Table 5.1 are relatively low. In particular, J0651 has S/N $\sim$ 10. This may not satisfy S/N $\gg$ 1, one of the criteria under which FIM studies are valid. To exclude the effects of S/N, we place the verification binaries at a closer distance so that they all have S/N of $\sim$ 100. We find that all of the parameter uncertainties decrease as expected, except for the uncertainty in $\mathcal{A}$. However, the strong correlations we found for $c_{\mathcal{A}\iota}$, $c_{\phi_0\psi}$, $c_{f\phi_0}$ and $c_{f\dot{f}}$ listed above in the matrices remain the same. Furthermore, these correlations do not change when we consider the *six-link* configuration of the classic LISA with a five million km baseline and slightly different instrumental noise. From the *six-link* interferometer, three independent data streams can be synthesised, of which *A, E,* and *T* is one of the combinations. Naturally, this means that the S/N of the source will be higher, and that there may be additional information from these data streams. However, we found that when we consider these optimal TDIs, the strong correlations we found are unaffected. Additionally, the weak correlations between the rest of the parameters are also unaffected.

It is well-known that in the low-frequency regime there are many overlapping sources, which can significantly degrade the parameter uncertainty. Crowder & Cornish (2004) performed a thorough FIM analysis and show that the degradation of parameter uncertainties depends on the frequency, the number of binaries per frequency bin, and the observation time. However, the degradation is uniform for all the seven parameters, which means that each parameter is affected in the same way by the overlapping sources. Hence, the presence of overlapping sources affects the *uncertainties* in the parameters, but not the normalised *correlation* between the parameters. In addition the potential biases from imperfect subtraction of resolvable sources (Section 2.3) can affect the results, although this mostly affects the S/N degradation of the source and thus not the normalised correlations.

Our study should be used to implement EM priors in an MCMC data analysis based on a Bayesian framework. While the latter leads to more accurate results, the FIM tools provides useful predictions [Vallisneri, 2008]. In the case of Galactic binaries, it has been shown that the one-dimensional marginalised posterior PDFs are well-matched by the FIM predictions when the data analysis of a single source is considered [Cornish & Crowder, 2005].

In a forthcoming paper, we will discuss the dependence of the aforementioned correlations and accuracies on the sky position and polarisation angle. Our test calculations show that the strong correlations $c_{\mathcal{A}\iota}$, $c_{\phi_0\psi}$, $c_{f\phi_0}$, and $c_{f\dot{f}}$ found above do not vary as a function of these parameters.

Finally, we observe that the uncertainty in the inclination of a binary indicates whether the system is eclipsing. In Section 3.1, we found that for J0651, the uncertainties in ι, ϕ_0, and ψ are small compared to those of HM Cnc, even though its S/N is a factor of three lower than that of HM Cnc. An uncertainty of $\sigma_{\cos\iota} = 0.043$ translates to $\sigma_\iota \sim 2.5°$. Hence, for J0651-like systems with S/N's of ≥ 10, the small uncertainty inclination inferred from a GW analysis may be used to find candidate eclipsers.

2.5 Conclusion

We have performed Fisher-matrix studies to investigate whether there are correlations between the parameters that characterise Galactic binaries with short periods, between about six minutes and a few hours, which lie in the eLISA frequency band, 10^{-4} Hz -1 Hz. We focused on three verification binaries, AM CVn, SDSS J0651+2844, and the mildly chirping HM Cnc. Our main findings are:

1. There are strong correlations between the strain amplitude and inclination, and between the phase and polarisation angle for AM CVn and HM Cnc. For the latter, there is an additional strong anti-correlation between f and $\dot{f}$ when it is modelled as a mildly chirping source.

2. The remaining parameters are not or only weakly correlated for the binaries considered.

3. The correlation between strain amplitude and inclination can be very useful in constraining the amplitude of the binary, which is a function of the two masses, the distance to the binary, and its frequency. Since the frequency is very accurately determined (of the order of 10^{-9} Hz) by the GW data analysis, a combination of the masses and the distance can be constrained by using an EM constraint on the inclination.

4. These correlations depend strongly on the inclination of the system: approximately face-on ($\iota \leq 45°,\ \iota \geq 135°$) binaries have strongly correlated parameters, whereas for edge-on binaries, the correlations become very weak.

5. For binaries with very low inclinations ($\iota < 10°$ and $\iota > 170°$), the uncertainties in amplitude, inclination, phase, and polarisation angle derived from GW data are very large.

6. We have found that the influence of S/N on the correlations is not significant; placing the sources at shorter distances to give them higher S/N yields the same normalised correlations.

7. The strong correlation between amplitude and inclination is the most useful correlation found, since inclinations are typically measured to a higher accuracy by EM observations than with GW measurements alone. Hence, this correlation can be used to constrain the amplitude by a factor of six for systems with orientations and S/N's similar to those of AM CVn.

8. We have found that some correlations also depend on sky position and polarisation angle, which we will discuss in a forthcoming paper.

9. Even for signals with an S/N of ~ 10, we have been able to reliably determine the inclination when the system is edge-on. This will enable efficient searches for eclipsing systems with EM instruments.

Acknowledgements

This work was supported by funding from FOM. We are very grateful to Michele Vallisneri for providing support with the *Synthetic LISA* and *Lisasolve* softwares. We thank the anonymous referee for the helpful suggestions to improve the paper.

2.A 1. Stabilisation of the variance-covariance matrix

Here we give an example of the Stabilisation of the variance-covariance matrix for AM CVn. The $d\theta_i$ are varied for each parameter over seven orders of magnitude as described in Section 2.4. In this example, $d\theta_{\mathcal{A}}$, $d\theta_f$, $d\theta_\iota$, $d\theta_\psi$ are varied from $(10^{-4}, ..., 10^{2}) \times \sqrt{\epsilon} \times \theta_i$, where, θ_i are the true values for AM CVn. The values of $d\theta_\phi$, $d\theta_\beta$, $d\theta_\lambda$ are varied from $10^{-6}, ..., 10^{0}$, more than for parameters above, because the numerical derivatives of ϕ, β, and λ are unstable for lower values . The first row of the uncertainties in the parameters correspond to the first set of $d\theta_i$, et cetera. In principle, the uncertainties σ_i should level off around the third row. The uncertainties for all our verification binaries are calculated in this way.

TABLE 2.2: Parameter uncertainties, σ_i, in a range of $d\theta_i$ for the case of AM CVn, with S/N $\sim$ 11 for $T_{\text{obs}} = 2$ years. The values start to level off from the third to fifth row.

$\sigma_{\mathcal{A}}$	σ_ϕ	$\sigma_{\cos\iota}$	σ_f	σ_ψ	$\sigma_{\sin\beta}$	σ_λ
1.417×10^{-23}	0.317	0.072	6.517×10^{-10}	0.128	0.027	0.029
7.934×10^{-23}	1.693	0.426	6.533×10^{-10}	0.846	0.028	0.034
1.037×10^{-22}	2.234	0.555	6.541×10^{-10}	1.120	0.028	0.038
1.041×10^{-22}	2.242	0.557	6.541×10^{-10}	1.124	0.028	0.039
1.041×10^{-22}	2.242	0.557	6.541×10^{-10}	1.124	0.028	0.039
1.035×10^{-22}	2.250	0.554	6.556×10^{-10}	1.126	0.029	0.04
8.756×10^{-23}	2.301	0.473	8.259×10^{-10}	0.942	0.113	0.122

2.B 2. Sampling

In Fig 2.8, we show the effect of the sampling time Δt on the noise PSD of the instrumental noise, which is the average spectrum of the TDI X observable. At $f < 5 \times 10^{-3}$ Hz, the sampling time does not affect the level of the PSD. Above these frequencies, the PSD with a relatively long sampling time of 64s underestimates its true level.

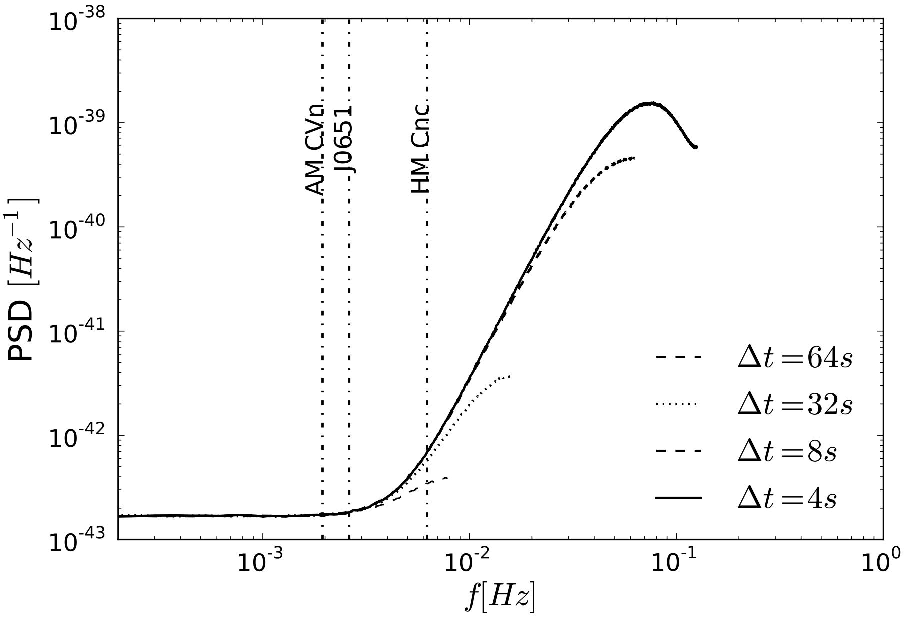

Figure 2.8: Average PSDs of instrumental noise for eLISA with varying sampling time, Δt. For lower-frequency sources such as AM CVn and J0651, a sampling as fine as 64s can be used. However, for HM Cnc, whose frequency is higher, a high Δt would overestimate its S/N, since the level of the noise is too low for the longest sampling times.

CHAPTER 3

USING ELECTROMAGNETIC OBSERVATIONS TO AID GRAVITATIONAL-WAVE PARAMETER ESTIMATION OF COMPACT BINARIES OBSERVED WITH LISA II:THE EFFECT OF KNOWING THE SKY POSITION

S. Shah, G. Nelemans & M. v.d. Sluys

A&A, 553:A82, May 2013

Abstract

In this follow-up paper, we continue our study of the effect of using knowledge from electromagnetic observations in the gravitational wave (GW) data analysis of Galactic binaries that are predicted to be observed by the new *Laser Interferometer Space Antenna* in the low-frequency range, $10^{-4}\,\mathrm{Hz} < f < 1\,\mathrm{Hz}$. In the first paper, we have shown that the strong correlation between amplitude and inclination can be used for mildly inclined binaries to improve the uncertainty in amplitude, and that this correlation depends on the inclination of the system. In this paper we investigate the overall effect of the other orientation parameters, namely the sky position and the polarisation angle. We find that after the inclination, the ecliptic latitude of the source has the strongest effect in determining the GW parameter uncertainties. We ascertain that the strong correlation we found previously, only depends on the inclination of the source and not on the other orientation parameters. We find that knowing the sky

position of the source from electromagnetic data can reduce the GW parameter uncertainty up to a factor of ~ 2, depending on the inclination and the ecliptic latitude of the system. Knowing the sky position and inclination can reduce the uncertainty in amplitude by a factor larger than 40. We also find that unphysical errors in the inclinations, which we found when using the Fisher matrix, can affect the corresponding uncertainties in the amplitudes, which need to be corrected.

3.1 Introduction

Even though population synthesis studies have predicted $\sim 10^8$ galactic white-dwarf binaries [e.g. Nelemans et al., 2001b], there are only about ~ 50 compact binary sources that have been studied at optical, UV, and X-ray wavelengths [e.g. Roelofs et al., 2010]. A space-based gravitational wave (GW) detector, such as the proposed ESA mission eLISA, is expected to observe millions of these predicted compact Galactic binaries with periods shorter than about a few hours [Nelemans, 2009; Amaro-Seoane et al., 2013], amongst other astrophysical sources, and resolve several thousands of these binaries [Nissanke et al., 2012]. In a recent paper, we investigated the effect of using knowledge from electromagnetic (EM) observations in the gravitational wave data analysis of Galactic binaries by exploring the correlations that might exist between these parameters. We found that for binaries with relatively low inclinations ($\iota \leq 45°$), an EM constraint on inclination can improve the estimate of the GW amplitude by a significant factor [Shah et al., 2012, Paper I, hereafter]. The improvement depends on the signal-to-noise ratio (S/N) of the source and on the EM constraint on inclination itself. We also found that this correlation is a strong function of the inclination of the system, but that it is independent of other angular parameters that describe the binary, in particular, sky position, and polarisation angle. From the initial results we also found that several other correlations that were rather small as a function of inclination (e.g. Figure 4 in Paper I) change drastically when computed as a function of sky position. We address this problem here and also investigate the general dependence of parameter uncertainties on the orientations of the binary. Additionally, we discuss the influence of knowing the sky position from EM data on the parameter uncertainties of the binary sources.

The angular resolution of cLISA[1] for monochromatic binaries has been studied previously [Peterseim et al., 1997; Cutler, 1998; Rogan & Bose, 2006; Błaut, 2011]. Peterseim et al. [1997] have shown the uncertainty in ecliptic latitude and ecliptic longitude as a function of both the parameters for a specific case of a cross-polarised source radiating at $f = 3$mHz, which would be observable by cLISA. For a source with $S/N = 115$, depending on the values of the ecliptic latitude and longitude, they found the uncertainties

---

[1] classic LISA refers to the detector configuration in consideration prior to eLISA (see Paper I).

in these angles to range from 1 to 8 milliradians. However, they assumed that except for the sky position, all other parameters are known *a priori.* Their study was also limited by a very simplified detector response and was tailored for a system at an inclination which is favourable in extracting its parameters. Relaxing the assumption of prior knowledge of other parameters, Cutler [1998] has shown that for a binary for a few sets of sky positions, the solid angle uncertainty (σ_Ω) ranges from 3 to 300 square degrees, depending on the frequency of the source. In subsequent work by Rogan & Bose [2006], sky position uncertainties were estimated for signals modelled for cLISA. They included chirp as an additional parameter, and these signals were not limited to a certain polarisation. Recently, Błaut [2011] has shown sky position uncertainties for various combinations of data channels from cLISA and included detailed detector response for the two distinct cases of low- and high-frequency sources. For a 10^{-3} Hz source with an edge-on orientation and an S/N of 10, an observation of one year is predicted to give a solid angle resolution of ~ 0.1 steradians which is a result very similar to the study by Rogan & Bose [2006]. However, none of these previous authors provided an overall effect of varying multiple angular parameters, which can have a significant effect on parameter uncertainties. In this paper we aim to generalise the uncertainties in all parameters for all possible orientations of the binary and calculate the improvement in these uncertainties that is possible thanks to prior knowledge of the sky position and/or inclination of the system. We show this for eLISA.

A monochromatic binary expected to be observed by eLISA is completely described by seven parameters: dimensionless amplitude ($\mathcal{A}$), frequency (f), polarisation angle (ψ), initial GW phase (ϕ_0), inclination ($\cos\iota$), ecliptic latitude ($\sin\beta$), and ecliptic longitude (λ). The inclination of the binary is defined as $\cos\iota = \vec{n}\cdot\vec{L}$, where $\vec{n}$ is the line-of-sight vector from the observer to the source and can be described by the sky position parameters β and λ. $\vec{L}$ is the orientation of the orbital plane of the binary (or angular momentum vector), which can be specified by θ_L and ϕ_L. One of the main findings of Paper I is that the parameter uncertainties of a monochromatic binary and the three strongest correlations between these parameters (the correlation between amplitude and inclination $c_{\mathcal{A}\,\cos\iota}$, the correlation between phase and polarisation $c_{\phi\psi}$, and the correlation between phase and frequency $c_{f\phi}$) are strong functions of the source's inclination ι. Furthermore, we found that the parameter uncertainties of such a binary also change as a function of other orientation parameters. These are parameters that describe the relative geometry of the binary in relation to the detector: ψ, λ, and β. It is natural to then ask the questions, how the possible strong correlations between the parameters due to these four orientation parameters influence these uncertainties, and to which extent knowledge from the EM data can improve the remaining parameter determinations. Of the remaining three parameters, $\mathcal{A}$ (see Eq. 3 in Paper I) is intrinsic to the source and does not depend on its relative orientation to the detector. Since it only scales the S/N of the system, varying the amplitude thus will affect parameter uncertainties as expected, where larger $\mathcal{A}$ will give smaller uncertainties and *vice versa.* The initial phase ϕ_0, which does not evolve for a monochromatic binary in the eLISA band, has no effect on the signal. On the other hand, the effect of frequency on the parameter accuracies can be significant; the strength of the modulations in the signal (which is caused by the motion of the detector around the Sun and relative to the source) affects low-f sources differently than high-f sources. This has been addressed in detail in previous studies, e.g. Błaut [2011]. Hence, here we focus on the effects on the parameter uncertainties of a Galactic binary due to sky position and the orientation parameters.

In this study, we consider low-frequency binaries. We start by briefly summarising the analysis methods and then describe our Monte Carlo (MC) simulations in Section 2. In Section 3, we summarise the important results and our interpretation. In Section 4 we show that uncertainties can be severely overestimated for parameters with clear physical bounds, such as inclination, and thus also for parameters that are tightly correlated with them. We also briefly discuss the S/N limit for which the results are valid in Section 4, and present our conclusions in Section 5.

3.2 Monte Carlo simulations

Our signal and noise modelling and our data analysis method have been described in Paper I and we briefly summarise them here. The signals from the binaries that are expected to be observed by eLISA are modelled as monochromatic sources characterised by seven parameters, as mentioned above. Most of these sources radiate at low frequencies (milliHertz), including some of the *verification* binaries like AM CVn, and at these low f, the detector response can be derived in the long-wavelength approximation. The noise is composed of instrumental noise described as a Gaussian random process, and a foreground noise mostly arising from the millions of double-detached Galactic white-dwarf binaries. After removing the binaries, which are predicted to be resolved due to their strong signals, the foreground noise is also described by a Gaussian distribution. Given that a signal has a known waveform and the noise is Gaussian, we can use the Fisher matrix to estimate the uncertainties in the parameters that describe the waveform. The inverse of the Fisher information matrix (FIM), known as the variance-covariance matrix (VCM), gives the uncertainties and the correlations between the parameters. Given a number of parameters n, one can calculate the $n \times n$ VCM. For details we refer to Paper I.

Uncertainties in parameters are proportional to the inverse of the S/N, but they are also influenced by the correlations between parameters. Generally, a system with higher S/N has smaller parameter uncertainties and *vice versa*. However, if there is a strong correlation between any two parameters, this (in addition to the S/N) will influence their uncertainties. As mentioned in the previous section, we find that the overall effect of the sky position and the orientation parameters of a binary has not been investigated and this is one of the goals of this study. To do this, we fixed the values of $\mathcal{A}$, f, and ϕ_0 to those of AM CVn (see Paper I) and varied its ψ, ι, β, and λ within their allowed ranges using a Monte Carlo method. We carried out a number of of MC simulations. Each simulation corresponds to varying a different (sub)set of these four parameters simultaneously. The motivation is to understand how each of the four parameters above influence the GW data analysis individually and in combination with each other. We explain these motivations briefly below, which will become clearer in section 4 where the choice of each MC simulation is explained in more detail.

First of all, we set the distance of the AM CVn system close enough so that the S/Ns are sufficient to believe the Fisher matrix results (see section 4). The first set of simulations we performed for an AM CVn of a fixed $\mathcal{A}$, f, and ϕ_0, while its position and orientation parameters λ, β, ψ, and ι were all varied simultaneously 4000 times. Thus, from the sample of these 4000 systems with various orientation parameters we first ascertained that the dominant effect on the parameter uncertainties is indeed the inclination of the system (result from Paper I). Next, we can quantify how the other three angles affect the parameter uncertainties globally. We performed another set of calculations where we fixed inclination (to a few choices explained later), frequency, and the phase (like above), and we varied the amplitude (by changing the distance, d), the sky position, and the polarisation angle. For each choice of the inclination, MC simulations were performed for 500 systems to quantify the effect of varying the S/N (by changing the distance) and the ecliptic latitude, longitude, and the polarisation angle on the parameter uncertainties. Finally, to quantify the possible improvement in the parameter uncertainties gained by prior (EM) knowledge of the sky location, we carried out 500 MC simulations for an AM CVn at a fixed inclination and varied the rest of the orientation parameters and the distance. However, instead of a full 7×7 VCM, we calculated a 5×5 VCM, where for each system the randomly chosen sky locations were fixed to that value. Similarly, we repeated this exercise to quantify the improvement in the parameter accuracies gained by EM knowledge of inclination in addition to sky position, and thus we calculated a 4×4 VCM for each system. For clarity, we briefly summarise these four sets of MC simulations below:

1. MC1: Fix $\mathcal{A}$ (i.e. d, m_1, and m_2 where, m_i is the mass), f, and ϕ_0. Randomly pick the orientation of the binary, $\vec{L}(\phi_L, \theta_L)$, λ, and β over their physical ranges. The parameters ψ, and ι are then given by the following equations [Cornish & Rubbo, 2003]:

$$\cos\iota = \cos(\theta_L)\ \sin(\beta) + \sin(\theta_L)\ \cos(\beta) + \cos(\phi_L - \lambda) \ \text{ and} \tag{3.1}$$

$$\tan\psi = \frac{\sin\beta\ \cos(\lambda - \phi_L) - \cos(\theta_L)\ \sin(\theta_L)}{\sin(\theta_L)\ \sin(\lambda - \phi_L)}. \tag{3.2}$$

2. MC2: For each $\iota = 30^\circ, 60^\circ, 90^\circ$, randomly pick λ, β, ψ, and d.

3. MC3: Like MC2, but fix λ, and β assuming an *a priori* known sky position [5×5 FIM].

4. MC4: Like MC2, but fix λ, β, and ι assuming an *a priori* known sky position and inclination [4×4 FIM].

Each of the four parameters are randomly picked from their uniform distribution in the following range: $\lambda \in [0, 2\pi]$, $\sin\beta \in [-1, 1]$, $\phi_L \in [0, 2\pi]$, $\theta_L \in [0, \pi]$, and $d \in [0.01, 0.3]$ kpc. The corresponding ranges in ι and ψ are $[0, \pi]$. We also define the following inclinations for presenting the results below (unless specified): face-on:= $0° \leq \iota \leq 45°$ or $135° \leq \iota \leq 180°$, mildly face-on:= $45° \leq \iota \leq 60°$ or $120° \leq \iota \leq 135°$, mildly edge-on:= $60° \leq \iota \leq 80°$ or $100° \leq \iota \leq 120°$, and edge-on:= $80° \leq \iota \leq 100°$.

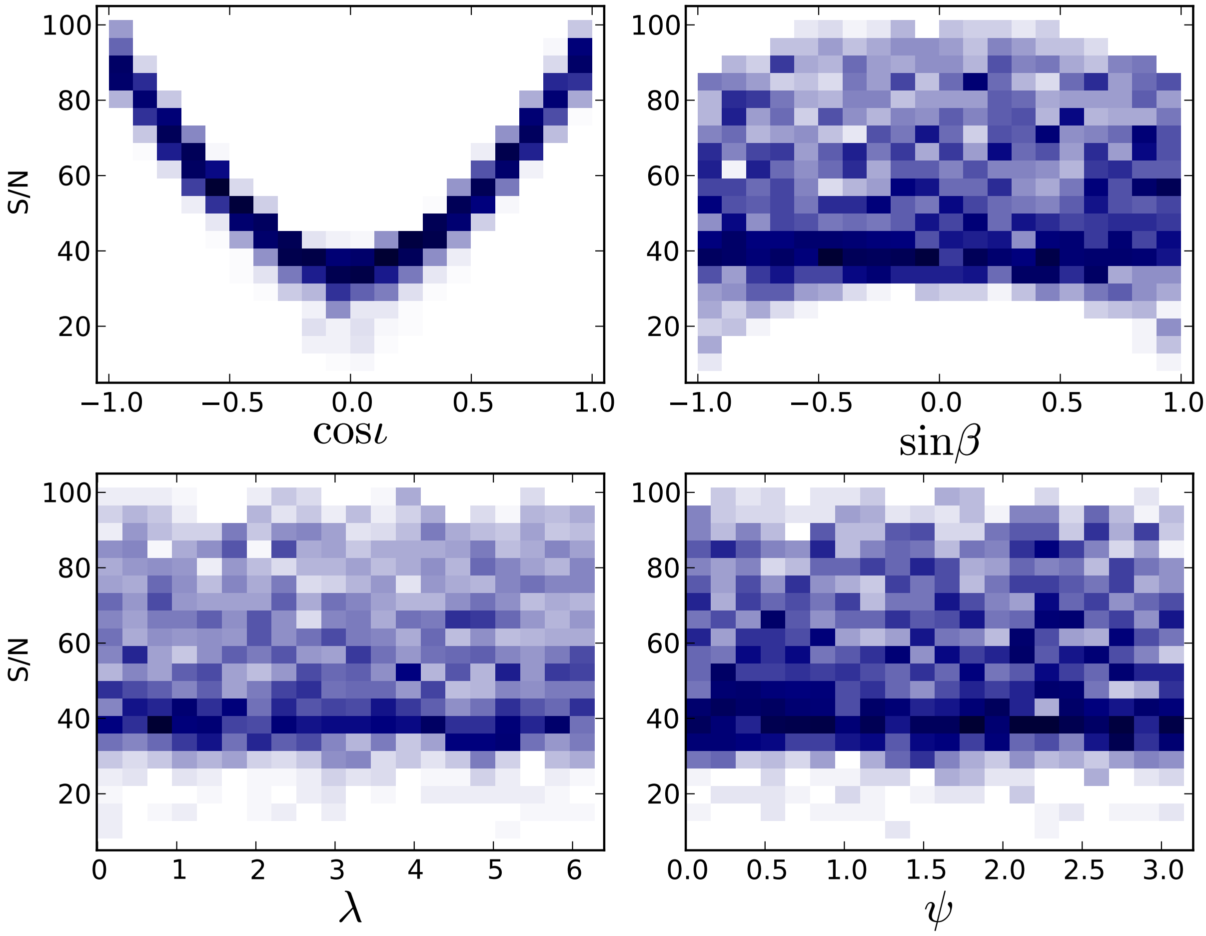

Figure 3.1: Two-dimensional distributions of signal-to-noise ratio as a function of $\cos\iota$, $\sin\beta$, λ, and ψ. Face-on, mildly face-on, mildly edge-on, and edge-on systems (whose exact bounds are specified in Section 2) can be read off from the top-left panel. In the other panels, the trend from face-on to edge-on systems follows from the top of the distribution to the bottom.

3.3 Results

3.3.1 Global dependence of the uncertainties: dominance of inclination (MC1)

We have seen in Paper I that the parameter uncertainties are a strong function of the inclination of the system, which is due to the strong dependence of the signal strength, i.e. S/N, on the inclination and to the strong correlations. In this section, we first discuss the global behaviour of the parameter uncertainties as a result of varying the sky position, inclination, and the polarisation angle at the same time. We verify the result from Paper I that inclination has a dominant effect on the parameter uncertainties. We show that after the inclination, the ecliptic latitude, β, of the system has the strongest influence on the parameter uncertainties.

Using the results from MC1, we show in Figure 3.1 the S/N of binary systems as a function of the four angular parameters over which they are randomly picked. As expected, there is a strong dependence of S/N of a system on inclination, as shown in the top-left panel. Due to this dependence on the inclination, in the other panels we find that the face-on systems form a band at the top of these plots, followed by bands of mildly face-on, mildly edge-on, and edge-on systems, in that order. In the top-right panel, there is a mild but noticeable increase in S/N, for the binaries at the ecliptic plane, $\sin\beta = 0$, whereas the ecliptic longitude and the polarisation angle have no significant effect on the binaries' S/N, as shown in the bottom panels. Figures 3.2, 3.3 is a plot of parameter uncertainties as a function of $\sin\beta$ taken from MC1. In the top panels, uncertainties in $\mathcal{A}$, ι, ϕ, and ψ are smallest for edge-on systems (forming a band at the bottom) and progressively increase for the face-on systems (the top of distribution). This is discussed in Paper I and results from the correlations between these parameters. The lower inclination systems $\iota \leq 45°$ or $\iota \geq 135°$ have very similar signal shapes in those ranges, whereas systems with close to edge-on orientations are distinguishable by both the shape and structure for small differences in inclinations. For face-on systems a small change in inclination is indistinguishable from a small change in its intrinsic amplitude, whereas for an edge-on system, a small change in inclination produces a noticeably different signal. Thus even for their lower S/Ns, the inclinations of the edge-on systems are better determined than those of the face-on systems. A similar argument based on the strong correlation between ϕ and ψ for face-on systems can explain the huge uncertainties of these parameters despite their strong signals (see Paper I). Since there are no such correlations between f, λ, and β (or the solid angle Ω), their uncertainties should be a consequence of the S/N, i.e. from the top panels of Figure 3.1: a higher S/N implies lower values for the uncertainties and *vice versa*, which indeed holds for σ_f and σ_λ. From Figures 3.1 and 3.2, 3.3 it is evident that inclination has the strongest effect on the S/N and so to the leading order this parameter affects the parameter uncertainties, which confirms our results in Paper I. After inclination, the strongest effect on the S/N

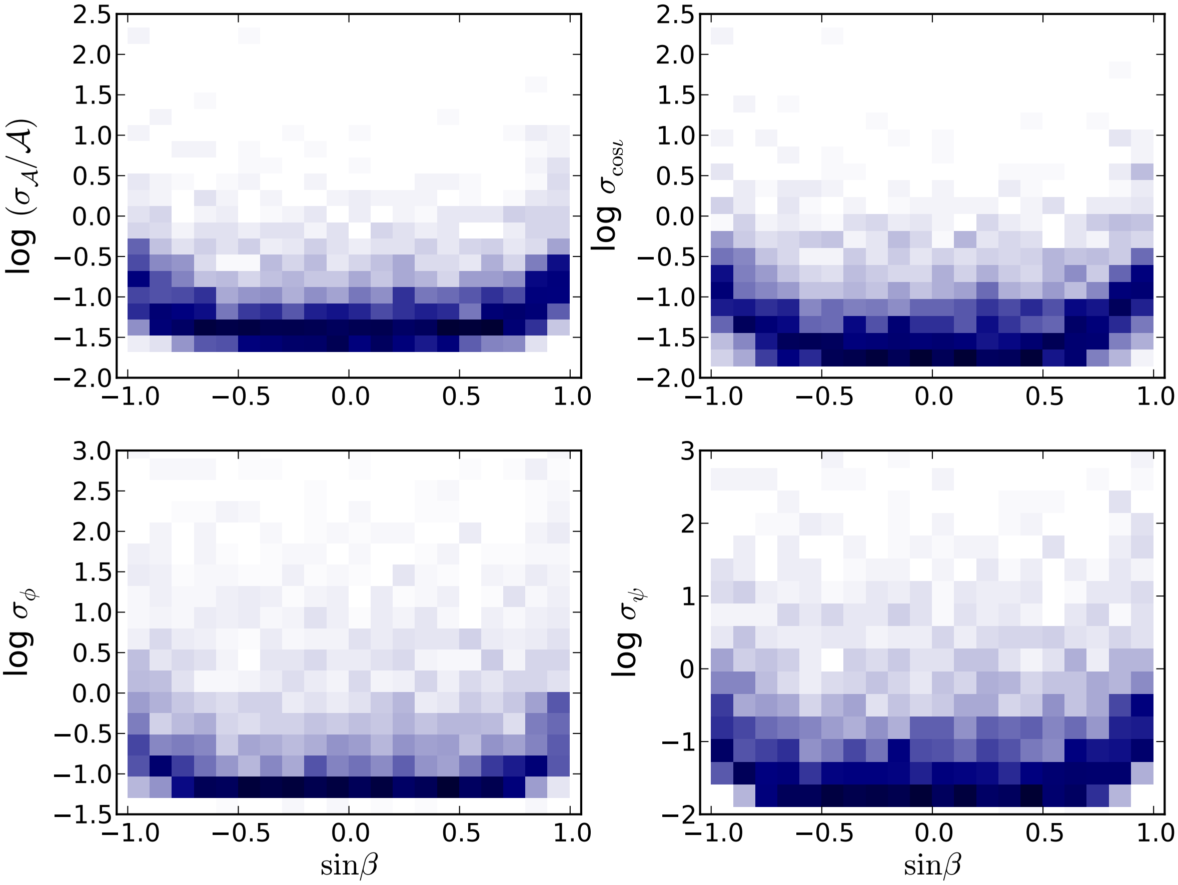

Figure 3.2: Two-dimensional distributions of the uncertainties in the seven GW parameters of the galactic binary systems as a function of $\sin\beta$ from MC1 as described in the text. Units of the angles are in radians.

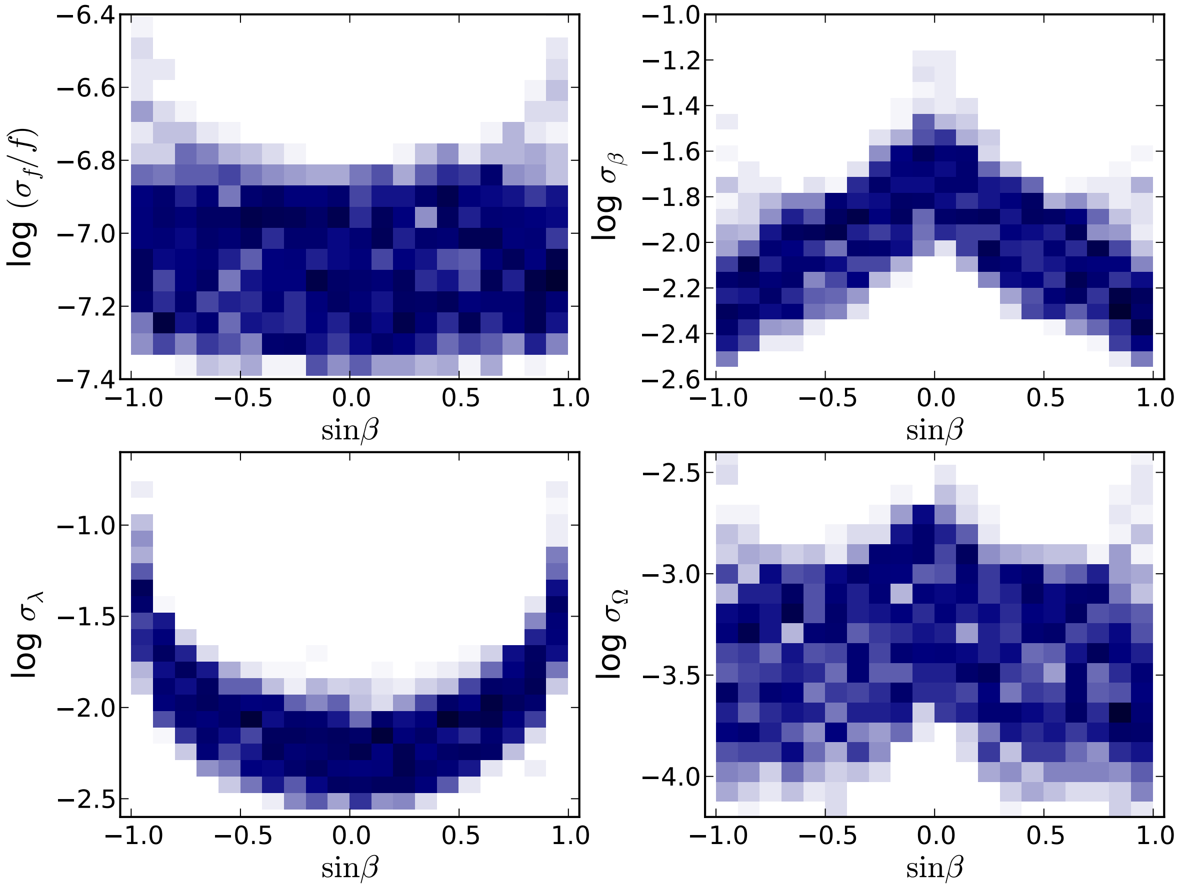

FIGURE 3.3: Two-dimensional distributions of the uncertainties in the seven GW parameters of the galactic binary systems as a function of $\sin\beta$ from MC1 as described in the text. Units of the angles are in radians.

of the systems is produced by the ecliptic latitude. Thus, we expect the uncertainties in the parameters also to be affected by β (see top-right panel in Figure 3.1); sources at the ecliptic poles should have larger uncertainties than those at the ecliptic plane. In Figure 3.3 we can see that for a fixed distance to the source d, most uncertainties ($\sigma_\mathcal{A}$, σ_ι, σ_ϕ, σ_ψ, σ_f, and σ_λ) are indeed smaller towards the plane than close to the poles. This is probably largely due to the S/N as a function of $\sin\beta$. The unusual behaviour of σ_β, which increases at the plane compared to its value at the poles ($\sin\beta = \pm 1$), has been pointed out in Cornish & Larson [2003] and is caused by the Doppler modulation Φ_D (Eq. 9 in Paper I). This behaviour is surprising since Φ_D has the largest magnitude on the plane (since it is proportional to $\cos\beta$), and so we naively expect the sky resolution to be better on the ecliptic plane. However, the resolution in β is determined by the *rate of change* of the Doppler modulation with respect to β (i.e. proportional to $\sin\beta$), which is the highest at the pole and lowest at the plane. This is also evident in the solid angle uncertainty σ_Ω in the bottom-right panel in Figures 3.2, 3.3, where $\sigma_\Omega = 2\pi(\sigma_{\sin\beta}\sigma_\lambda - \mathcal{C}_{\sin\beta\lambda})$, $\mathcal{C}_{\sin\beta\lambda}$ being the unnormalised correlation between $\sin\beta$ and λ [Cutler, 1998]. We also observe that σ_λ has a distinct U shape, becoming very severe at the poles. This is merely because λ becomes progressively less well-defined as a source lies closer to the pole. Note that at the pole λ is not defined, which means that it can take any value.

3.3.2 Dependence of the uncertainties on β: S/N or correlations (MC2)?

The general behaviour of the parameter uncertainties (except σ_β, hence σ_Ω) in Figures 3.2, 3.3 shows a minimum at the ecliptic plane that could be attributed to the S/N, since it is the highest for sources in the plane. To investigate this change in the uncertainties as a function of $\sin\beta$, we consider the results from MC2 and the correlations between parameters from MC1. In MC2 we varied S/N (by varying the distance to the binary, d), λ, β, and ψ for a few fixed inclinations. We fixed the ι for each of the MC2 simulations because we established its dominant effect through the S/N in the previous section, therefore the goal now is to determine which contributes most to the behaviour observed in Figure 3.2, 3.3: the S/N (top-right panel of Figure 3.1), or the correlations as a function of $\sin\beta$. If the larger uncertainties at the pole compared to the plane are solely due to the corresponding S/Ns, then we should see from the MC2 simulations that uncertainties anti-correlate tightly with the S/N of the sources. In Figures 3.4, 3.5 we show three distinct curves in S/N vs. parameter uncertainty that roughly show monotonic functions where all the uncertainties decrease with increasing S/N. However, all uncertainties except σ_f have a significant horizontal scatter. In the figure, the size of the symbol represents the magnitude of the ecliptic latitude. Higher values of $|\beta|$, which represent regions around both ecliptic poles, concentrate towards the right-hand side of the plots (with the exception of σ_β), and the opposite is true for the lower values of $|\beta|$, which roughly represent the ecliptic plane. In the top panels, from left to right, the curves correspond to $\iota = 90°, 60°$, and $30°$ respectively, and these overlap in the bottom panels. As explained above, $\sigma_\mathcal{A}$, σ_ι, σ_ψ, and σ_ϕ are larger for face-on systems ($\iota = 0, 30°$) than for edge-on systems ($\iota = 90°$), owing to the correlations between these parameters even though face-on systems have higher S/Ns. Since these correlations are very weak for λ, β, and ψ for all inclinations (see Paper I), their uncertainties overlap in the bottom panels of Figures 3.4, 3.5. This spread across the horizontal axis must be due to changes in their correlations as a function of the ecliptic latitude. This is indeed shown in Figures 3.6, 3.7, which is taken from MC1. In the figure we show a 2d histogram to display the global dependency of the correlations on the ecliptic latitude. We notice that the correlations involving λ, ι, ψ, ϕ, and $\mathcal{A}$ ($c_{\mathcal{A}\lambda}$, $c_{\phi\iota}$, $c_{\phi\lambda}$, $c_{\iota\lambda}$, and $c_{\psi\lambda}$) are generally weaker at the ecliptic plane. However, at the poles these correlations can take any value from 0 to ±1 and concentrate at ±1. This is the case for all inclinations. Accordingly, close to the ecliptic poles, there are sets of λ and ψ for which the correlations can become very strong, which explains the horizontal spread of uncertainties in Figures 3.2, 3.3. Note that in Figure 3.6, 3.7, we have shown (only) the normalised correlations c_{ij}, whose absolute

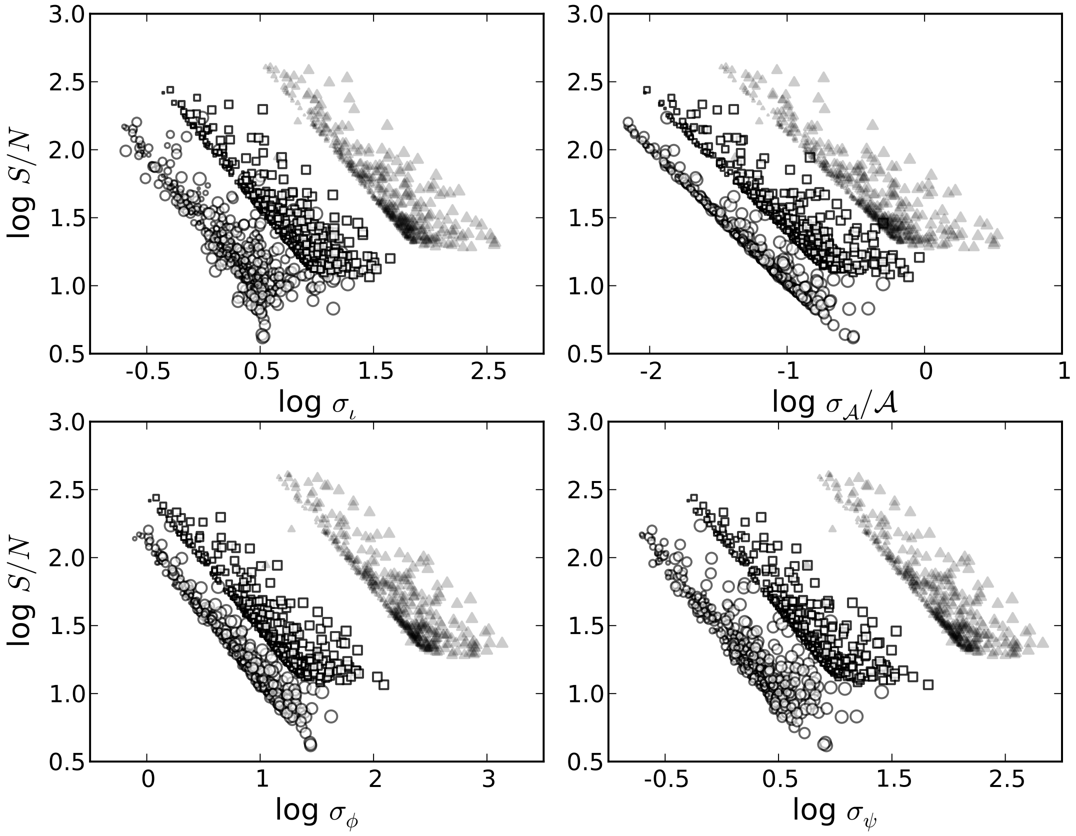

FIGURE 3.4: Uncertainties in all seven parameters of the systems as a function of S/N from MC2. Open circles, squares, and filled triangles represent binary systems at fixed inclinations of $90°, 60°$, and $30°$ respectively. The size of the symbol represents the magnitude of $|\beta|$ for each simulated binary. In the bottom panels the different groups of symbols overlap.

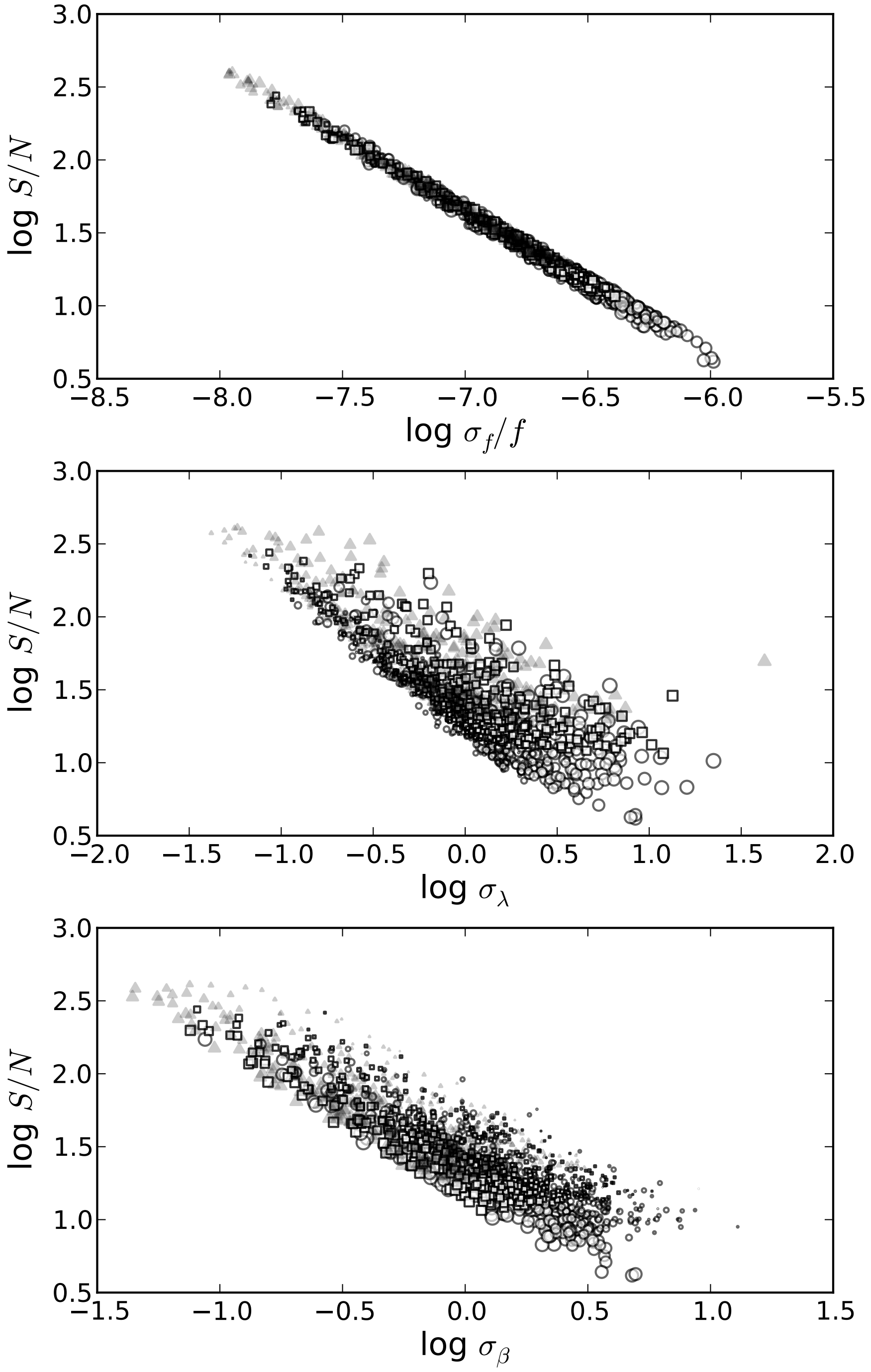

FIGURE 3.5: Uncertainties in all seven parameters of the systems as a function of S/N from MC2. Open circles, squares, and filled triangles represent binary systems at fixed inclinations of $90°, 60°$, and $30°$ respectively. The size of the symbol represents the magnitude of $|\beta|$ for each simulated binary. In the bottom panels the different groups of symbols overlap.

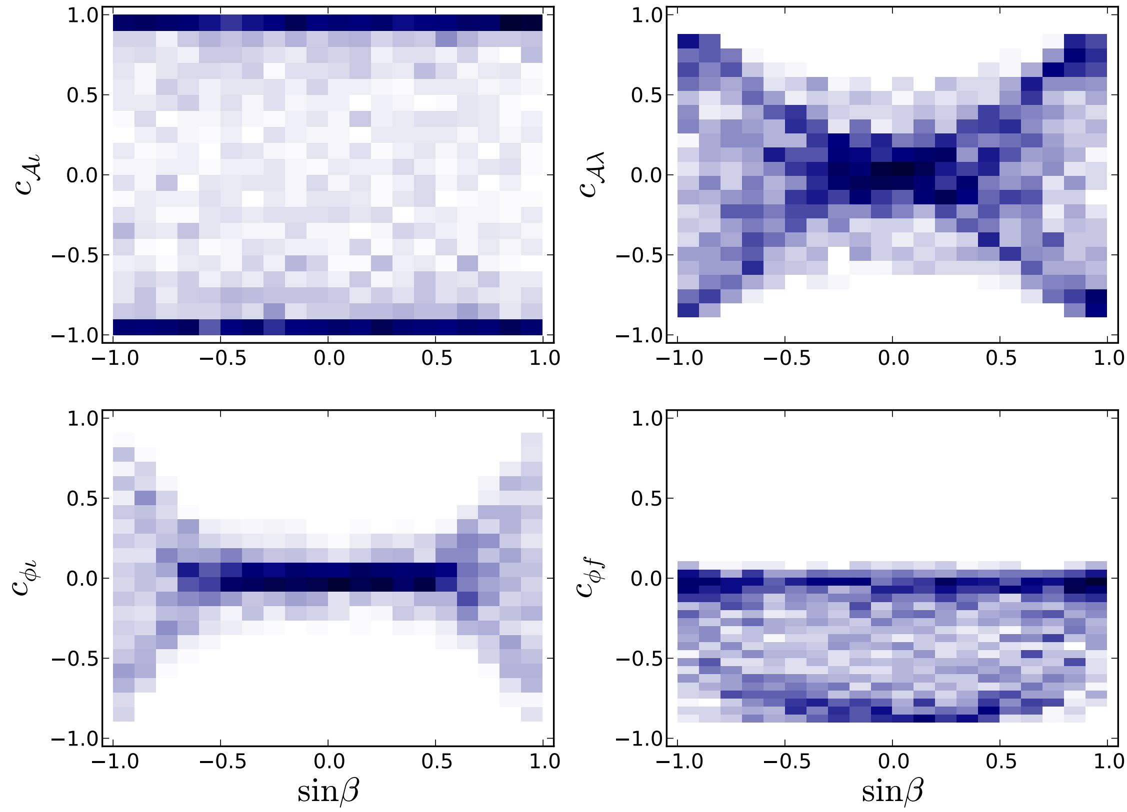

Figure 3.6: Two-dimensional distributions of the normalised correlations as a function of $\sin\beta$ from MC2. We show here only the strong (normalised) correlations, meaning $|c_{ij}| > 0.5$.

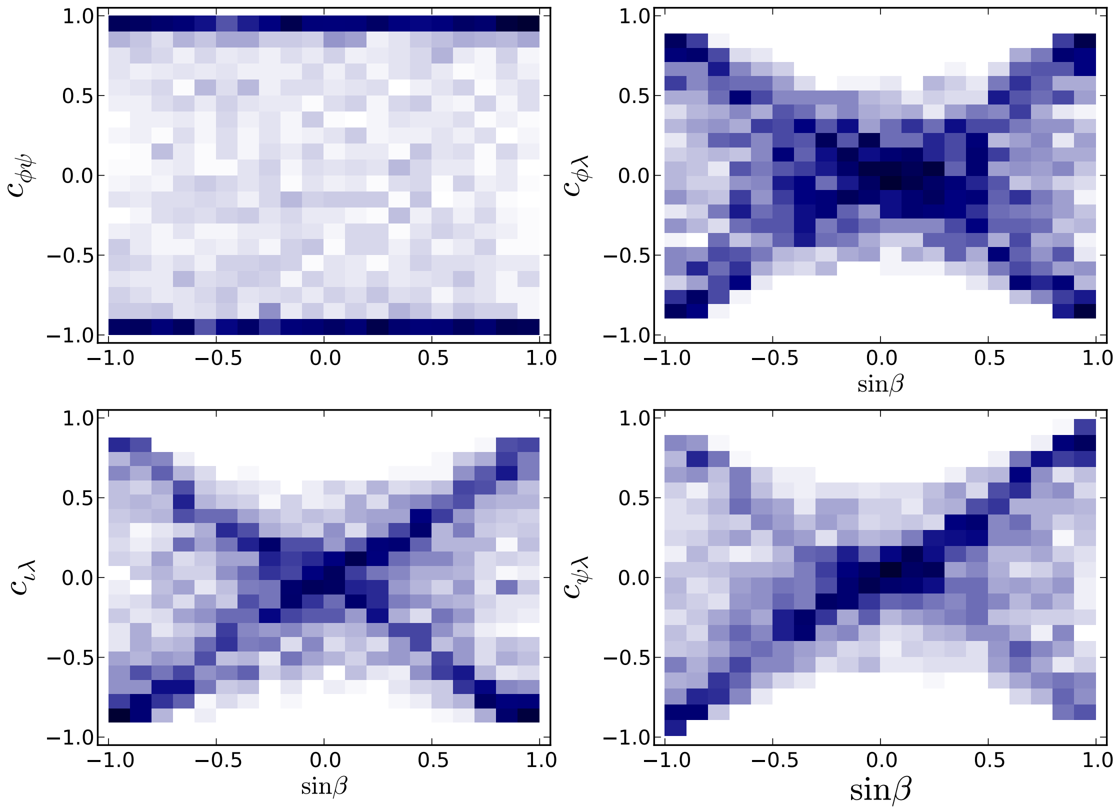

Figure 3.7: Two-dimensional distributions of the normalised correlations as a function of $\sin\beta$ from MC2. We show here only the strong (normalised) correlations, meaning $|c_{ij}| > 0.5$.

values can exceed 0.5. A detailed explanation of these correlations can be found in the Appendix.

3.3.3 Gain from a priori knowledge of sky position and inclination (MC and MC4)

From Figures 3.2, 3.2, 3.4, and 3.5 we observe that uncertainties in sky location are rather large (which has also been pointed out in previous studies). For the S/Ns in this study ($\sim 8-100$), the uncertainties in σ_Ω range from ~ 0.2 to 6 square degree, as shown in Figure 3.1. If EM data can provide a more accurate sky position and possibly an inclination for AM CVn system, we can use these independent (EM) measurements to improve accuracies in other parameters. To see by which factors the uncertainties improve, we fixed the sky position of each source and calculated the corresponding 5×5 VCM. The ratios of uncertainties from using a 7×7 VCM to using a 5×5 VCM, i.e. the improvement when knowing the sky position (ecliptic latitude and longitude) exactly, are shown in Figures 3.8 3.9, calculated from MC2 and MC3. In the figures, the size of the symbol represents the S/N of that system. The figure shows that the improvement factor depends on the inclination of the source: for edge-on systems (in yellow circles with $\iota = 90°$) σ_ψ can improve by a factor of ~ 3, but for systems closer to a face-on configuration in squares and blue the improvement can only be up to a factor of ~ 2.2. One useful result from this figure is that $\sigma_\mathcal{A}$ and σ_ι can improve by a factor of ~ 2 for the systems close to the ecliptic poles. This gives a motivation for independent EM observations of the sky location. However, for edge-on systems there is no improvement in $\sigma_\mathcal{A}$ even though σ_ι improves[2]. This is simply due to the lack of correlation between these two parameters for $\iota = 90°$.

In Paper I we found that for the HM Cnc system, the improvement of $\sigma_\mathcal{A}$ by using the EM constraint in ι was smaller than for AM CVn, although the two have similar inclinations (thus the same (normalised) correlation between $\mathcal{A}$ and ι). This was due to the relatively high S/N of HM Cnc compared to the latter and thus the individual improvement factors shown in Figures 3.8 3.9 and 3.10 will also depend on the individual S/N of the systems (see Paper I).

If in addition to sky position the inclination can be constrained, as discussed previously in Paper I, the improvement factor in amplitude can be much larger because of the decoupling of the correlation between amplitude and inclination. We show the ratio of parameter uncertainties from calculating the 7×7 VCM to the uncertainties from a 4×4 VCM (where λ, β and ι are fixed) in Figure 3.10. The improvements in σ_ψ and σ_ϕ are roughly similar to the case in Figures 3.8 3.9. A remarkable difference is seen in the improvement of $\sigma_\mathcal{A}$ for binaries with $\iota = 30°$ represented in filled triangles plotted in the bottom-right panel of Figure 3.10. This is expected because by fixing ι, the strong correlation between amplitude

---

[2] Depending on the precision of the GW accuracy of the inclination, this may aid in finding eclipsing binaries.

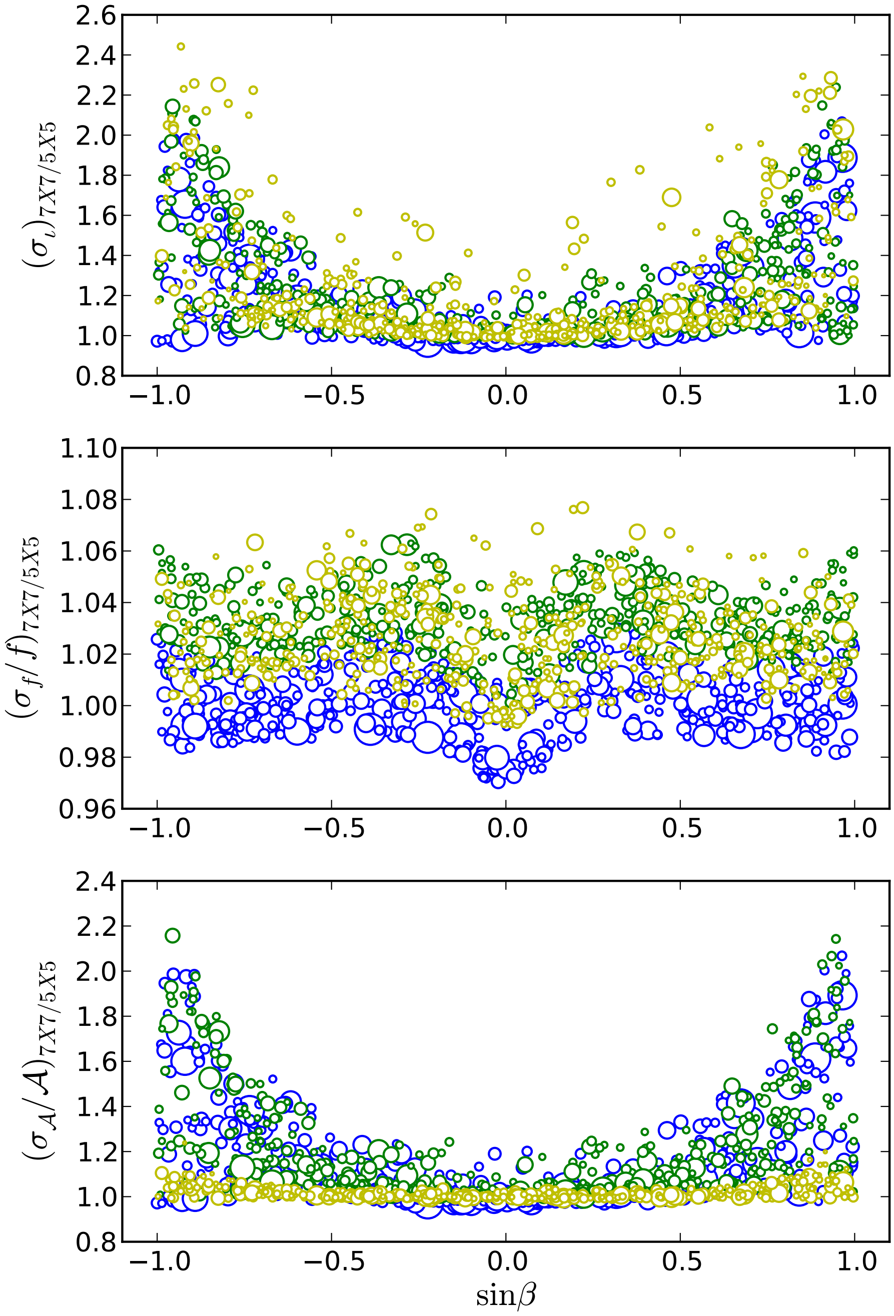

Figure 3.8: Uncertainty ratios of the parameters between analyses using a 7×7 VCM and a 5×5 VCM, where the sky position is fixed in the latter, as a function of $\sin\beta$ (from the MC2 and MC3 simulations). Blue, green and yellow represent systems at fixed inclinations of $30°, 60°$ and $90°$ respectively. The size of the symbol for each binary represents the S/N of the system.

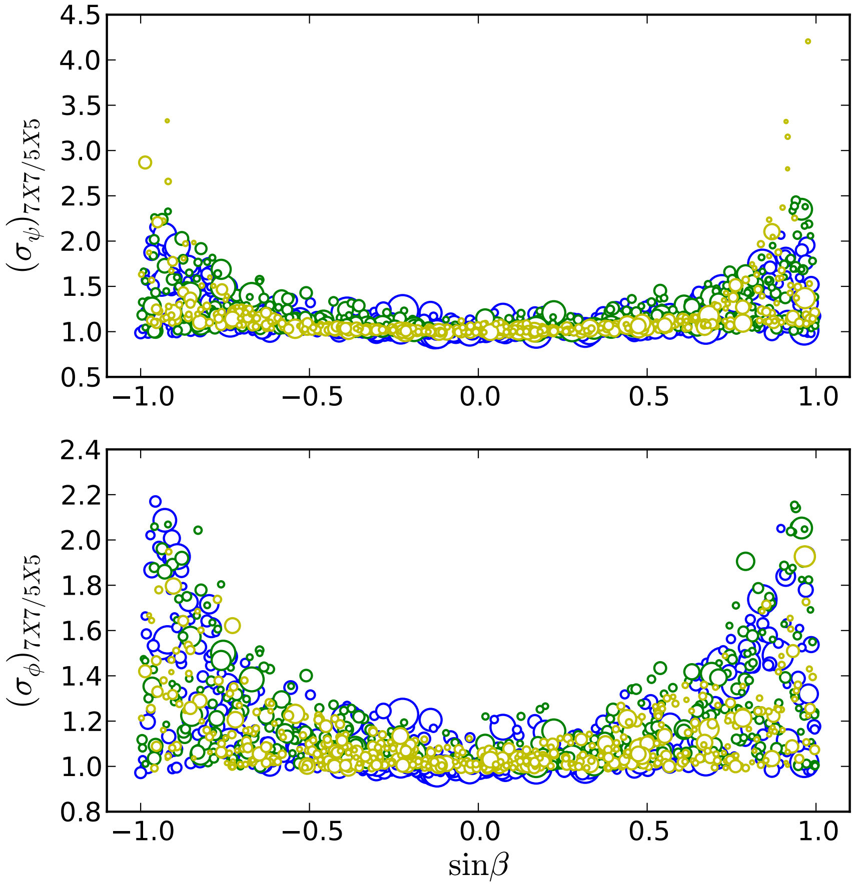

FIGURE 3.9: Uncertainty ratios of the parameters between analyses using a 7×7 VCM and a 5×5 VCM, where the sky position is fixed in the latter, as a function of $\sin \beta$ (from the MC2 and MC3 simulations). Blue, green and yellow represent systems at fixed inclinations of $30°, 60°$ and $90°$ respectively. The size of the symbol for each binary represents the S/N of the system.

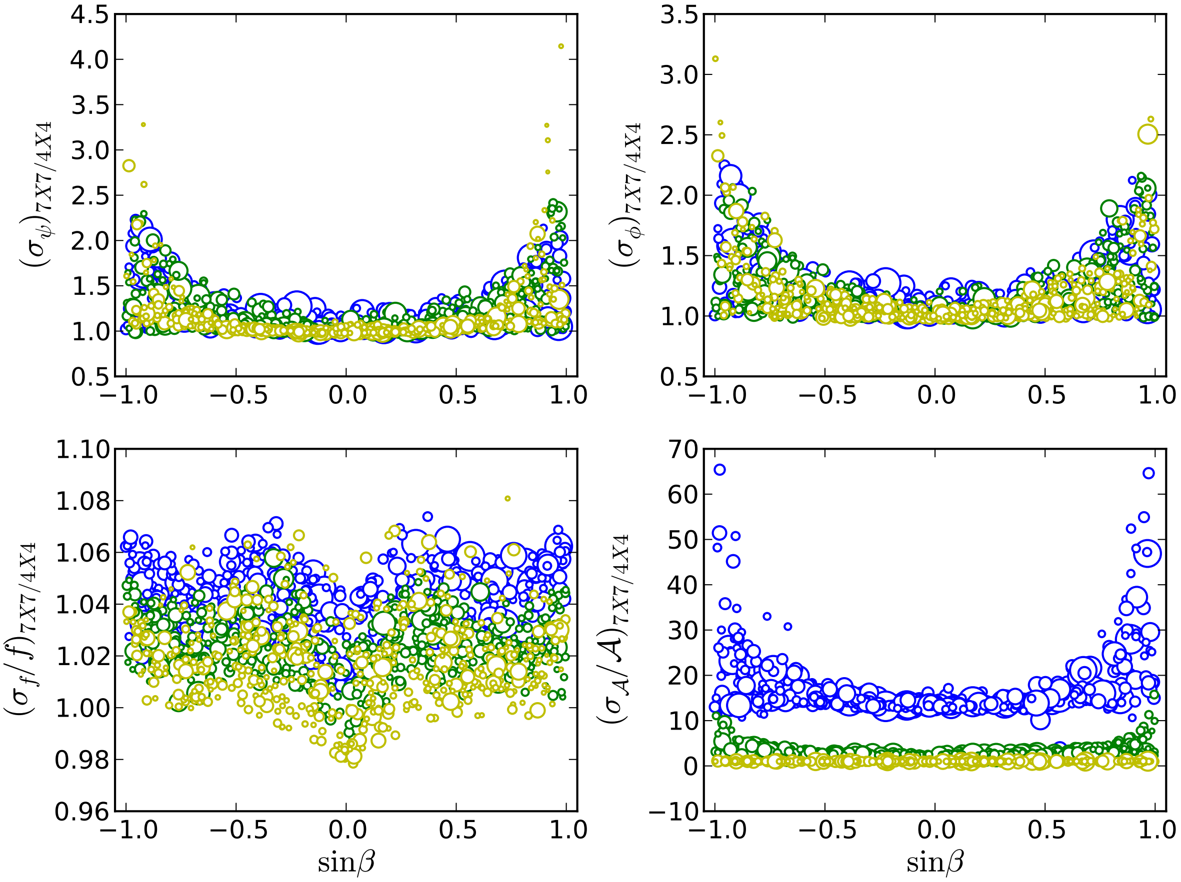

Figure 3.10: Same as in Figures 3.8 3.9 but now we assume that in addition to sky position we also know the inclination of the binary. The uncertainty ratios of the parameters are between 7 × 7 VCM (MC2) and 4 × 4 VCM (MC4). The improvement factors in amplitude include corrections due to overestimated uncertainties in the amplitudes of face-on systems (see Section 4.1) Note that the last panel is plotted in log scale in order to highlight the relatively large improvements for the systems with smaller inclinations.

and inclination is decoupled. Hence for the higher S/Ns of close to face-on systems, the uncertainties in $\mathcal{A}$ is significantly reduce. Note that here we assumed that the inclination is known exactly.

3.4 Discussion

3.4.1 Limiting inclinations to their physical range

Some of the uncertainties in ι in Figure 3.2 from MC1 are noteworthy in that they exceed their physical bounds, for example $\sigma_\iota = 7$ radians. The cause for this is that the linearised signal approximation that is internally employed in the Fisher matrix studies is not sensitive to the bounded[3] parameters that describe the model signal, as has been pointed out in Vallisneri [2008]. Thus, when an uncertainty in a (cyclicly) bounded parameter like the inclination exceeds its physically allowed range, it means the quantity cannot be determined from GW data analysis alone. For the parameter ι, we can further ask what the unphysical uncertainty in ι implies for the uncertainty in $\mathcal{A}$ for the mildly inclined systems that has a strong correlation between the two parameters. Since the Fisher matrix estimates σ_ι to unphysical values while in reality it is constrained within $[0°, 90°]$, does this mean that the uncertainty in the amplitude (due to the correlation with ι) is also overestimated? Or should we not trust the uncertainty in all those parameters where the σ_ι becomes unphysical? Consider the $\mathcal{A} - \iota$ error ellipse for a given signal h, with true signal values ι_0 and $\mathcal{A}_0$, where the two parameters are strongly correlated and where $\sigma_\iota >> \pi$. The corresponding accuracy $\sigma_\mathcal{A}$ is then also highly inflated. Now consider a second signal $h(\mathcal{A}_1, \iota_1)$, inside the error ellipse, but far from the true values, and such that $\iota_1 = \iota_0 + 2n\pi$ with $n > 1$. From its cyclic behaviour, $h(\mathcal{A}_1, \iota_1) = h(\mathcal{A}_1, \iota_0)$ should hold. However, this last point would typically lie far outside the error ellipse in the $\mathcal{A} - \iota$ plane, which would indicate that this is actually a signal that is very *dissimilar* to the true signal. Hence, the fact that the inclination is physically limited to the range $[0, \pi]$ and that this is not taken into account in the FIM method means that we should not only limit the uncertainty in inclination to its physically allowed range, but that we should limit the uncertainty in amplitude accordingly. Specifically, the corrected amplitude uncertainty, $\sigma'_\mathcal{A}$, is given by,

$$\sigma'_\mathcal{A} = \sigma_\mathcal{A}[\mathrm{VCM}] \times \frac{\sigma'_\iota}{\sigma_\iota[\mathrm{VCM}]}, \tag{3.3}$$

where σ'_ι is the corrected inclination uncertainty.

---

[3] Note that choosing $\cos\iota$ instead of ι does not alleviate this problem since $\cos\iota$ is also a bounded quantity and there is no formalism in FIM to handle bounded quantities, whether cyclic or not. In fact, for the FIM calculations we evaluate uncertainties in $\cos\iota$ and $\sin\beta$, while in quoting our results they are converted to uncertainties in ι and β by scaling them as $\sigma_\iota = \sigma_{\cos\iota}/\sin\iota$ and $\sigma_\beta = \sigma_{\sin\beta}/\cos\beta$, since these quantities are more intuitive.

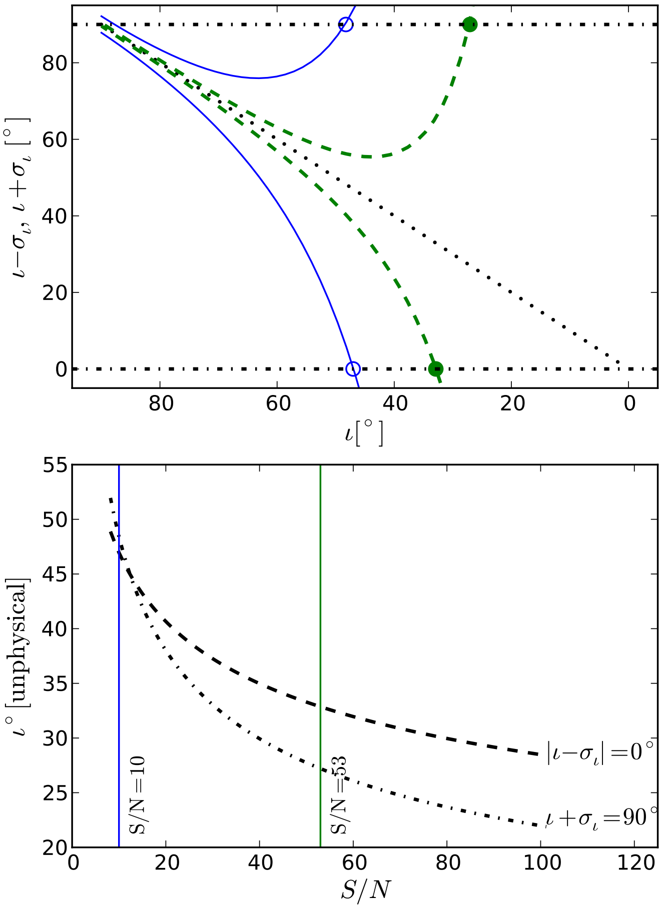

FIGURE 3.11: Top: 1-σ uncertainty in the inclinations vs. source inclinations for two values of S/N: blue lines (outer curves) correspond to S/N=10, green dashed-lines (inner curves) correspond to S/N=53. The curves above the dotted line correspond to $\iota + \sigma_\iota$, and those below to $\iota - \sigma_\iota$. The thick horizontal dashed-dotted lines are the physical limits of ι: below the line of $\iota \pm \sigma_\iota = 0^\circ$ and above the line of $\iota \pm \sigma_\iota = 90^\circ$, σ_ι can be truncated, since that value of ι is bounded between $[0^\circ, 90^\circ]$. Bottom: 'Unphysical ι' versus S/N for the systems from MC1. The thick dashed-dotted line calculated from the condition $\iota - \sigma_\iota = 0^\circ$, and the thick dashed line from the condition $\iota + \sigma_\iota = 90^\circ$ demonstrated in the left panel. At an S/N of 10, the blue line shows lower limit and the green line shows an upper limit at the intersections with the two curves from the conditions above.

The value of inclination where its uncertainty becomes unphysical can occur at two places, i.e. where $\iota+\sigma_\iota > \pi/2$ [4], and/or $\iota-\sigma_\iota < 0$, as shown in the left panel of Figure 3.11. In the panel, the 1-σ uncertainty ranges of the inclination are plotted against the sources' inclination for two cases of constant S/N of 10 and 53. The thick horizontal dashed and dashed-dotted lines indicate the conditions where σ_ι becomes unphysical. At a fixed S/N of 10 (in plusses), these values are at $\iota \sim 48°$ and $\iota \sim 47°$, respectively, as indicated by the open circles, whereas for a higher S/N of 53 (in stars) the above conditions for σ_ι occur at $\iota \sim 27°$ and $\iota \sim 32°$ indicated by filled circles. We calculated the inclinations at which these intersections occur for a range of S/Ns, $10 - 110$ and show the results in the right panel of Figure 3.11. These curves can be used to apply corrections to the limits of σ_ι in Figure 3.2 from MC1, which in turn can be used to limit $\sigma_\mathcal{A}$ from Eq. 3. In Figure 3.12 we compare the uncertainties in $\mathcal{A}$ corrected in this way with those from Figure 3.2. The corrected values for $\sigma_\mathcal{A}$ differ for the high S/N systems, as can been seen by comparing the two right-hand panels in Figure 3.12. In particular, the tail at the large $\sigma_\mathcal{A}/\mathcal{A}$ present in the top panel is absent from the bottom panel.

There is a caveat to applying these corrections. In the left panel of Figure 3.11 we can understand the cut-off at 0° at the bottom of the figure. However, at the top, the cut-off of 90° is not so clear. A system with a lower inclination (e.g. 20°) cannot have an error larger than $\sim 50°$ because a system with an inclination in the range $\sim 80° - 90°$ is distinguishable from a system with an inclination of $\sim 0 - 60°$, as has been pointed out in Paper I. Thus the cut-off of $\iota + \sigma_\iota = \pi/2$ for lower inclinations is a conservative estimate. The estimated posterior probability distribution functions (PDFs) obtained using the FIM do not predict the real PDFs for lower inclinations and lower S/Ns. Thus a full Bayesian analysis that takes into account the limits of the cyclic parameters as priors is needed to fully determine the PDF. This is beyond the scope of this paper, and we used these (probably) over-estimated uncertainties to give the corresponding bounds in the amplitude.

In the same manner that $\sigma_\mathcal{A}$ was corrected in Figure 3.12, we corrected for the MC2 calculations. The predicted improvement factors of the amplitude in the bottom-right panel of Figure 3.10 already include the corrections mentioned above.

3.4.2 Use of FIM at $S/N \sim 15$

Another problem regarding the trustworthiness of the Fisher matrix is the limit of the S/N at which one can trust the values from VCM matrix. This has been addressed in Nicholson & Vecchio [1998], where the authors have performed Fisher matrix studies in predicting the uncertainties of the parameters of the coalescing binaries. They have compared these predictions with calculations from Bayesian uncertainties, and their main finding is that above an S/N of 15, the uncertainties from the Bayesian calculations converge to Fisher matrix predictions. At an S/N of 10, the analytic predictions of Fisher matrix deviate by

---

[4] Since ι is symmetric about $\pi/2$, we only considered the inclinations in the range $[0, \pi/2]$.

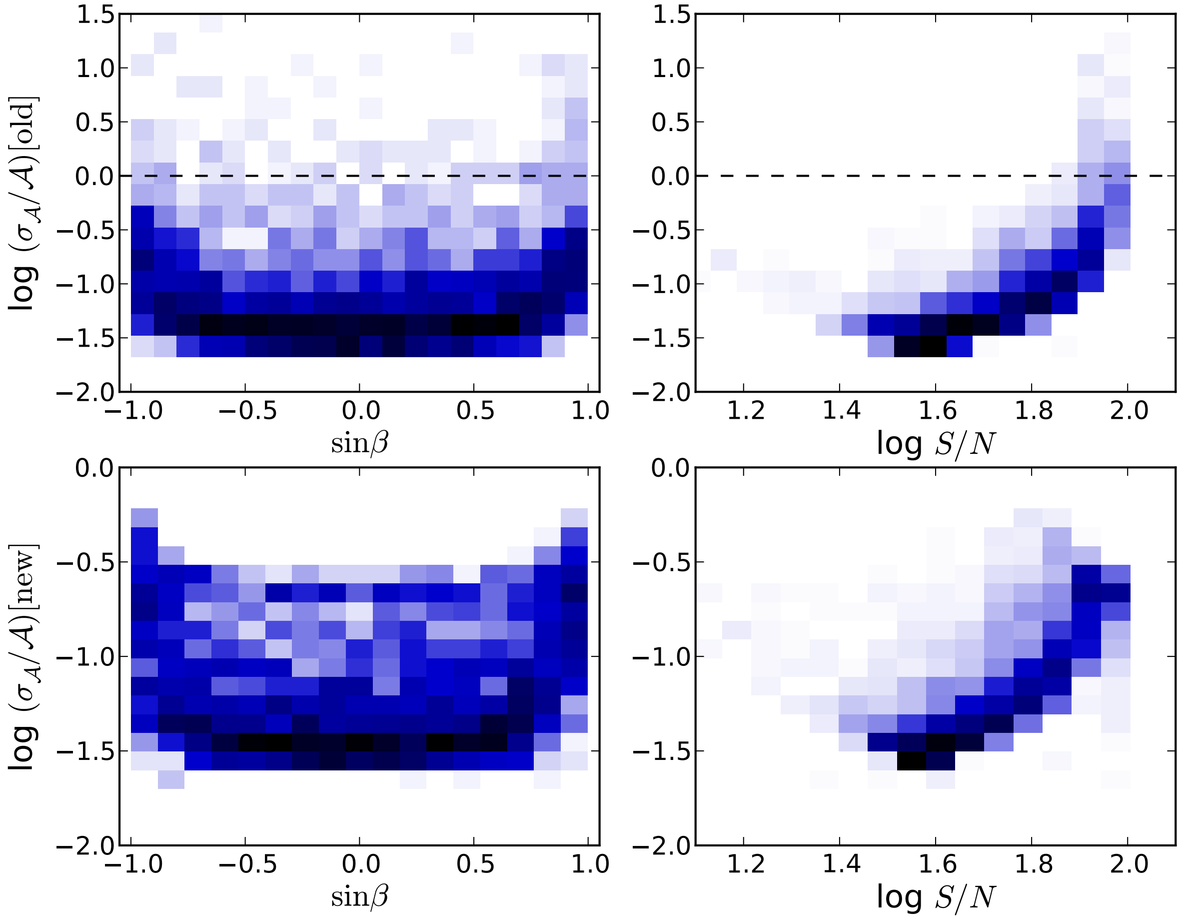

Figure 3.12: Corrections applied to the uncertainties in amplitude and inclination from Figure 3.2. The row titled 'new' was produced using the curves from the right panel of the Figure 3.11 on MC1 simulations.

about 6% and at a lower S/N of 7, they increase to about 25%. For MC1, the lowest S/N we considered is above ~ 15, as indicated in Figure 3.1, and consequently the results following MC1 are reasonable. However, real observations for eLISA will of course also contain lower S/Ns.

3.5 Conclusion

We presented a follow-up study of correlations between parameters that characterise Galactic binaries that will be observed by eLISA in the frequency range 10^{-4} Hz $< f <$ 1 Hz. In Paper I we investigated the correlations between parameters by considering three of the verification binaries (which are already known optically and are thus guaranteed sources for eLISA), and we explained these correlations and parameter uncertainties as a function of the inclination of the system. In this paper, we addressed the effect of all position and orientation parameters on the uncertainties and the possible strong correlations between them. We found that the overall effect is dominated by sky position and explained that dependence. Our main conclusions are:

1. After inclination, the ecliptic latitude of the source has the strongest influence on its parameter uncertainties, mainly due to its dependence on the signal-to-noise ratio and the correlations that can become very strong at the poles. For a given source distance, the parameter uncertainties (except for σ_β) are larger for a source at the ecliptic pole than for a source at the ecliptic plane. This is because a signal received from a source at the plane is stronger than that from a source at the pole.

2. In general, the uncertainty in sky location σ_Ω is large, i.e. in the order of square degrees. By constraining λ and β from optical data, the uncertainties in ψ, ϕ, ι, and $\mathcal{A}$ in the GW analysis can be improved by a factor of ~ 2. This factor is dependent on the inclination and the ecliptic latitude of the system.

3. By constraining ι in addition to the sky location, the improvement in $\sigma_\mathcal{A}$ is remarkably large (factors of 10 depending on the S/N of the source). Systems with $\iota = 30°$ can have improvement factors as high as 60.

4. The remaining angular parameters λ and ψ do not influence the correlations or uncertainties significantly.

5. The uncertainties in amplitude for low-inclination systems for which the corresponding uncertainties in the inclinations are unphysical (i.e. beyond their physical bounds) are also exaggerated. Fisher matrix predictions for these uncertainties have to be corrected for such systems.

Acknowledgements
This work was supported by funding from FOM. We are very grateful to Michele Vallisneri for providing support with the *Synthetic LISA* and *Lisasolve* softwares.

3.A Correlations as a function of β

We found that several correlations between source parameters become amplified at certain ecliptic latitudes and thus are a strong function of β, as shown in Figure 3.6, 3.7. Several of these correlations do not have preference on the inclination of the system, and therefore we show a 2d histogram to show the dependency on the ecliptic latitude. In the figure we show (only) the correlations that become strong, i.e. where the normalised correlation $|c_{ij}| > 0.5$. Some of these correlations have been explained in Paper I and are only dependent on the inclination of the system; we show them here to confirm that claim. The remaining correlations and their dependency on the latitude can be understood by considering the orientation of the binary relative to the detector. We comment on or explain each of them below,

1. $c_{\mathcal{A}\iota}$: Explained in Section 3.1.

2. $c_{\phi\psi}$ and $c_{\phi f}$: Similarly to $c_{\mathcal{A}\iota}$, these are strongly influenced by the source's inclination. The correlation $c_{\phi\psi}$ in the bottom-left panel has a distribution that looks very similar to the case of $c_{\mathcal{A}\iota}$ and here too, phase and polarisation are strongly correlated for face-on and mildy face-on systems, since these two angles describe similar properties. For edge-on systems, the two angles are defined on two planes that are perpendicular to each other, making them distinct. The correlation $c_{\phi f}$ in the top-right panel is strong for edge-on systems because a small shift in phase is very similar to a small change in frequency. However, for face-on systems, the phase and frequency become degenerate owing to the uncertainty in ϕ, which is inflated due to the strong correlation with ψ. There is a slight dependency of this correlation on $\sin\beta$ for the edge-on orientations since the correlation has a larger spread at the ecliptic poles. This is due to the spread of the $c_{\phi\psi}$ for $\iota > 80°$ systems where the spread in the phase at the poles also inflates the frequency. However, $\iota < 60°$, $c_{\phi\psi}$ for has no such spread, and thus the distribution of $c_{\phi\psi}$ vs. $\sin\beta$ for these systems lies in a narrow band throughout.

3. $c_{\psi\lambda}$: This can be understood by considering a binary with $\iota = 90°$ close to one of the poles; rotating the binary about its line-of-sight is equivalent to changing its ψ and λ because they are defined on the same plane (perpendicular to the line-of-sight). This also holds for a face-on binary, and thus if a source is close to the poles, ψ and λ can be highly correlated. The spread of this correlation is most likely due to the fact that λ is not well defined at the poles and thus the inflated uncertainty in the longitude implies a spread of correlations at the poles.

4. $c_{\phi\lambda}$: This correlation is explained by the combination of $c_{\psi\lambda}$ and $c_{\phi\psi}$, which are explained above. Since ψ and λ can be highly correlated at the poles and ϕ and ψ are strongly correlated for face-on systems, we found that ϕ and λ should also be highly correlated at the poles, at least for the systems with (mildly) face-on orientations. For the edge-on systems, this strong correlation can also exist because even though $c_{\phi\psi}$ is not as strong in this case, the values of this correlation (as pointed out above) spread at the poles for $\iota = 90°$. This spread is responsible for the spread of $c_{\psi\lambda}$ around the poles for edge-on systems.

5. $c_{\iota\lambda}$ and $c_{\mathcal{A}\lambda}$: A strong correlation between inclination and the longitude is intuitively not as clear. However, this correlation combined with $c_{\mathcal{A}\iota}$ for face-on systems would explain the correlation between amplitude and longitude, $c_{\mathcal{A}\lambda}$.

6. $c_{\phi\iota}$: Like above, the correlation between phase and inclination follows from the combination of $c_{\phi\lambda}$ and $c_{\iota\lambda}$, both of which are stronger close to the poles.

Chapter 4

Constraining parameters of white-dwarf binaries using gravitational-wave and electromagnetic observations

S. Shah, & G. Nelemans

ApJ, 790, 161, July 2014

Abstract

The space-based gravitational wave (GW) detector, *evolved Laser Interferometer Space Antenna (eLISA)* is expected to observe millions of compact Galactic binaries that populate our Milky Way. GW measurements obtained from the *eLISA* detector are in many cases complimentary to possible electromagnetic (EM) data. In our previous papers, we have shown that the EM data can significantly enhance our knowledge of the astrophysically relevant GW parameters of Galactic binaries, such as the amplitude and inclination. This is possible due to the presence of some strong correlations between GW parameters that are measurable by both EM and GW observations, for example, the inclination and sky position. In this paper, we quantify the constraints in the physical parameters of the white-dwarf binaries, i.e., the individual masses, chirp mass, and the distance to the source that can be obtained by combining the full set of EM measurements such as the inclination, radial velocities, distances, and/or individual masses with the GW measurements. We find the following 2σ fractional uncertainties in the parameters of interest. The EM observations

of distance constrain the chirp mass to $\sim 15\% - 25\%$, whereas EM data of a single-lined spectroscopic binary constrain the secondary mass and the distance with factors of two to $\sim 40\%$. The single-line spectroscopic data complemented with distance constrain the secondary mass to $\sim 25\% - 30\%$. Finally EM data on double-lined spectroscopic binary constrains the distance to $\sim 30\%$. All of these constraints depend on the inclination and the signal strength of the binary systems. We also find that the EM information on distance and/or the radial velocity are the most useful in improving the estimate of the secondary mass, inclination, and/or distance.

4.1 Introduction

Gravitational wave (GW) observations and electromagnetic (EM) observations can be used to study compact Galactic binaries independently and often these two ways provide different measurements of the same system. There are about ~50 of these binaries that have been studied in the optical (UV), and X-ray wavelengths [e.g., Roelofs et al., 2010]. This number is expected to grow by a factor of ~100 [Nissanke et al., 2012] when a space-based GW observatory like the recently *evolved Laser Interferometer Space Antenna (eLISA)*[1] will be in operation. This detector is expected to observe millions of compact Galactic binaries with periods shorter than about a few hours [Nelemans, 2009; Amaro-Seoane et al., 2013], among other astrophysical sources. Of those millions of binaries, we will be able to resolve several thousands. It has been shown [Shah et al., 2012, ,-,hereafter Paper I] that for a non-eclipsing binary system (for example AM CVn), its EM measurement of the inclination, ι, can improve the error on the GW amplitude ($\mathcal{A}$) significantly depending on the strength of the GW signal and the magnitude of the EM uncertainty in the inclination. $\mathcal{A}$ is a GW parameter that is given by a combination of the masses, orbital period, and distance to the source:

$$\mathcal{A} = \frac{4(G\mathcal{M}_c)^{5/3}}{c^4 d}(\pi f)^{2/3}, \tag{4.1}$$

where, d is the distance to the source, f is the source's GW frequency ($2/P_{\rm orb}$), and $\mathcal{M}_c$ is the chirp mass defined as:

$$\mathcal{M}_c \equiv (m_1\, m_2)^{3/5}/(m_1 + m_2)^{1/5}. \tag{4.2}$$

From the GW observations alone, one typically cannot measure the individual masses or the distance since they are degenerate via Equations 5.10, 4.2. In the rare cases that a precise orbital decay ($\dot{f}$), can be measured from GW data then the distance can be estimated (with the assumption that the frequency evolution is dictated by GW radiation only) by

---

[1] In preparation by ESA, expected launch in ~2034

determining $\mathcal{M}_c$ from the measured f and $\dot{f}$ via the equation [Peters & Mathews, 1963]:

$$\dot{f} = \frac{96\,\pi}{5} \frac{G^{5/3}}{c^5} \, (\pi\, \mathcal{M}_c)^{5/3}\, f^{11/3}. \tag{4.3}$$

For the compact binaries that have been observed with the optical telescopes, a subset of which will also be detected by *eLISA*, their EM data often provide measurements of the orbital period P_{orb}, the primary mass (m_1), sometimes the secondary mass (m_2), the distance (d) and the radial velocity amplitude (K_i). We use these measurements for a few binaries to show the quantitative improvements in their GW and other physical parameters. Many of these binaries can/could still be found electromagnetically before or after *eLISA* discoveries.

We have previously shown that finding sky positions from EM data can improve the GW uncertainties on $\mathcal{A}$ and ι depending on the particular geometry and orientation of the binary systems [Shah et al., 2013]. Thus we have so far, quantitatively studied the improvement factors in the uncertainties of the parameters that can be gained from *prior* knowledge of parameters that are common to both GW and EM observations, for example, inclination, and sky position.

In this paper, we go beyond constraining *only* those GW parameters that are *also* measured independently from the EM data. We explore various combinations of *any* possible EM observations and the GW measurements in constraining the *useful parameters* of the binaries that are astrophysically interesting, for example, the individual masses. Because their GW signal is significantly affected, we consider high-inclination (sometimes eclipsing) and (low inclination) binary systems. We review the GW data analysis methods in Section 2. In Section 3, we explore the information gained by combining EM measurements in different ways in which the EM data can be the radial velocity of one of the binary components, K_i, m_1, m_2, d, and P_{orb}. Specifically, we classify various combinations into a number of scenarios in discussing the parameter constraints.

4.2 Parameter uncertainties from GW observations

For our analyses below, we consider one of the *eLISA verification binaries* J065133.33+284423.3 (hereafter J0651, Brown et al. [2011]). We also consider a second (hypothetical) system with higher masses which we will refer to as "the high-mass binary". Their GW parameter values are listed in Table 1. Before looking at the EM data, we briefly recap our GW data analysis method. We have used Fisher matrix studies [e.g Cutler, 1998] to extract the GW parameter uncertainties and correlations in the GW parameters that describe the compact binary sources. Our method and application of Fisher information matrix (FIM) for *eLISA* binaries together with their signal modeling and the noise from the detector and the Galactic foreground have been described in detail in Paper I. Most of the binaries will be monochromatic sources and such sources are completely characterized by a

TABLE 4.1: GW Parameter Values of J0651

	$\mathcal{A}$ $[\times 10^{-22}]$	$\mathcal{M}_c$ $[M_\odot]$	ϕ_0[rad]	$\cos\iota$	f $[\times 10^{-3}]$[Hz]	ψ[rad]	$\sin\beta$	λ[rad]	S/N
J0651	1.67^a , 6.71^b	0.32^a , 0.70^b	π	0.007	2.61	$\pi/2$	0.101	1.77	$\sim 13^a$, 50^b

(a) For $m_1 = 0.25 M_\odot$, $m_2 = 0.55 M_\odot, d = 1.0$ kpc (b) For $m_1 = 0.8 M_\odot$, $m_2 = 0.8 M_\odot, d = 1.0$ kpc

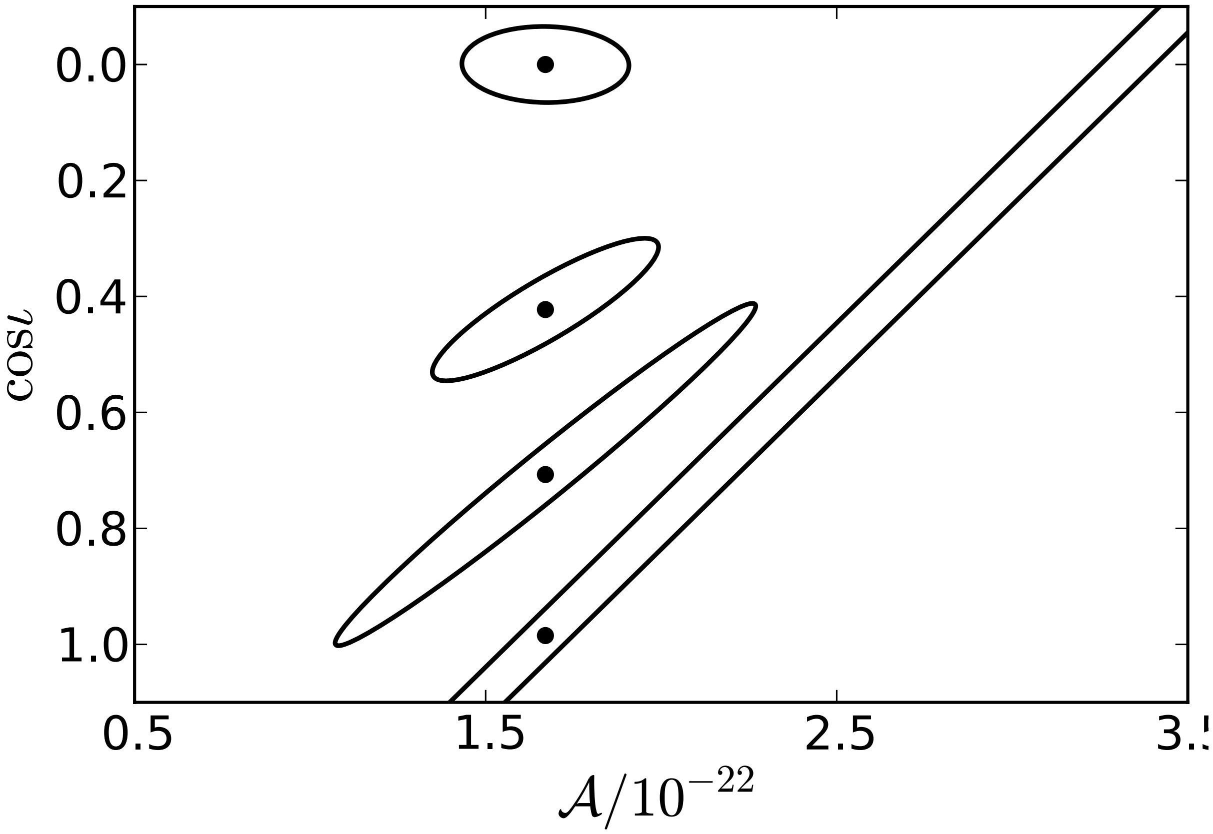

Figure 4.1: Two-dimensional error ellipses of $\mathcal{A}$ and $\cos\iota$ extracted from the variance-covariance matrix for the J0651 binary system with varying orientation in its ι. The distributions with larger to smaller ellipses correspond to $\iota = 10°, 45°, 65°$, and $90°$ respectively. The black dots are the GW parameter values (see Table 1)in which the FIM is evaluated for the corresponding orientations.

set of seven parameters: dimensionless amplitude ($\mathcal{A}$), frequency (f), polarization angle (ψ), initial GW phase (ϕ_0), inclination ($\cos\iota$), ecliptic latitude ($\sin\beta$), and ecliptic longitude (λ). From the GW signal of a binary and Gaussian noise we can use the FIM to estimate the parameter uncertainties. The inverse of the FIM is the variance-covariance matrix whose diagonal elements are the GW uncertainties and the off-diagonal elements are the correlations between the two parameters. We do the GW analyses of the above mentioned binaries for *eLISA* observations of two years. We note that the Fisher-based method is a quick way of computing parameter uncertainties and the correlations in which these uncertainties are estimated locally at the true parameter values and therefore by definition the method cannot be used to sample the entire posterior distribution of the parameters. Additionally Fisher-based results hold in the limit of strong signals with a Gaussian noise [e.g., Vallisneri, 2008, see also Appendix]. The two-dimensional (2D0 GW distribution in amplitude and inclination given by the variance-covariance matrix for

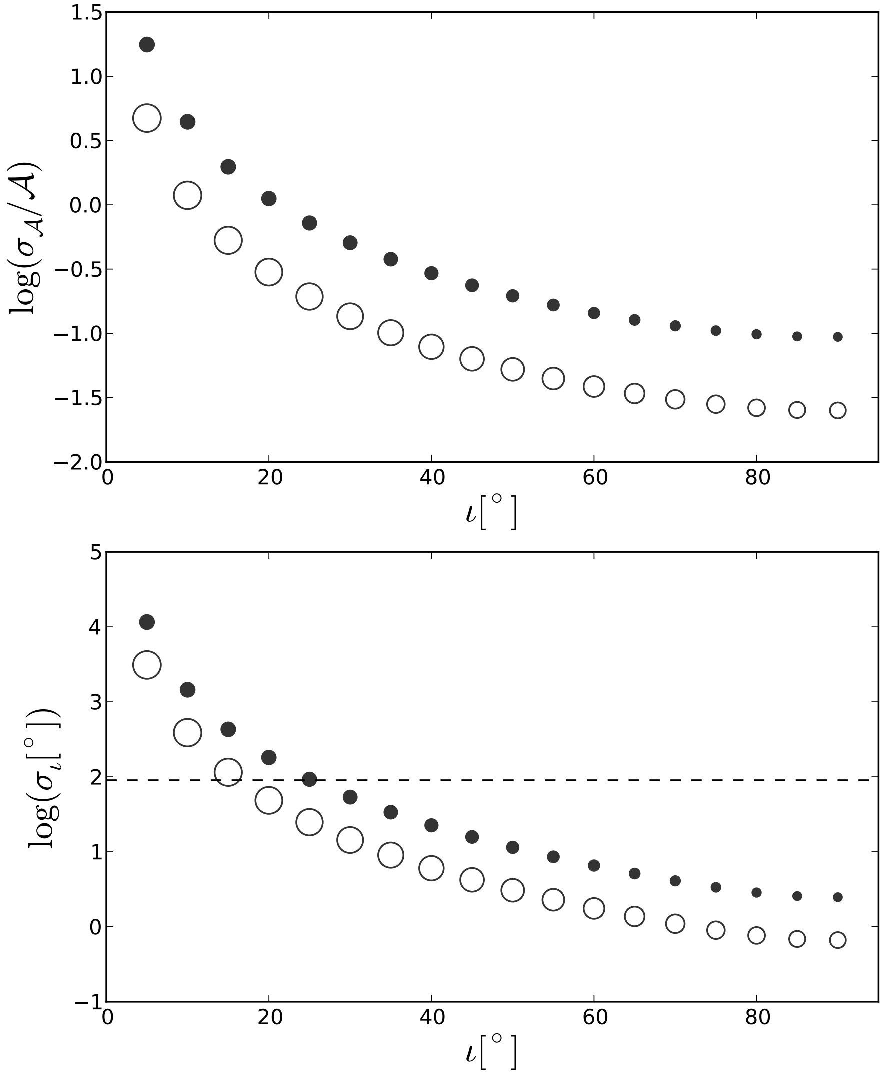

Figure 4.2: GW uncertainties in amplitude and inclination for J0651 as a function of inclination calculated from the Fisher matrices. Filled circles are for J0651 with $m_1, m_2 = 0.25, 0.55M_\odot$ and open circles are for the case of the high-mass binary with $m_1, m_2 = 0.8, 0.8M_\odot$. The size of the marker represents the S/N at each inclination. The dashed line on the rightpanel marks the unphysical values for the inclination (see the text).

J0651 parameters are shown in Figure 4.1 for a number of inclinations. The largest and most highly correlated distribution is that with $\iota = 10°$ and the weakest correlation is that with $\iota = 90°$. The behavior of these distributions reflect the strength of the correlation between amplitude and inclination. As discussed in Paper I, the low-inclination systems $\iota \leq 45°$ have very similar signal shapes, whereas systems with high inclinations are distinguishable by both the shape and structure for small differences in inclinations. Thus, for low-inclination binaries a small change in ι is indistinguishable from a small change in its $\mathcal{A}$. On the other hand for high-inclination binaries, a small change in inclination produces a noticeably different signal explaining the uncertainties in $\mathcal{A}$ and ι becoming large to small with increasing inclination. The GW uncertainties for the amplitude and inclination as a function of inclination are shown in Figure 4.2 for J0651 (in filled circles) and the high-mass binary (open circles). The strong increase in uncertainty trends for low-inclination systems is due to the correlation between amplitude and inclination [Shah et al., 2012]. Clearly, the high-mass binary has larger signal-to-noise ratio (S/N), which gives smaller uncertainties in both of its parameters shown with open circles in the figure compared to that of J0651. Observe that inclination is a cyclic parameter and is bounded between $0° \leq \iota \leq 90°$ and yet we get very large uncertainties from Fisher matrix for lower inclinations systems shown in the right panel of in Figure 4.1. This is due to the fact that Fisher matrix methods are based on the linearized signal approximation as a result of which it is not sensitive to the bounded parameters that describe the signal model [Vallisneri, 2008]. In other words, in FIM, one computes the uncertainties in parameters based on variations of the signal with respect to the parameters at the true parameter values, and the fact that far away from the true value, the parameter has a bound is not taken into account by the FIM. When the uncertainty in a bounded parameter exceeds its physically allowed range, it means the quantity cannot be determined from GW data analysis. The dashed line in in Figure 4.2 indicates the value (at 90°) beyond which the uncertainties in ι imply unphysical values for the inclination. Since the low-inclination systems on the left side of the plot are affected by this, corrections have to be applied to the corresponding (overestimated) uncertainties in amplitude in the left panel by discarding the unphysical range in the inclination [Shah et al., 2013]. One way to correct these unphysical values is by taking a rectangular prior on the inclination. In effect, this will cut off the posterior distribution in the parameters at the physical bounds described by the prior. Note that cutting off the error ellipses at lower inclinations in Figure 4.1 is reasonable because taking strict bounds far away from the real value, about which the computed Fisher uncertainties will not change the shape and slope significantly. The cut off in the posterior distributions due to rectangular priors will skew the means of the parameter distributions away from the real value [Rodriguez et al., 2013, Equation (C4)]. Furthermore, we stress the fact that the Fisher matrix method is an *estimate* and cannot, follow the posterior in detail (see the Appendix). The normalized correlations between all seven parameters for an eclipsing and non-eclipsing orientations of J0651 are listed in the variance-covariance matrices (VCM) in the Appendix. We will make use of these parameter uncertainties and their corresponding correlations when combining with various EM data in Section 3.

4.2.1 GW Information Only

We start by considering the case where we only have the GW data. From the GW observations, the astrophysical parameters of interest for a monochromatic source are its f, $\mathcal{A}$, and ι. From the GW data analysis, the frequency of the source will be very well determined, $\sigma_f/f \sim 10^{-6}$ Hz (e.g., Paper I) for a 10^{-3} Hz source, so we consider that f is essentially known with a fixed value. Given that most of the binaries that we will observe with *eLISA* will be binary white-dwarfs (WD) [Nelemans et al., 2001a], we can restrict their masses to $m_i \epsilon [0.1, 1.4]\ M_\odot$. For simplicity we take *uniform* distributions for both masses in this range. This provides a distribution in the system's chirp mass, which will provide an upper limit on the distance for the source. In Figure 4.3, we show these estimates in d with their 95 percentile (or 2σ uncertainties) as a function of inclination for both J0651 (black) and for the high-mass binary with equal high-mass components (in yellow). The dashed line (in red) is the real value of the distance for both systems. The lower medians of distances at the lower inclinations for both systems are explained by the fact that at $\iota = 5°$, the GW distribution of $\mathcal{A}$ has a long uniform tail. This is shown in Figure 4.4 where we compare the distributions of $\mathcal{A}$ for two inclinations: 5° (in black), and 90° (in blue) in the top panel. For a fixed distribution of $\mathcal{M}_c$, the corresponding distributions in d are shown in the bottom panel where the solid vertical lines are the distribution medians and dashed vertical line is the real value. We can see that $\mathcal{A}^{5°}_{\rm median} > \mathcal{A}^{90°}_{\rm median}$, thus giving $d^{5°}_{\rm median} < d^{90°}_{\rm median}$ via Equation 5.10 for a fixed $\mathcal{M}_c$. Also, observe that the median distances are overestimated for J0651 for all inclinations and this is because the real value of the median in $\mathcal{M}_c$ is much smaller than that computed from uniform distributions in m_i, which is the same for all inclinations. For the high mass binary the computed median in $\mathcal{M}_c$ is close to its real value, thus translating into smaller offsets in the median distances in Figure 4.3. In the figure, the 95 percentiles in the distance slightly increase as a function of inclination even though the uncertainties in $\mathcal{A}$ have the opposite behavior (see Figure 4.2). This is because the $\mathcal{M}_c$ has a very large fractional uncertainty compared to that of the $\mathcal{A}$ and thus the relative error uncertainties in the chirp mass dominate those in the distance, which remain roughly constant for all inclinations.

4.3 Combining EM & GW observations

In all the various scenarios we analyze below, we take the EM parameters with an uncertainty of 10%, which is inspired by observational uncertainties of J0651. This binary is a well-known EM source and also a guaranteed source for *eLISA*. J0651 is an eclipsing system and such an orientation of a nearby binary allows accurate EM measurements of its or-

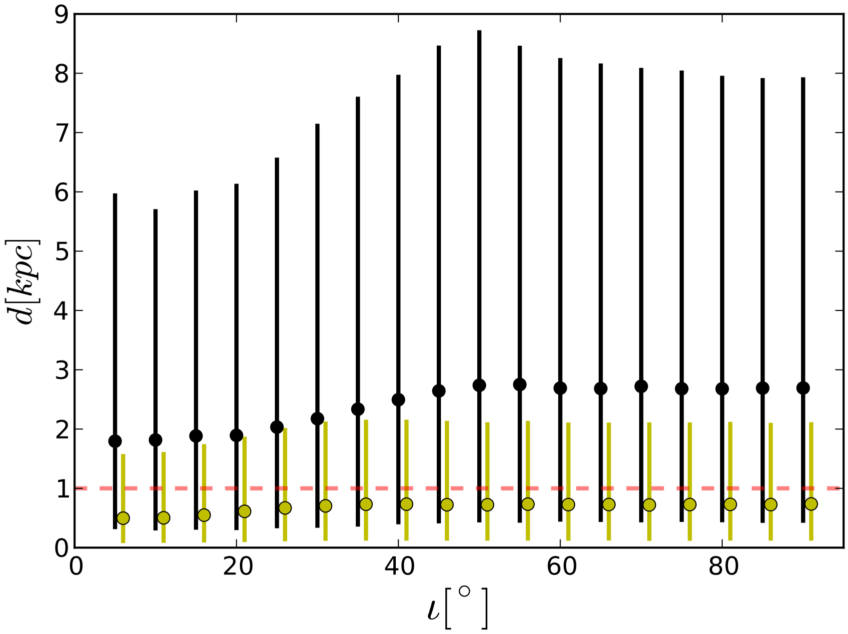

FIGURE 4.3: *GW data only*: 95 percentile in distance assuming finite chirp mass for J0651 in black lines and the high-mass binary in yellow lines. The dashed line (in red) is the true value. For clarity the constraints for the high-mass binary are shifted to the right. We do this for all the cases below.

bital parameters, and the masses (accuracies of $\sim$ 15% primary mass; 8%, secondary mass) from observing the spectra, radial velocities, and eclipses of each star by the other [Brown et al., 2011]. Furthermore its rate of change of orbital period has also been measured from follow-up high speed photometry from $\sim$ one year. worth of data to an accuracy of $\sim$ 30% [Hermes et al., 2012]. This will improve in the course of time. In this section, we classify specific (possible) scenarios where we could have one or more EM data on the WD binary parameters. We explicitly state how much the knowledge of any of the various parameters that describe the *physical* properties of a binary system can be further improved if we can fold in various combinations of the existing EM and/or GW observations. We construct three specific scenarios below based on the typical knowledge from the EM observations:

- EM data on distance,
- single-line spectroscopic data (complemented with or without the distance measurement), and
- double-line spectroscopic data

In all the scenarios the GW information on amplitude, inclination and frequency from Secttion 2.1 are used.

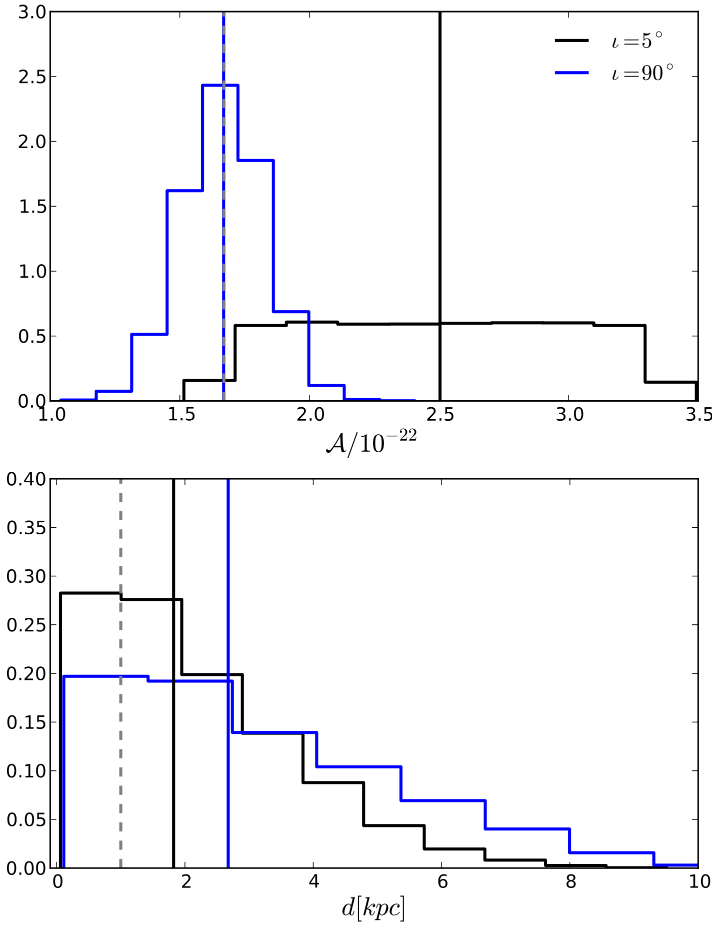

Figure 4.4: *GW data only*: Top: Example of 1D distributions in $\mathcal{A}$ from GW data for two inclinations as labeled and their corresponding distributions. Bottom: Assuming a finite $\mathcal{M}_c$, this gives corresponding distributions in distance. The solid lines (in blue and black) are the medians of the distributions. The real values of the parameters are shown in vertical dashed lines (in grey). Note that in the top panel the real value is the same as the median of the grey distribution and thus they overlap.

4.3.1 Scenario 1: EM Observation of the Distance

Measuring distances accurately is made feasible by the *Gaia* mission [de Bruijne, 2012], a new astrometric satellite. *Gaia* is expected to measure stellar parallaxes of millions of stars with μas accuracy depending on how bright a star is. For example, at 1 kpc, J0651 ($g = 19.1$ mag) would have a $\sim 300\mu$as accuracy in the parallax measurement corresponding to a fractional accuracy in distance of $\sim 10\%$ [e.g., Bailer-Jones, 2009]. There is also some indication of the distance of the binary from its absolute magnitude. The uncertainties in d from such measurements are also of the order of several percent, or 10% for the case of J0651 [Brown et al., 2011].

A sole EM measurement of the distance of a WD binary might be possible in cases where the system is identified as a WD binary but it is too faint to measure other parameters. For instance, from the wide-field surveys, it is often possible to identify WD from their colors [Verbeek et al., 2013]. Given the distance and the GW uncertainty in amplitude, we can trivially solve for the chirp mass $\mathcal{M}_c$ using Equation 5.10. The resulting probability distribution functions (pdfs) are computed by randomly drawing points from the given distributions and computing the parameter of interest for each draw. The 95 percentiles in the $\mathcal{M}_c$ are shown in the top panel of Figure 4.5 for J0651 (in black) and the high-mass binary (in yellow) as a function of inclination. The dashed lines (in black for J0651 and in yellow for the high mass binary) are the real values. The decreasing medians of the chirp mass with inclination follows from the GW distributions in the amplitude that is shown in Figure 4.4 where the median $\mathcal{A}$ is overestimated for $\iota = 5°$ (in black line) compared to that of $\iota = 90°$ (in blue line). For a fixed distribution in distance the corresponding distribution of $\mathcal{M}_c$ is therefore overestimated for $\iota = 5°$ shown in the bottom panel of Figure 4.5 compared to that of $\iota = 90°$. The 95 percentiles of the chirp masses for both J0651 and the high mass binary are affected by these overestimated medians of the amplitudes at lower inclinations which cause significant offsets of the $\mathcal{M}_c$ from their respective real values as can be seen in the top panel of Figure 4.5. Thus at lower inclinations where the medians in the amplitude are overestimates, the 95 percentiles in the chirp mass can be interpreted as upper limits of the chirp mass. In order to calculate reliable constraints in $\mathcal{M}_c$ at these small inclinations we have to do full (Bayesian) data analyses that take into account the physical priors and give us a better estimate of the expected posterior distributions in the desired parameters. The 95 percentiles in $\mathcal{M}_c$ for both systems decrease as a function of inclination as is expected from the propagation of uncertainty where $\sigma_{\mathcal{M}_c} \propto \sigma_{\mathcal{A}}$. Thus, knowing the distance from the EM observation gives us an estimate of the chirp mass where the constraints are tighter for the higher inclination (eclipsing) systems.

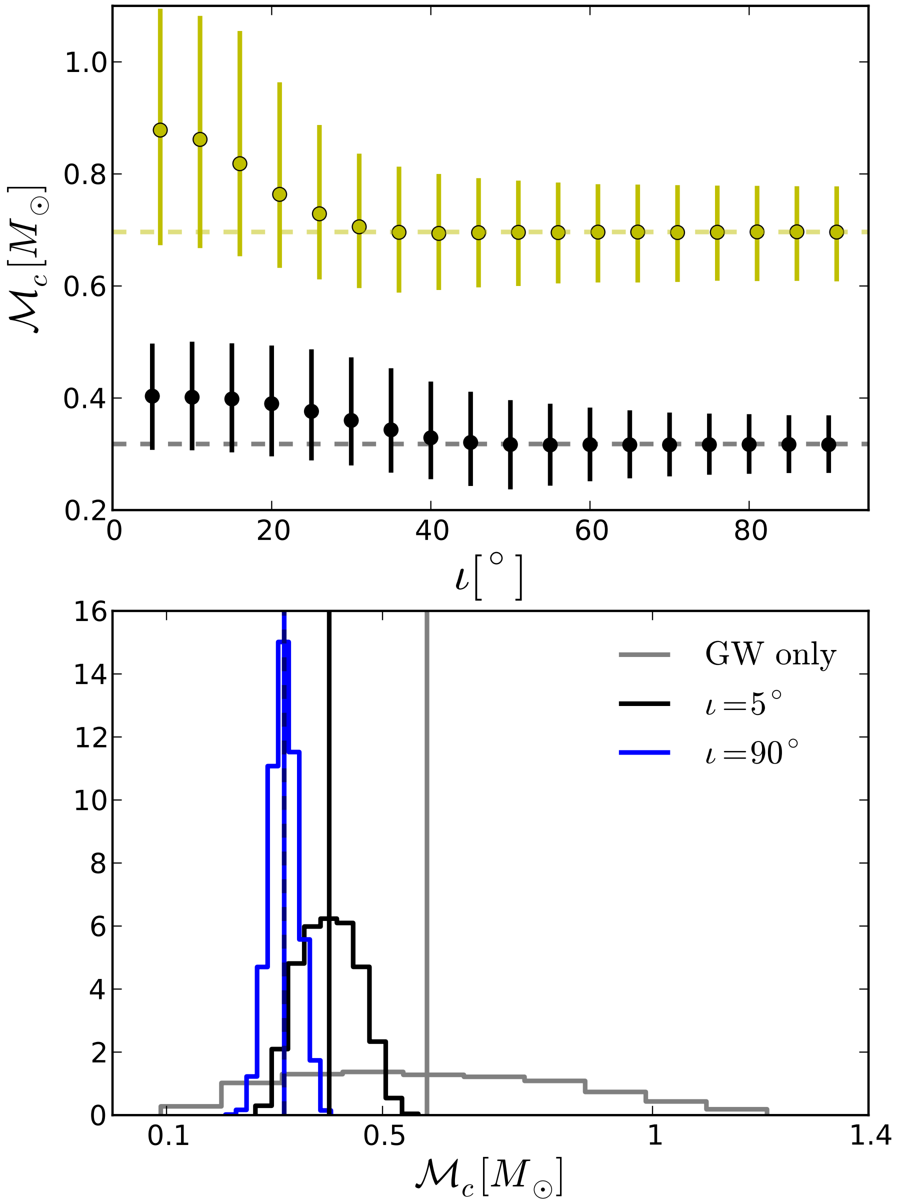

FIGURE 4.5: *Scenario 1 (known distance)*: Top: 95 percentile in chirp mass given GW data on $\mathcal{A}$ and EM data on distance for J0651 (in black) and high mass binary (in yellow). Bottom: Example of 1D distributions in the $\mathcal{M}_c$ for two inclinations as labeled for the J0651. The solid lines are the medians of the distributions whereas the dashed line (over-plotted on thick black solid line) is the real value of the $\mathcal{M}_c$. For comparison, the $\mathcal{M}_c$ computed from uniform distribution of masses is shown in grey.

4.3.2 Scenario 2: EM observations of single-lined spectroscopic binary

Some measurements are unique to EM observations such as the radial velocity K_1, of one of the components (m_1) of the binary:

$$K_1 = \sin\iota \, \frac{m_2}{(m_1+m_2)^{2/3}} \, \left(\frac{2\pi\, G}{P_{\rm orb}}\right)^{1/3}, \tag{4.4}$$

which can be used to measure inclination. We adopt the convention from the optical studies of the binary sources where the primary mass, m_1 is the brighter object and the dimmer secondary mass, m_2. Note that the inclination measurement from the GW data analysis, ι[GW] and from the radial velocity equation above i.e. ι[RV] are two independent measurements for the same system. We will show that these two are anti-correlated below in Sect. 3.2.3, yielding radial velocity measurements very useful.

4.3.2.1 Scenario 2a: EM data on m_1

Before looking at a real single-lined spectral binary we first consider the case that only the mass m_1 is known from the EM data. This is a viable scenario when determining K_1 is impossible and we may get an estimate of the primary mass from the photometry or the spectra. Assuming a double WD system, we take a uniform distribution for m_2, which together with the given m_1 constrains the d. The estimates of distance with their corresponding 95 percentiles as a function of inclination are shown in Figure 4.6 for both the J0651 (in black) and the high mass binary (in yellow). The real value of distance is shown in the dashed (black) line. The offsets of the medians in the distance at low inclinations for both the binary systems can be explained in a similar way as in the previous sections, which is due to the overestimated medians of $\mathcal{A}$ at lower inclinations as shown in the top panel of Figure 4.4. Additionally, the significant discrepancy between the median distance for J0651 vs. the high mass binary (at $\iota \geq 40°$) is again due to the over-estimated value of the $\mathcal{M}_c$ for J0651 assuming a uniform distribution m_2 distribution. This is shown in the bottom panel of Figure 4.6 where the vertical dashed lines are their corresponding true values of the $\mathcal{M}_c$ and the vertical solid lines are the medians of the corresponding distributions. The simulated distribution of $\mathcal{M}_c$ from an EM measurement of m_1 with a Gaussian width in its uncertainty together with an assumed uniform distribution in the unknown m_2 results in an overestimated median of the $\mathcal{M}_c$ for J0651 compared to that of the high mass binary. This propagates in overestimating the median d for J0651 at higher inclinations unlike for the high mass binary since its median $\mathcal{M}_c$ is slightly underestimated. The flat priors on m_2 is affecting this and if we already know the secondary mass is low, we may take a distribution in m_2 weighted towards lower masses and that will affect the constraints obtained in the d. The constraints in the distance from Figure 4.6 can be compared with those in Figure 4.3 where there was no EM information on any of the masses: the upper limits on d for both

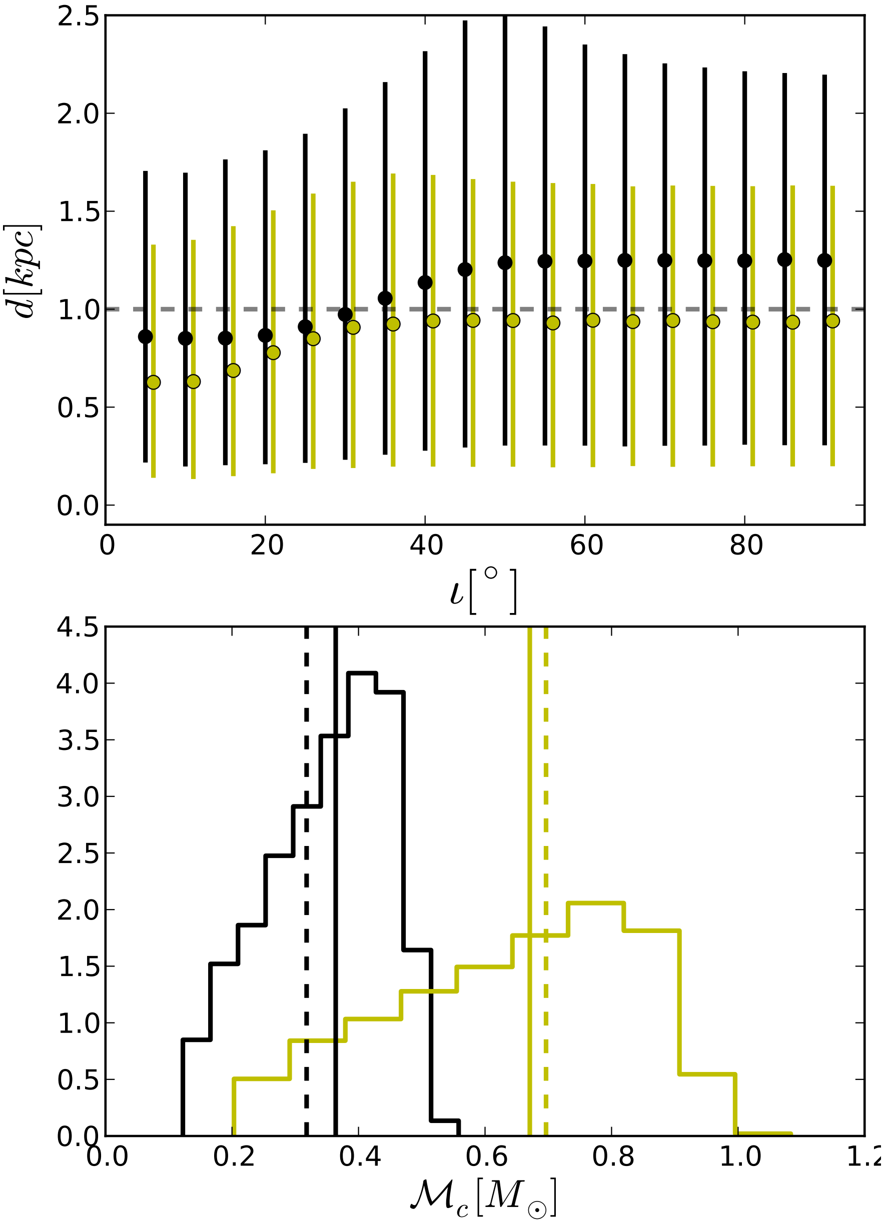

Figure 4.6: *Scenario 2a*: Top: 95 percentile in the distance given GW data on $\mathcal{A}$ and EM data on m_1 for J0651 (in black) and the high-mass binary (in yellow). Note that $\mathcal{M}_c$ distribution is same at all inclinations for each binary. Bottom: Comparison of $\mathcal{M}_c$ for J0651 (in black) and for the high-mass system (in yellow) where solid lines are the medians of the distributions and dashed lines are the real values.

J0651 and the high mass binary are constrained by a up to factor of ~ 4 better when m_1 is known for both binaries with 10% accuracy.

4.3.2.2 Scenario 2b: EM data on m_1 & K_1

In this case we consider EM measurements of a *single-lined spectroscopic* binary where resolving one of the masses of the binary spectroscopically typically provides measurements on the primary mass and its radial velocity. We assume an uncertainty in radial velocity amplitude of 10% corresponding to the typical accuracy of 10km/s found in the EM measurements [for e.g., Roelofs et al., 2006]. Given m_1 and K_1 from the EM data and inclination from GW data ι[GW], we can numerically solve for m_2 via the K_1 formulation in Eq. 4.4. Assuming it is a WD, the m_2 is restricted to lie in $[0.1 - 1.4]M_\odot$. Then a fixed pair of [$\mathcal{A}$, ι[GW]] and the masses give us a distance. We calculate the resulting distributions in m_2 and the distance from the Gaussian distributions of m_1 and K_1 about their typical EM uncertainties and GW distributions in the inclination and amplitude. The 95 percentile in the secondary mass and the distance are shown in Figure 4.7 as a function of inclination for both J0651 (in black) and the high mass binary (in yellow). Like in the scenarios discussed above, for the lowest inclinations, the over estimated FIM uncertainties of $\mathcal{A}$ propagates into erroneous constraints on m_2, and d. Thus, at lower inclinations we have to use Bayesian methods to get their accurate GW uncertainties. Observe that the 95 percentile in the m_2 and the distance roughly similar and large from $5° < \iota < 45°$. This is again due to the influence of the GW distributions in $\mathcal{A}$ at the lower inclinations, which have uniform distributions resulting into over-estimated medians (see Figure 4.1). However, for $\iota > 45°$ the uncertainties for both m_2, and d decrease with inclination and their medians stabilize at the true values. This is caused by the fact that at higher inclinations, the medians of GW amplitudes are close to the true values of the systems where the constraints on the GW parameters are also tighter with increasing inclination. Thus, the decreasing uncertainties in ι[GW] as a function of ι (see bottom panel of Figure 4.2) should result in the same behavior of σ_{m_2} via Eq. 4.4. Since distance is computed using these m_2, the same behavior holds for the distance in the right panel.

4.3.2.3 Scenario 2c: EM data on m_1, K_1 & d

Here the EM measurements of a *single-lined spectroscopic* binary in the previous subsection is complemented with a distance measurement from *Gaia* or from an estimate of the absolute magnitude. From the primary mass m_1, distance and the amplitude we immediately get the secondary mass, m_2. We will call this as the preliminary m_2 since this can be further improved by folding in the radial velocity measurement. As mentioned before the radial velocity measurement essentially provides an independent measurement of the inclination via Eq. 4.4. This can be seen in the following way: The GW parameters of the non-eclipsing J0651 are: $\mathcal{A}_0$, $\iota_0 = 1.67 \times 10^{-22}, 45°$ whose VCM uncertainties are: $\sigma_\mathcal{A}/\mathcal{A} = 0.231$, and

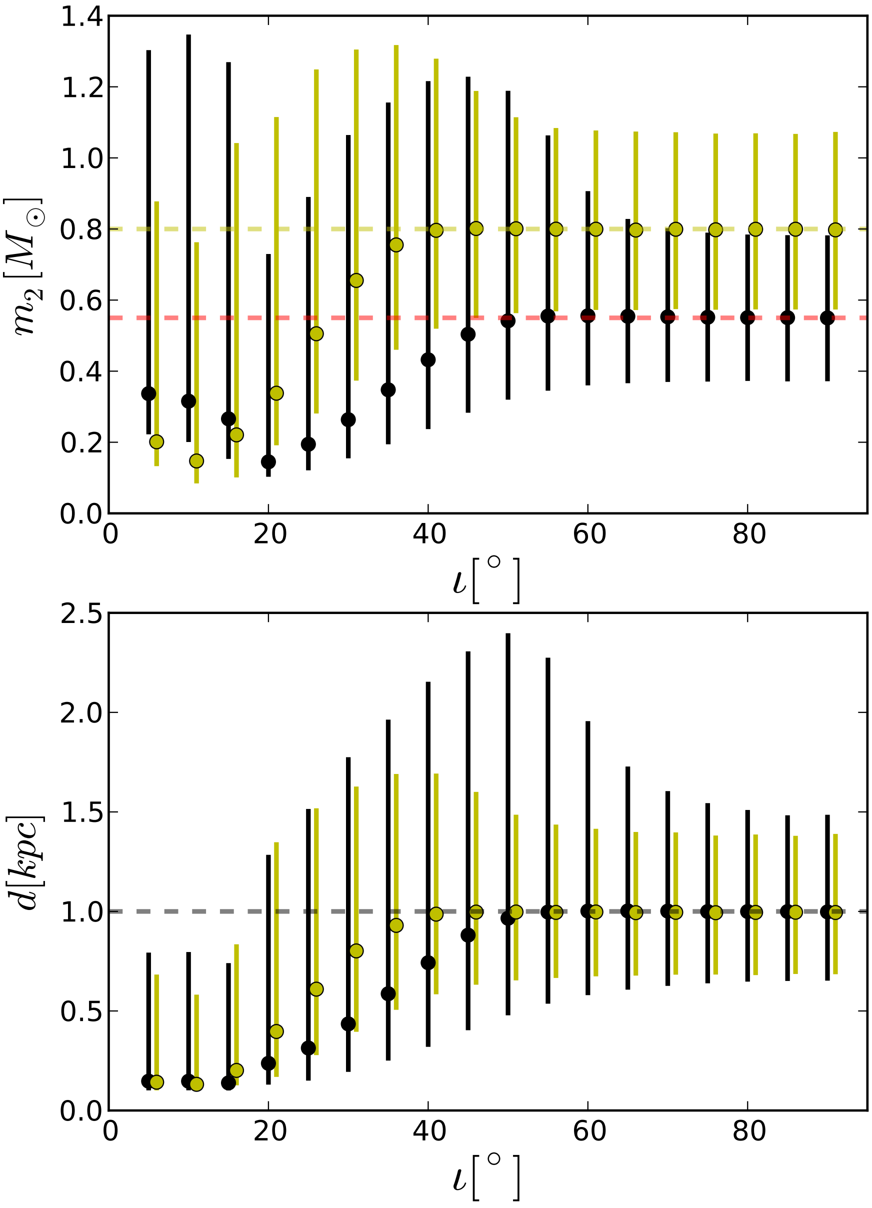

Figure 4.7: *Scenario 2b*: Constraints on the secondary mass and distance from combining *single spectroscopic* EM data: m_1, and K_1 with GW data on $\mathcal{A}$, ι for J0651 (black) and the high mass binary (in yellow).

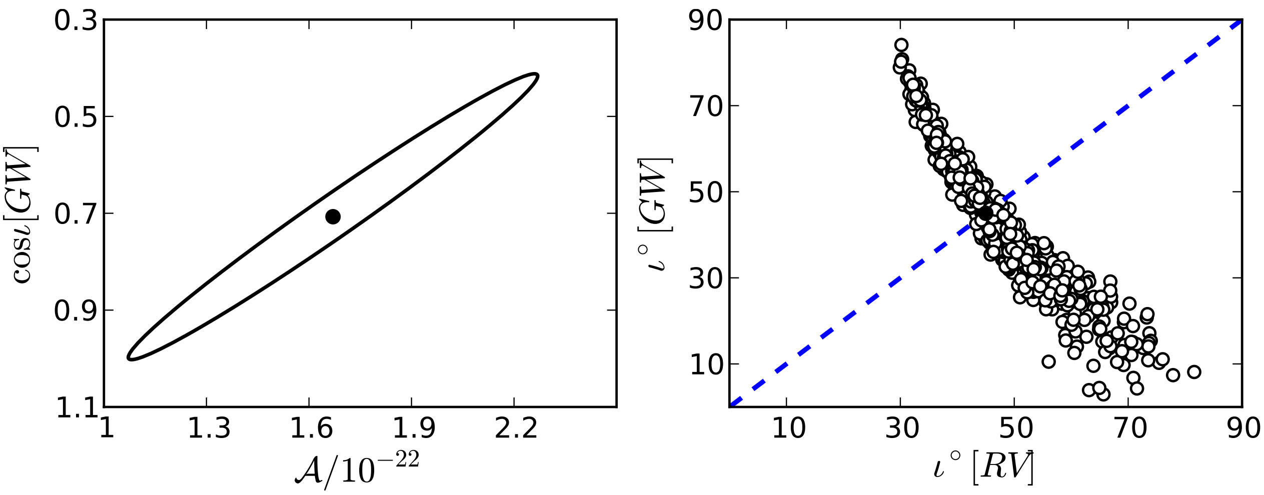

Figure 4.8: Relation between inclination from GW observation vs. that from EM observations. *Left* 2-d error ellipse from the GW data analysis in amplitude and $\cos\iota$ for J0651 with $\iota = 45°$. *Right*: Relation between inclination from the left panel and inclination from Eq. 4.4.

$\sigma_\iota = 0.75$ rad respectively. We also take a fixed radial velocity, K_0 corresponding to m_1, m_2 (listed in Table 1), and ι_0. The 2-d Gaussian distribution from GW data with $1-\sigma$ uncertainties for these parameters is shown in the left panel of Figure 4.8. For each randomly selected pair of $[\mathcal{A}, \cos\iota[\mathrm{GW}]]$ and for a fixed m_1, and d, we can solve for the m_2 from Eq. 5.10. Using this m_2 for that fixed m_1 and K_0, we solve for $\iota[\mathrm{RV}]$. For many points randomly picked in the $[\mathcal{A}, \cos\iota[\mathrm{GW}]]$ space the computed $\iota[\mathrm{RV}]$ are compared with the corresponding $\iota[\mathrm{GW}]$ in the right panel. The inclinations measured in two ways roughly anti-correlate. However we know that values of $\iota[\mathrm{RV}]$ that are different from $\iota[\mathrm{GW}]$ cannot be true. Thus, constraining the inclination of the system in a small area around 45° along the diagonal line in the right panel also constrains m_2 and the amplitude. We make use of this in the case considered in this subsection. The preliminary m_2 and their 95 percentiles computed from EM data on m_1, d, and the GW data on $\mathcal{A}$ as a function of inclination is shown in Figure 4.9 in grey lines in the left panel for J0651. The same for the high mass binary is also shown in the right panel in grey lines. From this m_2, given m_1, and $\iota[\mathrm{GW}]$, the radial velocity, K_{GW} is computed which is compared with the K_1 from the EM data. Since the EM measured K_1 is more precise, we keep the subset of those K_{GW} and the respective $\iota[\mathrm{GW}]$ weighted with a probability distribution function of the K_1 given by:

$$\mathcal{P}_i = \frac{1}{\sqrt{2\pi}\,\sigma_{K_1}} \exp\left(\frac{-0.5\,(K_{1,i}[\mathrm{GW}] - K_1)^2}{\sigma_{K_1}}\right) dK_1. \tag{4.5}$$

The final reduced 95 percentiles in m_2 are shown in black lines for J0651 in top panel, and the same is shown in dark green lines for the high mass binary in the bottom panel. Observe that the uncertainties in m_2 calculated in this way for lower inclinations is the similar to those at the higher inclinations. Thus, the advantage of folding in K_1 measurement is

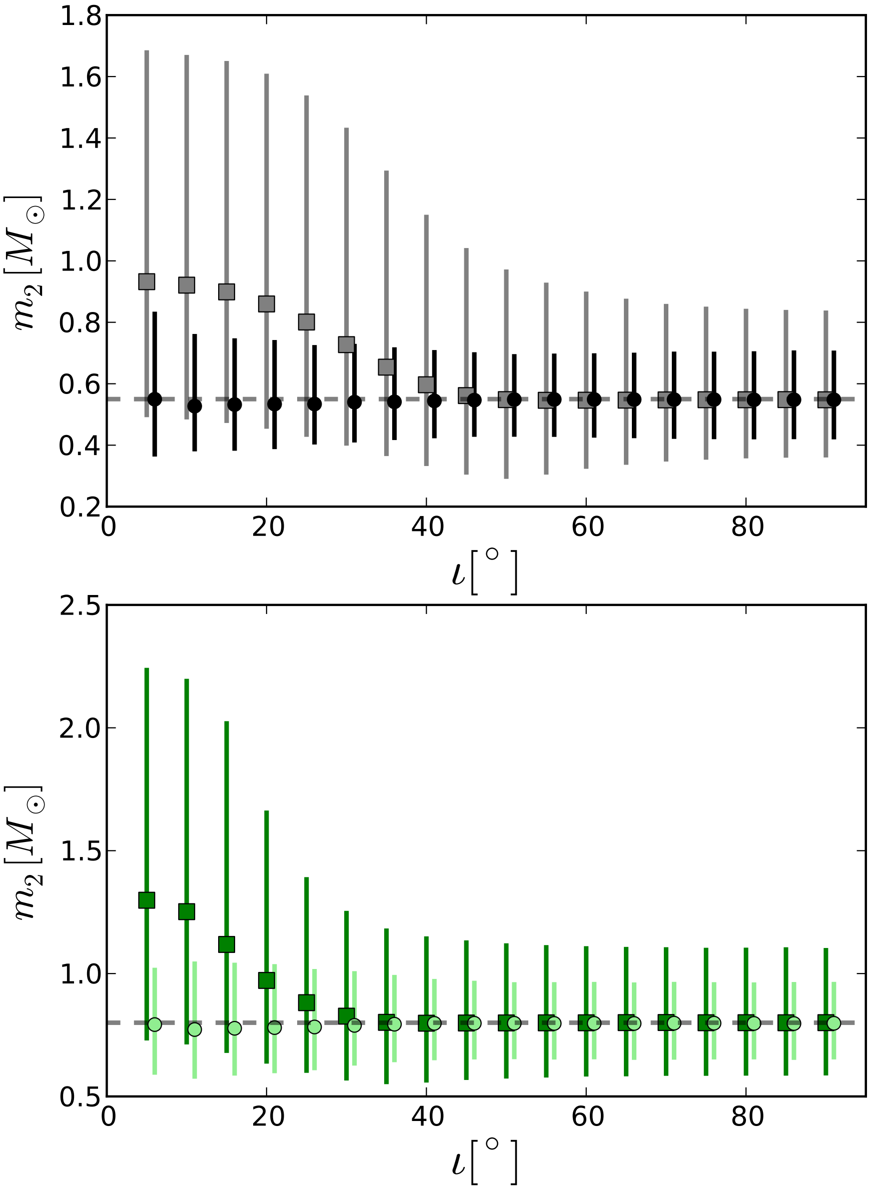

FIGURE 4.9: *Scenario 2c*: Same scenario as in Figure 4.7 with an additional EM measurement on the distance. Top: $2-\sigma$ uncertainties for the secondary mass for J0651 where the grey colored lines are constraints from EM information on m_1, d and GW $\mathcal{A}$. These reduce to the tighter constraints shown in black lines when EM data on K_1 is also used (see text). The dashed line in grey is the real value of m_2. Bottom: Same for the high mass binary.

especially useful for lower inclination systems with S/N ~ 10, where large GW uncertainties $\mathcal{A}$ influence the constraints of the physical parameters in question. Furthermore, the constraints in m_2 can also be compared with the previous case in Figure 4.7 where we find that for the single-lined spectroscopic binary, knowing its distance to 10% significantly improves knowledge of the secondary mass at lower inclinations. The key point in Scenarios 2b and 2c is that not all the $[\mathcal{A}, \iota[\mathrm{GW}]]$ pairs are consistent with the EM observations. Therefore both constraints on the GW data and other parameters also constrain the GW error ellipses. The $2-\sigma$ uncertainties in the GW amplitude and GW inclination for these scenarios are shown in the Appendix.

4.3.3 Scenario 3: EM data on m_1, K_1, m_2 & K_2

In this section we consider EM observations of a *double-lined spectroscopic* binary which translates to a set of measurements in the mass and radial velocity for each of the components: m_1, K_1, and m_2, K_2. Given the two masses and GW measurement on the amplitude we can immediately compute a preliminary distance. Additionally, we can also derive two sets of inclinations independently from the individual radial velocities and the masses, $\iota_{\mathrm{K}_1}, \iota_{\mathrm{K}_2}$ from Eq. 4.4. These inclinations can be compared with the one measured from GW data, $\iota[\mathrm{GW}]$. At lower inclinations, large uncertainties in $\iota[\mathrm{GW}]$ essentially imply that those systems' inclinations are undetermined and this also affects the amplitude due to the strong correlation between them. Thus, the independent estimates of $\iota_{\mathrm{K}_1}, \iota_{\mathrm{K}_2}$ from the EM data can be useful in constraining the GW amplitude. This reduced amplitude will further constrain the distance which is shown in the third panel in Figure 4.10. In the figure both the observed K_1, K_2 are shown in the top panel in green and blue lines respectively. The inclination and the distance given the GW amplitude and both the masses are shown in grey line in the middle and bottom panels respectively. Both the inclination and distance derived from K_1 and K_2 are plotted in green and blue lines respectively. Observe that a 10% fractional error in each K_1 and K_2 translate into similar uncertainties of the distance and thus in the following figures we show the constraints from using K_1 data only. The constrained distances estimated in this way as a function of inclination is shown in Figure 4.11 for J0651 in top panel (also in black) and for the high mass binary in the bottom panel (in light green). The grey line in the top panel and dark green line in the bottom panel are the 95 percentiles in d using only the masses from the EM data and the GW amplitude. Observe that at lower inclinations knowing masses and a radial velocity can improve the constraint in distances significantly. The uncertainties are smaller for J0651 at lowest inclinations because the relative 10% uncertainties in the K_1 have lower absolute uncertainties that propagate into the uncertainties of the distance.

Note that typically in practice EM data provides measurements of both the masses and only one of the radial velocities with $\sim 10\%$ precision. From the radial velocity formulation we have the relation: relation $m_1/m_2 = K_2/K_1$ which can be used to compute the remaining

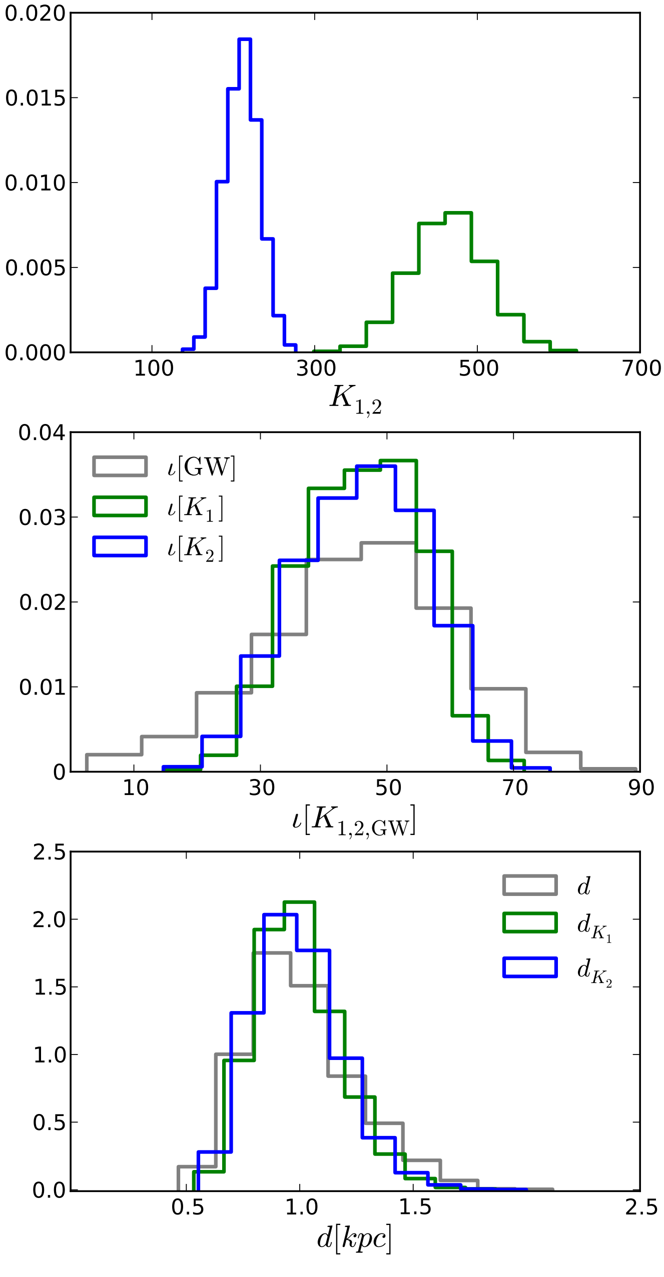

Figure 4.10: *Scenario 3*: Left: Distributions of the radial velocities from EM data for J0651 masses with the binary orientated at $\iota = 45°$. Middle: Given EM data on m_1, m_2, and the corresponding K_1, K_2, the inclinations are calculate using Eq. 4.4 which is compared with inclination from GW data. Right: Constraints on the distance obtained solving Eq. 5.10 with: EM data on m_1, K_1, m_2, K_2 and GW data on $\mathcal{A}$, ι.

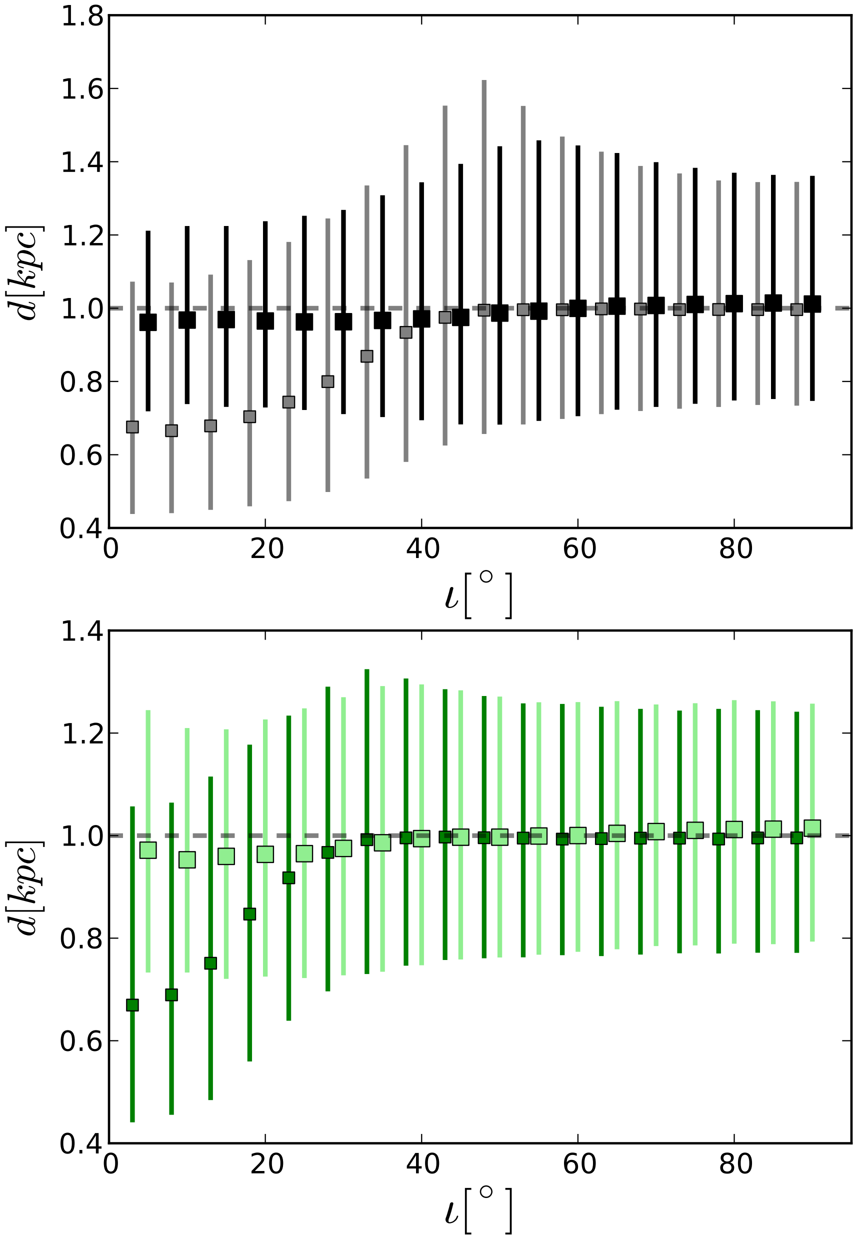

Figure 4.11: *Scenario 3*: Same as in Figure 4.10 but for all inclinations for J0651 in top panel and the for the high mass binary in bottom panel. In the top (bottom) panel, the constraints in black (light green) lines are from using $\iota[K_1]$ and the constraints in grey (dark green) are from using $\iota[\mathrm{GW}]$. The dashed line (in grey) is the real values of the d.

K_i. This provides a consistency check between EM and GW data. The EM data can be used to derive inclination measured from the radial velocities, ι[RV] which can be verified against the ι[GW] as shown in the middle panel in Figure 4.10.

4.4 Conclusions

We have quantified the possible constraints/improvements in the physical parameters of the white-dwarf (WD) binaries that are observable by the eLISA detector in the future when combined with the EM data. We do this for the binary parameters that are astrophysically interesting (masses and distance). For the GW observations from eLISA, we calculate the source's variance-covariance matrix using the Fisher methods where the Galactic binary source is described by seven parameters (or eight if $\dot{f}$ is measurable). We have taken J0651 and a higher mass binary in our analyses where J0651 is a *verification* source for eLISA. We consider various possible cases depending on the availability of the EM measurements and combine those with GW uncertainties in the amplitude and inclination in order to solve for the unknown parameters as a function of inclinations for both J0651 and the high mass binary. For clarity we list all the cases below:

1. *GW data only*: Assuming a double white-dwarf system this scenario somewhat constrains the distance.

2. *Scenario 1*: GW data + distance d: This scenario constrains the chirp mass $\mathcal{M}_c$.

3. *Scenario 2a*: GW data + primary mass m_1: This scenario constrains the chirp mass and the distance.

4. *Scenario 2b*: GW data + single-lined spectroscopic binary i.e. m_1, K_1: This scenario constrains the secondary mass m_2 and the distance.

5. *Scenario 2c*: GW data + single-lined spectroscopic binary + d: This scenario also constrains the secondary mass m_2.

6. *Scenario 3*: GW data + double-lined spectroscopic binary i.e. m_1, K_1 and m_2, K_2: This scenario constrains the distance.

All the $1-\sigma$ EM accuracies are taken to be 10% of the real/measured values which is inspired by several EM observations. We compare below the constraints in the physical parameters of interest: secondary mass m_2, chirp mass $\mathcal{M}_c$ and the distance d as a function of the scenarios depending on the EM information available. Since the GW parameter uncertainties are significantly different for a low inclination (face-on) orientation than for a high inclination (edge-on) orientation, we do the comparison for a non-eclipsing J0651 with $\iota = 25°$ and an almost eclipsing J0651 with $\iota = 85°$ in Figures 4.12 and 4.13 respectively and conclude the following:

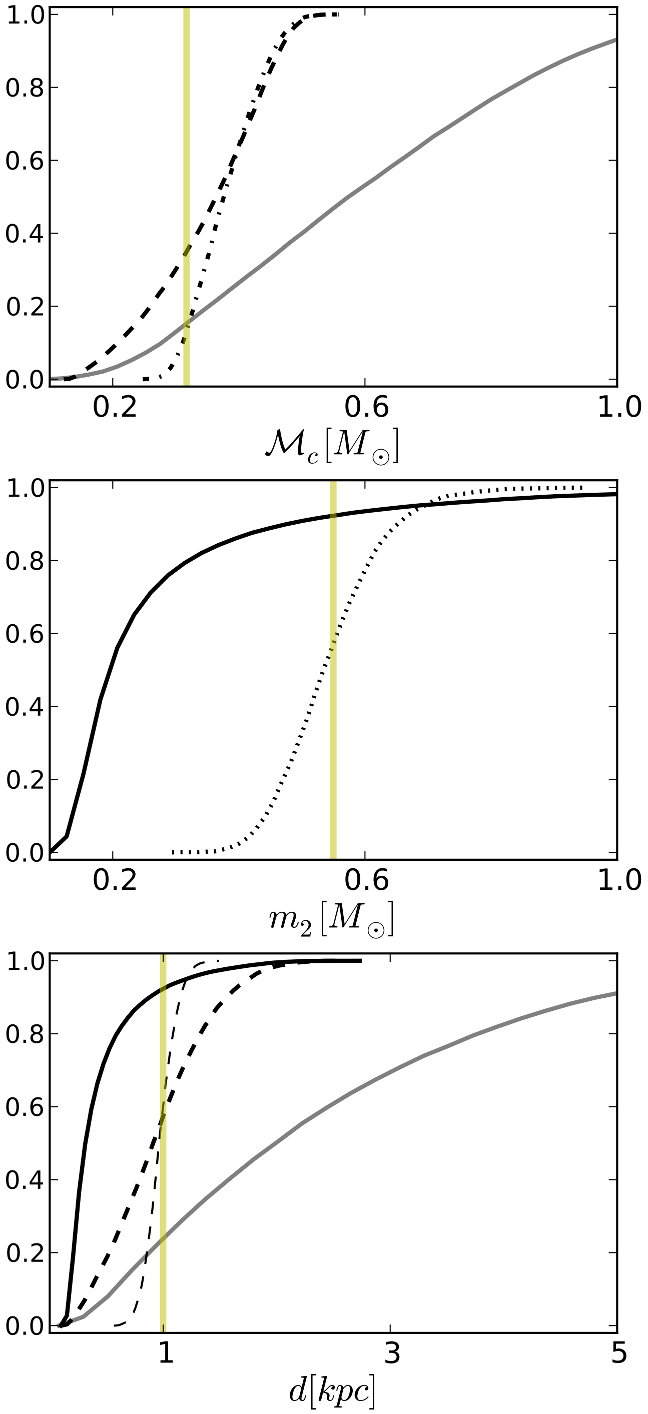

Figure 4.12: Comparison of normalized CDFs in $\mathcal{M}_c$, m_2, and d for all the scenarios above for J0651 with $\iota = 25°$. The vertical lines in all the panels are the true values of the parameters. The solid curves in grey are CDFs for the parameters when only GW data is available. Curves in dash-dotted lines are constraints for *Scenario 1 (known distance d)*, dashed curves are for *Scenario 2a (known primary mass m_1)*, solid curves are for *Scenario 2b (known primary mass m_1 and radial velocity K_1)*, dotted curves are for *Scenario 2c (known m_1, K_1 and d)* and thin-dashed lines are for *Scenario 3 (known both masses m_1, m_1 and radial velocities K_1, K_2)*.

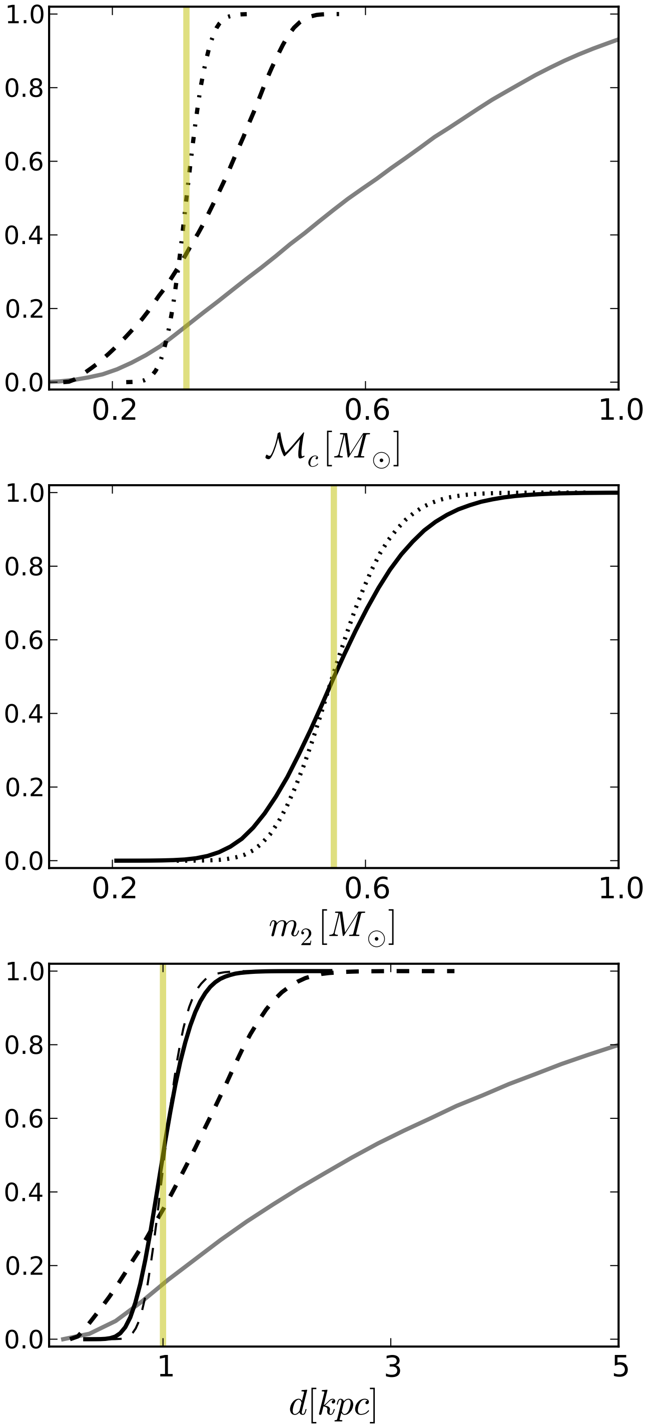

Figure 4.13: Same as in Figure 4.12, for $\iota = 85°$.

1. *Constraints on chirp mass, $\mathcal{M}_c$:* In the left panels of Figures 4.12 and 4.13, EM data on d constrains the 95 percentile of the system's chirp mass (dash-dotted line) to $0.38^{+0.11}_{-0.09}M_\odot$ and $0.32^{+0.05}_{-0.05}M_\odot$ for face-on and eclipsing J0651 respectively. EM data on m_1 constraints the $\mathcal{M}_c$ (in thick-dashed line) to $0.36^{+0.13}_{-0.21}M_\odot$ which does not depend on the inclination. The normalized cumulative distributions (CDF) of the constraints on the distance are compared to that from GW data only which is shown in the grey line in both panels.

2. *Constraints on secondary mass, m_2:* In the middle panels of Figures 4.12 and 4.13, EM data on the m_1, K_1 constrain the 95 percentile of secondary mass, m_2 to $0.19^{+0.69}_{-0.07}M_\odot$ and $0.55^{+0.23}_{-0.18}M_\odot$ for face-on and eclipsing J0651 respectively (shown in solid lines). The same set of data complemented with the distance further constrain the 95 percentile in m_2 with $0.55^{+0.18}_{-0.13}M_\odot$ and $0.55^{+0.16}_{-0.13}M_\odot$ for face-on and eclipsing J0651 respectively (shown in dotted lines). For comparison, the CDF of m_2 using only the GW data is shown in grey.

3. *Constraints on distance, d:* In the right panels, of Figure 4.12 and 4.13, EM data on m_1 constrains the distance to $0.91^{+0.98}_{-0.69}$ kpc and $1.25^{+0.95}_{-0.95}$ kpc for face-on and eclipsing J0651 respectively (in thick-dashed lines). EM data on the m_1, K_1 constrain the 95 percentile in d with $0.32^{+1.17}_{-0.16}$ kpc and with $0.99^{+0.49}_{-0.35}$ kpc accuracy for face-on and eclipsing J0651 respectively (in solid lines). EM data on m_1, m_2, K_1 and K_2 constrain the 95 percentile in d to $0.96^{+0.29}_{-0.24}$ kpc and $1.01^{+0.35}_{-0.26}$ kpc for face-on and eclipsing J0651 respectively (in thin-dashed line). For comparison, the CDF of d using only the GW data and the assumption that the masses are WDs is shown in grey.

Thus, knowing distance and/or radial velocity of the primary component can significantly improve our knowledge of the binary system. These constraints change as a function of inclination of the binary that is shown in previous sections. In a forthcoming paper we will address the effect on these improvements by including the (possible) EM measurement of rate of change of the orbital period.

Acknowledgements
This work was supported by funding from FOM. We are very grateful to Michele Vallisneri for providing support with the *Synthetic LISA* and *Lisasolve* softwares.

4.A Variance-covariance matrixes of J0651

We have listed the VCM matrices for the J0651 system with eclipsing and non-eclipsing configurations in our analysis. There are 7 parameters that describe them which are listen in the first row of the matrices below and for each binary, the values are listed in the row with θ_i. The diagonal elements are the absolute uncertainties in each the 7 parameters and

the off-diagonal elements are the normalized correlations, i.e. $c_{ii} = \sqrt{\mathcal{C}_{ii}} \equiv \sigma_i$, $c_{ij} = \frac{\mathcal{C}_{ij}}{\sqrt{\mathcal{C}_{ii}\mathcal{C}_{jj}}}$. The strong correlations between parameters (i.e. whose magnitudes are ≥ 0.9) are marked in bold in the VCMs below. These correlations have been explained in Paper I.
VCM 1: Eclipsing J0651 ($\iota = 5°$), S/N = 10.5.

$$\begin{array}{c|ccccccc}
 & \mathcal{A} & \phi_0 & \cos\iota & f & \psi & \sin\beta & \lambda \\
\theta_i & 1.67\times10^{-22} & \pi & 0.007 & 2.61\times10^{-3} & \pi/2 & -0.08 & 2.10 \\
\hline
\mathcal{A} & 0.08\times10^{-23} & -0.0 & 0.0 & 0.01 & 0.02 & 0.03 & -0.06 \\
\phi_0 & & 0.907 & -0.01 & \mathbf{-0.91} & 0.01 & 0.11 & 0.08 \\
\cos\iota & & & 0.172 & 0.01 & -0.01 & 0.07 & -0.33 \\
f & & & & 2.982\times10^{-10} & -0.01 & -0.08 & -0.15 \\
\psi & & & & & 0.035 & -0.02 & 0.05 \\
\sin\beta & & & & & & 0.059 & 0.08 \\
\lambda & & & & & & & 0.017
\end{array}$$

VCM 2: Not-eclipsing J0651 ($\iota = 45°$), S/N = 24.

$$\begin{array}{c|ccccccc}
 & \mathcal{A} & \phi_0 & \cos\iota & f & \psi & \sin\beta & \lambda \\
\theta_i & 1.67\times10^{-23} & \pi & 0.707 & 2.61\times10^{-3} & \pi/2 & -0.08 & 2.10 \\
\hline
\mathcal{A} & 3.86\times10^{-23} & 0.03 & \mathbf{-0.98} & -0.02 & 0.03 & -0.13 & 0.35 \\
\phi_0 & & 0.739 & -0.03 & -0.19 & 0.16 & 0.15 & 0.10 \\
\cos\iota & & & 0.19 & 0.02 & -0.01 & 0.13 & -0.36 \\
f & & & & 1.688\times10^{-9} & \mathbf{-0.98} & -0.06 & -0.21 \\
\psi & & & & & 0.36 & 0.13 & 0.07 \\
\sin\beta & & & & & & 0.031 & -0.13 \\
\lambda & & & & & & & 0.009
\end{array}$$

4.B Constraints in $\mathcal{A}$ and ι of J0651

Figure 4.14 shows how the error ellipses of amplitude and inclination from GW observations reduce using EM observations for the different scenarios that we have described in Sects. 1 and 2. Knowing one of the masses (Scenario 2a) from the EM does not constrain the $[\mathcal{A}, \iota]$ any more than the GW data alone. In other words the m_2 and d are free parameters to satisfy the amplitude. The 95 percentiles in the amplitude are shown in grey in the figure which are the same as the case where we have GW data only. In fact these constraints in the amplitude decrease as a function of inclination as expected from the GW measurements (see Figure 4.2). Adding an EM measurement of the measured mass's radial velocity (Scenario 2b) can constrain the $[\mathcal{A}, \iota]$ slightly or significantly depending on inclination of the system which are shown in thick black lines. Finally complementing the mass and radial velocity of the brighter companion with the distance to the binary (Scenario 2c) significantly constraints the $[\mathcal{A}, \iota]$ which is strongest for the lower inclinations as shown in the figure in thin black lines. Observe that EM information provide strongest improvements for low inclination systems where GW uncertainties in the amplitude and the inclination are very large.

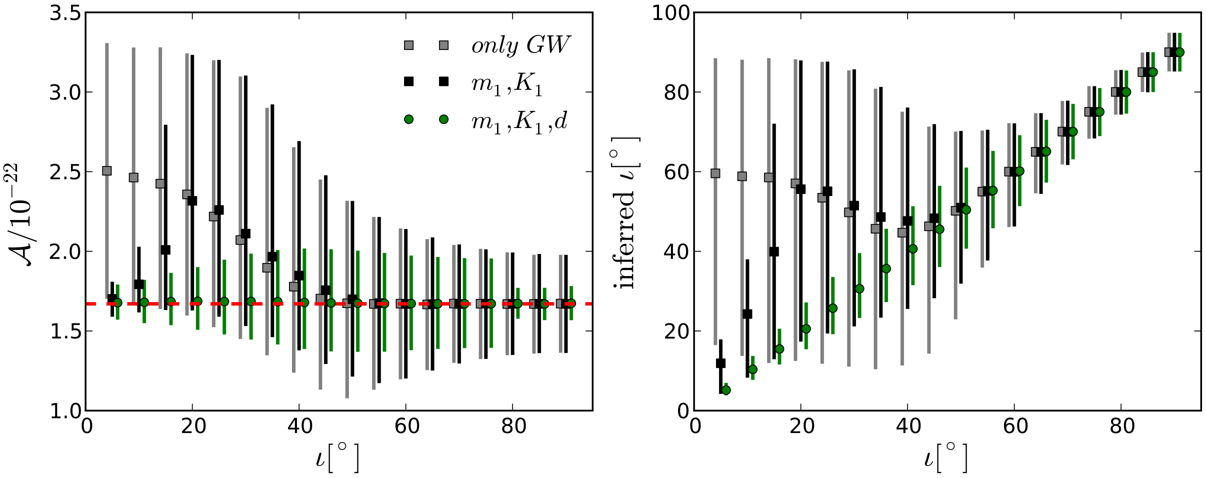

Figure 4.14: 95 percentiles in the GW amplitude as a function of inclination for various sets of EM information as labeled. The real value for the amplitude is shown in black dashed-line.

4.C The distribution of $\mathcal{A}$ and ι at lower inclinations

Here we show that while Fisher method gives an estimate on the parameter uncertainties and correlation between them without following the posterior in detail, it gives a reasonable estimate of the above quantities as long as the priors in the parameters are rectangular (i.e. not Gaussian) and are large enough to preserve the overall orientation of the posterior. We compute an estimate of the likelihood with a simple χ^2 procedure on a 2D parameter distribution of $\mathcal{A}_i$ and $\cos\iota_j$, where the $\chi^2 = (1/(N-1))\Sigma_{t=0,N}(h_0(t) - (h[i,j](t) + n(t))^2$, h_0 = true signal, $h[i,j]$ = signal at a grid point and n is a noise realisation, N =total time samples. For an evenly placed parameters in a 10×10 grid, we take the average χ^2 computed for 10 different noise realisations. Figure 4.15 shows the colored contours of 2D χ^2 distribution for the case of $\iota = 65°$ (in the left-panel) where the Fisher uncertainties are well within the physically allowed bounds. The over-plotted contour in thick solid line is $1-\sigma$ uncertainty ellipse computed from Fisher matrix about the true values of $\mathcal{A}$ and $\cos\iota$ labelled with the white circle. This just shows that the χ^2 distribution follows the shape and the slope of the Fisher distribution roughly, but not exactly as expected. The same is shown for $\iota = 10°$ in the right-panel where the uncertainties hit the physical bounds and both the methods show a sharp cut-off at $\cos\iota = 1$. Here we see that again the Fisher uncertainties and correlation roughly follow that of the χ^2, but with truncations at the boundaries. The deviation in the top-right is discussed in Shah et al. [2012]. It was argued that although the results of Fisher-based uncertainties imply that the $\iota = 5°$ system is very similar to $\iota = 90°$, this is unlikely because of the anti-correlation between $\mathcal{A}$ and $\cos\iota$ at high inclinations. At $\iota \geq 45°$ correlation between $\mathcal{A}$ and $\cos\iota$ decreases ι and the high accuracy in the inclination itself actually suffices to distinguish the higher inclination systems. Thus we expect that that χ^2 deviates from the Fisher estimate towards the top-right region of the Figure 4.15 in the right-panel.

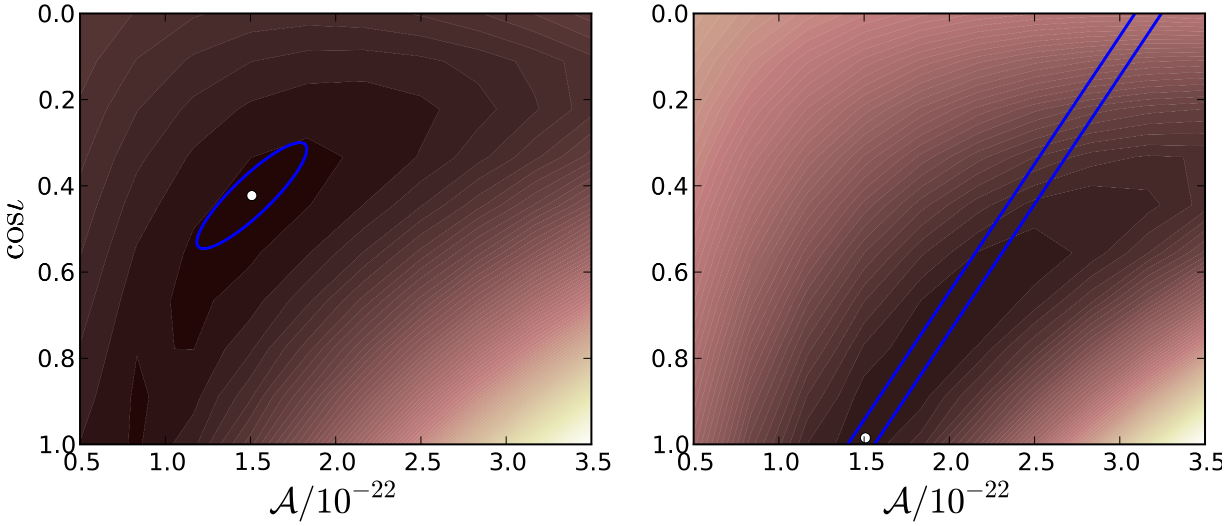

FIGURE 4.15: Filled contour plot of the 2D χ^2 averaged over 10 noise realisations for an evenly distributed grid of $\mathcal{A}$ and $\cos\iota$ compared with the $1-\sigma$ error ellipse (shown in thick solid line) from Fisher matrix $\iota = 65°$ in the left-panel and $\iota = 10°$ in the right-panel. The χ^2 values are represented by the darker to lighter colors corresponding to lower to higher values in χ^2.

CHAPTER 5

MEASURING TIDES AND BINARY PARAMETERS FROM GRAVITATIONAL WAVE DATA AND ECLIPSING TIMINGS OF DETACHED WHITE DWARF BINARIES

S. Shah, & G. Nelemans

ApJ, 791, 76, July 2014

Abstract

The discovery of the most compact detached white dwarf (WD) binary SDSS J065133.33+284423.3 has been discussed in terms of probing the tidal effects in white dwarfs. This system is also a *verification source* for the space-based gravitational wave (GW) detector, evolved *Laser Interferometer Space Antenna* (eLISA) which will observe short-period compact Galactic binaries with $P_{\rm orb} \leq$ 5 hrs. We address the prospects of doing tidal studies using eLISA binaries by showing the fractional uncertainties in the orbital decay rate and the rate of that decay, $\dot{f}, \ddot{f}$ expected from both the GW and EM data for some of the high-f binaries. We find that $\dot{f}$ and $\ddot{f}$ can be measured using GW data only for the most massive WD binaries observed at high-frequencies. Form timing the eclipses for $\sim$ 10 years, we find that $\dot{f}$ can be known to $\sim$ 0.1% for J0651. We find that from GW data alone, measuring the effects of tides in binaries is (almost) impossible. We also investigate the improvement in the knowledge of the binary parameters by combining GW amplitude and inclination with EM data with and without $\dot{f}$. In our previous work we found that EM data on

distance constrained 2-σ uncertainty in chirp mass to $15-25\%$ whereas adding $\dot{f}$ reduces it to 0.11%. EM data on $\dot{f}$ also constrains 2-σ uncertainty in distance to $35\%-19\%$. EM data on primary mass constrains the secondary mass m_2 to factors of 2 to $\sim 40\%$ whereas adding $\dot{f}$ reduces this to 25%. And finally using *single-line spectroscopic constrains 2-σ uncertainties in both the m_2, d to factors of 2 to $\sim 40\%$. Adding EM data on $\dot{f}$ reduces these 2-σ uncertainties to $\leq 25\%$ and $6\%-19\%$ respectively.* Thus we find that EM measurements of $\dot{f}$ and radial velocity will be valuable in constraining eLISA binary parameters.

5.1 Introduction

The discovery of a detached white dwarf (WD) eclipsing binary system, SDSS J065133.33+284423.3 (J0651, hereafter) [Brown et al., 2011] has generated a number of discussions on the subject of tidal physics of compact objects [e.g. Piro, 2011; Fuller & Lai, 2012, 2013; Burkart et al., 2013; Dall'Osso & Rossi, 2013]. The small orbital period of $P_{\rm orb} \approx 765$s, and the compact nature of the stars which are not yet transferring mass, makes it one of the most interesting candidates for studying the level of tidal interactions between the components and the possible astrophysical implications for WDs. J0651 is also a *verification binary* for eLISA[1] [Amaro-Seoane et al., 2013] radiating gravitational wave at $f = 2.6$mHz with an estimated signal-to-noise ratio (S/N) of $\sim$10 for an observation length of 2 years. In this paper, we investigate detectability of the tidal effects from the GW and EM data and their implications on the astrophysical knowledge of the WDs in the binary and similar systems. In addition we discuss the effect of using measured EM period changes on the GW parameter estimates.

eLISA will observe Galactic binaries with periods shorter than a few hours. While the majority of the binaries (which are mostly double WD objects) are radiating GWs in the low-frequency range ($f \leq 3$mHz), there are a handful of high-frequency sources with significant orbital decay as predicted by population synthesis simulations [Nelemans et al., 2004]. Despite the limited number of such high-f objects, they present a unique opportunity to do tidal studies of compact objects as these relatively high-f binaries will have a strong gravitational signal strength and larger values for their rate of change of the orbital periods both aiding accurate GW measurements of their orbital parameters. Here, we use Fisher studies[Cutler, 1998] to address the detectability of the rate of change of the source's GW frequency, $\dot{f}$ and $\ddot{f}$ from the GW data for the detached J0651-like binary systems. The GW parameters, f, $\dot{f}$ and $\ddot{f}$ of a circular binary are trivially related to the more familiar quantities in EM observations, $P_{\rm orb}$, $\dot{P}_{\rm orb}$, and $\ddot{P}_{\rm orb}$ via: $f = 2/P_{\rm orb}$, $\dot{f} = -2\dot{P}_{\rm orb}/P_{\rm orb}^2$, $\ddot{f} = 2(\dot{P}_{\rm orb}^2 - 2\, P_{\rm orb}\, \ddot{P}_{\rm orb})/P_{\rm orb}^3$.

---

[1] a space-based gravitational wave mission with expected launch in 2034

As a compact binary ages via GW dissipation, the orbital period changes as a result of increasing $\dot{f}$. If the stellar components in the binary are close enough to each other, an additional source of dissipation of orbital energy can ensue through tides and this may reflect in its GW *phase shift*. In this paper we consider only detached WD systems where both the GW emission and tidal torque (including dynamical tides) can enhance the orbital decay rate. The orbital evolution in the presence of mass transfer and GW (see Eq. 12 in Nelemans et al. [2004]) competes with dissipations from the tides. In these cases, their orbital evolution can be influenced by short-term variations like the nova explosions and this could dramatically increase $\dot{f}, \ddot{f}$. This means that in the millions of binaries that eLISA will observe, if a number of such (mass-transferring) systems undergo such orbital perturbation, their $\dot{f}, \ddot{f}$ will increase by orders of magnitude making it possible to measure them, however this is very unlikely in the lifetime of eLISA [Stroeer & Nelemans, 2009].

Recent studies using EM data have shown that for the case of J0651, the period change can be enhanced by roughly up to 5% due to the tides[Burkart et al., 2013; Benacquista, 2011; Piro, 2011]. Based on parametrized equilibrium tide theory, Piro [2011] has shown that for the J0651 system, in addition to the GW radiation, the tidal interactions between the WDs will imprint a shift in the time of eclipses by 0.3s after one year of timing. The dominant GW contribution advances the shift by 5.5s. Benacquista [2011] also calculated the deviation from the pure GR-driven inspiral, under the assumption that the WDs are tidally locked with the orbit and the GW radiation causes a small mismatch between the WD spin and orbital period. This causes a tidal distortion of the lower mass WD and assuming that this tidal energy is mostly transferred from orbit to the spin keeping the system tidally locked, the tidal deviations were computed for J0651. Both of these works are corroborated byBurkart et al. [2013] who compute the tidal response of J0651-like system assuming that both WDs are in resonance lock where the orbit and spin vary uniformly. It has been further claimed that for J0651, one should be able to detect the effect of tides in the GW phase shifts [Fuller & Lai, 2012]. These results are based on modeling dynamical tide in a carbon/oxygen WD. The prospect of detecting such a phase shift in the GW data is very exciting as this could lead to measurements of the components' moment of inertia. However in order for the tides to significantly shift in the collective phase of the GW signal, one needs to observe the system for millions of cycles according to the estimate of the evolution in the number of cycles only due to the tides [Eq. 88, Fuller & Lai, 2012] which is not feasible with currently planned eLISA mission.

In order to investigate the measurability of the above-mentioned orbital parameters, we calculate the predicted GW uncertainties in those parameters as a function of orbital period. We summarize the data analysis and the selection of the binaries in Section 2. In Section 3 we estimate the expected EM uncertainties from mid-eclipse timing measurements. This is followed by a comparison of the accuracies from two types of measurements in Section 4. Finally we summarize prospects of measuring deviation in evolution due to tides and the improvement in the knowledge of the WDs from combining the accuracies of GW and EM

TABLE 5.1: GW parameter values of J0651, high-mass and the high-f binary systems

	$\mathcal{A}[\times 10^{-22}]$	ϕ_0[rad]	$\cos\iota$	$f[\times 10^{-3}]$[Hz]	$\dot{f}$[Hz/s]	$\ddot{f}$[Hz/s^2]	ψ[rad]	$\sin\beta$	λ[rad]	S/N
J0651	$1.67^{(a)}$	π	0.007	2.61	-3.35×10^{-17}	1.57×10^{-31}	$\pi/2$	0.101	1.77	$\sim 13^{(a)}$
high-mass	$6.71^{(b)}$	π	0.007	2.61	-1.07×10^{-16}	1.61×10^{-29}	$\pi/2$	0.101	1.77	$\sim 50^{(b)}$
high-$f^{(c)}$	3.69	5.41	-0.86	17.69	-1.99×10^{-13}	8.19×10^{-23}	0.75	0.94	1.97	~ 135

(a) for $m_1 = 0.25M_\odot$, $m_2 = 0.55M_\odot, d = 1.0$ kpc (b) high-mass system with $m_1, m_2 = 0.8M_\odot$, $d = 1.0$ kpc (c) For the given $f, \dot{f}, \ddot{f}$, $m_1, m_2 = 1.01M_\odot$, $d = 9.95$ kpc measurements from the measurement of the rate of change of orbital period.

5.2 eLISA binaries and uncertainties from the GW data

We obtain the GW accuracies by carrying out Fisher information matrix (FIM) calculations in order to determine whether the GW parameters $\dot{f}, \ddot{f}$ can be measured over the two year GW observations by eLISA mission. We consider three binary systems for this purpose: the verification source J0651, a hypothetical high-mass J0651 system and the highest-$\dot{f}$ source we find in the population synthesis predictions [Nelemans et al., 2004]. In the rest of the paper we will refer to them as J0651, high-mass and high-f systems respectively. We list the GW parameter values of all these systems in Table I. For J0651 only P_{orb}, and $\dot{P}_{\mathrm{orb}}$ are measured [Hermes et al., 2012]. These have been converted to f, and $\dot{f}$ with relations mentioned above. Since $\ddot{P}_{\mathrm{orb}}$ is not yet measured a fiducial $\ddot{f}$ has been chosen such that it agrees with the GR predictions. These values are slightly higher for the high-mass J0651 in accordance with the masses. For the high-f system, the values $\dot{f}, \ddot{f}$ are given by the simulation.

Our method and application of FIM to extract the GW parameter uncertainties has been described in detail in Shah et al. [2012]. In this paper, we extend our previous FIM analyses to include *nine* GW parameters: dimensionless amplitude ($\mathcal{A}$), frequency (f), polarisation angle (ψ), initial GW phase (ϕ_0), inclination ($\cos\iota$), ecliptic latitude ($\sin\beta$), ecliptic longitude (λ), orbital decay rate ($\dot{f}$), and rate of change of that decay ($\ddot{f}$). Given these (GW) parameters, we calculate a 9 × 9 FIM for all three systems. This implies not knowing any of the parameters *a priori*. By inverting this matrix we get the variance covariance matrix (VCM) which provides the uncertainties in the parameters and the correlations between them. We refer to our previous paper for the signal and noise modeling in computing the expected parameter uncertainties and the correlations between them. We list the full VCM matrices for J0651, and the high-f systems in the Appendix, which include the normalized correlations between the 9 parameters. The normalized correlations between parameters of J0651 and high-f are different because of the difference between their angular parameters (see Shah et al. [2013]) and also due to their respective GW frequencies [Błaut, 2011].

5.3 Uncertainties from the EM data

In this section we describe the prospects of extracting the uncertainties in f, $\dot{f}$ and $\ddot{f}$ from the electromagnetic data. J0651 has a measured $\dot{\mathrm{P}}_{\mathrm{orb}} = -9.8 \pm 2.8 \times 10^{-12}$ s s^{-1} which is consistent with GR predictions [Hermes et al., 2012] within the error. The way this is typically measured is to compare the observed (O) mid-eclipse times with computed (C) values from a model with constant orbital period and fit the O-C values as function of time [e.g. Kepler et al., 1991]. A possible resulting parabola gives an evidence of a finite value of $\dot{\mathrm{P}}_{\mathrm{orb}}$ [Sterken, 2005]. The phase of the signal in cycles at an arbitrary time t after a reference time evolves and it is given by a Taylor expansion of the phase:

$$\phi = \phi_0 \, + \, f\,(t - t_0) + \frac{\dot{f}}{2}\,(t - t_0)^2 \, + \, \frac{\ddot{f}}{6}\,(t - t_0)^3 \, + \, ... \, , \tag{5.1}$$

where t_0 is the epoch, and t is measured in the barycentric co-ordinates. As the source is observed for a longer time, the second and third terms gain significance. Given a duration of observation, $\mathrm{T_{obs}}$ and for a fixed resolution in phase (σ_ϕ), the uncertainties in the three orbital parameters can be estimated by [Mattox et al., 1998]:

$$\sigma_f \sim \frac{\sigma_\phi}{\mathrm{T_{obs}}} \quad ; \quad \sigma_{\dot{f}} \sim 2\frac{\sigma_\phi}{\mathrm{T_{obs}}^2} \quad ; \quad \sigma_{\ddot{f}} \sim 6\frac{\sigma_\phi}{\mathrm{T_{obs}}^3} \tag{5.2}$$

Considering an uncertainty of eclipse timing for J0651 of Hermes et al. [2012] $\sigma_{T_0} \sim 0.725$s (see Table 2) gives a fractional phase error of $\sigma_{T_0}/P_0 \sim 9.5 \times 10^{-4}$ turns. Assuming a constant phase error timing this source for a long time, for e.g. $\mathrm{T_{obs}} \sim 10$ years using the above equation we get, $\sigma_f \sim 10^{-12}$Hz, $\sigma_{\dot{f}} \sim 10^{-21}$Hz/s and $\sigma_{\ddot{f}} \sim 10^{-30}$Hz/s^2. This implies for J0651 the relative uncertainties are $\sigma_{\dot{f}}/\dot{f} \sim 10^{-5}$, $\sigma_{\ddot{f}}/\ddot{f} \sim 6$. Thus timing J0651 will be very useful to pin down the rate of change of frequency, however the uncertainty in $\ddot{f}$ is very large. Below we will compare the uncertainties in decay rate and rate of the decay for all three binaries using GW and EM observations for a range of orbital periods.

5.4 Measurability of $\dot{f}$, $\ddot{f}$

A straight forward way to distinguish the tidal contribution from that of the GW radiation in the evolution of the binary is to measure the quantities $f, \dot{f}, \ddot{f}$ with sufficient accuracy. The general relativistic predictions of the orbital decay in a binary orbit due to GW radiation *alone* gives the following relation [Webbink & Han, 1998]:

$$\left(\frac{\ddot{f}\,f}{\dot{f}^2}\right)_{\mathrm{GW}} := y \, = \, \frac{11}{3}, \tag{5.3}$$

thus, a measure of any deviation from this numerical value measured within the parameter accuracies for detached binaries will provide a testbed for effects of the tides.

To get a rough estimate of the percentage of tidal contribution in the binary evolution of J0651-like systems, we can estimate Eq. 5.3 for J0651 where the tidal contribution is taken into account since the individual masses and radii of this system have been measured from its light curve. This gives us an idea of what the uncertainties in $\dot{f}, \ddot{f}$ must be in order to measure any deviation from the GR driven binary evolution. Under the influence of GW radiation only, the rate of change of GW frequency changes according to

$$\dot{f}_0 = \frac{96\,\pi}{5}\frac{G^{5/3}}{c^5}\,(\pi\,\mathcal{M}_c)^{5/3}\,f^{11/3}, \tag{5.4}$$

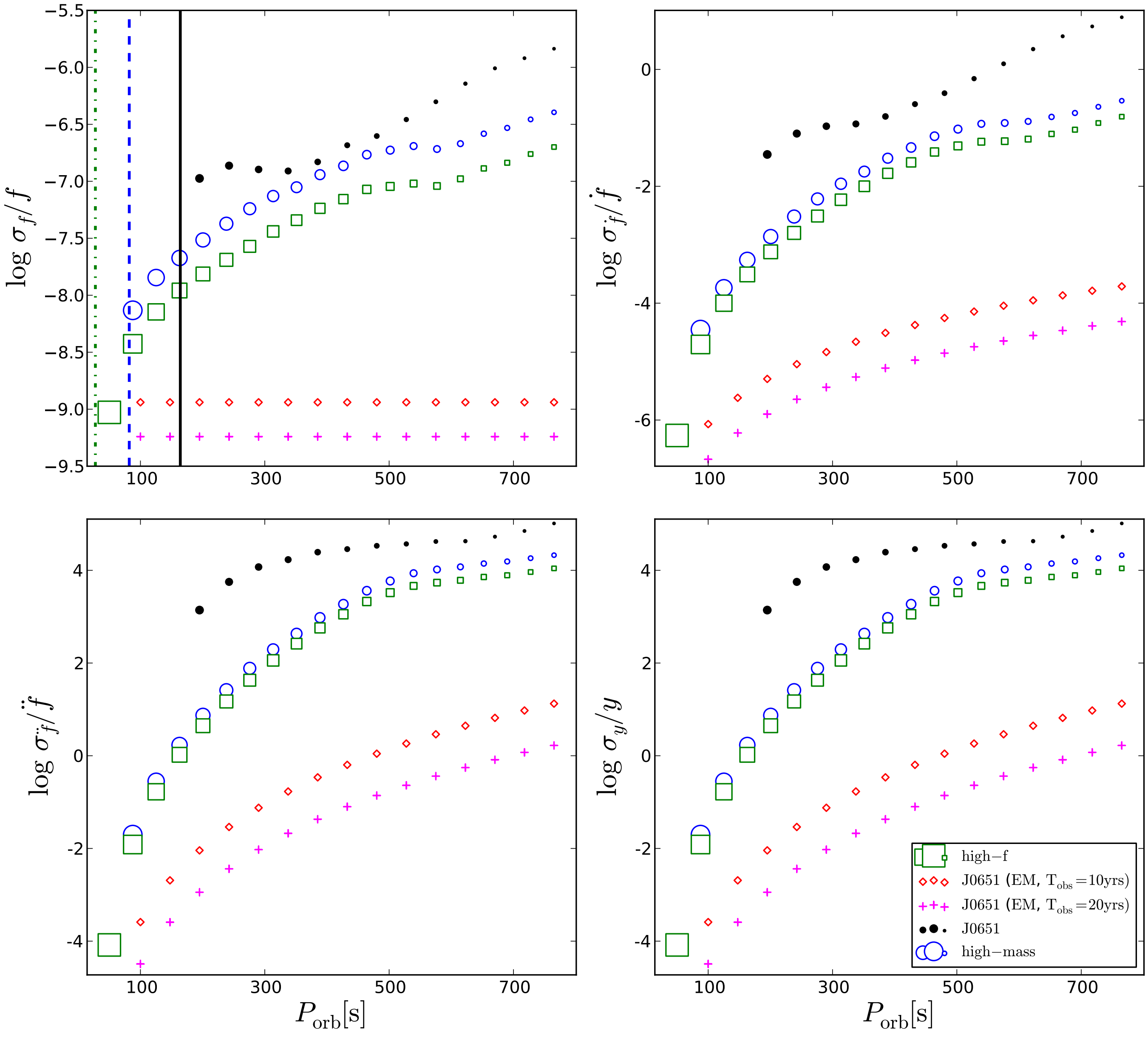

FIGURE 5.1: Relative uncertainties in frequency (f), decay rate ($\dot{f}$), rate of decay rate ($\ddot{f}$) and braking index (y) using gravitational wave data of J0651, the high-mass counterpart and the high-f binary. All the GW uncertainties are represented by (black) filled circle, (blue) open circle and (green) square for the three binary systems respectively listed above. Also the same uncertainties are shown for J0651 using its electromagnetic observations of its eclipse timings which are represented by (red) diamonds for $T_{\rm obs}$ = 10yrs and by (magenta) crosses for $T_{\rm obs}$ = 20yrs. The marker sizes of filled/open circles and open squares represent the signal-to-noise ratio from the GW data of each system at that orbital period. The vertical lines in the top-left panel are the values of minimum orbital period at which a given system will start mass transfer. The (black) solid line is for J0651, (blue) dashed line is for the high-mass counterpart and the (green) dash-dotted line is for the high-f binary.

where $\mathcal{M}_c$ is the chirp mass given by:

$$\mathcal{M}_c = (m_1 m_2)^{3/5}/(m_1 + m_2)^{1/5}. \tag{5.5}$$

Including the contribution of tides and assuming that the WD spins are synchronized with the orbital period, the rate of change of *orbital* frequency changes according to [Benacquista, 2011]:

$$\dot{f} = \dot{f}_0\,(1\ + 5\,\Delta_Q + 3\,\Delta_I), \tag{5.6}$$

In the equation above,

$$\Delta_Q = \frac{Q\,(\pi\,f)^{4/3}}{G^{2/3}M^{5/3}},\quad \Delta_I = \frac{(I_1\ +\ I_2)\,(\pi\,f)^{4/3}}{\mu G^{2/3}M^{2/3}} \tag{5.7}$$

where $Q = k_2 I_i$ is the quadrupole moment, k_2 describes the structure of the star and $I_i = m_1 r_1^2$ is the moment of inertia of each star (with radius r_i). This can be translated in terms of $\mathrm{P_{orb}}$, ω, or f_{EM} via: $\omega = 2\pi/\mathrm{P_{orb}} = 2\pi f_{\mathrm{EM}} = \pi f$. Thus, including the orbital decay due to tides the GR formulation in Eq. 3 will then change according to:

$$\left(\frac{\ddot{f}\,f}{\dot{f}^2}\right)_{\text{tides+GW}} = \frac{\frac{11}{3}\ +\ 25\Delta Q\ +\ 15\Delta I}{1\ +\ 5\Delta Q\ +\ 3\Delta I}, \tag{5.8}$$

Given the measured masses, radii and the present orbital period (or equivalently GW f) of J0651 and the assumptions from [Benacquista, 2011], we get $\left((\ddot{f}\,f)/\dot{f}^2\right)_{\text{tides+GW}} = 3.73138$. This is a deviation from GR driven case of 11/3 by only 1.7650%[2]. In deriving this value we only accounted for the lower mass white dwarf which is distorted whereas the higher mass white dwarf is relatively undistorted and thus its quadrupole moment can be ignored. The deviation above implies that the measured quantities from which y is derived should have accuracies at the level of less than a few percent in order to distinguish tidal dissipation from GW radiation in J0651-like systems.

In Figure 5.1 fractional accuracies $f, \dot{f}, \ddot{f}, y$ are plotted as a function of orbital period for the three binaries with GW parameter values listed in Table 1. In the figure, the size of the open and filled circles and the square represent the S/N of the system at that orbital period (or equivalently the GW frequency) from the GW observations. These GW uncertainties decrease with increasing GW frequency as expected since they have higher S/N and at high-f the resolution of the GW parameters decrease as doppler modulation gains significance (see discussion in Shah et al. [2013]; Cornish & Larson [2003]). The vertical lines in the top-left panel from right to left are the lowest limit of the orbital periods of the high-f system, high-mass system and J0651 respectively where the mass transfer will ensue. This is derived simply by setting the Roche-lobe of donor WD [Eggleton, 1983] equal to the size

---

[2] This estimate depends strongly on the moment of Inertia I_i of each of the binary masses; in fact the term I_2 (i.e. of the lower of the masses which is more tidally deformed by the more massive mass) derived from a model for a tidally deformed star is the term that most affects the ratio in Eq. 5.8

of its predicted zero-temperature radius from the mass [Verbunt & Rappaport, 1988]. A more accurate estimate of the period at which mass transfer starts is obtained by fitting the spectra with the best matching He WD models and this gives a larger value for the $P_{\rm orb}$, for e.g. for J0651 the mass transfer will start when it evolves to a period of $\sim$ 420s the [Panei et al., 2007] and making it difficult to disentangle the tidal effects. In the figure, the accuracies in the parameters from observing the EM timing measurements for J0651 are shown for an observation length of 10 years (in diamond) and for 20 years (in plus). The accuracy in y for both the cases of GW and EM uncertainties is computed using propagation of errors using Eq. 5.3. The timing accuracy is assumed constant for all periods and this implies the uncertainties in the phase increase for smaller periods however, the values of $\dot{f}, \ddot{f}$ increase more steeply and thus we predict **increasing** accuracies of $\dot{f}, \ddot{f}$ for smaller periods. It is clear from these uncertainties that using only GW data measuring a tidal contribution is only possible if it is huge for a system like J0651 during their evolution until mass transfer starts. However the EM and GW fractional uncertainties in $\dot{f}, \ddot{f}$ for the high-f binary are both very precise at $\sim 10^{-5}, 10^{-3}$ respectively with which a small deviation in y can be measured. However, the chances of observing an eclipsing high-f binary and within 1kpc is almost 0 and thus measuring tides for such a system only with EM is most likely not possible.

5.5 Combining EM $\dot{f}$ and GW measurements

We find that from the timing measurements with 20 year duration the orbital decay will be observed with fractional accuracies with up to 5 orders of magnitude better than the GW accuracy for a system like J0651. Coincidentally a timing length of 20 years coincides with eLISA's launch giving us an opportune time to combine the EM measurements with the GW ones in improving our knowledge of J0651-like system parameters. In this section we address to what extent we can measure the tidal deviation terms introduced in Sect. 4. We also address how the knowledge of $\dot{f}$ improves the measurement of J0651's physical parameters of astrophysical interest such as the masses, inclination and the distance to the source.

5.5.1 Constraining the tidal deviation terms, Δ_Q, Δ_I

The measurement of $\dot{f}$ can put constraints on the tidal contributions. Here we explore these constraints formulated in Benacquista [2011] that are expressed as Δ_Q and Δ_I in Eq 5.6. Under the same formulation, the GW amplitude that takes into account the quadrupole correction to the potential of the tidally distorted primary mass (less massive of the two) can be expressed as:

$$\mathcal{A} = \mathcal{A}_{\rm o}(1 + \Delta Q), \tag{5.9}$$

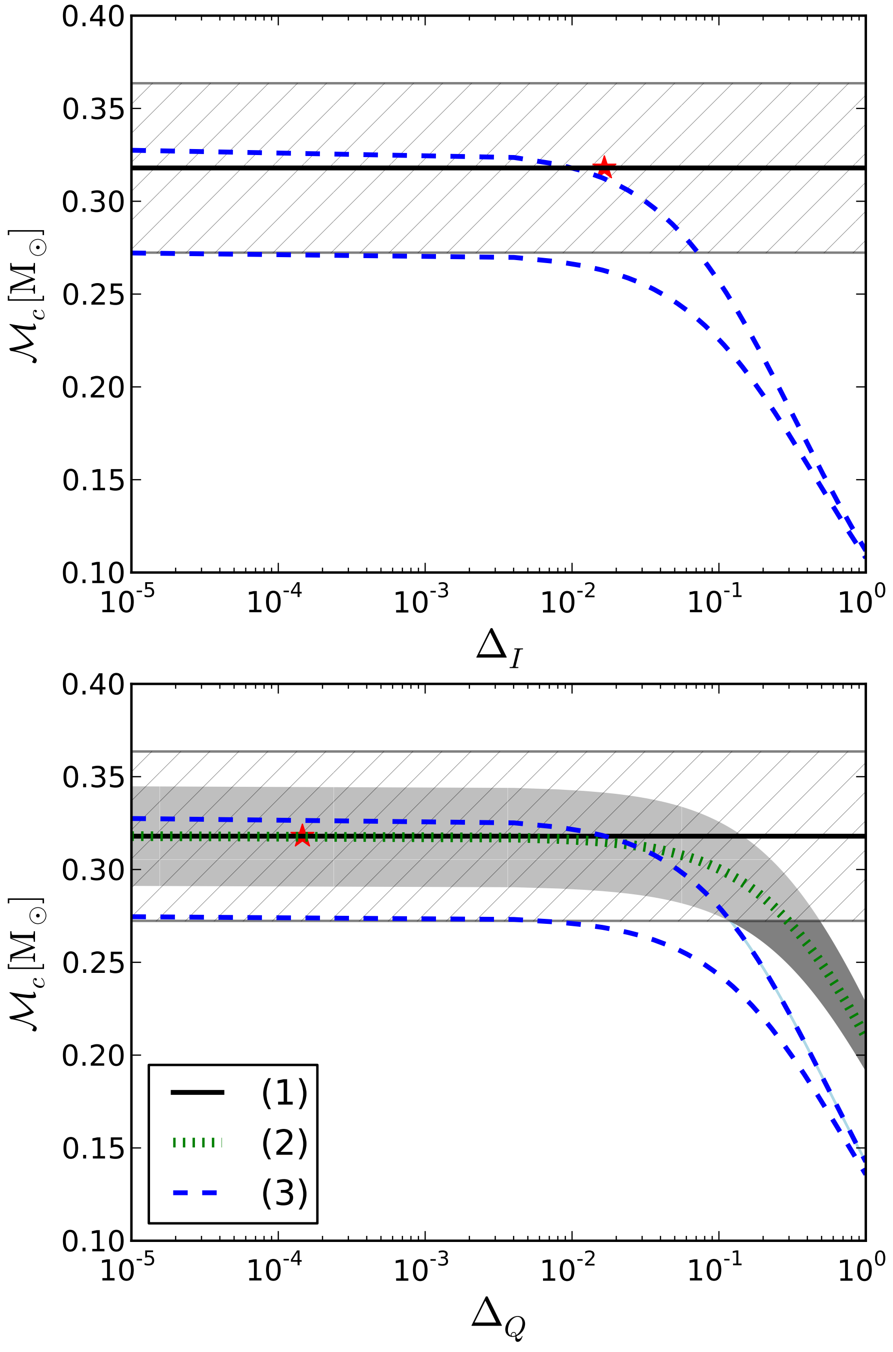

Figure 5.2: See caption of Figure 5.3

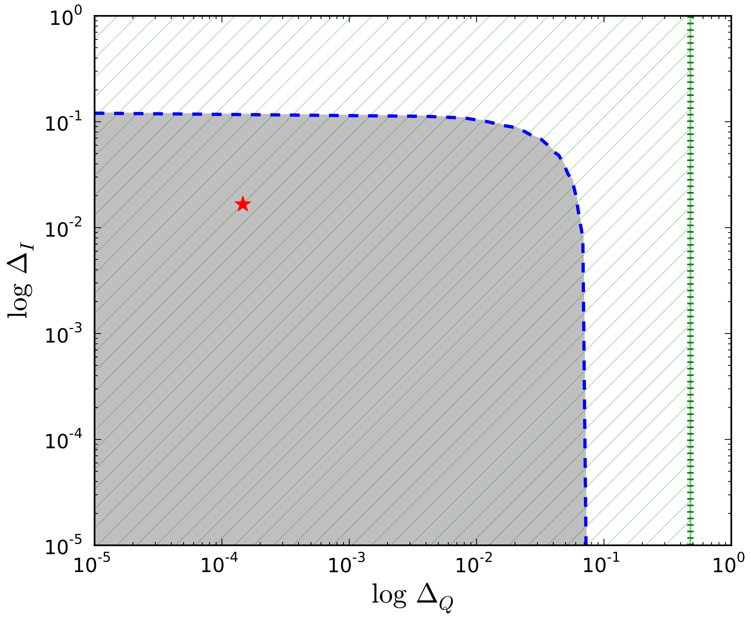

Figure 5.3: Measurability of tidal effects by determining the *inconsistency* between chirp mass $\mathcal{M}_c$ measurement from different methods as a function of the tidal deviation terms Δ_I and Δ_Q (characterizing the strength of the tides) for J0651 system. The methods are: (1) using m_1 and m_2 in Eq 5.5 (2) using $\mathcal{A}$ and d in Eqs 5.9, 5.10 (3) using $\dot{f}$ in Eq 5.6. Top-left and right panels show the $\mathcal{M}_c$ computed from method 1 (shown in (black) solid line), from method 2 (in (green) dotted line) and from method 3 (in (blue) dashed lines). Method 1 is not influenced by tides (i.e. no dependence on Δ_I, Δ_Q) whereas method 2 depends on Δ_Q only and method 3 depends on both Δ_I and Δ_Q. The $1-\sigma$ uncertainties in the $\mathcal{M}_c$ for method 1 are from $\sigma_{m_1}, \sigma_{m_2}$ shown in (grey) hatched area; for method 2 are from $\sigma_{\mathcal{A}}, \sigma_d$ shown in grey filled area (in top-right panel); for method 3 is from $\sigma_{\dot{f}}$ is not visible since the relative uncertainty is $\sim 10^{-3}$. In the top-left panel, the top and bottom (blue) dashed curves correspond to two values of $\Delta_Q = 10^{-5}, 0.0683$ and in the top-right panel the same correspond to two values of $\Delta_I = 10^{-5}, 0.1205$ as $\mathcal{M}_c$ measurement via $\dot{f}$ (method 3) depends on both the tidal deviation terms. Observe that the three methods (in top panels) show inconsistency in chirp mass with increasing Δ_I, Δ_Q, however the measurement uncertainties are too large in order to measure the inconsistency for small Δ_I, Δ_Q. The deviations at which the inconsistency can be measured within the uncertainties are determined by where the (blue) dashed lines and (grey) shaded area cross with the (grey) hatched area in the top panes. In the bottom panel these crossings are shown as a joint boundary in Δ_I and Δ_Q. The estimated Δ_I, Δ_Q for J0651 system are marked by the red star. It shows that constraining the tidal deviation terms is not feasible (for J0651-like systems) because typically the values of Δ_I and Δ_Q are smaller than the measurement uncertainties in m_1, m_2, $\mathcal{A}$, and d.

where the GR driven GW amplitude is given by:

$$\mathcal{A}_\mathrm{o} = \frac{4(G\mathcal{M}_c)^{5/3}}{c^4 d} (\pi f)^{2/3} \tag{5.10}$$

Assuming binary evolution is only driven by gravitational waves, we compute chirp mass in three ways for J0651 system: (1) measurements of m_1 and m_2 ($\mathcal{M}_c$, Eq 5.5), (2) measurements of $\mathcal{A}$ and d ($\mathcal{M}_c(\mathcal{A}_\mathrm{o}, d)$, Eqs 5.9, 5.10) and (3) measurement of $\dot{f}$ ($\mathcal{M}_c(\dot{f}_\mathrm{o})$, Eq 5.6). The uncertainties in the measurements of m_1, m_2 and d are taken to be 10% for the masses and distance. Uncertainty in amplitude is taken from the FIM matrix $\sim 10\%$ for eclipsing J0651 and the uncertainty in $\dot{f}$ is taken to be 0.01%, a conservative estimate from Figure 5.1. For the three estimates of chirp masses we compare for what values of Δ_Q and Δ_I are the $\mathcal{M}_c(\mathcal{A}_\mathrm{o}, d)$ and $\mathcal{M}_c(\dot{f}_\mathrm{o})$ inconsistent with $\mathcal{M}_c$. In the top panels of Figure 5.3 $\mathcal{M}_c$ is shown in black line with the corresponding $1-\sigma$ uncertainty shown by (grey) hatched area. This estimate of $\mathcal{M}_c$ does not depend on Δ_Q, Δ_I. Since $\mathcal{M}_c(\dot{f})$ depends on both Δ_Q, Δ_I, it is plotted for two values of $\Delta Q = [10^{-5}, 0.12]$ shown in upper and lower (blue) dashed lines respectively in the top-left panel. In the top-right panel $\mathcal{M}_c(\dot{f})$ is shown for two values of $\Delta I = [10^{-5}, 0.068]$ corresponding to the upper and lower (blue) dashed lines respectively. The predicted deviations from average measurements of the masses and radii for J0651 are marked by the (red) star. Benacquista [2011] estimate that $\Delta_Q, \Delta_I = 1.46 \times 10^{-4}, 0.0166$ for J0651. The relative uncertainties of $\mathcal{M}_c(\dot{f})$ are in the level of 10^{-3} not visible in the figure. Finally $\mathcal{M}_c(\mathcal{A}, d)$ can constrain ΔQ only and it is shown in dotted line with uncertainties in grey shaded area in the middle panel. The range of values of Δ_Q and Δ_I for which the three sets of chirp masses are inconsistent with each other within their uncertainties can be read from the figure which are, $\Delta_I > 0.120, \Delta_Q > -0.478$. In the bottom panel the constraints in Δ_Q and Δ_I using both EM and GW data are shown by the (blue) dashed curve (via method 2) and (dotted) vertical line (via method 3). From the bottom panel it can be seen that measuring tidal deviation Δ_Q is not feasible within the uncertainties in $\mathcal{A}, d$ marked by the (green) hatched area. Also measuring the deviation term Δ_I which is larger (at $\leq 10^{-2}$) is not feasible within the uncertainties in m_1, m_2 marked by the (grey) shaded area. Even though we expect strong tidal influence in detached white-dwarf systems such as J0651, measuring that contribution is unlikely unless the measurements in GW amplitude, distance or the individual masses should be also in the order of $\leq 10^{-2}$ for J0651-like systems. We conclude that tidal physics can be studied for high-mass binaries at opportune frequencies which implies larger values of decay rate measurable from the GW data.

5.5.2 Constraining the binary parameters

In our earlier work (Shah & Nelemans ApJ, SN2014, hereafter) we studied the effect of combining GW and EM observations, where we considered the following EM measurements: the d from *Gaia* satellite, primary mass m_1 from spectroscopy, radial velocity K_1 also from spectroscopy and possibly inclination ι from the fact that the binary can be eclipsing. We found that adding one or more of these measurements significantly improves our knowledge of the unknown astrophysical parameters of the binary and the improvement depends on the inclination of the source. In this study we add the EM information of the orbital decay rate $\dot{P}_{\rm orb}/\dot{f}$ (from Sect. 4) to the above list of EM observations and study if and how much this improves the binary parameters secondary mass m_2 and distance d compared to scenarios considered in SN2013. The uncertainties in m_1, K_1, d are taken to be 10% as explained in SN2013, whereas $\dot{f}$ is taken to have an accuracy of $\sim 0.1\%$ as measured from the timing eclipses J0651 (see Sect. 4). Our method of combining each set of EM data with that of the GW data (i.e. amplitude $\mathcal{A}$ and inclination) is described in SN2013 and here we will summarize the advantage of including $\dot{P}_{\rm orb}$ for each of the scenarios discussed in the earlier paper. Each of the scenarios below include GW measurements $\mathcal{A}$, ι of J0651 system as a function of its inclination. We also assume the GW frequency of the source is known exactly since its relative uncertainty from GW observation for J0651 system is 10^{-7}Hz.

1. Scenario 0: GW data + $\dot{f}$ vs. GW data only In SN2013 we found that distance can be estimated using GW amplitude. The chirp mass in this case was simply estimated for WDs using uniform distributions of the masses ($m_i \,\epsilon\, [0.1, 1.4] M_\odot$) which is shown in grey in the top-left panel of Figure 5.4. The 95 percentile in distances as a function of inclination are shown in the bottom-left panel in grey. Adding EM data of $\dot{f}$ with 0.1% accuracy will constrain the 95 percentile in $\mathcal{M}_c$ to a much better accuracy of 0.11% compared to the SN2013 which is shown in blue in the top-left panel of Figure 5.4. The medians of these distributions are shown in solid lines and the real value is shown in dashed black line. Hence the distances can be also constrained to much better accuracies shown in blue in the bottom-left panel where we find that the (relative) 95 percentile uncertainties in distances range from 36% to 19% for inclinations of 5° (face-on orientation) to 90° (edge-on orientation) which are significantly better compared to the grey lined found in SN2013.

2. Scenario 1: GW data + $\dot{f}, d$ vs. GW data + d In SN2013 we found that using distance d and $\mathcal{A}$ we could estimate $\mathcal{M}_c$ as a function of inclination where the 95 percentile in $\mathcal{M}_c$ fared better at higher inclinations with $\sim 16\%$ and worse at lower inclinations. As shown above, adding EM data from $\dot{f}$ already constrains $\mathcal{M}_c$ much better to 0.11% for all inclinations. Thus adding EM data on d does not add much unless both d and $\mathcal{A}$ are known to better accuracies that $\dot{f}$.

3. Scenario 2a: GW data + $\dot{f}, m_1$ vs. GW data + m_1 n SN2013 we found that combining EM data on m_1 with GW $\mathcal{A}$ provided an estimate of the secondary mass m_2 and constraints on the distance as a function of inclination. The distribution of m_2 (which is simply solved using grey distribution in $\mathcal{M}_c$ in the top-left panel) is shown also in

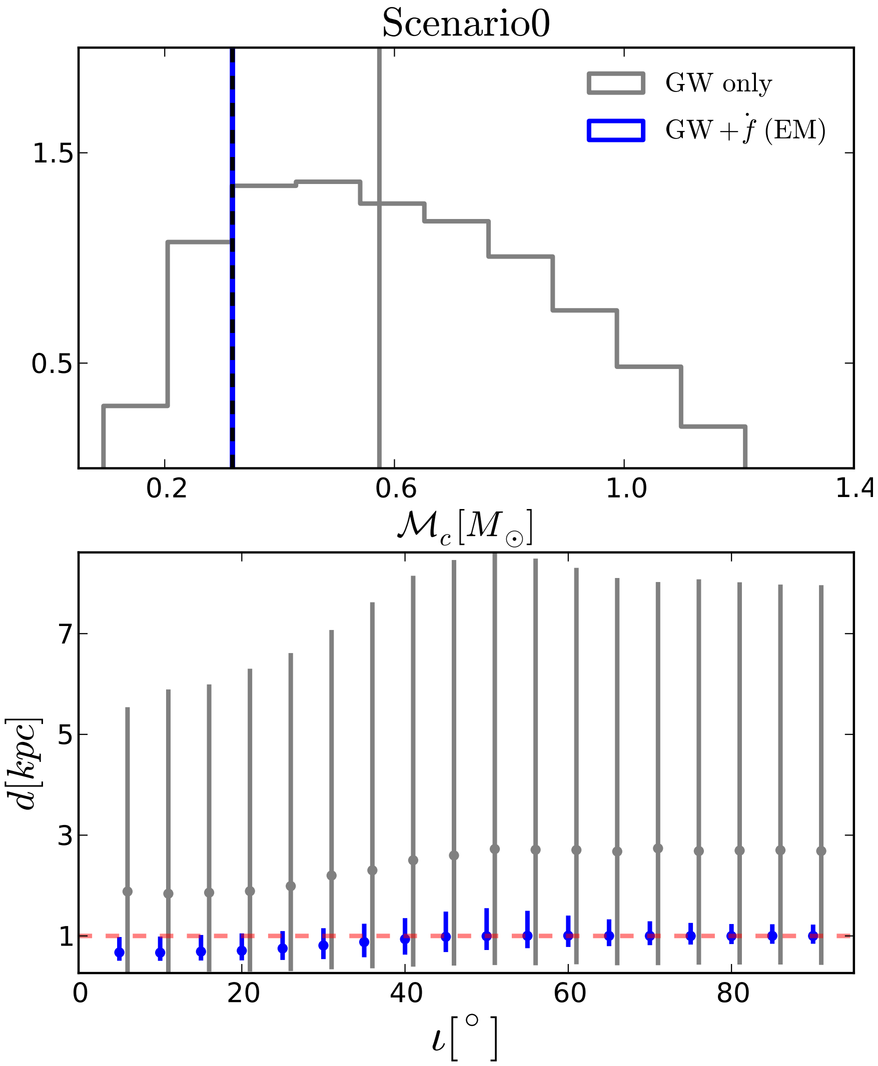

Figure 5.4: Constraints in the binary parameters of J0651 given by complementing GW observations with EM data for three scenarios. *Scenario 0*: comparison of $\mathcal{M}_c$ and 95 percentile uncertainties in d as a function of inclination with EM data on $\dot{f}$ (shown in blue) versus GW data only (shown in grey). The vertical (grey and blue) lines are distribution medians and vertical dashed line is the *real* value of the system and the (red) horizontal is the *real* value of the source parameter.

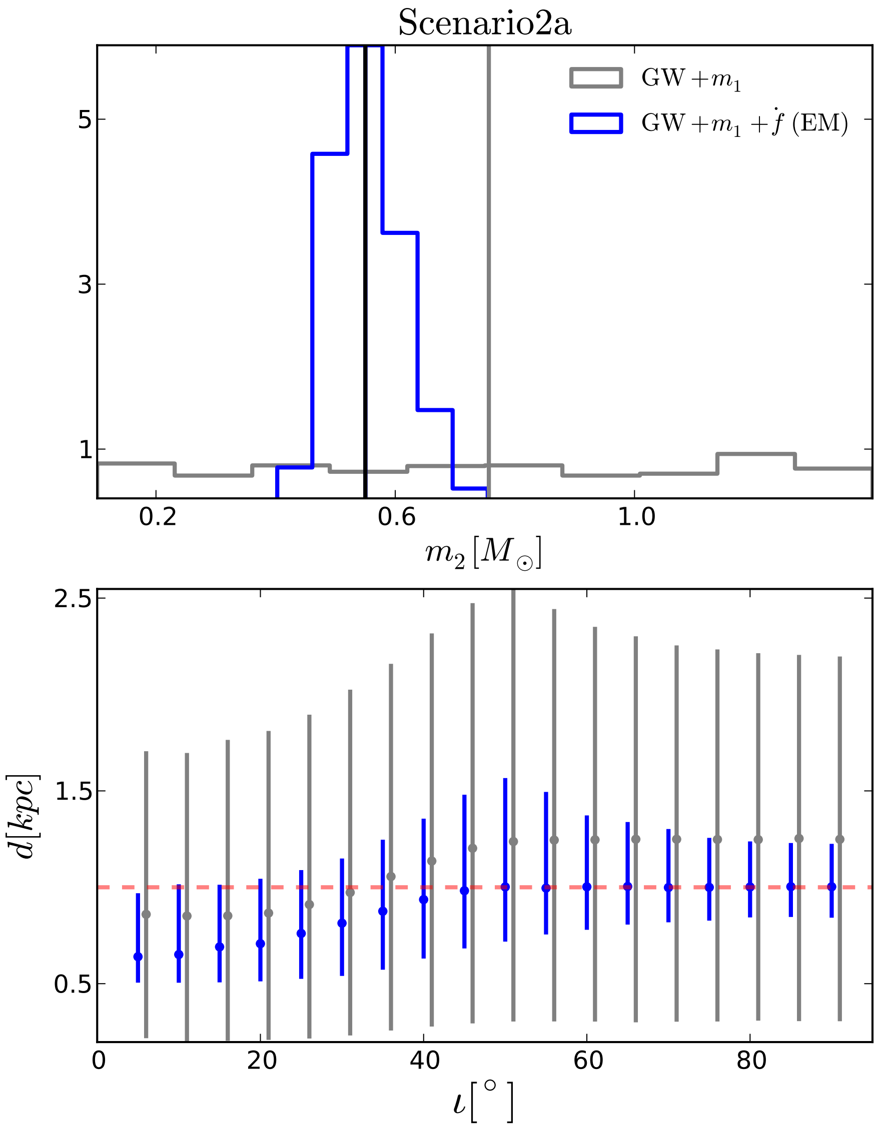

FIGURE 5.5: Constraints in the binary parameters of J0651 given by complementing GW observations with EM data for three scenarios. *Scenario 2a*: comparison of m_2 and d with EM data on $\dot{f}, m_1$ (shown in blue) versus GW data + m_1 only (shown in grey). The vertical (grey and blue) lines are distribution medians and vertical dashed line is the *real* value of the system and the (red) horizontal is the *real* value of the source parameter.

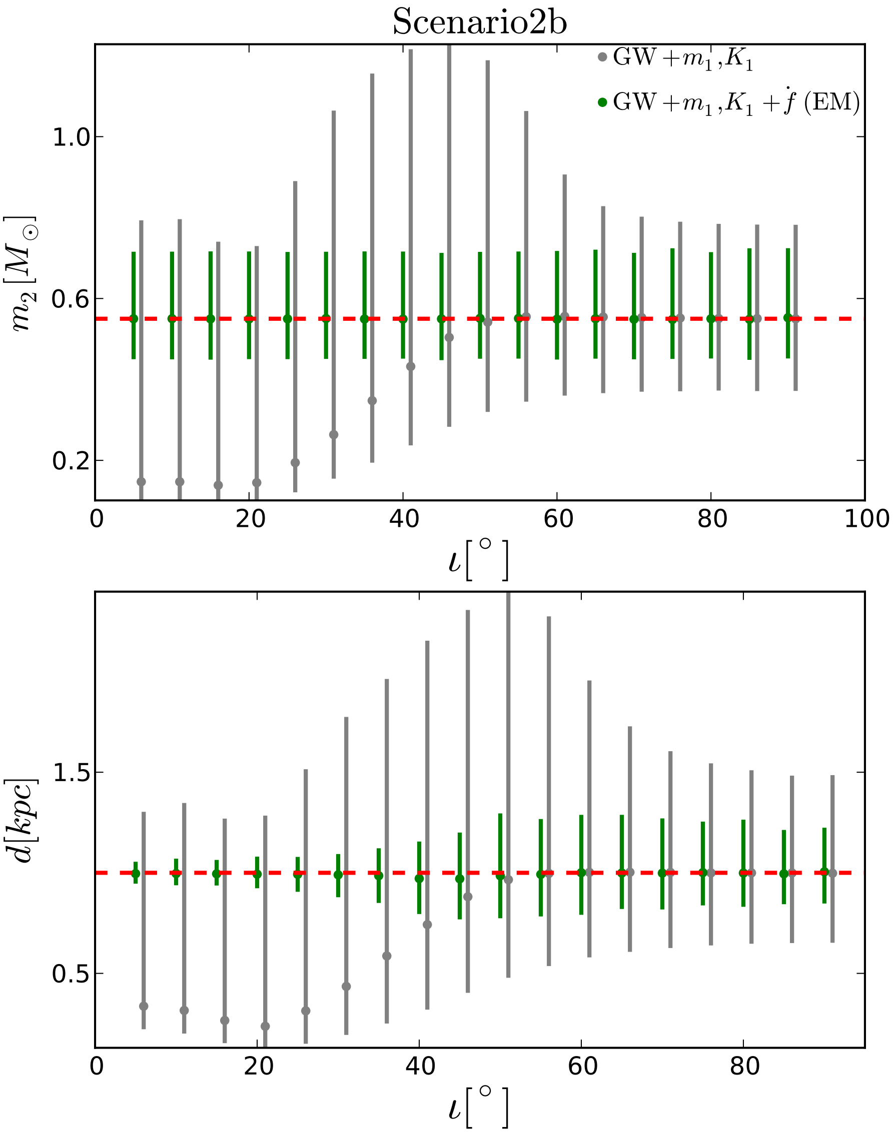

Figure 5.6: Constraints in the binary parameters of J0651 given by complementing GW observations with EM data for three scenarios. *Scenario 2b*: comparison of the same with added information of K_1 for both cases which are shown in green. As expected adding $\dot{f}$ improves the distance estimates significantly in all three cases when compared to the corresponding cases address in SN2013. The vertical (grey and blue) lines are distribution medians and vertical dashed line is the *real* value of the system and the (red) horizontal is the *real* value of the source parameter.

grey in the top-middle panel of the figure. The 95 percentiles in d using this m_2 and $\mathcal{A}$ are shown in grey in the bottom-middle panel. Adding EM data of $\dot{f}$ will improve the accuracy of m_2 reducing the 95 percentile uncertainty to 25% accuracy owing to a very accurate $\mathcal{M}_c$ (as discussed above). This reduced distribution in this m_2 is shown in blue in the top-middle panel. This m_2 in combination with the GW $\mathcal{A}$ constrains the distance with better accuracies compared to SN2013 whose 95 percentiles are also shown as a function of inclination in blue lines in the bottom-left panel of the Figure. Thus adding $\dot{f}$ in this scenario improves m_2 and d significantly.

4. Scenario 2b: GW data + $\dot{f}, m_1, K_1$ vs. GW data + m_1, K_1 In SN2013 we found that combining single-line spectroscopic data, i.e. m_1, K_1 with the GW $\mathcal{A}$ constrained both the m_2 and d as a function of inclination whose 95 percentiles are shown in grey in top-right and bottom-right panels of Figure 5.4 respectively. Here we find that adding $\dot{f}$ will improve both of these quantities significantly whose respective 95 percentiles are shown in green lines. To explain these improvements we briefly explain how these quantities are estimated. As explained in the case above we have an accurate constraint on m_2 using m_1 and $\mathcal{M}_c$. Using the GW inclination and the masses we compute the radial velocity at each inclination, K_{GW}. At each inclination K_{GW} is compared against the measured K_1. Using the observed distribution selecting a subset of K_{GW} with a probability distribution of K_1 constrains a subset in the rest of the parameters: $m_1, m_2, \mathcal{A}, d$ even further. The reduced uncertainties in m_2, d calculated in this way are are shown in green in the top-right and bottom-right panels of the Figure. The method described is akin to Scenario 2c discussed in SN2013 in detail. Thus adding EM data of $\dot{f}$ to m_1, K_1 improves the distance estimates significantly especially at lower inclinations. We find the (relative) 95 percentile in m_2 range from $25\% - 17\%$ for face-on to edge-on systems. And the same for d range from $6\% - 19\%$.

5. Scenario 3: GW data + $\dot{f}, m_{1,2}, K_{1,2}$ vs. GW data + $m_{1,2}, K_{1,2}$ In SN2013 we found that combining $m_{1,2}$, $K_{1,2}$ with GW data improves the $\mathcal{A}, \iota$ especially for lower inclination systems and this in turn constrains the distance of the binary (to roughly 30%). Those distances can be compared with the independent estimate of the same using $\dot{f}$ explained above in Scenario 0. Since $m_{1,2}$ are considered to have 10% accuracies much larger than 0.1% accuracy in $\dot{f}$, the chirp mass is still better determined in the case where $\dot{f}$ is known and thus adding information from $m_{1,2}$, $K_{1,2}$ does not improve the constraint in distance any further.

5.6 Conclusion

We investigated the feasibility of detecting tides in detached (white-dwarf) binaries from eLISA detector by calculating uncertainties of the parameters, $\dot{f}, \ddot{f}$ as a function of the orbital frequency. We implement Fisher-matrix methods to compute the GW parameters uncertainties and compares them with the accuracies from the mid-eclipsing timing measurements where the observation length is taken to be $\geq$10 years. We also study the quantitative improvements in binary parameters when an EM data on $\dot{P}_{\rm orb}$ is combined with GW data and other possible sets of EM data. From our analyses of J0651 and higher mass systems (see Table 1), we conclude:

1. Unless eLISA can discover systems like the high-f binary, GW data alone will not suffice in measuring $\dot{f}, \ddot{f}$ precisely enough for a system like J0651. However finding such high-f binaries near by ($\leq$ 1kpc) is very unlikely.

2. Eclipse timing measurements for 10 years for J0651-like systems will provide a very precise measurement of $\dot{f}$ to less than 1%. However, measuring a 2-5% contribution from tides in $\dot{f}$ for such binaries is *only* possible if the $\mathcal{M}_c$ and/or d are also known to $\sim$ 1% accuracies. Additionally detecting a collective phase shift in the GW phase using *only* GW data for J0651 as has been suggested [Fuller & Lai, 2012] is not possible.

3. For systems driven by *only* GW radiation, an EM measurement of $\dot{f}$ combined with GW measurement of $\mathcal{A}$ provides us a very precise measurement of $\mathcal{M}_c$. We compare this to our previous study in SN2013 where we computed improvement in binary parameters for the case of J0651 as a function of its inclination. We find that $\dot{f}$ can constrain m_2 and d more accurately when considering various scenarios where EM data on m_1, K_1 are known. We find that knowing only $\dot{f}$ constrains the 1-sigma in $\mathcal{M}_c$ to $0.3179 \pm 0.0002 M_\odot$. This further constrains d from $0.70^{0.95}_{0.46}$kpc (face-on) to $1.00^{1.32}_{0.70}$kpc (edge-on). Adding EM data on m_1 constrains the m_2 to $0.55^{0.62}_{0.49} M_\odot$. Finally adding EM data on m_1, K_1 constrains distance from $1.00^{1.03}_{0.96}$kpc (face-on) to $1.00^{1.10}_{0.91}$kpc (edge-on). We conclude that compared to the scenarios in SN2013 our knowledge of the chirp mass, secondary mass and the distance improve significantly when the eclipse timing measurements in $\dot{f}$ will be included in the GW-EM synergy.

Acknowledgements
This work was supported by funding from FOM.

5.A Variance-covariance matrixes of J0651, and B2

We have listed the VCM matrices for the binary systems that we used in our analysis. There are 9 parameters that described them which are listen in the first row of the matrices below and for each binary, the values are listed in the row with θ_i. The diagonal elements are the absolute uncertainties in each the 9 parameters and the off-diagonal elements are the normalized correlations, i.e. c$_{ii} = \sqrt{\mathcal{C}_{ii}} \equiv \sigma_i$, c$_{ij} = \frac{\mathcal{C}_{ij}}{\sqrt{\mathcal{C}_{ii}\mathcal{C}_{jj}}}$. The strong correlations between parameters (i.e. whose magnitudes are âĽě 0.7) are marked in bold in the VCMs below.

VCM 1: J0651, S/N $\sim$ 13.

$$\begin{array}{l|ccccccccc}
 & \mathcal{A} & \phi_0 & \cos\iota & f & \dot{f} & \ddot{f} & \psi & \sin\beta & \lambda \\
\theta_i & 1.67\times10^{-22} & \pi & 0.007 & 2.61\times10^{-3} & -3.35\times10^{-17} & 1.57\times10^{-30} & \pi/2 & 0.01 & 1.77 \\
\hline
\mathcal{A} & 1.586\times10^{-23} & -0.0 & 0.0 & 0.01 & -0.01 & -0.0 & 0.02 & 0.03 & -0.06 \\
\phi_0 & & 0.364 & -0.01 & \mathbf{-0.91} & \mathbf{0.82} & -0.01 & 0.01 & 0.11 & 0.08 \\
\cos\iota & & & 0.044 & 0.01 & -0.01 & 0.0 & -0.01 & 0.07 & -0.33 \\
f & & & & 3.807\times10^{-9} & \mathbf{-0.98} & 0.01 & -0.01 & -0.08 & -0.15 \\
\dot{f} & & & & & 1.059\times10^{-16} & -0.04 & 0.01 & 0.04 & 0.19 \\
\ddot{f} & & & & & & 1.047\times10^{-26} & 0.0 & 0.0 & 0.08 \\
\psi & & & & & & & 0.041 & -0.02 & 0.05 \\
\sin\beta & & & & & & & & 0.069 & 0.08 \\
\lambda & & & & & & & & & 0.019
\end{array}$$

VCM 3: high-frequency binary, S/N $\sim$ 135.

$$\begin{array}{l|ccccccccc}
 & \mathcal{A} & \phi_0 & \cos\iota & f & \dot{f} & \ddot{f} & \psi & \sin\beta & \lambda \\
\theta_i & 3.698\times10^{-22} & 3.666 & -0.331 & 17.695\times10^{-3} & 1.988\times10^{-13} & 8.191\times10^{-24} & 1.97 & 0.685 & 5.411 \\
\hline
\mathcal{A} & 5.02\times10^{-24} & -0.15 & \mathbf{0.79} & 0.05 & -0.05 & 0.05 & 0.28 & 0.29 & -0.21 \\
\phi_0 & (0.0136) & 0.048 & -0.07 & \mathbf{0.87} & \mathbf{0.82} & \mathbf{-0.76} & -0.36 & -0.26 & 0.02 \\
\cos\iota & & & 0.008 & 0.07 & -0.06 & 0.05 & 0.04 & 0.39 & -0.07 \\
f & & & & 8.228\times10^{-10} & \mathbf{-0.98} & \mathbf{0.92} & -0.02 & 0.24 & 0.22 \\
\dot{f} & & & & (4.65\times10^{-8}) & 5.169\times10^{-17} & \mathbf{-0.98} & -0.0 & -0.27 & -0.17 \\
\ddot{f} & & & & & (2.6\times10^{-4}) & 1.4476\times10^{-24} & 0.02 & 0.30 & 0.14 \\
\psi & & & & & & (0.176) & 9.86\times10^{-3} & -0.09 & -0.58 \\
\sin\beta & & & & & & & & 2.5\times10^{-4} & 0.14 \\
\lambda & & & & & & & & & 4.1\times10^{-4}
\end{array}$$

Chapter 6

The role of spin in the mass measurements of neutron star-black hole and low mass binary black hole systems

S. Shah, S. Bose & G. Nelemans

in prep. 2014

Abstract

In this paper we investigate the parameter uncertainties of spin-aligned inspiraling binaries comprising of neutron stars (NS) and black holes (BH) which are one of the main target sources of the advanced ground-based gravitational wave (GW) detectors. In particular we want to understand the effect of spins in the binaries on the parameter uncertainties of the mass parameters and whether spinning systems will have any effect in telling NSBH systems apart from binary BH (BBH) systems at lower masses where their chirp masses are similar. In this study using Fisher methods we find that having one or two spinning objects influences the mass parameters significantly. For inspiraling GW signals the spinning systems worsen the parameter uncertainties of total mass and the symmetric mass ratio relative to a non-spinning system. However if only one of the masses is spinning then these uncertainties reduce giving smaller ranges in the individual masses. For instance, if only the BH is spinning (with a magnitude of 0.99) in an NSBH system then the errors in total mass and the ratio reduce by $\sim 50\%$ at signal-to-noise ratio of ~ 20. These findings are

comparable to some of the example cases studied in the literature. We also find that for systems with the same total mass and symmetric mass ratio, we may distinguish a BBH from an NSBH system if both the BHs have large spin. This is due to to the fact that there is a small error in the spin for BBH which is not the case for NSBH system. However if the BH has low spin it will be hard to distinguish the two types of binaries with GW data alone and will require an electromagnetic counterpart from the NS in the binary.

6.1 Introduction

In a couple of years gravitational waves (GW) from compact binaries made of neutron stars (NS) and/or black holes (BH) will be directly detected [Phinney, 1991; Abadie et al., 2010]. The ground-based GW interferometers LIGO[1] and Virgo[2] are being currently upgraded and in $\sim$ 2016 it is expected that they will reach sensitivities sufficient to make the GW detections. One of the most well studied sources are compact binaries made of NS and/or a BH making them main target sources for these GW interferometers. Besides the fact that by directly detecting GWs we can start testing Einstein's general theory of relativity (GR), the new way of observing the Universe will bring us into a new era of studying astrophysical systems. The observations of compact binaries made of NS and BH will be crucial in understanding the stellar evolution processes and the physics of the formation of compact objects in our Universe [e.g. Dominik et al., 2012]. The implications of measuring binary parameters (especially their individual masses, stellar radii and binary separation) to good precision is huge for understanding the physics of stellar processes such as close binary interactions [Lorimer, 2005] for the equation of state of nuclear dense matter [Lattimer & Prakash, 2010] and whether there is a physical mass gap between NS and BH [Özel et al., 2010]. Given the importance of the measurement of masses there have been numerous studies determining the parameter uncertainties from GW observations [e.g. Cutler & Flanagan, 1994; Poisson & Will, 1995; Arun et al., 2005; Ajith & Bose, 2009; Nissanke et al., 2010; Hannam et al., 2013]. The fact that GW signals from the binary systems can be modelled very accurately and are parametrisable by combining a variety of analytical and numerical approaches in general relativity has allowed several studies in parameter estimates of binary NS systems (BNS), NSBH systems and BBH systems allowing for spins.

The GW signals from the above mentioned coalescing objects consist of *inspiral, merger and ring-down* stages. In this study we concern ourselves with only the inspiraling GW waveforms which is the stage that dominates the number of cycles for lower mass binary systems ($M \leq 12M_{\odot}$) [Buonanno et al., 2009]. In computing the GW signal of such a two-body problem, in this phase, is well modelled by the so-called post-Newtonian (pN)

---

[1] www.ligo.caltech.edu/

[2] www.ego-gw.it/

approximation to general relativity (GR) [e.g. Blanchet, 2002] where the objects are well separated and relatively slowly moving (i.e. $v/c \ll 1$). This method is a perturbative approximation to Einstein's equation in GR. More accurate methods like BH perturbation theory or numerical relativity are required to model the later stages of the binary coalescence. From the GW inspiral signal, it is well known that the GW phasing depends to leading pN order on the chirp mass, $\mathcal{M}_c = (m_1 m_2)^{3/5}/M^{1/5}$ where m_i is the individual mass and $M = m_1 + m_2$ is the total mass of the system. Hence, $\mathcal{M}_c$ will be the most accurately determined parameter from the GW signal. To obtain the individual masses however, we also need to measure the symmetric mass ratio $\eta = m_1 m_2/M^2$ which depends on the GW phasing at higher pN orders and therefore is not as accurately measured. Furthermore, if the binary component has a spin which is the angular momentum of each of the masses $\chi_i = J_i/m^2$ the parameter accuracies become worse due to the a strong correlation between the parameters M and χ. Poisson & Will [1995] showed that including spins of the compact objects in the GW data analysis worsens the parameter uncertainties by factor of 10. This was for the case where GW inspiraling waveforms were derived to 2.5 pN order where the 2.5 refers to the power of the velocity (i.e. v^5) of the system in pN expansion of the energy and flux expressions for the binary. The current state-of-the-art is that the energy function has been solved up to 3pN (v^6) order and the flux function to 3.5 (v^7) order [e.g. Blanchet et al., 2005; Arun et al., 2009]. With the improving accuracies with which the inspiral can be modelled, it has also been shown that including these higher order pN terms in the GW phase expression for non-spinning binary systems improves the parameter uncertainties [Arun et al., 2005].

In this paper we wish to globally analyse the parameter uncertainties of lower mass compact binaries where the BH may have spins alined with that of the binary orbit and study how the spin influences these uncertainties for a single detector case. We also want to study how well we can distinguish an NSBH from a low mass BBH (if they have similar chirp masses) and determine how useful the electromagnetic (EM) observations of the two systems will be. A number of studies have investigated the role of (anti-)aligned spins (in many of the references above) however, a lot of these studies have focused in Bayesian-based MCMC parameter estimation [e.g. van der Sluys et al., 2008; Rodriguez et al., 2013] which limits the number of systems that can be studied to a few as these methods are computationally expensive. The role of (aligned or precessing) spins has yet to be rigorously studied in the parameter estimation of binary systems in understanding the systematics of ignoring spin, including higher order spins for various masses and etc. In this paper we explore the role of spins in lower mass systems taking into account the high order GW signals and the spin terms. This paper is organised as follows: Section 6.2 presents the spinning waveforms used for the inspiral part of the waveform and the implementation of the Fisher method to get the parameter uncertainties. Section 6.3 presents the results on low mass NSBH and BBH binaries where the BH can be (non-)spinning and whether we will be able to distinguish an NS from a BH of similar mass from advanced LIGO data.

Finally Section 6.4 presents the limitations of this work, future work and conclusions.

6.2 Spinning Waveforms and parameter estimation

In this section we introduce the GW waveforms that take the spins of both the masses into account whose energy and flux functions can be found in Ajith [2011]; Arun et al. [2009]. We also summarise our implementation of the Fisher method in extracting the parameter uncertainties for NSBH and BBH systems where the NS can have large mass and BH can have low mass making it hard to distinguish the two systems (as their chirp masses would be similar). The spin effects in the case of (anti-)aligned systems are parametrised by χ_s and χ_a related to the individual spin of the binary components by $(\chi_1+\chi_2)/2$, $(\chi_1-\chi_2)/2$ respectively. The time-domain waveforms are transformed to Fourier domain GW signals in an analytical way using the stationary phase approximation:

$$\tilde{h}(f;\chi_1,\chi_2) = A(f)e^{-i[2\pi f t_0+\Psi_0+\Psi(f)-\pi/4]}, \tag{6.1}$$

where the amplitude, $A(f)$ is

$$A(f) = \mathcal{C}\frac{2\eta M}{d}v^2\left[\frac{dF(v)}{dt}\right]^{-1/2}, \tag{6.2}$$

where d is the luminosity distance of the source and M is total mass. The keplerian v is related to M by $v=(\pi M f)^{1/3}$ and $F(v)$ is the instantaneous GW frequency. The pre-factor $\mathcal{C} = 1/2\sqrt{(1+\cos^2\iota)^2F_+^2+4\cos^2\iota F_\times^2}$, depends on the inclination ι of the binary relative to the detector and the antenna sensitivities to the plus + and the cross × polarisations of the incoming GW signal. In this paper we consider optimally oriented sources for a single detector which implies $\mathcal{C}=1$. The time of arrival of the signal and corresponding phase are given by t_0 and Ψ_0 respectively.

The expression of $\Psi(f)$ which has been derived to 3.5pN order Poisson & Will [1995]; Arun et al. [2009]; Ajith [2011] and is given by:

$$\Psi(f) = \frac{3}{128\eta v^5}\left[1+\sum_{i=2}^{7} vi\right] \tag{6.3}$$

$$v2 = v^2\left(\frac{55}{\eta}+\frac{3715}{756}\right) \tag{6.4}$$

$$v3 = v^3(4\beta-16\pi) \tag{6.5}$$

$$v4 = v^4\left(\frac{3085\eta^2}{72}+\frac{27145\eta}{504}+\frac{15293365}{508032}-10\sigma\right) \tag{6.6}$$

$$v5 = v^5\left(\frac{38645\pi}{756}-\frac{65\pi\eta}{9}-\gamma\right) \tag{6.7}$$

$$v6 = v^6\left(-\frac{6848\gamma_E}{21} - \frac{12785\eta^3}{1296} + \frac{76055\eta^2}{1728} + \frac{2255\pi^2\eta}{12} + \frac{15737765635\eta}{3048192}\right) \\ -v^6\left(\frac{640\pi^2}{3} + c1 - \frac{6848\ln(4v)}{21}\right), \tag{6.8}$$

where $c1 = \frac{1158231236531}{4694215680}$.

$$v7 = v^7\left(-\frac{74045\pi\eta^2}{756} + \frac{378515\pi\eta}{1512} + \frac{77096675\pi}{254016}\right) \tag{6.9}$$

From the higher order corrections to the derivative of the instantaneous frequency dF/dt we can also write the 3.5pN expression for the amplitude which is given by:

$$A(f) = \frac{M^{5/6}}{d\pi^{2/3}}\left(\frac{5\eta}{24}\right)^{1/2} f^{-7/6}\left[1 + \sum_{i=2}^{7} vi'\right] \tag{6.10}$$

$$v2' = v^2\left(\frac{11\eta}{8} + \frac{743}{672}\right) \tag{6.11}$$

$$v3' = v^3(\beta/2 - 2\pi) \tag{6.12}$$

$$v4' = v^4\left(\frac{1379\eta^2}{1152}\frac{18913\eta}{16128} + \frac{7266251}{8128512} - \sigma/2\right) \tag{6.13}$$

$$v5' = v^5\left(\frac{57\pi\eta}{16} - \frac{4757\pi}{1344} + \epsilon\right) \tag{6.14}$$

$$v6' = v^6\left(-\frac{856\gamma_E}{105} - \frac{67999\eta^3}{82944} - \frac{1041557\eta^2}{258048} - \frac{451\pi^2\eta}{96} + \frac{10\pi^2}{3} + \frac{3526813753\eta}{27869184}\right) \\ -v^6\left(c2 - \frac{856\ln(4v)}{105}\right), \tag{6.15}$$

where $c2 = \frac{29342493792821}{500716339200}$.

$$v7' = v^7\left(-\frac{1349\pi\eta^2}{24192} - \frac{72221\pi\eta}{24192} - \frac{5111593\pi}{2709504}\right) \tag{6.16}$$

In the above equations,

$$\epsilon = \left(\frac{502429}{16128} - \frac{907\eta}{192}\right)\delta\chi_a + \left(\frac{5\eta^2}{48} - \frac{73921\eta}{2016} - \frac{502429}{16128}\right)\chi_s. \tag{6.17}$$

The terms β, σ, and γ are the leading spin-orbit coupling, spin-spin coupling and next order spin-orbit coupling terms, respectively which are related to χ_s, χ_a by:

$$\beta = \frac{113}{12}\left(\chi_s + \delta\chi_a - \frac{76\eta}{113}\chi_s\right) \tag{6.18}$$

$$\sigma = \chi_a^2\left(\frac{81}{16} - 20\eta\right) + \frac{81\chi_a\chi_s\delta}{8} + \chi_s^2\left(\frac{81}{16} - \frac{\eta}{4}\right) \tag{6.19}$$

$$\gamma = \chi_a \delta \left(\frac{140\eta}{9} + \frac{732985}{2268} \right) + \chi_s \left(\frac{732985}{2268} - \frac{24260\eta}{81} - \frac{340\eta^2}{9} \right) \tag{6.20}$$

For the GW waveform above we compute so-called Fisher matrix for the following parameters: $\vec{\theta} = \{\mathcal{A}, M, \eta, t_0, \Psi_0, \beta\}$ where

$$\mathcal{A} = \frac{M^{5/6}}{d\pi^{2/3}} \sqrt{\frac{5\eta}{24}}. \tag{6.21}$$

As such we present results for the Advanced LIGO detector whose one-sided noise power spectral density (PSD) is given by [3]:

$$S_n(f(x)) = 10^{-49} \left[x^{-4.14} - 5x^{-2} + 111 \left(\frac{1 - x^2 + x^4/2}{1 + x^2/2} \right) \right], \tag{6.22}$$

where x is dimensionless frequency $x = f/f_0$ normalised by $f_0 = 178$Hz. Assuming strong signals and Gaussian noise (as in the previous chapters) the uncertainties in the above parameters, $\delta\vec{\theta}$ and the covariance between them are given by the variance-covariance matrix which is the inverted Fisher matrix. The Gaussian noise implies that the maximum-likelihood estimators $\vec{\theta}$ will fluctuate around their true values [e.g. Vallisneri, 2008] with a random error whose magnitude can be approximated by Fisher method formalism. The Fisher matrix is given by:

$$\Gamma_{ab} = \sum_{i=1}^{N} \left(\partial_a \tilde{h}(f), \partial_b \tilde{h}(f) \right), \tag{6.23}$$

where the inner product between two quantities (x, y) is defined as:

$$(x, y) = 4 \int_0^\infty df \frac{\tilde{x}^*(f)\, \tilde{y}(f)}{S_n(f)}. \tag{6.24}$$

In the equations above, ∂_a denotes the partial derivative with respect to the parameter θ_a. The Fisher element in Eq. 6.23 is derived by computing analytical derivatives of $\tilde{h}(f)$ in the Eqs. 6.3,6.10 and substituting in Eq. 6.23 which can be shown to be:

$$\Gamma_{ab} \simeq 4 \int_{f_{\rm cut}}^{f_{\rm low}} df \; \frac{\partial_a A(f) \partial_b A(f) + A^2(f) \partial_a \Psi(f) \partial_b \Psi(f)}{S_n(f)}. \tag{6.25}$$

The $f_{\rm low}$ is for Advanced LIGO is taken to be 10 Hz and $f_{\rm cut}$ is determined by the frequency at which the merger of the binary takes over. It is typically given by the innermost stable circular orbit.

6.3 Results

In the following subsections we present results for binary parameters for various cases. First we analyse the errors in the mass parameters, distance and time-of-arrival for binary

---

[3] LSC Algorithms Library: http://www.lsc-group.phys.uwm.edu/daswg/projects/lal.html

NSBH/BBH for total mass ranging from $1 - 200 M_{\odot}$. We compare the errors for a number of different pN GW waveforms with and without spins and also include a comparison with GW waveforms constructed from phenomenological waveforms [Ajith & Bose, 2009]. Then we consider the NSBH systems where the BH may or may not have a spin aligned to the orbit and compare the errors in mass parameters for the case where the BH has spins versus where the BH has no spin for various mass ratios and total masses. Finally we pick a binary system that could be composed of a high mass NS and a low mass BH or both components could be low mass BH and try to determine whether spinning GW waveforms that includes 3.5pN orders in both phase and amplitude can distinguish the two components from the GW observations from advanced LIGO. We also will discuss the implication and usefulness of having EM knowledge on the NS in the NSBH binary in telling apart an NSBH system from a low mass BBH system whose M and $\mathcal{M}$ are similar. We make comparisons with the results in the literature.

6.3.1 Parameter uncertainties versus total mass

We present results for binary parameter errors using Fisher matrix information for a single GW detector, Advanced LIGO. We compute uncertainties in $\vec{\theta} = \{\mathcal{A}, M, \eta, t_0, \Psi_0, \beta\}$ i.e. 6×6 variance-covariance matrix. The errors in chirp mass $\mathcal{M}_c$ and distance d can be propagated from total mass M, symmetric mass ratio η and $\mathcal{A}$ using the covariances between them as follows:

$$\left(\frac{\delta\mathcal{M}_c}{\mathcal{M}_c}\right)^2 = \left(\frac{\delta M}{M}\right)^2 + \frac{9}{25}\left(\frac{\delta\eta}{\eta}\right)^2 + \frac{6}{5}\mathcal{C}_{\mathcal{M}\eta}\left(\frac{\delta M}{M}\right)\left(\frac{\delta\eta}{\eta}\right) \tag{6.26}$$

$$\begin{aligned}\left(\frac{\delta d}{d}\right)^2 = \frac{25}{36}\left(\frac{\delta M}{M}\right)^2 + \frac{1}{4}\left(\frac{\delta\eta}{\eta}\right)^2 + \left(\frac{\delta\mathcal{A}}{\mathcal{A}}\right)^2 + \frac{5}{6}\mathcal{C}_{M\eta}\left(\frac{\delta M}{M}\right)\left(\frac{\delta\eta}{\eta}\right) \\ -\frac{5}{3}\mathcal{C}_{M\mathcal{A}}\left(\frac{\delta M}{M}\right)\left(\frac{\delta\mathcal{A}}{\mathcal{A}}\right) \\ -\mathcal{C}_{\mathcal{A}\eta}\left(\frac{\delta\mathcal{A}}{\mathcal{A}}\right)\left(\frac{\delta\eta}{\eta}\right)\end{aligned} \tag{6.27}$$

In figure 6.1 relative errors in percentage for the parameters M, η, $\mathcal{M}_c$ are plotted as a function of total mass at a distance of 1Gpc. In Figure 6.2, errors in t_0, d, and signal-to-noise ratio (SNR) are plotted and finally in Figure 6.3 the absolute error in the spin parameter β is plotted. For all the results we compute the 5×5 Fisher matrix for the following parameter uncertainties in M, η, t_0, Ψ_0, $\mathcal{A}$ and keep the spins χ_1, χ_2 to 0 which means that the spin parameters β, σ, γ are consequently 0. Thus all the results below are for GW signal expressions that neglect spin parameters with one exception where the leading 1.5pN order spin parameter β is included in the Fisher analysis where we compute 6×6 Fisher matrix for the parameters mentioned above with an additional sixth parameter β (pointed out below). In this case also we take the values of χ_1, χ_2 to be 0. The different line colors

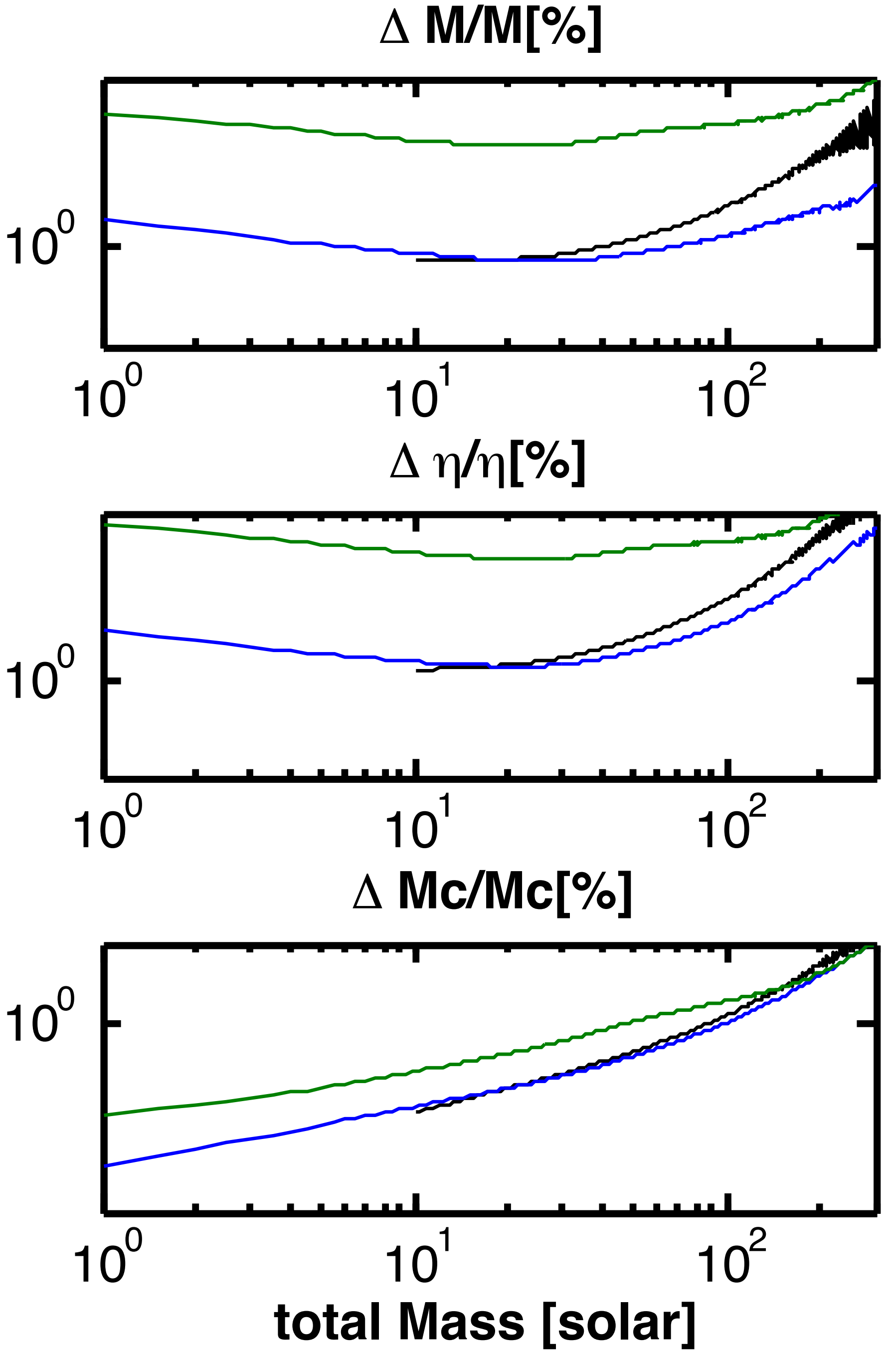

Figure 6.1: Relative uncertainties in percentage of binary parameters of total mass M, symmetric mass ratio η, and chirp mass $\mathcal{M}_c$ of equal mass binaries at lower masses as a function of total Mass. Various line colours are for different approximations of phase and amplitude implemented in the GW waveforms. All the uncertainties are for optimally oriented binaries at a distance of 1 Gpc and for a Advanced LIGO detector noise PSD. The uncertainties in black are for non spinning waveforms where phase is taken from phenomenological inspiral waveforms. Parameter uncertainties in blue are for spin-alined expressions of amplitude and phase that include 3.5 pN expansions and $\chi_{1,2} = 0$. Finally the green lines are for the case where we include the leading **(1.5pN)** order spin-orbit coupling parameter β (see text for explanation and its relation to $\chi_{1,2}$) in the Fisher analysis and $\chi_{1,2} = 0$.

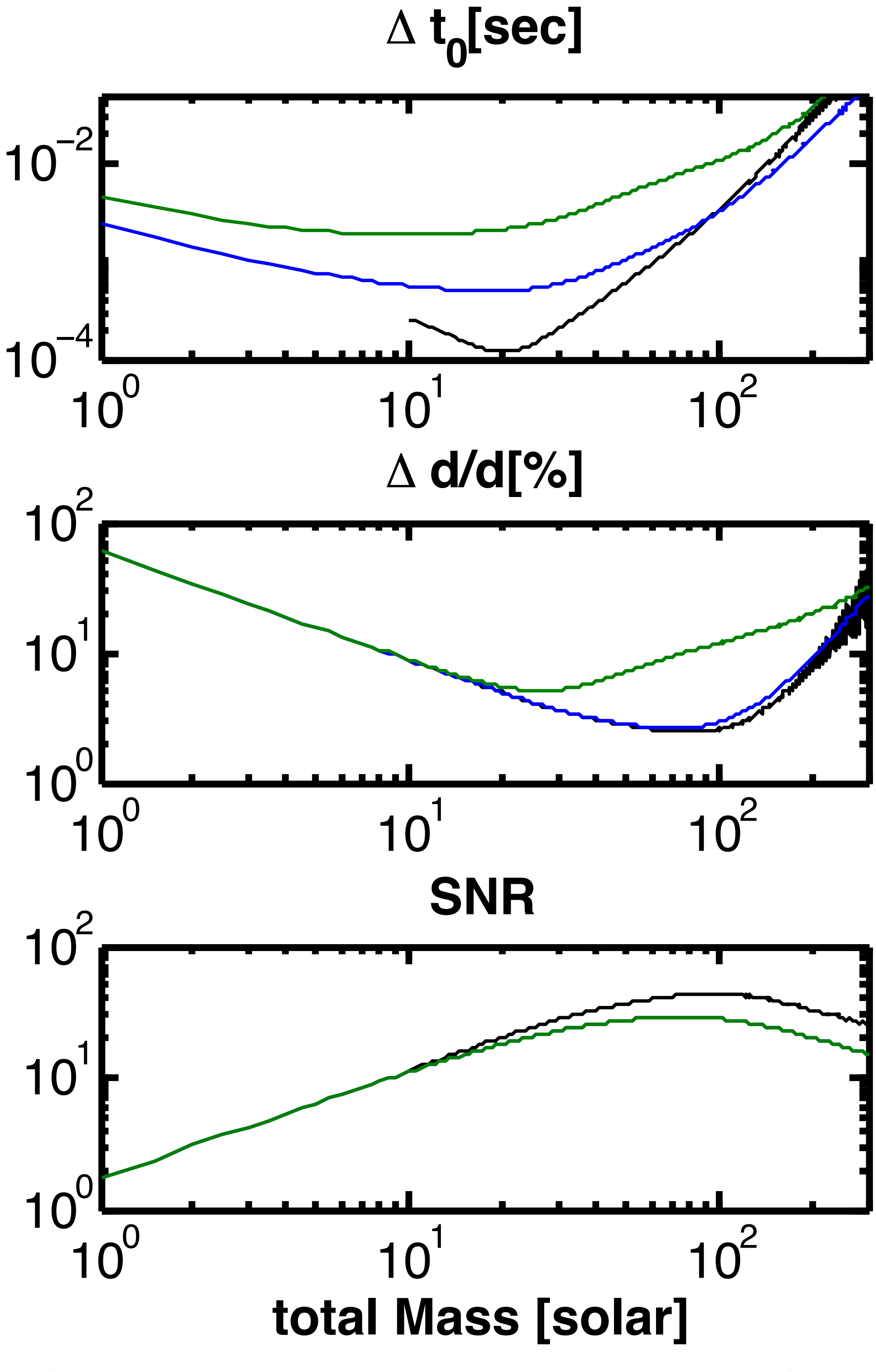

Figure 6.2: Same as in Figure 6.1 but now the uncertainties are shown for time of arrival t_0, distance d and signal-to-noise ratio SNR. All the uncertainties are for binaries with optimal orientation and located at 1Gpc.

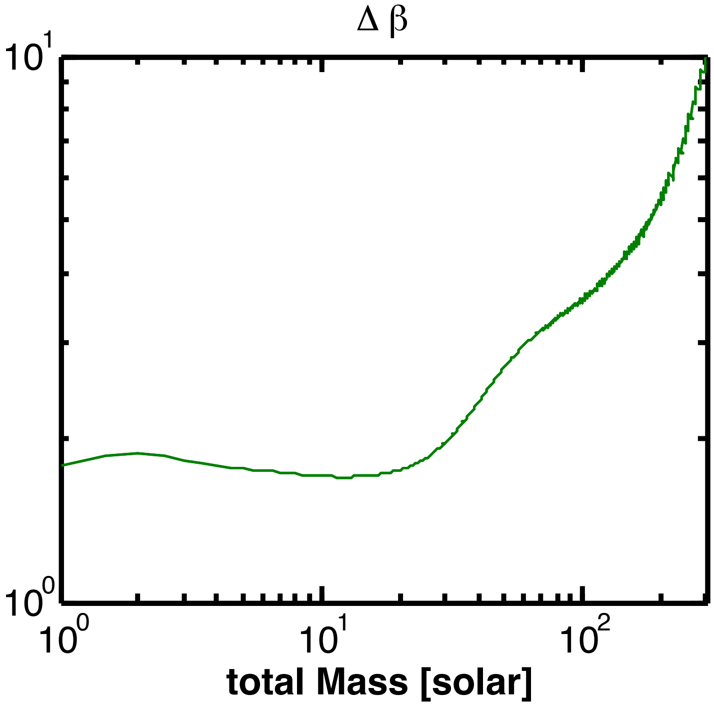

Figure 6.3: Same as in Figure 6.1 but now the uncertainties are shown for spin-orbit coupling parameter β.

represent various considerations in how the phase $\Psi(f)$ and amplitude $A(f)$ of the signal are computed: black – non-spinning phenomenological inspiral-ringdown merger waveforms where the signal is taken up to inspiral part (see Eqs. 2.12, 2.14 in Ajith & Bose [2009]); blue – non-spinning 3.5pN order $\Psi(f)$ and 3.5pN order $A(f)$ from Eqs. 6.3 6.10; green – like previous but the leading order spin-spin coupling parameter β is included in the Fisher analysis. We expect the parameter errors (in black) using non-spinning phenomenological inspiral phase expression to behave very similar with that using the 3.5pN order phase (in blue) and they roughly do. The black lines are only plotted for $M > 10M_{\odot}$ because the coefficients of the phase pN orders computed using phenomenological waveforms in the phase and amplitude expressions used in Ajith & Bose [2009] are valid for $M > 10M_{\odot}$ and may diverge at lower masses. We expect the uncertainty in $\mathcal{M}_c$ to increase with increasing total mass of the system since the number of cycles in the inspiral waveform decrease with increasing mass and this is what is observed in the third pane of Figure 6.1 where the relative errors (for all cases) increase monotonically with increasing mass for waveforms implementing 3.5 pN orders in phase and amplitude. Observe that when the spin parameter β is included in the Fisher analysis the parameter uncertainties in M, η, t_0 become worse (shown in green) by roughly a factor of 10 whereas the uncertainties in the remaining parameters become worse by factors of few. This is not due to SNR because as we can see in the third panel of Figure 6.1, the SNR including β in the Fisher analysis (shown in green) and without (shown in blue) almost overlap and therefore are very similar. This has been observed in previous studies [e.g. Poisson & Will, 1995] which is attributed to the strong correlation between spin and mass ratio: spinning binaries (aligned with orbital angular momentum) inspiral slower -an effect that can be mimicked by a more extreme mass ratio binary with the same total mass [Hannam et al., 2013]. Observe that the minimum in the uncertainties in distance at $M \sim 100 M_\odot$ is due to the SNR which is maximum at that mass as expected. However, the minimum in the error in the total mass and the mass ratio occurs at $M \sim 20 M_\odot$. Below $M \sim 100 M_\odot$ the error in the chirp mass and the SNR compete causing the minimum in σ_M, σ_η: the SNR trend increases the error in the mass ratio whereas the small error in the chirp mass reduces the error in the mass ratio due to its correlation with the chirp mass. Thus, this combination of the SNR and the chirp mass give the minimum in the errors of the mass parameters.

6.3.2 Case A: The effect of a spinning BH on parameter uncertainties in NSBH systems

In this section we show the parameter uncertainties in the lower mass $< 13 M_\odot$ binaries relevant for neutron star-black hole (NSBH) systems and compare uncertainties between cases where the BH is spinning and where the BH is not spinning. In all the following Fisher results we compute the 6×6 Fisher matrix for the parameters M, η, t_0, Ψ_0, $\mathcal{A}$, β where the spin values χ_1, χ_2 are either taken to be 0 or otherwise as mentioned below. In this study we assume that only the BH is spinning. Since NS can also have spins (see Section 6.4) we will include this in future study. In Figure 6.4 the relative uncertainties in total mass M, symmetric mass ratio η, chirp mass and SNR are plotted as a function of total mass and the mass ratio where the BH is considered to be non-spinning. All the parameter uncertainties are for the case where the binary is located at a distance of 1Gpc unless specified. The colour gradient represents the relative error (in percentage) or value of the SNR as specified to the right of each plot. The blue circle on the top of each of the sub panel represents the case where $m_1, m_2 = (2, 3) M_\odot$ where m_1 is NS and m_2 is BH. In the bottom-left panel of Figure 6.4, observe that the uncertainty in $\mathcal{M}_c$ is smaller for more extreme mass ratios at the same total mass, also seen in Ajith & Bose [2009] (see their Figure 2). This is because a smaller η for the same M gives a smaller $\mathcal{M}_c$ (via the relation $\mathcal{M}_c = M\eta^{3/5}$) and and we saw in Section 6.3.1 that the error in chirp mass decreases for smaller chirp mass (i.e. smaller total mass for fixed mass ratio, see bottom panel in Figure 6.1) as the GW signals at lower mass have more cycles. Also observe that the pattern of the colour of the uncertainty in $\mathcal{M}_c$ is different than that of the uncertainties in M, η. Even though the values of errors in M, η for smaller total masses and smaller mass ratios (bottom-left part of the first and second panels in Figure 6.4) are large, the corresponding errors in $\mathcal{M}_c$ are smaller. This is due to the strong anti-correlation between M and η given by the term $\frac{6}{5}\mathcal{C}_{M\eta}\left(\frac{\delta M}{M}\right)\left(\frac{\delta\eta}{\eta}\right)$ in Eq. 6.26. Finally the error in M decreases with increasing M which is also observed previously in Figure 6.1.

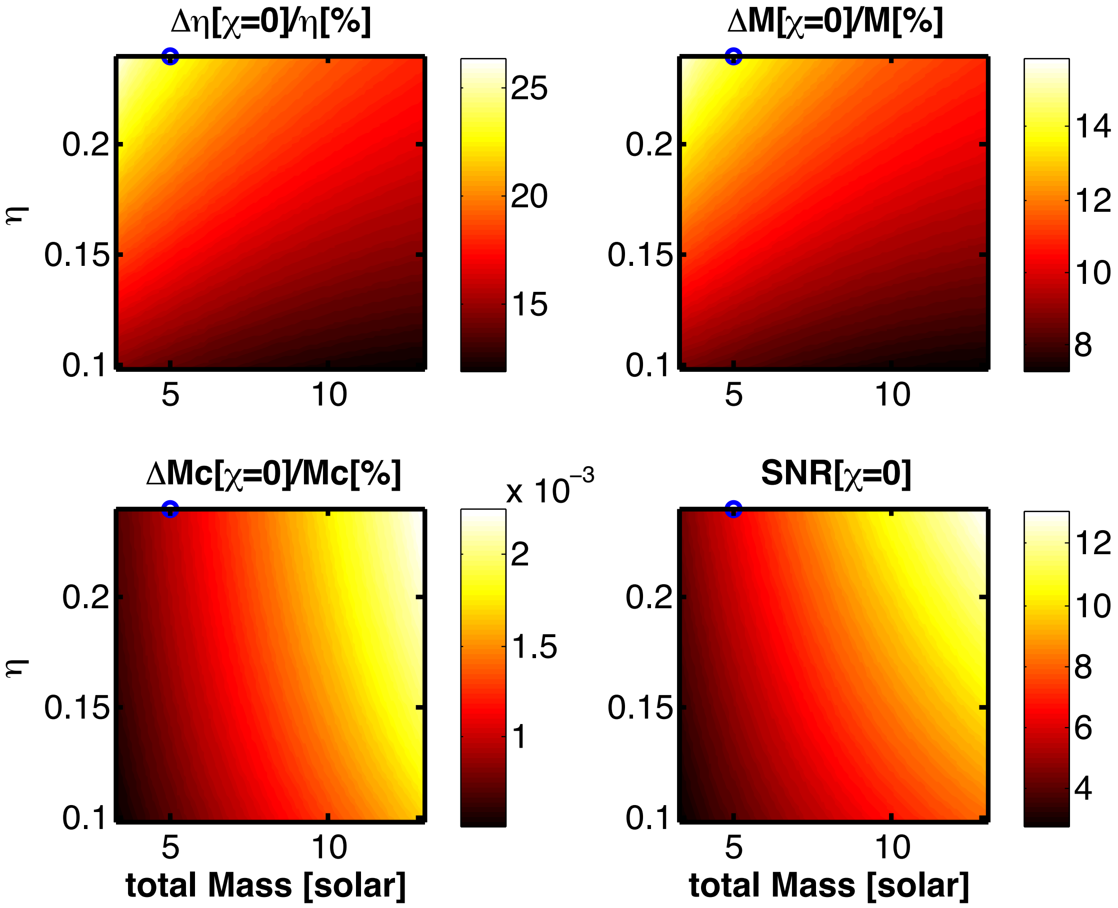

FIGURE 6.4: Relative uncertainties (in percent) in total mass, mass ratio and chirp mass and SNR in total mass and mass ratio space. The blue circle in each panel is the value for $m_1, m_2 = (2, 3)M_\odot$ where m_1 is NS and m_2 is BH and their respective spins are $\chi_1 = 0, \chi_2 = 0$. The colour bar indicates the value of the uncertainty/SNR. The dashed lines represent the space where the NSBH systems have a mass gap.

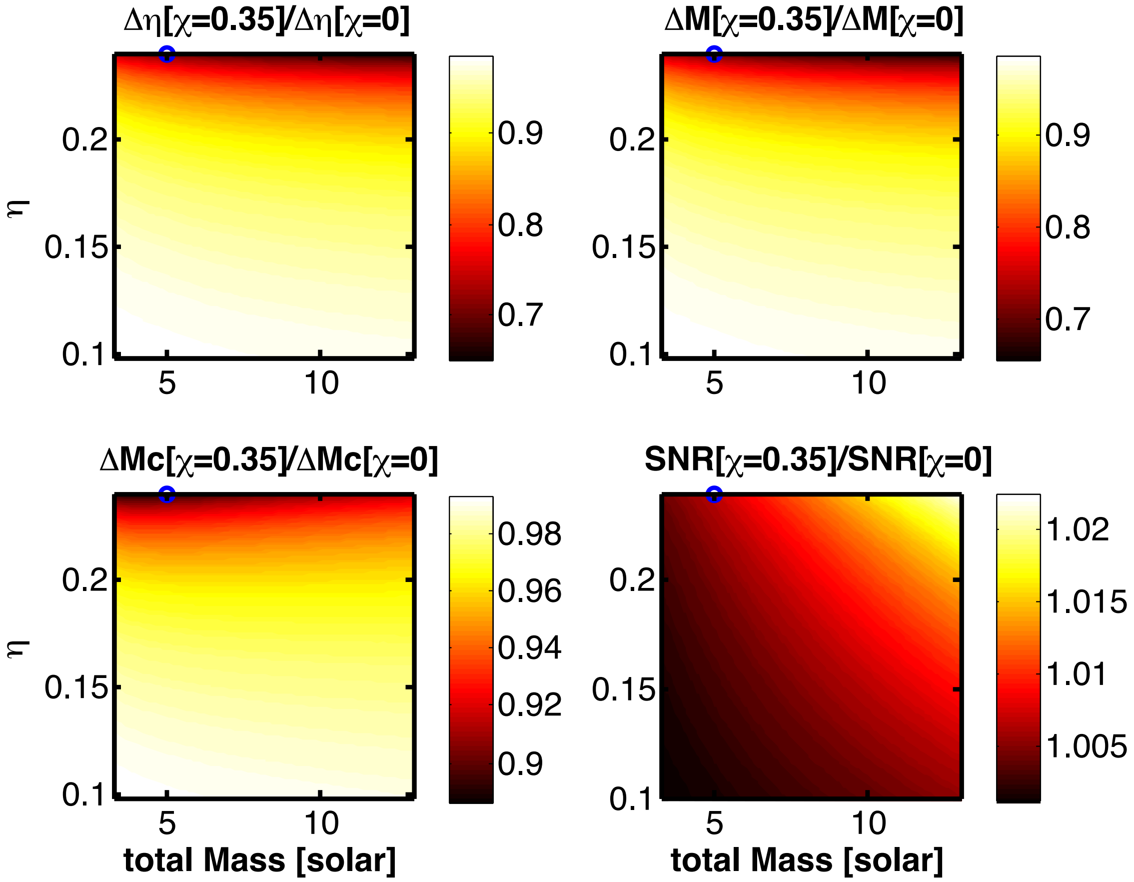

FIGURE 6.5: Ratio in the parameter uncertainties where the BH spin is taken to be $\chi_2 = 0.35$ and NS to be $\chi_1 = 0$. versus the case where both components' spins are taken to be 0. The colour bar indicates the ratio between the two cases and the dashed-blue line means the same as the dashed-white line in Figure 6.4.

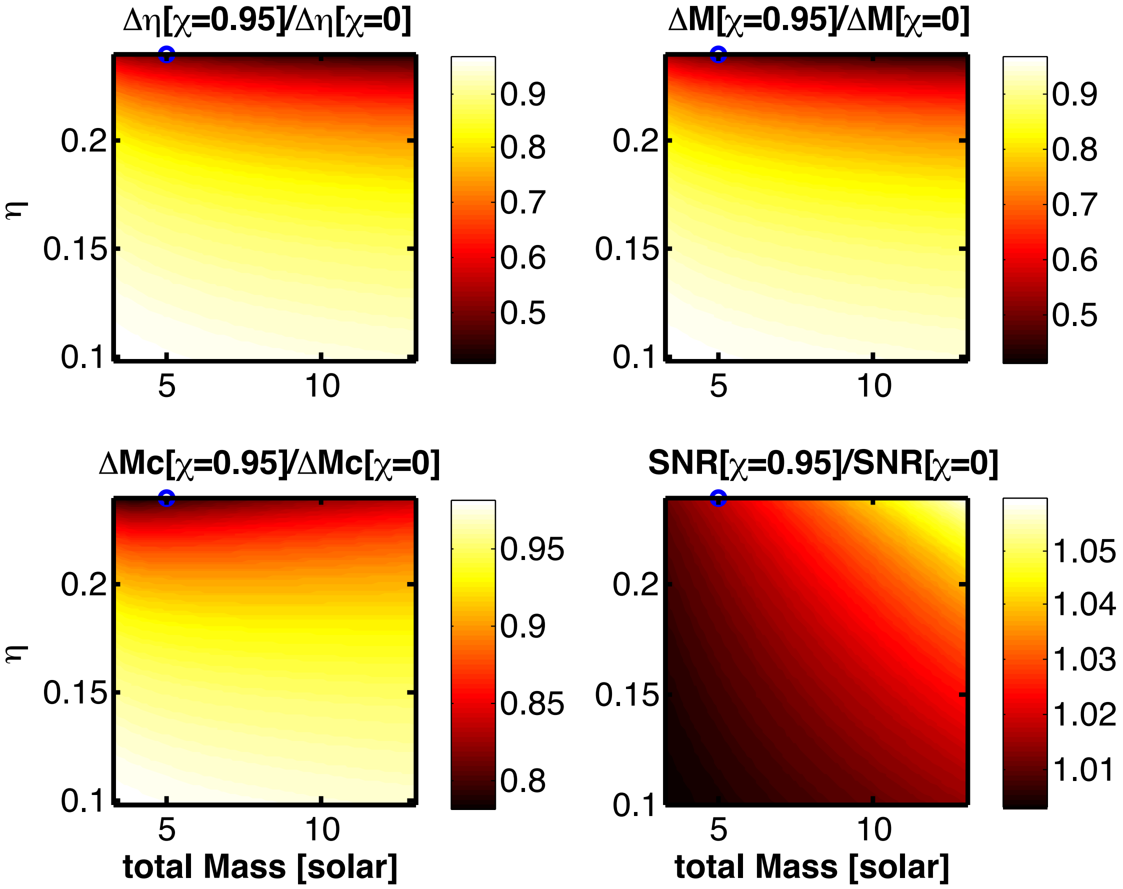

Figure 6.6: Same as in Figure 6.5 but now the BH spin magnitude is taken to be 0.95.

In Figure 6.5 we compare parameter uncertainties between the case where the BH is spinning with a magnitude of 0.35 to those where the BH is non-spinning. The same is shown in Figure 6.6 for the case where now the BH spinning with a magnitude of 0.95. In all the sub panels as before the blue circles represents the case of $m_1, m_2 = (2, 3)M_\odot$. Observe that in Figures 6.5, 6.6 all the ratios of parameter uncertainties are < 1 which means that having a spinning BH in the binary system improves the parameter errors in total mass and the symmetric mass ratio, M, η. This is interesting because the effect of two spinning components in binaries is to increase the errors in M, η (shown in Section 6.3.3). The latter is due to the dependence of mass ratio in the GW waveforms. The symmetric mass ratio η and the spin parameter β are strongly correlated and therefore for systems with both spinning components their mass ratios are more poorly determined because the effect of the spin can be mimicked by changing its mass ratio. And since the mass ratio is strongly correlated with total mass, the error in total mass also becomes larger. However having only a single spin (a physically different system) reduces the error in the mass ratio because of the dependence of the η in the GW waveforms at higher pN order. And due to the strong correlation between M, η, the error in M is also lower for this case and therefore the individual masses are better determined when compared with systems with both components that are either spinning or not.

In the case where spin-aligned BH has a spin magnitude of 0.35 the ratios in the parameter uncertainties are closer to 1 compared to the case where the spin magnitude is 0.95. The waveforms with a spinning BH of magnitude of 0.35 in an NSBH system will cause a deviation of $\leq 10\%$ in the chirp mass error as shown in bottom-left panel of Figure 6.5. These deviations depend more strongly on the mass ratios indicated by the pattern of the colour gradients and this dependency is large compared to that on the total mass. These deviations in the chirp mass error are slightly larger $\leq 20\%$ if the BH has a larger spin magnitude of 0.95 as shown in bottom-left panel of Figure 6.6. The deviations are not caused by SNR difference between non-spinning and spinning waveforms as can be seen by the ratio of SNR of waveform with spinning BH to that with a non-spinning in the bottom-right panels of Figures 6.5, 6.6.

Observe that these deviations of $10\% - 20\%$ in the figures are not very significant: in the Figure 6.4, the relative uncertainties in $\mathcal{M}_c$ for a the range of total masses from $1 - 13M_\odot$ range between $0.05\% - 0.2\%$, i.e. the value of the uncertainties themselves are small. Thus, variations of $10\% - 20\%$ in this uncertainty of the chirp mass for the binaries where the BH is spinning *versus* where the BH is non-spinning imply that the percentage of uncertainties in the chirp mass only changes by $< 1\%$. However note that the errors in M, η can have deviations up to $40\% - 60\%$ and this implies significant variations in the errors of total mass and symmetric mass ratio by up to a factor of 2 and the errors in these parameters are much larger compared to that of the chirp mass.

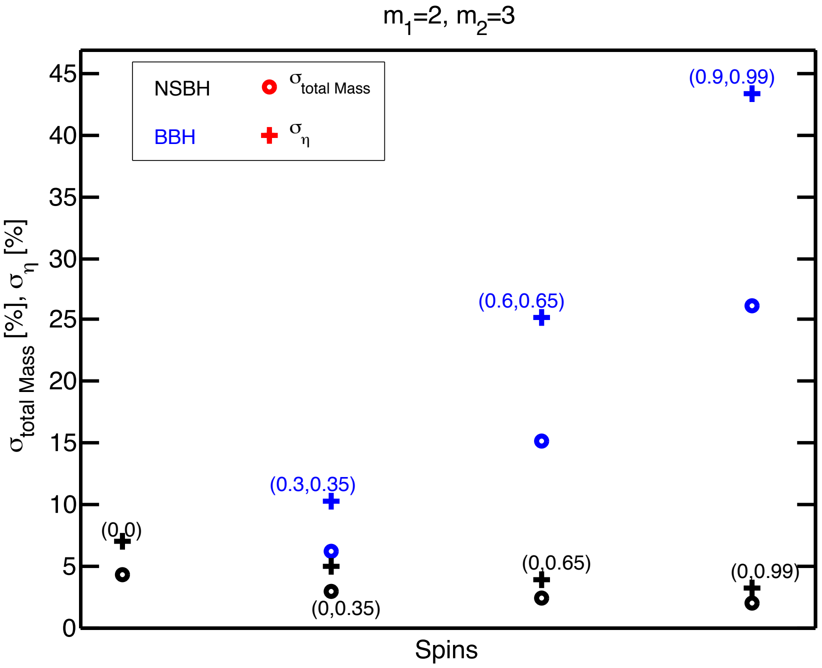

Figure 6.7: Errors in M, η for NSBH and BBH systems with $m_1, m_2 = 2, 3M_\odot$ with SNR of $\sim$ 20. The errors in M are represented by (thick) black circles for the NSBH systems and (thick) blue circles for the BBH systems. The errors in η are represented by (thick) black plusses for the NSBH systems and (thick) blue plusses for the BBH systems The spin magnitudes of NS and the BH for each of the system is specified above the corresponding error in η.

6.3.3 Case B: Distinguishing an NS from a BH

Telling a neutron star apart from a black hole, determining the minimum mass of a BH, maximum mass of an NS, maximum NS spin magnitudes, and knowing whether there is a mass gap between NS and BH compact objects remain important and yet unanswered questions in astrophysics. At very low masses $M < 5M_\odot$ there are possibilities to have for instance a $(2 + 3)M_\odot$ NSBH, BBH or in extreme cases, even BNS systems. We want to attempt to get an idea of what is the best we can do from the GW data from the first advanced detector in terms of telling apart an BNS, system from an NSBH system from BBH system where the BH may have a spin aligned with the orbit. We select $m_1, m_2 = (2, 3)M_\odot$ where our convention is $m_1 < m_2$ with the corresponding spin magnitudes of χ_1, χ_2.

In Figure 6.7, we show the relative errors (in percent) for total mass and the symmetric mass ratio as a function of various spins of the binary system introduced above. Only the BH is assume to have spin. Figure 6.8 is the (relative) error in the leading order spin parameter for various spins of the same binaries in Figure 6.7. The values of χ_1, χ_2 of (0,0), (0,0.35), (0,0.65), (0,0.99), (0.3,0.35), (0.6,0.65) and (0.9,0.99) translate to β of 0, 1.05, 1.95, 2.98, 2.51, 4.89 and 7.38 respectively. The colour of the symbol represents

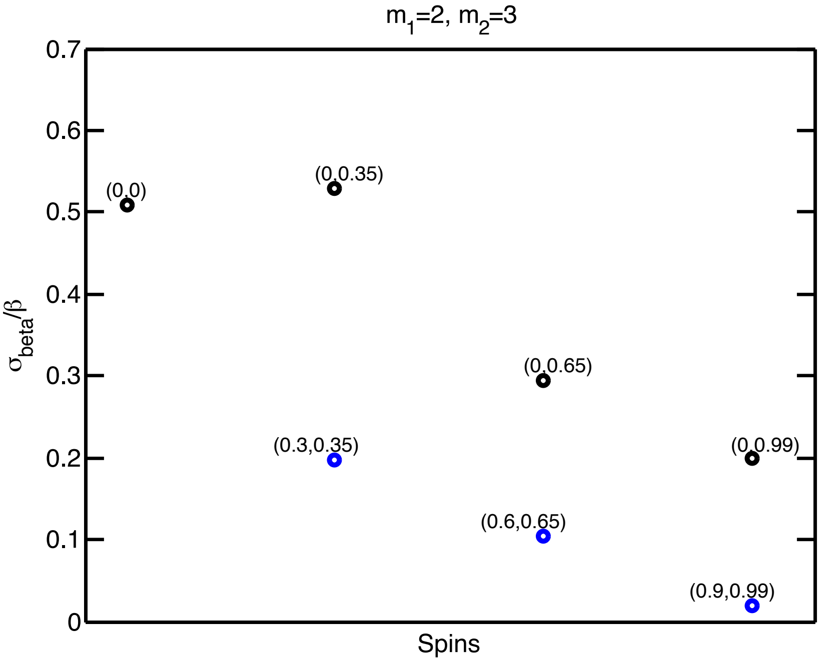

FIGURE 6.8: Errors in β for NSBH and BBH systems. The thick circles are the errors in β and colour means the same as in Figure 6.7.

the type of binary: BBH in blue (circles/plusses) or NSBH in black (circles/plusses). The symbol type represents the parameter uncertainty: σ_M/M in (blue/black) plusses and σ_η/η in (blue/black) crosses which are all labeled accordingly in the Figure. Observe that the both the uncertainties in M, η *increase* for the BBH systems (for which both the masses can have spins) as the magnitude of the spins increase. This has been explained in Section 6.3.2 and is due to the strong correlation between β and η. For the NSBH on the other hand the uncertainties *decrease* for an increasing spin magnitude of the BH. The reason why one spinning object in a binary gives smaller uncertainties compared to both spinning objects has been discussed in Section 6.3.2.

From the Fisher-based variance covariance matrix for a system with $M = 5M_\odot$ and $\eta = 0.24$ corresponding to the masses considered above we solve for the distribution in the individual masses from the Fisher uncertainties in $\delta M, \delta\eta$ and the covariance between them $\mathcal{C}_{M\eta}$. The binary is located at a distance (usually < 1 Gpc) in order to have a SNR of ~ 20 where the Fisher errors are considered to be reliable [Rodriguez et al., 2013]. The resulting distribution in individual masses are solved by randomly populating the two dimensional (Gaussian) posterior distribution (2D PDF) taken from Fisher uncertainties and covariances between total mass and the mass ratio distribution in $M - \eta$ space about the true value and solving for the m_1, m_2 for each pair in M, η. In Figure 6.9 the left panel is a random realisation of the 2d distribution in $M - \eta$ space with a very strong correlation between the two parameters about the true values marked by red dot. The corresponding solutions for m_1, m_2 which is a distinctly non-Gaussian distribution is shown on the right panel. The black crosses are the distribution for the case of $(2,3)M_\odot$ and $\chi_1, \chi_2 = 0, 0$. The green crosses are for the same masses but with a spinning BH, $\chi_1, \chi_2 = 0, 0.99$. Observe that if only one of the components is spinning the uncertainties in the mass parameters reduce. However if the system has two spinning BHs with $\chi_1, \chi_2 = 0.9, 0.99$ than the mass parameters suffer from larger uncertainties as shown in Figure 6.10. Below we specifically discuss three different astrophysical systems:

1. *BBH with (large) BH spin*: Interestingly even though the masses become less determined if both BH are spinning in a BBH compared to only one BH spinning in NSBH system, the spin parameter for BBH is more precisely determined than for NSBH system (see first row of Table 6.2). Therefore from GW data only given the pattern of the errors in M, η, β we may recognise a binary with both components spinning with large magnitudes thus, identifying it as a BBH system.

2. *NSBH vs BBH with BH spin*: Both a BBH with both components of small spin and an NSBH system with a large spin on BH will (see second and third rows in Table 6.2) have similar values of β and similar (small) uncertainty in β (≤ 0.19). However β is sufficiently well determined we can rule out either two large spins (case 1 above) or two non-spinning stars (case 3 below). The masses are quite well determined. Given the low mass and spin an NSBH would be more likely but can only be definitively determined from EM signature of these systems.

3. *BNS vs NSBH vs BBH with no BH spin*: For systems with no spin the uncertainty in β is sufficient to show that the components have no spin (compare row 4 with rows 2 and 3 in Table 6.2). However, this does not distinguish BH from NS components so in this case, we will need to rely on EM signature from the NS to distinguish an NSBH from a BBH binary. EM transients (e.g. Li & Paczynski 1998) for an NSBH system are short gamma-ray bursts (sGRBs) (e.g. Lee & Ramirez-Ruiz 2007), their optical and radio orphan afterglows (van Paradijs et al. 1997), and signatures of r-process nucleosynthesis in the tidal tails of the merger product (Lattimer & Schramm 1976; Kasen et al. 2013), potentially in the form of the recently observed kilonova (Tanvir et al. 2013). A kilonova is a radioactive decay of neutron rich matter in the merger of two compact objects where at least one component is an NS and powers a day to week long thermal transient [e.g. Metzger et al., 2010]. Regrading kilonovae, recent work suggest that unique features in the merger remnant of the NSBH make it an important counterpart to the GW source potentially encoding the information to distinguish it from BNS or BBH systems [Metzger et al., 2014].

TABLE 6.1: Parameter uncertainties for a binary system of $(2+3)M_\odot$ at a distance of $300Mpc$ whose SNR is ~ 20. The table compares the uncertainties in total mass, mass ratio and the spin parameter for the same mass binary with varying individual spins.

(χ_1, χ_2)	β	$\delta\beta/\beta$	$\delta M/M[\%]$	$\delta\eta/\eta[\%]$	$\delta\mathcal{M}_c/\mathcal{M}_c[\%]$
(0.9, 0.99)	7.38	0.0191	26	43	0.0006
(0.3, 0.35)	2.51	0.1973	6	10	0.0003
(0, 0.99)	2.98	0.1983	2	3	0.0002
(0,0)	0	0.507^a	4	7	0.0003

$^{(a)}$ absolute error

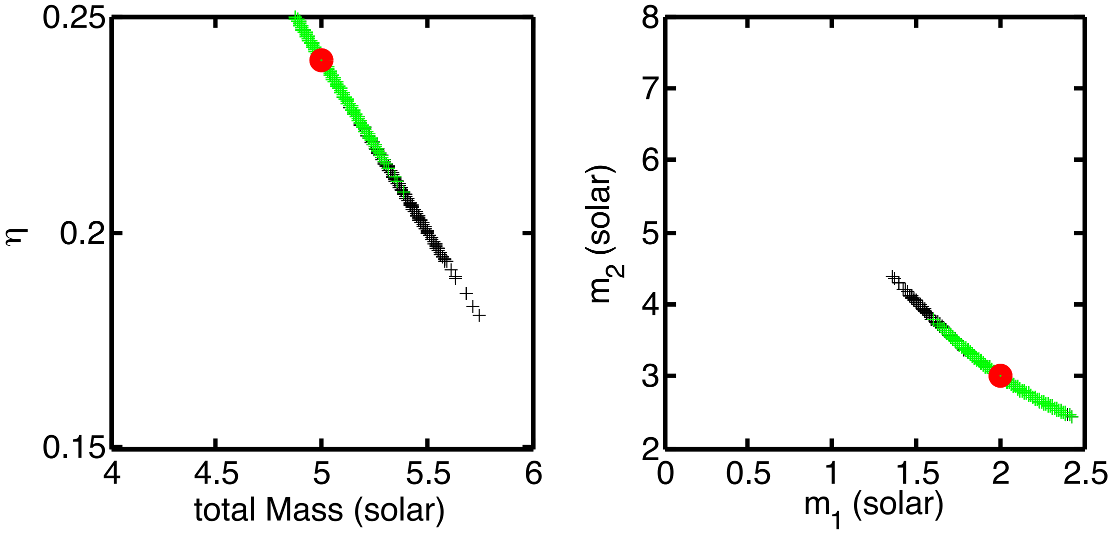

FIGURE 6.9: Two dimensional posterior distribution (2D PDF) in the mass parameters of a binary system where the Fisher-based variance covariance uncertainties have been used to generate a random realisation of the PDF for the binary with $m_1, m_2 = 2, 3M_\odot$ with SNR of ~ 20. In the left panel, the black crosses are the 2D Gaussian distribution in M, η for an NSBH system where the BH has no spin (fourth row in Table 6.2). The resulting distributions in the individual masses are show in black crosses in the right panel. The red dot is the true values of the parameters. The distributions in the green crosses are for the case where the BH in the NSBH system is spinning with a magnitude with 0.99.

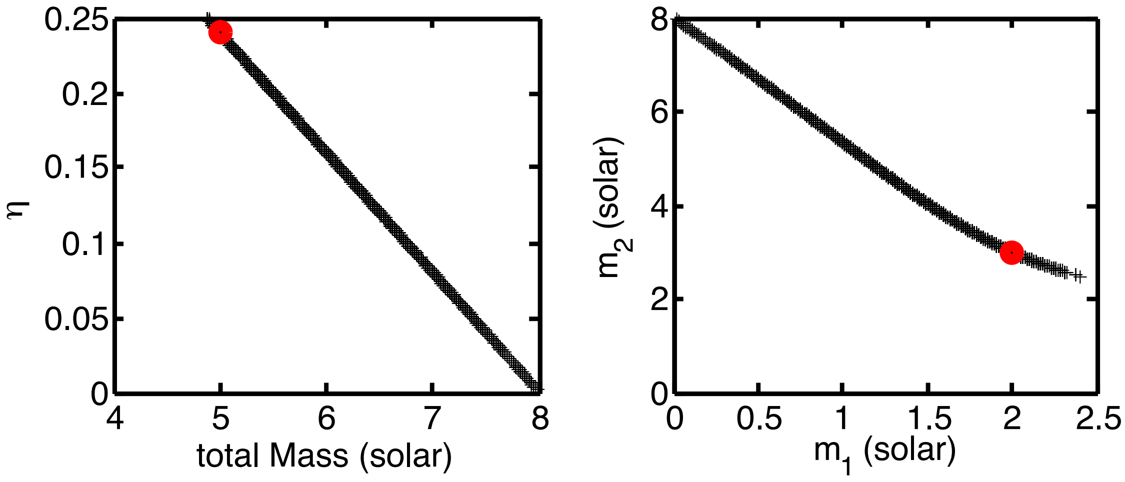

Figure 6.10: Same as in Figure 6.9 but for BBH system where both the BH have spins of 1 corresponding to the first row in Table 6.2.

6.4 Discussions & Conclusions

In this chapter we studied the statistical (Fisher-based) uncertainties in mass and spin parameters of spin-aligned systems observable by the ground based GW detector LIGO. We assumed only the BH to have a spin. The NSs may also have moderate spins ∼ 0.02 [Burgay et al. 2003] up to ∼ 0.3 [Hessels et al 2009] in magnitudes. In future work we will relax the assumption and study a few astrophysical BNS, and NSBH systems with spinning NS. The importance of taking the entire waveform that includes inspiral, ringdown and merger (IMR) has also been studied for non-spinning systems and a few limited cases for the spin-alined systems. These studies indicate that at higher masses (relevant for BBH systems) the ringown and merger add information in the waveforms which can break the degeneracy between the total mass and the symmetric mass ratio. We aim to extend this study for IMR spin-alined waveforms for binary systems. We also wish to investigate the effect on parameter uncertainties of knowing the inclination by observing a gamma ray burst (GRB). It is well known that for lower inclination systems there is a strong correlation between distance and inclination for inspiraling binaries and we will study this effect for binaries where the masses may be spinning comprehensively using Fisher methods. These studies will require us to take the geometry of the system relative to the detector into account and thus the implementation of Fisher studies will be slightly different from those done in this paper. From the first-stage study of the binary parameter errors (for the lower masses) using spin-aligned waveforms we find the following:

1. If the BH is spinning moderately (∼ 0.35) in an NSBH system, the errors in the symmetric mass ratio, the individual masses are smaller by up to ∼ 20% compared to the system where BH is non-spinning. The deviation goes up to ∼ 50% if the BH is has a spin magnitude of 0.95.

2. Distinguishing a high mass NS ($2M_\odot$) from a low mass BH ($3M_\odot$) is difficult due to the strong correlation between the total mass and mass ratio as established in the literature. However if the BH has a spin the parameter errors become small reducing the individual masses ranges for the NS and the BH.

3. A BBH with a low mass BHs with both BH spinning have the largest parameter error. However their spin parameter is known to a much better accuracy compared to the same masses without any spins (for e.g. BNS) or systems with only one large spin (i.e NSBH) and this could be used to distinguish the two types of binaries.

4. For BH in binaries with low spin EM information on transients or kilonovae involving the NS will be required to distinguish a low mass NSBH system from a BBH system which have same total mass and mass ratio.

5. Having a binary system where one component is spinning reduces the uncertainty in the mass ratio which in turn reduces their uncertainty in total mass via the strong anti-correlation $c_{M\eta}$. Thus having one or two spinning objects influences the mass parameters significantly.

BIBLIOGRAPHY

Abadie, J., Abbott, B. P., Abbott, R., et al. 2010, Classical and Quantum Gravity, 27, 173001

Ajith, P. 2011, Phys. Rev. D, 84, 084037

Ajith, P. & Bose, S. 2009, Phys. Rev. D, 79, 084032

Amaro-Seoane, P., Aoudia, S., Babak, S., et al. 2013, GW Notes, Vol. 6, p. 4-110, 6, 4

Armstrong, J. W., Estabrook, F. B., & Tinto, M. 1999, ApJ, 527, 814

Arun, K. G., Buonanno, A., Faye, G., & Ochsner, E. 2009, Phys. Rev. D, 79, 104023

Arun, K. G., Iyer, B. R., Sathyaprakash, B. S., & Sundararajan, P. A. 2005, Phys. Rev. D, 71, 084008

Bailer-Jones, C. A. L. 2009, in IAU Symposium, Vol. 254, IAU Symposium, ed. J. Andersen, Nordströara, B. m, & J. Bland-Hawthorn, 475–482

Benacquista, M. J. 2011, ApJ, 740, L54

Blanchet, L. 2002, Living Reviews in Relativity, 5, 3

Blanchet, L., Damour, T., Esposito-Farèse, G., & Iyer, B. R. 2005, Phys. Rev. D, 71, 124004

Błaut, A. 2011, Phys. Rev. D, 83, 083006

Brown, W. R., Kilic, M., Hermes, J. J., et al. 2011, ApJ, 737, L23

Bulik, T. 2007, Nature, 449, 799

Buonanno, A., Iyer, B. R., Ochsner, E., Pan, Y., & Sathyaprakash, B. S. 2009, Phys. Rev. D, 80, 084043

Burkart, J., Quataert, E., Arras, P., & Weinberg, N. N. 2013, MNRAS

Christensen, N. & Meyer, R. 1998, Phys. Rev. D, 58, 082001

Cornish, N. J. & Crowder, J. 2005, Phys. Rev. D, 72, 043005

Cornish, N. J. & Larson, S. L. 2003, Classical and Quantum Gravity, 20, 163

Cornish, N. J. & Larson, S. L. 2003, Phys. Rev. D, 67, 103001

Cornish, N. J. & Littenberg, T. B. 2007, Phys. Rev. D, 76, 083006

Cornish, N. J. & Rubbo, L. J. 2003, Phys. Rev. D, 67, 022001

Cutler, C. 1998, Phys. Rev. D, 57, 7089
Cutler, C. & Flanagan, É. E. 1994, Phys. Rev. D, 49, 2658
Dall'Osso, S. & Rossi, E. M. 2013, MNRAS, 428, 518
de Bruijne, J. H. J. 2012, Ap&SS, 341, 31
Dominik, M., Belczynski, K., Fryer, C., et al. 2012, ApJ, 759, 52
Duchêne, G. & Kraus, A. 2013, ARA&A, 51, 269
Eggleton, P. P. 1971, MNRAS, 151
Eggleton, P. P. 1983, ApJ, 268, 368
Finn, L. S. 1992, Phys. Rev. D, 46, 5236
Finn, L. S. & Chernoff, D. F. 1993, Phys. Rev. D, 47, 2198
Fisher, R. 1935, J. Roy. Stat. Soc., 98
Fuller, J. & Lai, D. 2012, MNRAS, 421, 426
Fuller, J. & Lai, D. 2013, MNRAS, 614
Hannam, M., Brown, D. A., Fairhurst, S., Fryer, C. L., & Harry, I. W. 2013, ApJ, 766, L14
Hermes, J. J., Kilic, M., Brown, W. R., et al. 2012, ApJ, 757, L21
in't Zand, J. J. M. 2005, A&A, 441, L1
Kepler, S. O., Winget, D. E., Nather, R. E., et al. 1991, ApJ, 378, L45
Kilic, M., Brown, W. R., Gianninas, A., et al. 2014, ArXiv e-prints
Królak, A., Tinto, M., & Vallisneri, M. 2004, Phys. Rev. D, 70, 022003
Lattimer, J. M. & Prakash, M. 2010, ArXiv e-prints
LISA Study Team. 1998, LISA: Laser Interferometer Space Antenna for the Detection and Observation of Gravitational Waves, Pre-Phase A Report, 2nd edn. (Garching, Germany: Max Planck Institut fur Quantenoptik)
Littenberg, T. B. 2011, Phys. Rev. D, 84, 063009
Lorimer, D. R. 2005, Living Reviews in Relativity, 8, 7
Mattox, J. R., Halpern, J. P., & Caraveo, P. A. 1998, ApJ, 493, 891
Metzger, B. D., Bauswein, A., Goriely, S., & Kasen, D. 2014, ArXiv e-prints
Metzger, B. D., Martínez-Pinedo, G., Darbha, S., et al. 2010, MNRAS, 406, 2650
Nelemans, G. 2003, in American Institute of Physics Conference Series, Vol. 686, The Astrophysics of Gravitational Wave Sources, ed. J. M. Centrella, 263–272
Nelemans, G. 2009, Classical and Quantum Gravity, 26, 094030
Nelemans, G. 2011, Wiki Verification Sources.
Nelemans, G., Yungelson, L. R., & Portegies Zwart, S. F. 2001a, A&A, 375, 890
Nelemans, G., Yungelson, L. R., & Portegies Zwart, S. F. 2004, MNRAS, 349, 181
Nelemans, G., Yungelson, L. R., Portegies Zwart, S. F., & Verbunt, F. 2001b, A&A, 365, 491
Nicholson, D. & Vecchio, A. 1998, Phys. Rev. D, 57, 4588
Nissanke, S., Holz, D. E., Hughes, S. A., Dalal, N., & Sievers, J. L. 2010, ApJ, 725, 496
Nissanke, S., Vallisneri, M., Nelemans, G., & Prince, T. A. 2012, ApJ, 758, 131
Özel, F., Psaltis, D., Narayan, R., & McClintock, J. E. 2010, ApJ, 725, 1918

Paczynski, B. 1976, in IAU Symposium, Vol. 73, Structure and Evolution of Close Binary Systems, ed. P. Eggleton, S. Mitton, & J. Whelan, 75

Panei, J. A., Althaus, L. G., Chen, X., & Han, Z. 2007, MNRAS, 382, 779

Peters, P. C. & Mathews, J. 1963, Physical Review, 131, 435

Peterseim, M., Jennrich, O., Danzmann, K., & Schutz, B. F. 1997, Classical and Quantum Gravity, 14, 1507

Petiteau, A. 2012, Configurations of the eLISA (NGO) mission.

Phinney, E. S. 1991, ApJ, 380, L17

Piro, A. L. 2011, ApJ, 740, L53

Poisson, E. & Will, C. M. 1995, Phys. Rev. D, 52, 848

Postnov, K. & Yungelson, L. 2014, ArXiv e-prints

Press, W. H., Teukolsky, S. A., Vetterling, W. T., & Flannery, B. P. 2002, Numerical recipes in C++ : the art of scientific computing

Rodriguez, C. L., Farr, B., Farr, W. M., & Mandel, I. 2013, Phys. Rev. D, 88, 084013

Roelofs, G. H. A., Groot, P. J., Benedict, G. F., et al. 2007, ApJ, 666, 1174

Roelofs, G. H. A., Groot, P. J., Nelemans, G., Marsh, T. R., & Steeghs, D. 2006, MNRAS, 371, 1231

Roelofs, G. H. A., Rau, A., Marsh, T. R., et al. 2010, ApJ, 711, L138

Rogan, A. & Bose, S. 2006, ArXiv Astrophysics e-prints

Schutz, B. F. 1996, Classical and Quantum Gravity, 13, A219

Shah, S., Nelemans, G., & van der Sluys, M. 2013, A&A, 553, A82

Shah, S., van der Sluys, M., & Nelemans, G. 2012, A&A, 544, A153

Skillman, D. R., Patterson, J., Kemp, J., et al. 1999, PASP, 111, 1281

Solheim, J.-E. 2010, PASP, 122, 1133

Sterken, C. 2005, in Astronomical Society of the Pacific Conference Series, Vol. 335, The Light-Time Effect in Astrophysics: Causes and cures of the O-C diagram, ed. C. Sterken, 3

Stroeer, A. & Nelemans, G. 2009, MNRAS, 400, L24

Stroeer, A. & Vecchio, A. 2006, Classical and Quantum Gravity, 23, 809

Strohmayer, T. E. 2005, ApJ, 627, 920

Takahashi, R. & Seto, N. 2002, ApJ, 575, 1030

Thorne, K. S. 1987, Gravitational radiation., ed. S. W. Hawking & W. Israel, 330–458

Timpano, S. E., Rubbo, L. J., & Cornish, N. J. 2006, Phys. Rev. D, 73, 122001

Tinto, M. & Armstrong, J. W. 1999, Phys. Rev. D, 59, 102003

Tinto, M. & Dhurandhar, S. V. 2004, ArXiv General Relativity and Quantum Cosmology e-prints

Toonen, S., Claeys, J. S. W., Mennekens, N., & Ruiter, A. J. 2014, A&A, 562, A14

Vallisneri, M. 2005a, Phys. Rev. D, 72, 042003

Vallisneri, M. 2005b, Phys. Rev. D, 71, 022001

Vallisneri, M. 2008, Phys. Rev. D, 77, 042001

Vallisneri, M. 2011, Lisasolve fastbinary package

Vallisneri, M., Crowder, J., & Tinto, M. 2008, Classical and Quantum Gravity, 25, 065005

van der Sluys, M. V., Röver, C., Stroeer, A., et al. 2008, ApJ, 688, L61

Verbeek, K., Groot, P. J., Nelemans, G., et al. 2013, MNRAS, 434, 2727

Verbunt, F. & Rappaport, S. 1988, ApJ, 332, 193

Webbink, R. F. 1984, ApJ, 277, 355

Webbink, R. F. & Han, Z. 1998, in AIPC, Vol. 456, Laser Interferometer Space Antenna, Second International LISA Symposium on the Detection and Observation of Gravitational Waves in Space, ed. W. M. Folkner, 61–67

SUMMARY & CONCLUSIONS

This thesis primarily investigates the synergy between electromagnetic (EM) and Gravitational wave (GW) data of compact Galactic binaries in constraining their parameters. It is motivated by the approval[4] of an L class GW mission by the European Space Agency (ESA) which will be a space-based GW detector, such as eLISA[5]. It will be sensitive to frequencies of $10^{-4} - 1$ Hz, the range in which Galactic binaries (made of white-dwarfs (WD), neutron stars (NS) and black holes (BH)) will be radiating GWs. This gives us an opportunity to use the complementary information on these sources in order to study them in more detail. It is likely that GW information will be complementary to that of EM data, however to which extent was not explored and is precisely what we attempt to answer in this thesis. So far all we know about the formation and evolution of these binaries is from a combination of EM data and theory. Even though we expect compact binaries to exist in great numbers ($\sim 10^8$) we do not know how exactly they form, how do they survive various evolutionary processes and which are the most important processes because most of the processes are not feasible to model in detail for such large number of binaries. Mostly we resort to studies such as binary population synthesis (BPS) which allows us to macroscopically study these systems in large numbers by modelling the binary processes which are then checked against the observations. From the EM data we know of only about ~ 100 compact binaries due to the fact that they are very faint optically and therefore very hard to find. However eLISA will observe millions of these sources most of which will be an unresolved background but several thousand of them will be *resolvable*, i.e. those sources will be significantly strong that their GW parameters can be measured. For a subset of those sources with dedicated EM surveys/observations we will be able to obtain their EM data as well and for those binaries much more can be learned than what either EM or GW data can alone provide. We summarise what the GW data will provide and how EM data can help break degeneracies between astrophysically useful parameters

---

[4] with a projected launch date of 2034

[5] evolved Laser Interferometer Space Antenna (eLISA) which is the working design

below. We also study the statistical (Fisher-based) parameter errors of the binaries made of neutron stars (NS) and/or black holes (BH) including BH spin that will be detected by ground-based GW detectors.

Chapter 2: Inclination-amplitude degeneracy

From the GW observatories (eLISA and other ground based GW detectors) we are interested in obtaining the GW parameters and their uncertainties. For the sources concerned in this thesis, which are well studied and whose GW signal models are easily obtainable, we wish to establish what are the parameter degeneracies in the binary sources and what are the parameter uncertainties that GW observatories are capable of attaining. The main goal of this thesis is not to do parameter estimation but to determine what we can learn from the GW observations of the binaries. Thus, we use analytical methods to compute the parameter uncertainties expected from eLISA for compact binaries mentioned above. We find that apart from the signal-to-noise ratio (SNR), the inclination parameter ι which is the angle made by the line-of-sight with the orbital plane of the binary strongly affects the parameter uncertainties and the correlations between the parameters. The astrophysically most relevant correlation is that between the amplitude and inclination which is largest for lower inclination(face-on) systems and decreases as the inclination increases (edge-on). It turns out that for lower inclination systems, $\iota \leq 45^\circ$ the signals cannot be distinguished from each other and thus that also implies that the parameter uncertainties in those two parameters are larger compared to the identical system with a higher inclination. At SNR of 10 for $\iota \leq 45^\circ$ the inclination has uncertainty of $\sim \pm 45^\circ$ which means the inclination cannot be determined at all, while for the same binary with $\iota \sim 89^\circ$ the inclination will have an error of $\sim \pm 2^\circ$. This result shows the importance of complementary EM observations for low inclination systems which can measure the inclination [e.g. Roelofs et al., 2006] and thus can be used to reduce the amplitude error via the correlation with inclination. Similarly an inclination error of $\sim \pm 2^\circ$ at typical small SNRs imply the systems are eclipsing and this knowledge can be used in EM surveys.

Chapter 3: Importance of Sky position

It turns out that there exist many more correlations between the binary parameters depending on the relative orientation of the binary to the detector. To understand this we performed a Monte Carlo study where we varied the orientation and angular parameters (ι, polarisation, ψ, ecliptic latitude and longitude β, λ) of the binaries in their physically allowed ranges to investigate the combined effect on the parameter uncertainties. We find that after inclination the ecliptic latitude has the strongest effect on the parameter uncertainties and their correlations, especially for binaries located at the ecliptic poles. The

SNR of the sources taken at a fixed distance increases to the ecliptic plane and decreases at the poles making most of the parameter uncertainties less precise at the poles compared to the plane. However there is a larger spread of parameter uncertainties at the poles and this is caused by various correlations between the parameters: phase ϕ, GW amplitude $\mathcal{A}$, λ, and ψ. This means that knowing the sky position for the binaries at the poles reduces their parameter uncertainties and the improvements factors in the astrophysically interesting parameters $\mathcal{A}$ and ι can be by a factor of 2. Knowing both sky position and inclination simultaneously give improvement factors in the amplitude to a factor of 60 for low inclination systems located at the ecliptic poles. In doing these analyses one has to be careful in interpreting the errors in $\mathcal{A}$ and ι since they are highly correlated and the uncertainty in ι can exceed to unphysical values especially for lower inclination systems. This has to be corrected since due to the correlation with the amplitude its error is also inflated.

Chapter 4: Limits on individual masses and distance

The main goal of GW observations of the compact binaries will be to provide us with accurate parameters and the first two chapters show that due to the inherent correlations between GW parameters that describe the binaries, their parameter uncertainties may not be as precise depending on where it is on sky and what its orientation is relative to the detector. In fact, the most valuable parameters which are the individual masses and radii will not be measured by GW observations for sources that are monochromatic (i.e. the inspiral is much slower than the detector lifetime). For monochromatic sources the masses are measured in a combination with distance in the amplitude parameter. And even if the inspiral may be detected for certain high frequency sources, we can only determine the combination of masses by measuring the chirp mass $\mathcal{M}_c$. In order to measure the individual masses we need complementary EM information. In this chapter we show what are the limits on masses, distance and inclination if we can simultaneously observe these sources electromagnetically. We considered typical EM observations where either just the primary mass is known (Case 2a), or single-line spectroscopic data (Case 2b), or single-line spectroscopic data with distance (Case 2c), or double-line spectroscopic data (Case 3) for binaries made of double WDs. We find that for a GW detection of a binary WD with a SNR of 10, Case 2b constrains the 2-σ uncertainties in the secondary mass and distance to factors of two – 40% depending on the inclination of the source. Case 2c would constrain the 2-σ uncertainty secondary mass to $25\%-30\%$. And Case 3 would constrain the distance to 30%. Thus, we find that EM observation of distance and/or radial velocity are the most useful and complementary to GW observations in constraining the secondary mass which is typically not resolved in EM observations. Observation of radial velocity can also be used to constrain the inclination of the source independently and can be compared with that measure by the GW observations.

Chapter 5: Chirping binaries

In this chapter we took the analysis of WD binaries further by including those sources which are radiating at higher frequencies and whose inspiral could be measured giving us a GW measurement of the parameter $\dot{f}$. We investigated what are the constraints on the orbital parameters: the GW frequency, rate of change of frequency $\dot{f}$ and the acceleration of the frequency $\ddot{f}$. The goal was to establish if we will have the precision required to do tidal physics in WD binaries and how combining eclipse timing measurements from EM data will improve the parameter estimates. The main result we found regarding tidal physics is that the parameters $\dot{f}$ and $\ddot{f}$ could be measured using GW data only for the most massive WD binaries observes at frequencies $\geq$ 6mHz. From timing the eclipses for 10 years (which is reasonable amount of time given the timescale at which eLISA will be launched) the chirp can be measured to a staggering precision of 0.1% for an astrophysical system like J065133.33+284423.3 (J0651,hereafter) [Brown et al., 2011]. J0651 is a verification source which is an almost edge-on system (eclipsing source) with a predicted GW SNR of ~ 10. Thus for systems like J0651 EM data will provide much better accuracy in the chirp compared to the precision from GW data. However the rate of the chirp, $\ddot{f}$ is only measured to a a factors of few. The importance of measuring $\dot{f}, \ddot{f}$ in regard to doing tidal physics can be seen in the ratio $\ddot{f}f/\dot{f}^2$. If the binary evolves only under the influence of GW radiation then the ratio is a fixed constance of 11/3 [Webbink & Han, 1998]. Any deviation from this ratio may imply there is a contribution to the binary evolution due to tides and the measured deviation can be used to constrain tidal parameters of the binary. We find that even with the combined GW and EM observations this ratio will be hard to measure unless we discover extremely massive WDs at frequencies > 100mHz. However combing a precise $\dot{f} = 0.1\%$ from EM data on timing with GW measurements of amplitude and inclination constrains the 2-σ uncertainty in chirp mass to 0.11% and distance to $35-19\%$. Single line spectroscopic data together with $\dot{f}$ constrains the distance to $\leq 25\%$ and secondary mass to $6-19\%$ and thus combining $\dot{f}$ and radial velocity from EM data with GW are valuable in constraining WD binary parameters observable by eLISA.

Chapter 6: Coalescing neutron star and/or black hole binaries

In the final chapter we investigate the parameter uncertainties of coalescing binaries made of neutron stars (NS) and black holes (BH) which are observable by the ground-based GW detectors. We investigate the effects of spin-alined BH in neutron star black hole (NSBH), and binary black hole (BBH) binaries on their parameter uncertainties as a function of total mass and the symmetric mass ratio from the inspiraling GW signals. It is well known that the chirp mass will be determined to very good accuracies due to its strong dependence on the GW phase, the quantity that can be very accurately measured. It is also known that distinguishing the individual masses only from inspirals will be difficult because the mass ratio is not as precisely measured as the GW signals depend on it only at higher post Newtonian orders. Furthermore numerous studies have shown that the binary systems with spinning masses make the parameter uncertainties even worse because of the strong correlations between spin and mass ratio parameters. We extend the study of the spin-aligned systems using analytical GW inspiral waveforms to binaries with total mass ranging from $1 - 13M_{\odot}$. We find that having only one spinning object actually *reduces* the parameter uncertainties for the range of total masses considered above and for a range of symmetric mass ratios of $0 - 0.25$. Another important result is that having a single spinning object with sufficiently high spin in a binary system with NS will be useful in distinguishing an NSBH system from a BBH system. If both the binary masses have large spins, the uncertainties in the spin parameter β (which represents the spin-orbit coupling) is the most precisely determined when compared to other binaries with same total mass for lower spin magnitudes. And thus even though the individual masses are less precisely determined for spinning binary systems, the spins are more precisely determined which can be used to distinguish systems with neutron stars from BBH systems.

Outlook

The first four chapters on the long-lived Galactic binaries basically show the capacity of the (currently planned) GW detectors in measuring the most fundamental properties of those sources. The chapters also show the usefulness of the electromagnetic information in resolving the degeneracies between the most important parameters of the binaries that cannot be measured with the current capabilities of the GW detectors. This work can be taken further in a few ways. One of the obvious things to do is to check some of the results with more robust data analysis methods, namely Bayesian-based Monte Carlo methods. This will especially be useful for verifying some of the results we quote for low-inclination systems which are based on Fisher method where the uncertainties in certain parameters are undetermined and can inflate to unphysical values. In turn the parameters that are correlated with the undetermined parameters suffer as they also become poorly determined owing to the limitedness of the Fisher methods in which there is only limited way of taking priors into account to avoid the unphysical values. Additionally Fisher method by definition does not do real parameter estimate which could be very different in real life. This and for other reasons, it is important to test some of our results with a robust parameter estimation method. This work can be taken forward by investigating in detail which masses (of WD) can produce what type of astrophysical transients. If we look at m_1, m_2 space of WD binaries, it is roughly known what are the fate of certain combinations of masses, whether they merge, start transferring mass in a stable or non-stable way. However the fate of all the combinations of masses in the binary remain to be known and this could be very important in understanding the various types of transients to be expected from WD binaries (that populate our galaxy in great numbers) and recognise them as counterparts to their GW signals. This will eventually allow us to understand them in more detail than what EM or GW information alone can allow us to do.

The final chapter, which is on short-lived binary mergers of binary systems made of NS and/or BH is the first step in a more extensive project. So far in this study we looked at the single-detector case and the binary waveforms consisted of only the inspiral parts. It has been shown that for non spinning sources, the merger and the ringdown signals add significant information to the GW signals which in turn break degeneracies between some of the astrophysically useful parameters such as total mass and symmetric mass ratio and this giving us a much better estimate of the individual masses in the binary. Thus we can also include the merger and the ringdown signals for the spin-aligned pN waveforms and see if the parameter errors also become smaller. We also intend to study the effect of distance-inclination degeneracy on spinning systems across all total mass space for multi detector network which in someway will extend the work of [Nissanke et al., 2010]. One of the most important open questions in this subfield of GW astronomy is what will the absence or presence of EM information in combination with their GW observations help us learn about these binary coalescences and the nature of their components which are NS and BH. Chapter 6 is a first step towards a comprehensive study of the importance of the synergy between EM and GW data.

SAMENVATTING

Dit proefschrift onderzoekt hoofdzakelijk de synergie tussen elektromagnetische (EM) en zwaartekrachtdata van compacte galactische (binnen ons melkwegstelsel gelegen) dubbelsystemen. Een van de aanleidingen is de goedkeuring[6] van een L klasse GW (Gravitational Wave) missie van de Europese ruimtevartorganisatie (ESA). Deze missie zal een satelliet zijn zoals met eLISA[7] die zwaartekrachtgolven (ZG) detecteert. De detector zal gevoelig zijn voor zwaartekracht-trillingen met frequenties tussen de $10^{-4} - 1$Hz. Dit is het bereik waarin galactische dubbelsystemen zwaartekrachtgolven zullen creeeren en uitstralen. Bij een dubbelsysteem draaien er twee objecten om elkaar heen door de wederzijdse aantrekkingskracht. De dubbelsystemen waar wij in geïnteresseerd zijn bestaan uit witte dwergen, neutronensterren en zwarte gaten. Dit worden compacte dubbelsystemen genoemd omdat de objecten die om elkaar heen draaien de meest compacte objecten zijn in het heelal, objecten waar er extreem veel massa in een klein volume is geperst. Deze missie biedt ons nu de mogelijkheid om de van deze bronnen al bekende EM data met de zwaartekracht metingen te combineren en zo meer over deze bronnen te leren. Het is waarschijnlijk dat de zwaartekracht-metingen complementair zijn aan EM metingen, maar tot dusver is er geen onderzoek gedaan naar wat deze complementaire informatie in de praktijk kan opleveren. Daar gaat dit onderzoek over. Wat we tot nu toe weten over de vorming en evolutie van deze dubbelsystemen is afgeleid uit de EM metingen en onze huidige theoretische kennis. Alhoewel we verwachten dat compacte dubbelsystemen in grote getalen aanwezig zijn in ons melkwegstelsel, van de orde $\sim 10^8$, weten we niet precies hoe deze tot stand komen en hoe ze verschillende evolutionaire processen overleven. Deze evolutionaire processen zijn het belangrijkste onderzoeksdoel omdat het simpelweg niet mogelijk is om zo een grote hoeveelheid dubbelsystemen in detail na te bootsen met de computer. We maken voornamelijk gebruik van studies als dubbelsysteem populatie-synthese. Dit stelt ons in staat om deze systemen globaal te bestuderen voor grote aantallen door middel van het versim-

---

[6] met 2034 als gepland jaar van lancering

[7] evolved Laser Interferometer Space Antenna (eLISA), het voorlopige ontwerp

peld modelleren van dubbelsysteem processen. De resultaten vergelijken we dan met de waarnemingen. Van de EM metingen kennen we ongeveer 100 compacte dubbelsystemen. Omdat het optisch licht dat deze systemen uitstralen erg zwak is zijn ze moeilijk te vinden. eLISA daarentegen zal in staat zijn om miljoenen van deze systemen waar te nemen, waarvan velen zich tot een achtergrond van zwaartekrachtgolven vermengen, maar waar alsnog duizenden duidelijk van deze achtergrond onderscheidbaar zullen zijn. Hiermee bedoelen we dat bij deze systemen de zwaartekrachtgolven sterk genoeg zijn om ze induvidueel waar te nemen. Een deel van die bronnen kunnen we ook met EM telescopen waarnemen en van deze EM data kunnen we ook gebruik maken. Van de combinatie van de EM metingen en zwaartekrachtgolfmetingen zullen we een stuk meer kunnen leren dan van de onafhankelijke EM en zwaartekrachtgolfdata. Hieronder zetten we kort uiteen wat de zwaartekrachtgolf metingen opleveren en hoe de EM data van hulp kan zijn bij het verhelderen van astrofyisch interessante parameters die anders meervoudig interpreteerbaar zijn. We onderzoeken ook de onzeherheden van de metingen aan neutronenster dubbelsystemen en/of zwartegat dubbelsystemen die door de op aarde geplaatste zwaartekrachtdetectoren gedetecteerd zullen worden.

Hoofdstuk 2: Inclinatie-amplitude correlatie

We zijn geïnteresseerd in het verkrijgen van de ZG-parameters en hun onzekerheden met behulp van de ZG-observatoria (eLISA en andere op aarde gestationeerde ZG-detectoren). Voor de bronnen die in dit proefschrift beschouwd worden, namelijk de bronnen die goed bestudeerd zijn en waarvoor modellen voor het ZG-signaal gemakkelijk verkrijgbaar zijn, willen we vaststellen wat de correlaties tussen de parameters zijn en welke onzekerheden de parameters heeben. Het doel van dit proefschrift is niet om een inschatting maken van de parameterwaarden, maar om vast te stellen wat we kunnen leren van de waarnemingen van de ZGn van dubbelsystemen. Aan de hand van analytische methodes berekenen we de verwachte onzekerheden in de parameters voor eLISA bij het meten van de hierboven genoemde compacte dubbelsystemen. Uit onze berekeningen blijkt dat zowel de signaal-ruis-verhouding (SRV) als de inclinatie (de hoek van aanzicht, ofwel de hoek tussen de kijkrichting en het draaivlak van het dubbelsysteem) de onzekerheden in de parameters alsmede de correlaties tussen de parameters sterk beïnvloeden. De correlatie tussen de amplitude en de inclinatie is astrofysisch het meest interessant. Deze correlatie is het grootst voor systemen met een kleinere inclinatie ("face-on") en wordt kleiner met toenemende hoek (edge-on). Het blijkt dat bij systemen met een inclinatie van minder dan 45 graden de signalen voor verschillende inclinaties niet meer van elkaar te onderscheiden zijn. Dit betekent ook dat de onzekerheden in die twee parameters groter zullen zijn dan bij een identiek systeem dat onder een grotere hoek ten opzichte van ons staat. Bij een SVR van 10 en een hoek van aanzicht van minder dan 45 graden neemt de onzekerheid in de hoek toe tot ongeveer 45 graden. De onzekerheid in de hoek is dus net zo groot is als de hoek zelf en deze waarde is dus in feite niet meer vast te stellen, terwijl bij een dubbelsysteem met een inclinatie van ongeveer 89 graden er maar een onzekerheid is van ongeveer 2 graden. Dit resultaat laat duidelijk zien hoe EM metingen zouden helpen bij het verminderen van de fout in amplitude door middel van de correlatie met de inclinatie, omdat EM metingen een aparte meting van de inclinatie kunnen bepalen. En vice versa, een onzekerheid in de inclinatie van ongeveer 2 graden bij kleine SVR impliceert dat systemen voor elkaar langs bewegen; deze kennis kan van dienst zijn bij grootschalige toekomstige EM waarnemingen omdat deze 'eclipserende' dubbelsterren goed te herhennen zijn.

Hoofdstuk 3: Het belang van de hemelpositie

Het blijkt dat de correlaties tussen dubbelsysteem parameters voor systemen die voor een lange periode van twee jaar in het eLISA waarnemingveld vallen, gecompliceerder zijn. Er kunnen veel meer correlaties zijn, afhankelijk van de oriëntatie van een dubbelsysteem ten opzichte van de detector. Om dit te begrijpen hebben we een Monte Carlo studie uitgevoerd waar we de oriëntatie en de hoekparameters van de dubbelsystemen varieerden binnen de fysisch toegestane bereik om het gecombineerde effect op de onzekerheden in de parameters te onderzoeken. We hebben ontdekt dat met name de inclinatie en ook de ecliptische hoogte het sterkste effect op de onzekerheden in de parameters en hun correlaties hebben. Dit geldt met name voor de dubbelsystemen die aan de ecliptische polen staan gepositioneerd. De SVR van bronnen op een vaste afstand neemt toe in de richting van het ecliptisch vlak en af richting de polen. Dit heeft als gevolg dat de meeste onzekerheden in de parameters minder precies zijn bij de polen dan die voor bronnen gepositioneerd zijn in de buurt van het ecliptisch vlak. Er is daarentegen een grotere spreiding van onzekerheden in de parameters aan de polen. Dit wordt veroorzaakt door de verschillende correlaties tussen de parameters: fase ϕ, GZ-amplitude $\mathcal{A}$, de ecliptische lengte λ, en polarisatie ψ. Dit betekent dat het kennen van de hemelpositie van dubbelsystemen bij de polen de bijbehorende onzekerheden vermindert. De verbetering in de astrofysisch interessante parameters $\mathcal{A}$ en ι kan zo groot zijn alseen factor 2. Als zowel de hemelpositie als de inclinatie bekend zijn kan dit leiden tot een verbeteringsfactor van 60 in de amplitude voor systemen met lage inclinatie die gepositioneerd zijn in de buurt van ecliptische polen. Bij het uitvoeren van deze analyse moet men voorzichtig zijn in het interpreteren van de fouten in $\mathcal{A}$ en ι, omdat deze in hoge mate gecorreleerd zijn en de onzekerheid in ι groter kan worden dan fysisch realistische waarden, met name voor systemen met lage inclinatie. Hier moet een correctie op toegepast worden omdat door de correlatie van ι met de amplitude ($\mathcal{A}$) ook de fout in amplitude zal toenemen.

Hoofdstuk 4: Limieten op individuele massa's en afstand

Het voornaamste doel van observaties van zwaartekrachtgolven (ZGn) van compacte dubbelsterren is om ons accurate parameters te verschaffen. De eerste twee hoofdstukken laten zien dat door de inherente correlaties tussen de ZG-parameters die de dubbelsterren beschrijven, de onzekerheden in hun parameters wellicht niet zo precies zijn, afhankelijk van waar ze zich aan de hemel bevinden en afhankelijk van de oriëntatie ten opzichte van de detector. De meest waardevolle parameters, namelijk de individuele massa's en stralen, zullen niet door observaties van ZGn van monochromatische bronnen (i.e. de inspiral is veel trager dan de levensduur van de detector) gemeten worden. Voor monochromatische bronnen worden de massa's in combinatie met de afstand via de amplitude parameter gemeten. Zelfs als de inspiral wordt gemeten voor bepaalde hoog-frequente bronnen, kunnen we alleen een combinatie van de individuele massa's bepalen namelijk de tsjilp massa $M_c = (m_1 m_2)^{3/5}/(m_1+m_2)^{1/3}$. Om de individuele massa's te meten hebben we aanvullende EM informatie nodig. In dit hoofdstuk laten we zien wat de limieten op de massa's, afstand en inclinatie zijn als we deze bronnen tegelijkertijd met GW en EM telelscopen observeren. We beschouwden typische EM observaties waar ofwel de primaire massa bekend is (Geval 2a), ofwel de enkele-lijn spectroscopische data (Geval 2b), of de enkele-lijn spectroscopische data plus de afstand (Geval 2c), ofwel de dubbele-lijn spectroscopische data (Geval 3) voor de dubbelsteren van WDn. We vinden dat voor een ZG detectie van een WD dubbelster met een signaal-ruis verhouding van 10, Geval 2b de 95% onzekerheden in de secundaire massa en de afstand tot factoren van $2 - 40\%$ beperkt afhankelijk van de inclinatie van de bron. Geval 2c zou de 95% onzekerheid in de secundaire massa tot $25\% - 30\%$ beperken. En Geval 3 zou de afstand tot 30% beperken. Dus, we vinden dat EM observaties van de afstand en/of de radïale snelheid het meest waardevol zijn en complementair zijn aan de ZG observaties in het beperken van de secundaire massa die typisch niet in EM observaties wordt gemeten. Meting van de radiale snelheid kan ook gebruikt worden om de inclinatie van de bron onafhankelijk te bepalen en dit kan vergeleken worden met de meting van de inclinatie door middel van ZG observaties.

Hoofdstuk 5: Tsjilpende dubbelsterren

In dit hoofdstuk zetten we de analyse van de WD dubbelsterren voort met die bronnen die stralen op hogere frequenties en wiens “inspiral” (frequentie-evolutie) gemeten kan worden, wat ons een ZG meting van de parameter $\dot{f}$ geeft. We onderzochten wat de beperkingen op de baan-parameters zijn, te weten de ZG frequentie, de snelheid van de verandering van f en de versnelling van de frequentie ($\ddot{f}$). Het doel was om vast te stellen of we de precisie hebben die vereist is om de fysica van de getijden in WD dubbelsterren te bestuderen en uit te vinden hoe het combineren van ‘eclipse timing’ metingen van EM data de schattingen van de parameters zal verbeteren. Het voornaamste resultaat dat we hebben gevonden in de context van de fysica van de getijden is dat de parameters $\dot{f}$ en $\ddot{f}$ enkel voor de meest massieve WD dubbelsterren geobserveerd op frequenties $\geq$ 6mHz door ZG data gemeten kunnen worden. Door het meting van de eclipsen degurende 10 jaar (wat een redelijke tijd is gegeven de tijdschaal waarop eLISA zal worden gelanceerd) kan de tsjilp gemeten worden met een verbluffende precisie van 0.1% voor een astrofysisch systeem als J065133.33+284423.3 (hierna J0651 genoemd) [Brown et al., 2011]. J0651 is een verificatie bron die bijna edge-on is met een voorspelde ZG SRV van ~ 10. Dus voor systemen zoals J0651 zal EM data een veel betere nauwkeurigheid in the tsjilp geven dan ZG data. Maar, de snelheid van de tsjilp, $\ddot{f}$ heeft altijd een grote onzekerheid. Het belang van het meten van $\dot{f}, \ddot{f}$, in de context van de studie van de natuurkunde van getijden, treedt op in de verhouding $\ddot{f}f/\dot{f}^2$. Als de dubbelster enkel evolueert onder de invloed van ZG straling, dan is deze verhouding gefixeerd op 11/3 [Webbink & Han, 1998]. Een afwijking van deze waarde impliceert wellicht dat er een bijdrage van de getijden is aan de evolutie van de dubbelster. De gemeten afwijking kan gebruikt worden om de getijden-parameters van de dubbelster te beperken. We vinden dat zelfs met de gecombineerde ZG en EM observaties deze verhouding moeilijk te meten valt, tenzij we extreem massieve WDn waarnemen op frequenties $>$ 100mHz. Maar, het combineren van een precieze $\dot{f} = 0.1\%$ van EM data met ZG metingen van de amplitude en de inclinatie beperken de 2-σ onzekerheid in de tsjilp massa tot 0.11% en de afstand tot $35-19\%$. Enkele-lijn spectroscopische data tezamen met $\dot{f}$ beperkt de afstand tot $\leq 25\%$ en de secundaire massa tot $6-19\%$. Dus, het combineren van $\dot{f}$ en de radïeele snelheid van EM data met ZG is waardevol in het bepalen van de parameters van de WD dubbelster die observeerbaar zijn voor eLISA.

Hoofdstuk 6: Vereniging van dubbelsterren van neutronensterren en/of zwarte gaten

In het laatste hoofdstuk onderzoeken we de parameter-onzekerheden van samensmeltenden dubbelsterren bestaande uit neutronensterren (NSn) en zwarte gaten (BH), die observeerbaar zijn voor de ZG-detectoren op aarde. We onderzoeken de effecten de draaïng (“spin”) van het zwarte gat in neutronenster-zwart-gat-dubbelsterren (NSBH) op de onzekerheden van de parameters als functie van de totale massa en de symmetrische massaverhouding de dubbelster. Het is welbekend dat de tsjilp massa tot hoge nauwkeurigheid bepaald zal worden door zijn sterke afhankelijkheid van de ZG fase, de grootheid die zeer nauwkeurig gemeten kan worden. Het is ook bekend dat het onderscheiden van de individuele massa’s uit enkel inspirals moeilijk zal zijn, omdat de massaverhouding niet zo precies gemeten wordt aangezien de ZG signalen slechts afhangen van hogere post-Newtoniaanse ordes. Talrijke studies hebben aangetoond dat voor dubbelsterren met spinnende massa’s de onzekerheden in de parameters verslechteren, vanwege de sterke correlaties tussen de spin en de massaverhoudingen. We breiden onze studie van uitgelijnde spin-systemen uit met dubbelsterren met een totale massa variërend van 1 tot $13M_\odot$ door gebruik te maken van analytische modellen voer het ZG signaal. We vinden dat het hebben van slechts één spinnend object de onzekerheden in de parameters juist verminderd voor ze massa's en voor symmetrische massaverhoudingen van 0-0.25. Een ander belangrijk resultaat is dat het hebben van een enkel spinnend object met voldoende hoge spin in een dubbelster met een NS nuttig zal zijn in het onderscheiden van een NSBH system van een dubbel-BH systeem. Als beide dubbelsterrenmassa's grote spins hebben, dan zijn de onzekerheden in de spin-parameter β (die de spin-baankoppeling weergeeft) het klienste, vergeleken met andere dubbelsterren met dezelfde totale massa voor lagere mardes van de spin. Dus ondanks dat de individuele massa's onnauwkeuriger bepaald zijn, zijn de spins preciezer bepaald, wat gebruikt kan worden om dubbelsterren met neutronensterren (met altijd weinig spin) te onderscheiden van dubbel-BH systemen (met vaak veel spin).

Vooruitzicht

De eerste vier hoofdstukken over de langlevende galactische dubbelsterren laten in feite de capaciteit zien van de (momenteel geplande) ZG-detectoren in het meten van de meest fundamentele eigenschappen van deze bronnen. Deze hoofdstukken tonen ook het nut van elektromagnetische informatie in het onderscheiden van de correlatie van de belangrijkste parameters van de dubbelsterren die niet met de huidige capaciteiten van de ZG-detectoren gemeten kunnen worden. Dit werk kan ook op verschillende wijzen worden vervolgd. Een voor de hand liggende vervolgstap is het controleren van sommige resultaten met robuustere data-analyse methoden, zoals Bayesiaanse Monte Carlo methodes. Dit zal in het bijzonder nuttig zijn voor het verifiëren van enkele resultaten die we geven voor systemen met lage inclinaties, die gebaseerd zijn op de methode van Fisher waar onzekerheden in bepaalde parameters onbepaald zijn en die kunnen opblazen naar niet-fysische waardes. Ook de parameters die zijn gecorreleerd met ze onbepaalde parameters lijden hieronder, aangezien zij ook slecht bepaald worden door de beperkingen van de Fisher methode, waarin er slechts een gelimiteerde manier is om "priors" in beschouwing te nemen en niet-fysische waardes te vermijden. De Fisher methode doet bovendien per definitie geen echte schatting van de parameter, die in werkelijkheid heel anders kan zijn. Om deze en andere redenen is het belangrijk om enkele van onze resultaten te testen met een robuustere schattingsmethode. Dit werk kan ook vervolgd worden door grondig te onderzoeken welke (WD) massa's welk type astrofysische transients produceren. Als we kijken naar de m_1, m_2 ruimte van WD dubbelsterren, dan is het grofweg bekend wat het lot is van bepaalde combinaties van massa's: of ze smettensame, of ze gaa massa overdragen op een stabiele of onstabiele manier. Het lot van verscheidene combinaties van massa's daarentegen is onbekend, en dit kan erg belangrijk zijn in het begrip van de verschillende types transients die te verwachten zijn van WD dubbelsterren (die ons melkwegstelsel in grote aantallen bewonen) en in het herkennen van hen als tegenhangers van hun ZG-signalen. Dit zal ons uiteindelijk toestaan om ze in meer detail te begrijpen dan dat we zouden kunnen doen met ofwel enkel EM-informatie dan wel enkel ZG-informatie. Het laatste hoofdstuk, dat gaat over samenstellingen van kortlevende dubbelsterren van NS en/of BH, is de eerste stap in een omvangrijker project. Tot dusver hebben we in deze studie gekeken naar het geval van een enkele detector en de signaal van de dubbelsterren bestonden enkel uit de begin fase. Het is aangetoond dat voor bronnen die niet spinnen, de latere fasen berekenen significante informatie aan de ZG signalen toevoegen, die vervolgens de correlaties van sommige astrofysisch nuttige parameters zoals de totale massa en de symmetrische massaverhouding breken. Dit geeft ons een veel betere schatting van de individuele massa's in de dubbelster. Dus we kunnen ook deze samenvoeging en de ringdown signalen voor de uitgelijnde spin pN-golfvormen meerekenen en kijken of de fouten in de parameters ook kleiner worden. We zijn ook van plan om het effect van de correlatie in de afstand en inclinatie op spinnende systemen te bestuderen voor het complete domein in de totale massa en voor een multi-detector netwerk dat in bepaald opzicht het werk van [Nissanke et al., 2010] zal uitbreiden. Een van de meest belangrijke open vragen in dit deelgebied van de astronomie van ZGn is wat de afwezigheid of aanwezigheid van EM-informatie in combinatie met ZG observaties ons zal leren over deze samenstellingen van dubbelsterren en het karakter van zijn componenten, i.e. de NS en BH. Hoofdstuk 6 is een eerste stap in een omvangrijke studie van het belang van de synergie van EM en ZG data.

Curriculum vitæ

I was born in Patan Hospital in Kathmandu, Nepal on 4 October 1984. I have had the privilege of being educated at amazing schools and universities. I spent my kindergarden years in Reliance School in Kathmandu followed by Adarshya Vidya Mandir High School from grades 4-10. I briefly spent 1.5 years in Shuvatara School doing the Cambridge based O and A levels. I attended Linden Hall School for girls (the oldest girls boarding school in the USA) in Pennsylvania, from 11-12th grades with a full scholarship. Then I did a four year undergraduate in Ithaca College, NY with scholarships to fund my way through the college education. I started my astronomy research projects during my undergrad. During the first two years, I did compositional modeling and spectroscopy of X&E-type asteroids on the data I collected at the NASA Infrared Telescope Facility in Mauna Kea in Hawaii under the guidance of Prof. Beth Ellen Clark Jospeh. Then I received Dana Internship funds to do research on proto-planetary systems with intermediate mass stars using spectroscopic data from Spitzer infrared telescope, which I did with Prof. Luke Keller.

After receiving my dual undergraduate degrees in Physics (with Cum Laude) and Mathematics and a minor in the Humanities and Sciences in the US I started my MSc. in Astronomy in Leiden in the Netherlands in 2008. My education was funded by Oort scholarship and my stay was funded by Leiden University Fonds. I did a minor research project with dr. Jarle Brinchmann on the evolution of the fine-structure constant using archive on galaxies. For my major project, which lasted a year, I did a project on the structural properties of galaxies and their evolution with Prof. Marijn Franx.

Finally I moved to Nijmegen to do a PhD in astrophysics with Prof. Gijs Nelemans. I have presented my results during my PhD at various places, Netherlands (Veldhoven, Nikhef, Nijmegen, Astron), Italy (Rome), Japan (Kyoto), US (Maryland, Boston, New York, Chicago, Santa Cruz). I was invited to give one of the plenary talks at the LISA Symposium in Florida, USA.

During my PhD I have assisted in teaching the courses Compact binaries (2011, 2013), Planetenstelsels (2011), Het Heelal (2012).

PUBLICATIONS

Published

1. *Using electromagnetic observations to aid gravitational-wave parameter estimation of compact binaries observed with LISA*
   S. Shah, M. v.d. Sluys & G. Nelemans, A&A, 544:A153, 2012

2. *Using electromagnetic observations to aid gravitational-wave parameter estimation of compact binaries observed with LISA. II. The effect of knowing the sky position*
   S. Shah, G. Nelemans & M. v.d. Sluys, A&A, 553:A82, 2013

3. *Constraining parameters of white-dwarf binaries using gravitational-wave and electromagnetic observations*
   S. Shah, &G. Nelemans, ApJ, 790, 161, 2014

4. *Measuring tides and binary parameters from gravitational wave data and eclipsing timings of detached white dwarf binaries*
   S. Shah, &G. Nelemans, ApJ, 791, 76, 2014

Co-Author

5. *Initial Data Release of the Kepler-INT Survey*
   S. Greiss et al., AJ, 144, 24 (2012).

6. *PAH emission from Herbig Ae/Be stars*
   L. Keller, G. F. Sloan, S. Bus, W.J., Ayala, S., P. D'Alessio, **S. Shah** et. al., ApJ, 2008

7. *Observations of X/M asteroids across multiple wavelengths*
   M. Ockert-Bell et al., Icarus, 195, 2008

8. *E-Type Asteroid Spectroscopy and Compositional Modeling*
   B. E. Clark, S. Bus, A. Rivkin, T. McConnochie, J. Sanders, **S. Shah**, T. Hiroi, M. Shepard, Journal of Geophysical Research, 2004

9. *X-Type Asteroid Spectroscopy*
   B. E. Clark, S. Bus, A. Rivkin, M. Shepard, **S. Shah**, Journal of Geophysical Research, 2004

Collaboration

LIGO-Virgo Collaboration papers from 2013, 2014.

In prep

1. *The role of spin in the mass measurements of neutron star black hole and binary black hole systems*
   S Shah, S. Bose & G. Nelemans

Proceedings

1. *Observations of X/M Asteroids Across Multiple Wavelengths*
   M. Bell et al., AAS, DPS, 39, 2007

2. *Infrared Identification of Herbig AeBe stars in the Small Magellanic Cloud*
   S. Shah, L. D. Keller, N. Chitrakar, AAS, 38, 1140, 2006

3. *Mid-infrared Spectra of PAH Emission in Herbig AeBe Stars*
   L. D. Keller, G. F. Sloan, **S. Shah** et al., AAS, 38, 1006, 2006

4. *Deconvolving Terrestrial Alteration Mineral Spectral Signatures from Meteorite Reflectance Measurements*
   S. Shah, B. E. Clark, T. Hiroi, M. Zolensky, 35th Lunar and Planetary Conference, 1012 (2004).

5. *Multi-Wavelength Observations of Asteroid 2100 Ra-Shalom: Visible, Infrared, and Thermal Spectroscopy Results*
   B. E. Clark et al., 35th Lunar and Planetary Conference, 1120, 2004

ACKNOWLEDGMENTS

My dream of getting a PhD in astrophysics has been realised because I have had the fortune to attend excellent educational institutes in three continents and I have had encouragement from amazing teachers, mentors and friends that I have met during this journey. I feel very lucky to have ended up in our Department (in Nijmegen), where I have felt home right from the start and learnt to be humble and not take things too seriously. I have thoroughly enjoyed all the cakes and gatherings making my stay here very special.

This thesis is a direct outcome of an incredible collaboration with my advisor Gijs Nelemans. Thank you for hiring me and treating me like a colleague and giving me the freedom to explore the topics as I have wanted to but also knowing to balance that freedom with your much needed guidance. Besides the day-to-day research and presentation skills, the most important thing I have learnt from you is to relax and not stress too much. This has made my PhD years so much more enjoyable and perhaps contrary to popular belief, productive. I am also extremely grateful for your financial/moral support to send me on a US tour to present my results; it was one of my most cherished experiences and a great way to conclude my PhD.

I am also very thankful for Marc's collaboration. My early projects accelerated thanks to your expertise. I have really appreciated your patience and humility in our innumerable meetings. I am very grateful to Silvia, Emilio and Willem for listening to my presentation for the US tour and for all the time you gave me for an amazing and constructive feedback. Thanks to Michele for answering my (often very long) emails on LISA-related softwares that allowed me to get through my initial projects very smoothly. I have also had an amazing time with my officemates over the years: Lennart, Pim, Rocco, Satyendra and Jan.

Without my amazing friends my PhD years would have been a difficult one. At one point or another one of you have bore my rant in my difficult times or have been there to share my joyous times. I am grateful to my friends Nethra, Willem, Juliette, Salina, Prashu, Kaley, Carter, Kumar, for colouring my life. I am also grateful to have met Olja

and Ann-Marie during my Leiden years. Your encouragement has meant a lot to me.

I want to acknowledge my amazing professors, Beth, Luke and Bruce from Ithaca College who have given me every opportunity I could wish for and encouraged me through every step.

Pam and Ray, you have been an integral part of me and my education and I cannot express how grateful I am for your persistent support. Baba, thank you for showing me my own way of thinking from early on. Its the best teaching I have from you which serves me till today. Dada, you have always always pushed me towards my dreams, whatever they may be, there is no way I can thank you enough for the gift of your presence in my life. Thank you mummy for accepting my decisions even though it has been hard for you. And finally, my lil one, thanks for always being there. The consistency of your loving care moves me and I hope I can be there for you in that way.